Seismicity and elastic structure of the lithosphere in the Eifel volcanic fields

Zur Erlangung des akademischen Grades eines

DOKTORS DER NATURWISSENSCHAFTEN (Dr. rer. nat.)

von der KIT-Fakultät für Physik des
Karlsruher Instituts für Technologie (KIT)

genehmigte

DISSERTATION

von

M.Sc. Konun Koushesh

Tag der mündlichen Prüfung:	14. February 2025
Referent:	Prof. Dr. Joachim Ritter
Korreferent:	Prof. Dr. Thomas Bohlen

Abstract

A volcano is a consequence of magma intrusion from the asthenosphere into the Earth's lithosphere. Although the majority of the volcanoes are formed in vicinity of the boundaries of the Earth's tectonic plates, there are some few volcanoes that are formed far from these boundaries. The formation of these kind of intraplate volcanoes is explained by e.g., the existence of mantle plumes. Laacher See Volcano (LSV) in the East Eifel Volcanic Field (EEVF), Germany, is one of them. Its crater has a ~2.5 km diameter and it was formed after its last massive eruption (volcanic explosivity index V-VI) about 13,006 ± 9 years ago. LSV was and is known as a dormant volcano which still emits CO_2 and the noble gases He, Ne and Ar of mantle origin.
The occurrence of two typical magmatic weak (*ML* 0.7 and 0.9) deep (40-43 km depth) low-frequency (~2-8 Hz) earthquakes beneath the LSV (~8 km epicentral distance from the south-east of LSV) in Sep. 2013 opened a new chapter to the state of the volcano. Low-frequency (LF) earthquakes in volcanic regions are known as the sign of mass transport and/or volumetric change and/or resonance in the plumbing system of the volcano. Hence, seismologists from the Geophysical Institute at KIT started and conducted densifying the pre-existing permanent seismological station network in the region since July 2014 to increase the chance of recording/capturing such weak seismic signals. They called this experiment Deep Eifel Earthquakes Project - Tiefe Eifel Erdbeben (DEEP-TEE). DEEP-TEE experienced several phases of reconfiguration (keeping quiet / low-noise sites) and expansion (new installation supporting the requirements of a better earthquake detection and localization). The DEEP-TEE dataset is enough sensitive to capture small magnitude ($ML<1$) local events to the depth of uppermost mantle (~40-50 km depth).
An active volcano is a massive natural complex source of vibration. Shortly, the complexity comes from the fact that a volcano is built up of material with the three phases of solid, liquid and gas under a wide range of temperature and pressure. Vibrations in volcanic regions are characterized by their waveform features (ground motion in time), frequency content and partly by the responsible generation mechanism. Tectonic, volcano-tectonic, hybrid, LF, very LF, tremor, tornillo and explosion events are the different types of the typically observed signals in active volcanic regions in which each of these events carries specific features in time, frequency and conceptional domain. Detection of the LF events, as the first precursor sign of a possible eruption, is important for saving time and manage the possible hazard of an eruption, especially in populated regions. On the other hand, LF events are weak and diverse and their signals are easily masked by the environmental level of noise, specially by the noise of the human activities.
The detection of the weak and diverse signals originating from volcanic activities is a challenge, especially in the presence of moderate to high levels of noise conditions (a case matching with the records of the DEEP-TEE dataset). This becomes more challenging for the widely and commonly used template matching techniques (a technique which uses the cross-correlation coefficient between a template and sections of the records as a characteristic function of detection). For that technique the following cases are blind spots: a) there is no a priory waveform information to search for (a case matching with records of newly installed seismometers) and b) the source migrates and, therefore, wavefields select a different ray path than their previously selected source-receiver ray path and this change results in changes in the waveforms (the case matching with magma transportation within the plumbing system of the volcanoes). Also, the developments

in detection algorithms based on Artificial Intelligence still have a large dependency on the amount and diversity of the training dataset which makes it intractable for the case of detection of LF events in the EEVF. There only 75 examples of LF events were reported at the time of starting the development of a new detection algorithm presented in this thesis. On the other hand, the old concept of seismic signal detection, the short/long time average algorithm (STA/LTA) does not need a priory information regarding the features of the signals to search for. But STS/LTA detectors generate a large number of false detections when searching for weak signals with a low signal to noise ratio (SNR) of about 2, the goal for the EEVF. Hence, developing a new detection algorithm matching with the needs for the detection of weak and diverse signals, and matching with the properties of the DEEP-TEE dataset became the main priority of this thesis, after field work and data quality analysis/control of the DEEP-TEE dataset. The developed detection algorithm presented in this thesis, searches signals which match coincidences at neighboring recording stations in space, time and frequency domain. It combines a STA/LTA, a frequency range selection, an energy envelope matching, and a backprojection technique to find a robust detection model. It also initially classifies seismic detections based on their frequency content which plays a major role in searching LF events.

The LF events in the detection output lists are then localized after manually picking the first arrival onsets of the direct P and S waves of the events from the seismic records of the time period July 2014 – December 2022. Location of the LF events is done in several steps: a) the initial absolute hypocentral parameters of the events are obtained using the location program VELEST, b) for the EEVF region the new seismic velocity models KIT5 and KIT6 are generated matching with the observed picks of the events, c) events relocated using KIT6 models, d) the relative relocation algorithm HypoDD is applied to achieve a fine spatial hypocenter structure and e) a jackknifing validity test is used with HypoDD and 100 subsets of randomly selected events to achieve a reliable range of the hypocentral parameters. The results provide a high resolution and a well reliable 3-D projection of the 289 source locations of the LF events beneath the EEVF. These LF events are distributed vertically from 4 km to 45 km depth just southeast of Laacher See Volcano plus a distinct small cluster of LF events located ~12 km to the east of the center of the main cluster of LF events in the Neuwied Basin.

At the end of this thesis, I provide an estimation to the amount of the moved magma volume (MMV) beneath the EEVF within the time period July 2014 – Dec. 2022 using an updated version of the model presented by Aki et al. (1977) and Aki and Koyanagi (1981). This model establishes a relationship between the observed peak-to-peak amplitude of the seismic P- and S-wave pulses and the involved fluid or melt volume. The MMV value presented here is obtained by using twelve very good observations (amplitude measurements) and considering three possible scenarios for the geometry of the magma intrusions relative to the observation points (seismic stations).

The MMV in the studied time period is ~2.9 10^4 m^3 equivalent to a cube with ca. 31 m side length when the median of the all the estimations is taken. Calculation of the uncertainty of this estimation is a challenging issue because the distribution of these estimated MMV is not Gaussian. Therefore, the uncertainty is estimated from the variation of the data points in Fig. 6.4. This gives a range of 1 10^4 – 3 10^5 m^3 which seems to be a reasonable value in the context of petrological studies on the EEVF.

Table of Contents

1 Introduction and outline 1

1.1 Outline of the thesis 4

2 Seismic signals in volcanic regions and possible generation mechanisms 7

2.1 Typical seismic signals recorded in volcanic regions 7

2.1.1 Typical seismic signals recorded in the EEVF 7

2.2 Processes leading into volcanism and the seismic signs of magma ascent 10

2.2.1 Formation of initial magma in interplate volcanos 11

2.2.2 Formation of the initial magma in intraplate volcanos 12

2.2.3 Interaction between magma and the surrounding host rocks in the earth's lithosphere 14

3 Seismic phase picking and earthquake localization routines 23

3.1 Picking onsets of seismic phases 23

3.2 Event localization 26

3.2.1 VELEST (for initial absolute hypocentral parameters of seismic events) 26

3.2.2 HypoDD (in search of a finer map of seismicity) 32

3.3 Volcanism in the Eifel 34

4 The DEEP-TEE experiment 39

4.1 Abstract 39

4.2 Introduction 40

4.3 Monitoring Strategy 44

4.4 Station Selection Criteria and Installation 45

4.5 Noise Analysis and Detection Thresholds 46

4.6 Recording Examples 50

4.7 1-D Seismic Velocity Models (*vp*, *vs*) and Earthquake Relocations 50

4.7.1 Input Data 52

4.7.2 Inversion Strategy 56

4.7.3 Test runs / Probing the model space and resolution 56

4.7.4 Models KIT5 and KIT6 57

4.7.5 Station delay times 59

4.7.6 Stability test 62

4.7.7 Relocation of event catalog 63

4.8 Discussion and Preliminary Results 64

4.9 Conclusions 65

5 Detector A6-DFMSD 67

5.1 Abstract 67

5.2 Introduction 68

5.3 Method and parametrization 70

5.3.1 Input parameters 71
5.3.2 Configuration of Detection Model (CDM step) 71
5.3.3 Detection Field Preparation (DF preparation) 72
5.3.4 Single Station Detection (SSD step) 74
5.3.5 Multi-Station Detection (MSD step) 76
5.4 Test example and results 78
5.4.1 A6-DFMSD parameter setting 79
5.4.2 STA/LTA parameter setting 80
5.4.3 Detection summary 80
5.4.4 Event classification 84
5.4.5 Computational aspects 85
5.5 Discussion 86
5.6 Conclusion and outlook 92
6 An active translithospheric magmatic channel in Central Europe 95
6.1 Abstract 95
6.2 Imaging magma transfer through the continental lithosphere 95
6.3 Observation and identification of magmatic events 97
6.4 3-D image of a translithospheric channel 98
6.5 Discussion 99
7 Summary and outlook 103
8 Bibliography 107
Appendix A: for chapter four (the DEEP-TEE experiment) 121
Appendix B: for chapter five (Detector A6-DFMSD) 137
Appendix C: for chapter six (moved magma volume estimation) 153

1 Introduction and outline

In September 2013, two deep (~40-43 km depth) earthquakes were detected and reported in the East Eifel Volcanic Field (EEVF), Germany where the previously reported earthquakes had never exceeded a depth of about 30 km. From a larger perspective, the occurrence of an earthquake in such a deep position (in the Earth's upper mantle) was a unique feature in Central Europe.

These events were weak with the magnitudes 0.9 and 0.7 ML (Hensch, et al., 2019) and had a low frequency (LF) content (below 10 Hz) compared with the tectonic type events. Their epicenters were close to the Laacher See Volcano (LSV), where the Earth experienced a massive eruption 13,006 ± 9 years ago (Reinig, et al., 2021) which is considered as a young activity in geological time scales. This eruption was the latest eruption at LSV. It is known as a "very large explosion" with the volcanic explosivity index V-VI (the scale is ranged between I and VII) (Schmincke, 2007). The LSV crater with the diameter of 2.5 km (Tomlinson, Smith, & Menzies, 2020) remained after an eruption of >6 km^3 volume of magma (dense rock equivalent: DRE) (Schmincke, 2007).

Knowing these facts about the geological history of the LSV and the occurrence of these deep events raise several scientific questions which need a long period of seismological recording and observation to better answer them. Are these events in connection with the recharging of a possible magma reservoir beneath the volcano? If yes what is the present stage of the volcanic activity of the LSV? If the occurrence of LF events is the sign of magma intrusion into the lithosphere then localization of the events provides a picture of the plumbing system of the volcano, and now the question is: how is this structure distributed beneath the volcano, what is its geometry? How much is the speed of magma migration? How much is the magma volume or flux beneath the volcano? And there are many other scientific questions, however, answering them is out of the scope of this dissertation. To provide the first answers to the most urgent of the above questions, the changes in the spatial and temporal micro-seismic activity (ML <1) in the region must be investigated which requires the following steps to be done:

a) expanding and densifying the existing network of continuously recording seismological stations

b) searching for the seismic signals which do not have the common ordinary characteristics of the tectonic type events but also searching for the diverse set of signals in connection with magmatism

c) picking the first arrivals of the P- and S-phases of the events what is partly difficult for the low frequency events

d) generating/improving 1-D seismic P- and S-wave velocity models by adding the picked phases of the newly detected events (specially the deep events) into the process of obtaining velocity models

e) determining the initial absolute hypocentral parameters (latitude, longitude and depth) of the detected and picked events using the VELEST algorithm (Kissling, Kradolfer, & Maurer, 1995) and the obtained velocity models

f) increasing the resolution of the hypocentral parameters using HypoDD (Waldhauser F. , 2001), the algorithm which links events in the clusters and updates their hypocentral parameters considering that emitted wavefields from an events cluster travel along the same path to the recording stations under certain conditions
g) testing the validity of the obtained hypocentral parameters for each event using statistical methods like jackknifing (Tichelaar & Ruff, 1989)
To estimate the involved volume of magmatic fluids or melts which induce the recorded seismic events, spatial distribution of the events is then used in a model introduced by (Aki, Fehler, & Das, 1977) and (Aki & Koyanagi, 1981).

In connection with part (a):
The seismological group of KIT-GPI conducted the installation of several seismological continuously recording stations in the EEVF in between the existing permanent seismological stations in cooperation with GFZ (Deutsches Geoforschungszentrum Potsdam), since July 2014. They called this project Deep Eifel Earthquakes Project - Tiefe Eifel Erdbeben (DEEP-TEE). Since then, the network has experienced several phases of development and reconfiguration to fulfill the needs for the seismic event detection and localization. As the DEEP-TEE network is located in a region with a high cultural noise due to settlements, traffic, and loose sediments, careful site selection and then reconfiguration (in accordance with the analysed noise level at each station) were a major task. This part is explained in detail in the chapter four.

In connection with part (b):
A volcano is a massive natural complex source of vibrations. The complexity comes from the fact that a volcano is composed of three phases of solid, liquid and gaseous parts. Fluctuations in pressure, heat and the composition of the materials (which is altered/controlled by magma flux) can be rather followed by brittle failure in solid and/or even semi-liquid (magma) states of the volcano and/or followed by mass transport and volumetric change in the plumbing system of the volcano and/or followed by resonance in the conduits and/or followed by surface and subsurface deformations and explosions. On the other side monitoring micro-seismic activity of the volcanoes is a crucial task for hazard assessment specially in residential/industrial areas. It is noticeable that on the Earth 50-70 volcanoes erupt every year (Survey, n.d.) and "more than 800 million people live in proximity to active volcanoes and could be directly impacted by potential eruptions" (Caricchi, Townsend, Rivalta, & Namiki, 2021).
For the tectonic type events the source of vibration is simply a fault system which is partly or completely activated when the existing stress field in the region exceeds a certain limit. The frequency content of the emitted signals has a simple relationship with the magnitude of the events in which the bigger the tectonic event is, a wider frequency range of waves is generated, especially towards lower frequencies. If we consider the same magnitude for a tectonic type and a magmatic type event for comparison, the magmatic type event can be observed in a wider range of seismic signals in both frequency and time domain unlike the tectonic type event.
In the following I summarize arguments that led me to develop a new robust method of seismic event detection algorithm matching with the DEEP-TEE dataset properties and the goal of the

project. At the end, the idea was developed in a direction that might facilitate the detection of weak events in other datasets with wider scientific goals.

1- the existing local earthquake catalogues for the region (including the EEVF) were partly used for the template matching based methods. However, no occurrences of a new type of low-frequency (LF) source/earthquake were identified especially for the stations that were added in the expansion phase of the network. Here I also refer to the unsuccessful efforts of (Schwarz, 2020) in performing a template matching based method (cross-correlation methods) for detection of LF events in the EEVF.

2- the achievements in the AI for event detection still show a strong dependency between the amount of the training dataset and satisfying results whereas in case of detection of the DLFs in the EEVF there were only some tens of events at hand.

3- the region experiences many types of man-made noise in a way that in average the seismic noise level differs between the day-time (08:00 - 16:00 local time) and night-time (16:00 - 08:00 local time) up to 20 dB.

4- the level of seismic noise in the network varies in a way that the difference of the level in the worst case can reach up to 50 dB (comparing the most quiet and noisy station when the frequency range is considered between 1 Hz and 10 Hz, the range in which LF events occur within).

5- the densifying and expansion of the network means availability of more data and the new detector should benefit from this increase of data and at the same time it should keep the ratio of the false number of detection to the total number of detection in a fair/efficient range.

6- in space, the study region is limited to a certain area/zone and activity of the sources outside of this zone takes a minor attention to the project.

7- the network is installed above the sources and the new detector must cope with the large effect of the possible source radiation pattern in a way that if at a station, one of the P or S waves does not appear in the waveform/records, then the detector still should be able to detect the event.

8- in active volcanic regions a diverse set of waveforms are recorded like LF events, very LF events (VLF), tornillos, tremor, explosions, rockfalls, volcano tectonic (hybrid) and tectonic events (Malfante, et al., 2018) (Wassermann, 2011), (Neuberg, 2011), (Chouet, 1996) or (Kumagai, 2009). This fact makes the task of detection harder than in the case that detection of events is only limited to the tectonic type ones.

9- the new detector should support detection of events which may occur in a wide range of depths in the EEVF (potentially up to 50 km).

10- seismic activity in the region does not exceed the local magnitude of 2.9 for the tectonic type events and the magnitude of 1.8 for the magmatic origin type events. The above facts specially the latter one (searching for the small magnitude events) pointed me that any weak signal anomaly may have a potential to be considered as the sound of the volcano or its underlying magmatic processes. Therefore, each signal anomaly must be evaluated through the developed detection mechanism even if it is not seen at many recording stations. This part is explained in detail in chapter five and appendix B where an Adaptive 6-Dimentional Floating-search Multi-station Seismic-event Detector (A6-DFMSD) and its application to low frequency earthquakes in the East Eifel Volcanic Field, Germany is introduced.

In connection with parts (c), (d), (e), (f) and (g)

A first analysis by (Hensch, et al., 2019), using the collected DEEP-TEE dataset up to the end of the year 2018, revealed that 75 DLF events occurred just southeast of the LSV with a max. magnitude of ~1.8 ML. The events are located in four clusters inside a steeply dipping channel which reaches about 43 km depth. After applying A6-DFMSD to the DEEP-TEE dataset for the time period July 2014 – December 2022, close to 450 single LF events were detected in which 331 events could be picked and localized. Picking P- and S-wave first arrivals is done manually using a self-coded/developed toolbox in MATLAB (also in association with the existing KaSP toolbox of KIT-GPI) which supports well manual picking and signal analyzing requirements (it supports e. g. filtering, sorting traces by epicentral / hypocentral distances, providing component products (Plesinger, Hellweg, & Seidl, 1986), calculating signal spectra relative to the noise part of the signal and converting coordinate system from ZNE (Z: vertical, N: north-south and E: west-east motion) to ZRT (Z: vertical, R: radial and T: transversal motion, R and T conversion is in respect with the source-station direction). Instructions and advises for manually picked phases are taken from (Diehl, et al., 2012). The final 1-D P- and S-wave seismic velocity models which are used for determination of the initial absolute event location parameters are obtained in VELEST (Kissling, Kradolfer, & Maurer, 1995). Chapter three provides more details in this regard. The localization steps for LF events are explained in detail in chapter six. The results map the seismically active part below the LSV in a hitherto unresolved way.

1.1 Outline of the thesis

In chapter two, I provide overviews on the seismic signals reported in volcanic regions and on the possible generation mechanisms for seismic signals in these regions.

In chapter three, I expand my routines in picking of the seismic phases by giving waveform examples which include the common challenges in picking phases where the background noise is moderate to high plus a review on volcanism in the Eifel.

In chapter four (and appendix A), the DEEP-TEE experiment (the input dataset of this dissertation) is introduced. This chapter was published in Journal of Seismology in 2024. In connection with the DEEP-TEE dataset my tasks were, fieldwork for installation/servicing the seismological instruments in the EEVF and data analysis for generating sets of the probabilistic power spectral density plots for noise analysis plus the data quality control which helped for a better reconfiguration of the network supporting the detection and localization requirements. In this chapter, the KIT5 and KIT6 seismic velocity models (P- and S-wave) are presented for which my task was providing pick times of P- and S-wave onset from LF events and a catalog of initial absolute hypocentral locations for the deep LF events which increased the reliability of the models specially regarding the deeper velocity layers. There, also I present my picks for one of the relatively well recorded deep LF events.

In chapter five (and appendix B), I present the new method of detection (detection algorithm A6-DFMSD) which I developed in accordance with the DEEP-TEE dataset properties and the goal of the project. There, a diverse set of seismic signals is presented which A6-DFMSD could detect within the relatively moderate noise level dataset of the DEEP-TEE. This work was published in Journal of Applied Volcanology in 2024.

In chapter six (and appendix C), I present a high-resolution image of the seismically active magmatic sources in the EEVF. There, I present the following subjects: a summary in number of detected events and the strategies which I applied to eliminate the outliers after event localization steps, the most repeating values as the final hypocentral parameters of the events obtained through a jackknifing cross-validation test, the event migration in time and depth and the frequency index of the three types of events: LF, tectonic and quarry blasts for comparison. In addition, an estimation to the amount of the moved magma volume within the time period July 2014 – December 2022 beneath the EEVF is presented based on the modified model of Aki et al. (1977) and Aki and Koyanagi (1981). This chapter is prepared for submission to Nature Geoscience.

In chapter seven, I conclude my work with giving a summary and outlook.

2 Seismic signals in volcanic regions and possible generation mechanisms

2.1 Typical seismic signals recorded in volcanic regions

Seismic signals observed in volcanic regions are classified according to their signal properties in time and frequency, and to the possible mechanisms describing the generation of the waves, e. g. in (Wassermann, 2011), (Neuberg, 2011), (Chouet, 1996) or (Kumagai, 2009). In the following paragraph, I refer to the classification done by (Kumagai, 2009) where the physical responsible mechanisms for wave generation in each type of signal is explained shortly and clearly in connection with the volcanological and geophysical observations / evidences. The next section provides a mostly petrophysical review of the literature explaining the formation of magma and the possible mechanisms causing magma to ascend from the initial location of formation to the eruption sites on the Earth's surface.

(Kumagai, 2009) classifies source processes of volcanic signals into three main families: "
(i) brittle failure in volcanic rock triggered by fluid movement,
(ii) transient pressure disturbance caused by mass transport and/or volumetric change, and
(iii) resonance of a fluid-filled resonator excited by a pressure disturbance.
These three processes may be linked to the signals as follows:
(i) to VT (volcano tectonic) earthquake;
(ii) to VLP (very long period) event and explosion earthquake;
(iii) to LF (low frequency) or LP (long period) event, tremor, and VLP event; and
(i) + (iii) to hybrid event.

VT earthquakes, sometimes called high-frequency (HF) earthquakes, are indistinguishable from ordinary tectonic earthquakes but occur in volcanic regions due to process (i). LF or LP events have signals characterized by decaying oscillations, whereas the signature of tremor shows continuous oscillations. These oscillatory signatures can be interpreted as process (iii), in which the excitations are impulsive for LF or LP events and successive for tremor. Most VLP events are characterized by impulsive signatures, which may be generated by process (ii). However, some VLP events show sustained oscillations or decaying harmonic oscillations, which may reflect process (iii). Hybrid events show mixed characters of both VT earthquakes and LP events, suggesting that processes (i) and (iii) both take place at the source. Explosion earthquakes occur in association with eruptions in which process (ii) is dominant."

In Fig. 2.1 the waveforms belonging to each volcanic signal are shown referring to (Kumagai, 2009).

2.1.1 Typical seismic signals recorded in the EEVF

The first analysis of the seismological recordings of the DEEP-TEE dataset is presented by (Hensch, et al., 2019) where the deep LF earthquakes are linked to the ongoing magmatic recharge beneath LSV. There, the 75 LF events are distributed in four spatial clusters within the crust and

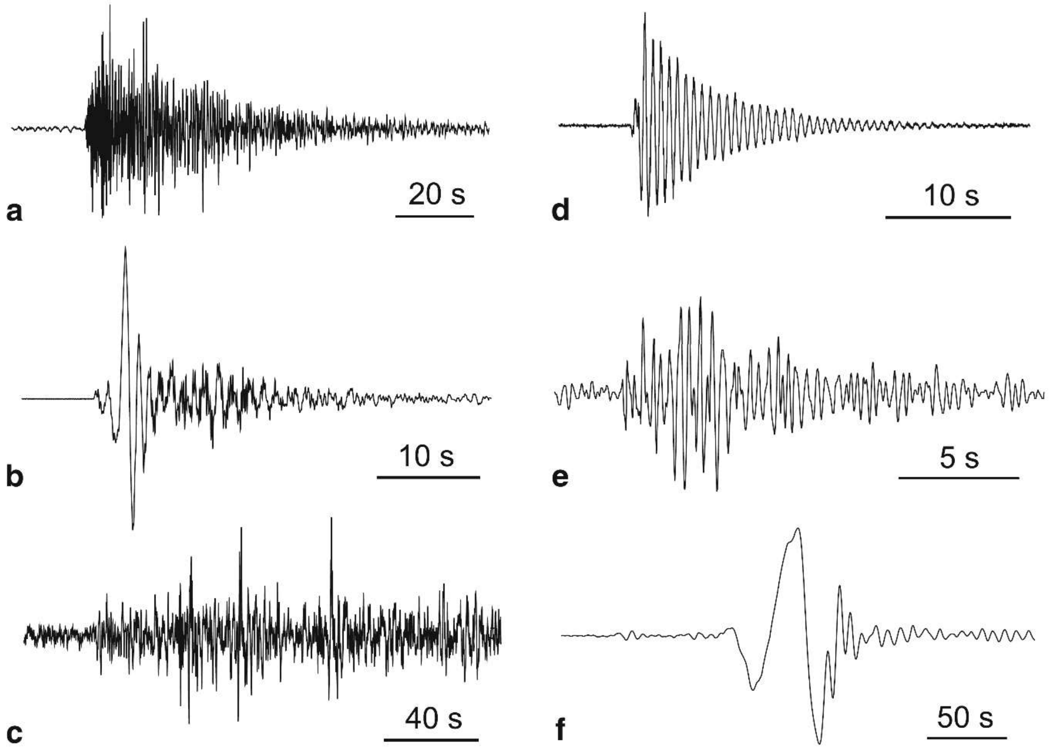

Fig. 2.1 (a) Volcano tectonic (VT) earthquake that occurred between Miyakejima and Kozujima volcanoes, Japan; (b) explosion earthquake observed at Asama volcano, Japan; (c) tremor that occurred beneath Mt. Fuji, Japan; (d) long-period event observed at Kusatsu-Shirane volcano, Japan; (e) long-period event observed at Guagua Pichincha volcano, Ecuador; (f) very-long-period event that occurred beneath Miyakejima, Japan (low-pass filtered at 20 s) (Kumagai, 2009).

upper mantle. Referring to the same work, in Fig. 2.2 “C-clusters are located in the (lower) crust, M-clusters in the upper mantle, numbered from shallow to deep”. The spatial distribution of the clusters forms “an approximately 80° dipping line from the southeast of the LSV to its southern caldera rim”. Tectonic activity of the region is limited mainly to the known Ochtendung fault with an exception. This exception is “a swarm of more than 100 small high-frequent (ML < 1.0) events clustering in depths between 3 and 10 km in two narrow spots close to the village of Glees”. They started “some days after occurrence of strongest C2-sequence in the beginning of June 2017” and their signals content a slightly lower corner frequencies (the frequency in which the spectral amplitude starts a dropping trend) rather than the tectonic events generated by the Ochtendung fault. Fig 2.3 shows the typical recorded signals in EEVF along with their spectrograms and in connection with each cluster of events / type of activities referring to (Hensch, et al., 2019).

Fig. 2.4 provides a set of examples of the detected LF waveforms after applying A6-DFMSD (see chapter five) to the DEEP-TEE dataset. It represents the challenges one might face in the detection of weak diverse types of signal anomalies in the seismological records in volcanic regions and in presence of a moderate noise level.

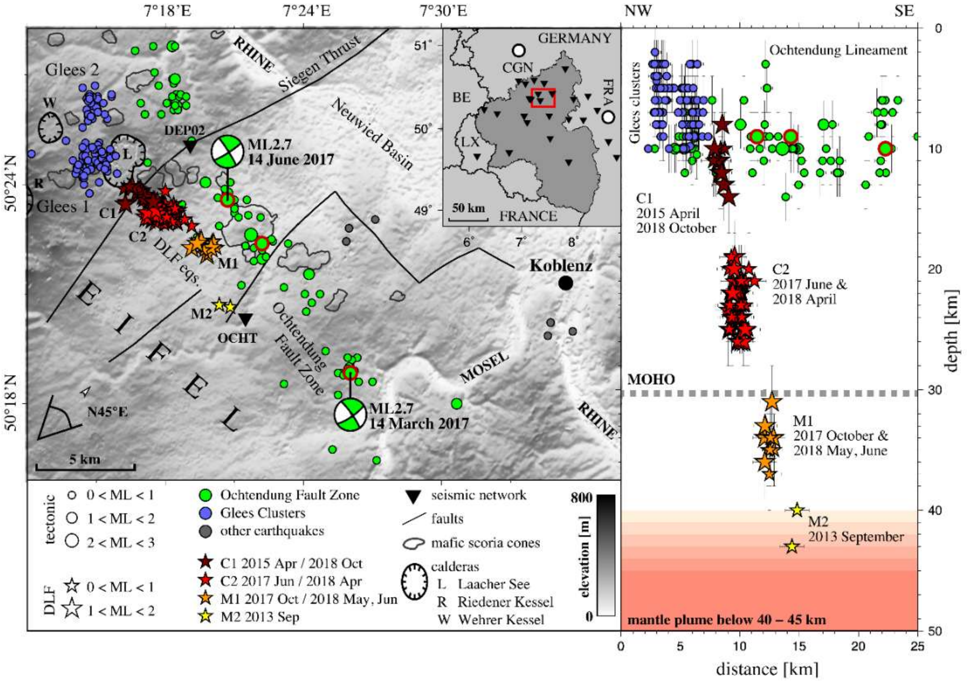

Fig. 2.2 Seismicity in the EEVF mapped by (Hensch, et al., 2019). Green circles denote tectonic type events depicting the trend of the most active fault in the region called Ochtendung Fault Zone. Violet circles denote the swarm of the tectonic type activity which occurred some days after LF activity in cluster C2 in June 2017. The stars colored by depth (cluster position) denote the LF type of activity (Hensch, et al., 2019).

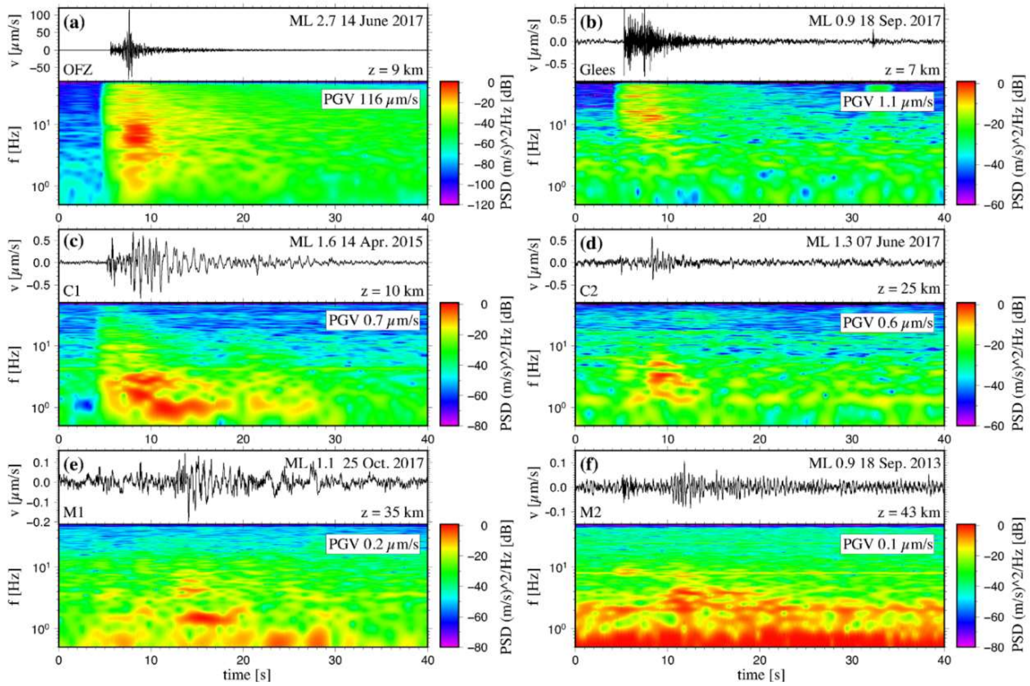

Fig. 2.3 Typical waveform examples and their spectrograms observed in the EEVF up to the end of the year 2018. Left-bottom labels beside the waveforms denote the spatial location of the event. OFZ: Ochtendung Fault Zone, Glees: name of the closest village to the epicenter of the swarm activity, C1: shallower cluster of LF events in the crust, C2: deeper cluster of LF events in the crust, M1: shallower cluster of LF events in the uppermost mantle and M2: deeper cluster of LF events in uppermost mantle (Hensch, et al., 2019).

08

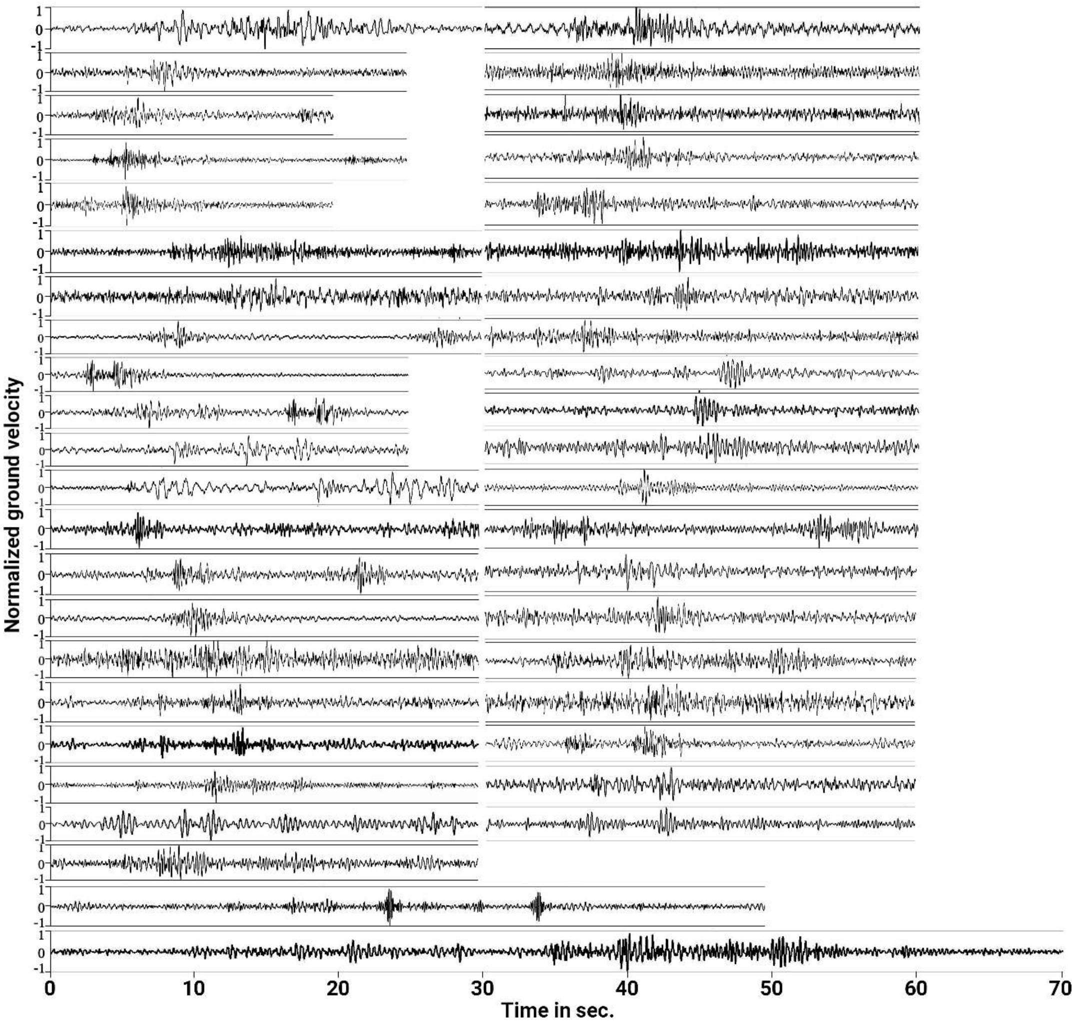

Fig. 2.4 Diversity of the LF signals generated by magmatic activity in the EEVF detected by A6-DFMSD. Waveforms are filtered with the most appropriate band-pass in respect to the frequency content of each event.

2.2 Processes leading into volcanism and the seismic signs of magma ascent

A volcano is a consequence of magma intrusion into the Earth's lithosphere. The most common volcanoes on the Earth are classified as interplate volcanos and they are located in vicinity of the convergent and divergent boundaries of the Earth tectonic plates. In contrast, there are few volcanoes (French & Romanowicz, 2015) on the Earth which formed often far from the tectonic plate boundaries and are called intraplate volcanoes. The difference between these two types of volcanoes is due to the processes which explain the formation of magma in the initial stage in each case and the composition of the magma. Fig. 2.5 is a cartoon which presents the possible geological processes describing volcanism on the Earth (Siebert, Cottrell, Venzke, & Andrews, 2015). There, the convergent plate boundaries (known as subduction zones and the corresponding volcanic arcs), divergent plate boundaries (mid ocean ridges and continental rift zones) and the mantle plume hypothesis are depicted as the three main known processes leading into volcanism on the Earth.

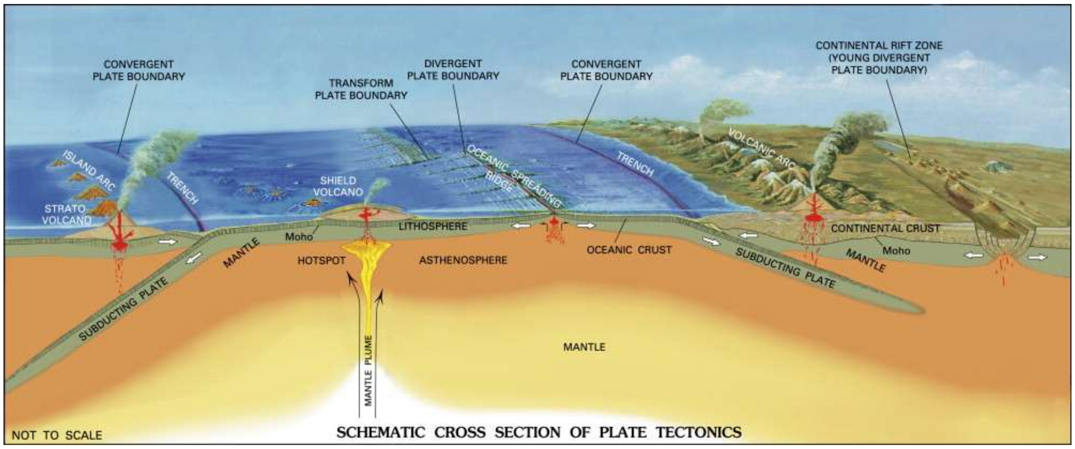

Fig. 2.5 Volcanism on the Earth in connection with the plate tectonic theory and the existence of mantle plume (Siebert, Cottrell, Venzke, & Andrews, 2015).

2.2.1 Formation of initial magma in interplate volcanos

Interplate volcanos are formed close to the tectonic plate boundaries. Volcanism along with the divergent boundaries (~ 65000 km long) on the Earth is explained by existence of convection flow in the upper most mantle (the same explanation for movement of the tectonic plates) which causes magma upwelling and generation of fresh crust. The beginning of this process might form the continental rifts (like the one happening in East African Rift) which in time (geological time scale) can turn into the mid-ocean ridges (MOR).

Volcanism along with the convergent boundaries forms the volcanic arcs. There, a denser plate subducts underneath the less dense plate in presence of gravity. Fig. 2.6 is an illustration of this type of volcanos as suggested by (Nielsen & Marschall, 2017) in a close-up view. Like the divergent boundaries, the driving force of the collision of the tectonic plates is explained by the convection flow in the uppermost mantle. When a plate is subducted, it experiences higher pressure and temperature. Starting from the depth of the asthenosphere, exsolution of H_2O from the hydrous minerals plays a specific role in formation and migration of magma toward the shallower depths. Indeed, the released H_2O decreases the melting point of the surrounding minerals which eases the melting process. Exsolution of H_2O is also suggested as the responsible process in formation of magma and consequently the occurrence of deep volcanic swarms as recently pointed out by (White, et al., 2019) in subduction zones. There, the observation of two deep earthquakes swarms beneath the Mariana Trough is linked to the dehydration of hydrous minerals up to depths of ~230 km. Tracking the depth migration of these deep events suggests that fluids/melts can be rapidly transported through the sub-arc mantle at rates in the order of km/hr.

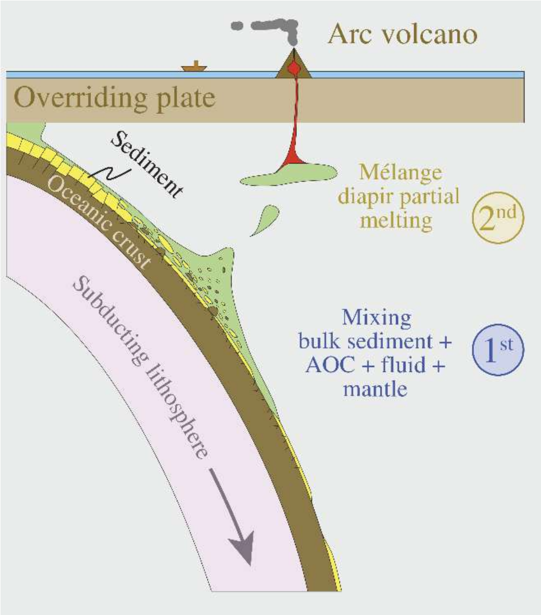

Fig. 2.6 Formation of initial magma beneath an interplate (arc) volcano illustrated by (Nielsen & Marschall, 2017). Arc volcanoes are formed as a consequence of the collision of two tectonic plates where the denser plate subducts under the less dense one and at a certain range of depth in the uppermost mantle the mixed materials of the subducted slab and the upper mantle materials start rising up due to the partial melting (AOC: altered oceanic crust).

2.2.2 Formation of the initial magma in intraplate volcanos

The formation of intraplate volcanoes is explained by transferring material and heat through convection from the core mantle boundary (2900 km depth) towards the Earth's surface. These huge structures are called mantle plumes and they are imaged by seismic tomography studies where the low seismic velocity anomalies are interpreted as a column/area of hot and therefore less dense and less viscose mantle material (French & Romanowicz, 2015) (Ritter J. , 2007) (Ritter, Jordan, Christensen, & Achauer, 2001). Fig. 2.7 presents the schematic elements of the Earth's mantle and the role of the convection flow on the Earth's surface like formation of the crust in mid-ocean ridge and deformation of the crust in subduction zones and hot spot volcanos (Koppers, et al., 2021). The large low-shear-velocity province (LLSVP) and the ultra-low velocity zones (ULVZ) are known as the root of the mantle plumes where they are pictured as the lowest deep velocity anomalies in tomography studies. Fig. 2.8 represents some results of the seismic tomography done by (French & Romanowicz, 2015) revealing the plume structures rooted at the base of the Earth's mantle beneath Hawaiian volcanos, St. Helena, Iceland and east Africa. Fig. 2.9 represents results of the tomography study done by (Ritter, Jordan, Christensen, & Achauer, 2001) in connection with the Quaternary Eifel volcanism revealing a 100 km wide low P-velocity anomaly structure which extends to at least 400 km depth.

Ascending mantle material from such a deep position toward the surface is explained by the buoyant force driven by the denser surrounding materials in presence of gravity (Westaway, 1993) and (Dannberg, 2016). Although magma ascent from the core mantle boundary (CMB) up to the lithosphere asthenosphere boundary (LAB) takes hundreds of million years, magma can pass through the lithosphere in thousands of years and can migrate from the shallow reservoir in the Earth's crust to the surface within some days or even some minutes (Dannberg, 2016). It is noticeable that, "almost all of Earth's most severe biotic crises, including four of the five mass extinctions, are associated with large igneous provinces" (Bond & Wignall, 2014), the events that were supplied by massive mantle plumes (Clapham & Renne, 2019).

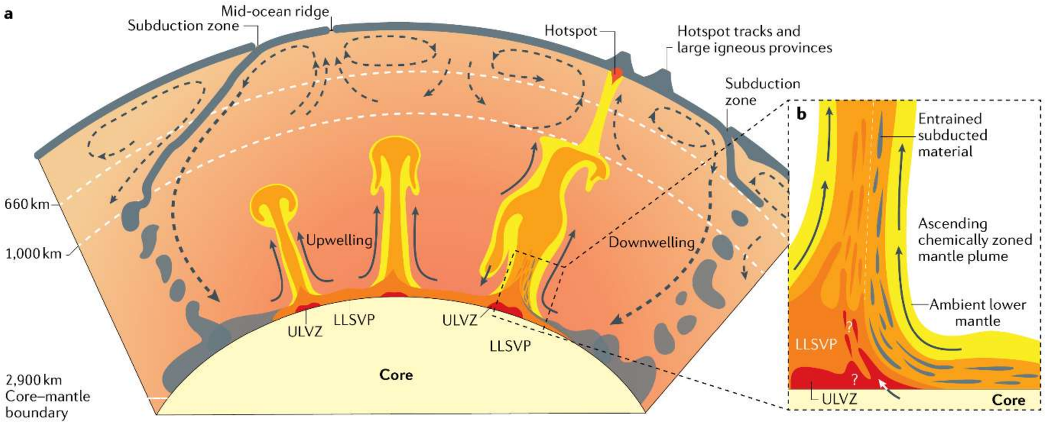

Fig. 2.7 Illustrates a cross section through the Earth focusing on the role of the temperature gradient in formation of mantle convection flow specially the mantle plumes rooted in the large low-shear-velocity provinces (LLSVP) and ultra-low velocity zones near the core–mantle boundary (Koppers, et al., 2021)

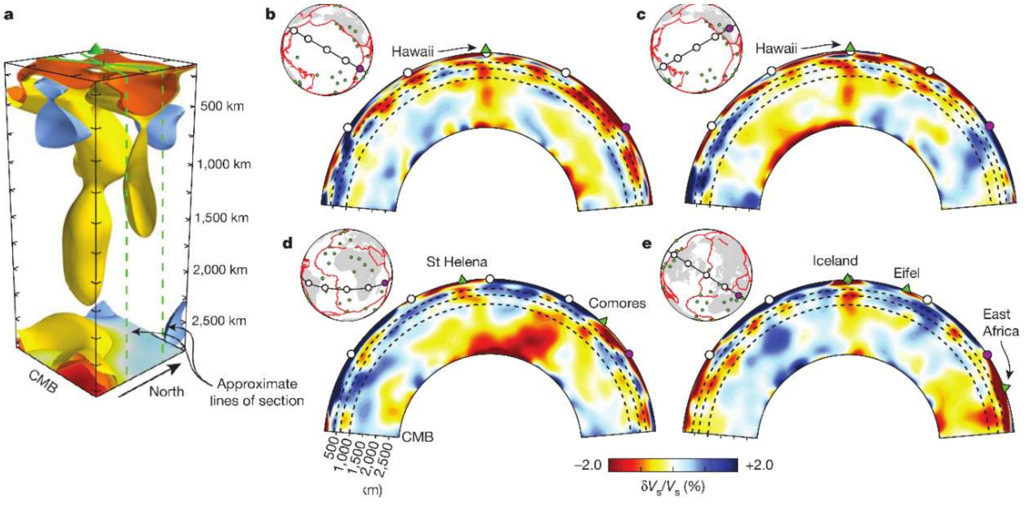

Fig. 2.8 Tomography results of (French & Romanowicz, 2015) reveal some of the mantle plume structures rooted at the base of the Earth's mantle. a) 3-D rendering of the Hawaiian plume, viewed from the southeast b) and c) the cross section of the Earth's mantle presenting the 2-D tomography image of the Hawaiian plume (reddish/yellowish) and the subducting slabs (dark blue), d) and e) the 2-D tomography images of the plumes beneath the St. Helena, Comores, Iceland and east Africa.

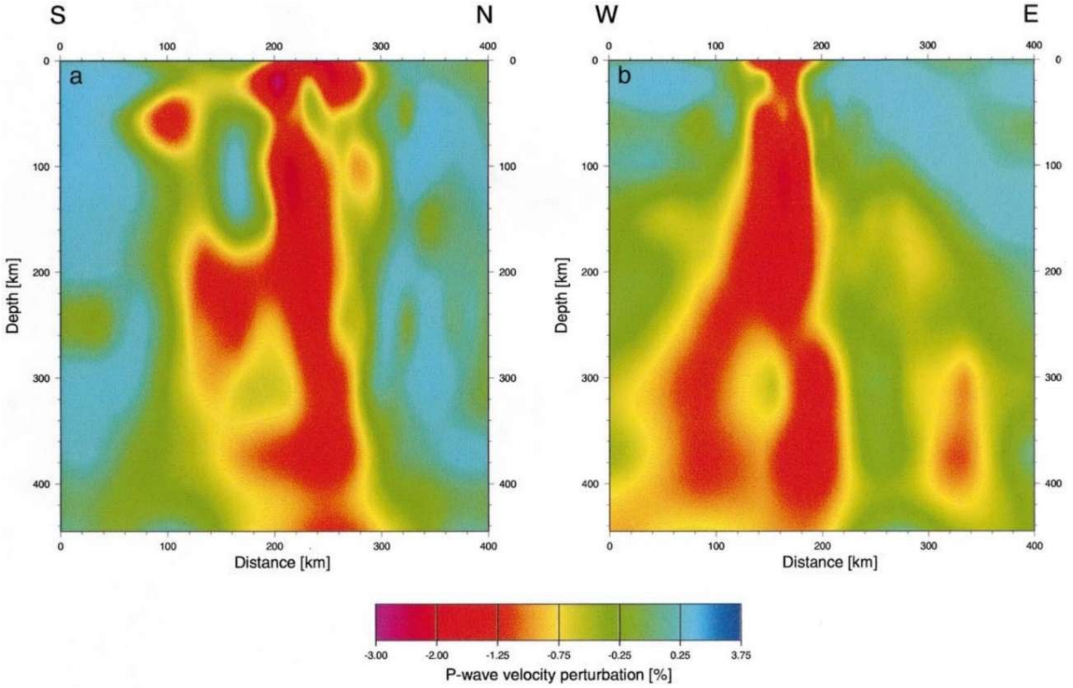

Fig. 2.9 Tomography results beneath the Quaternary Eifel volcanic fields determined by (Ritter, Jordan, Christensen, & Achauer, 2001) reveal a 100 km wide low P-velocity anomaly structure which extends to at least 400 km depth.

2.2.3 Interaction between magma and the surrounding host rocks in the earth's lithosphere

The differences of magma intrusion into the lithosphere in cases of interplate and intraplate volcanos are caused by the composition of the intruded magma in each case which influences e. g. the viscosity and explosivity of the magma and to the different stress regimes in the lithosphere which effect the fracturing / diking processes in the volcanic regions. From here we focus on the case of intraplate volcanoes as it matches with the formation of Laacher See Volcano (LSV) – in relation with this thesis.

a) From the lithosphere asthenosphere boundary (LAB) to the lower crust

By rising magma from a deep to a shallower position, the imposed surrounding pressure decreases. Close to the lithosphere asthenosphere boundary this bears a considerable consequence: there a part of the dissolved material is exsolved from the magma which eases melting of the surrounding hot host rocks (by reducing the melting point of the minerals) and increases the volume of melt. The accumulated magma at the LAB faces more rigid rocks with different rheology. These factors provide a barrier in the way of the magma ascent. Hence, magma expands horizontally and forms a semi-sill structure (Menand, 2011) which is referred to as head of the mantle plumes. Due to the same reasons magma accumulation occurs also below the Moho which is the next discontinuity in the way of magma ascent.

Transporting / penetrating magma from the head of the plume below the LAB through the lithosphere is explained by "buoyancy driven magma fractures" that occurs when the pool of magma reaches a critical size (Turcotte, 1987). There, the buoyancy force might provide the "excess pressure" on which (Aki, Fehler & Das, 1977) and (Aki & Koyanagi, 1981) build up their model for melt ascent. (Aki, Fehler & Das, 1977) propose a model for magma transport in the lithosphere based on a fluid-filled tensile cracks driven by the excess pressure of the fluid. Their revised model (Aki & Koyanagi, 1981) with of "a chain of cracks connected with narrow channels" well explains the features of the observed deep (~40 km) volcanic tremors in the Hawaiian volcanoes. Their model also explains the mechanism which might be responsible for the change in frequency content of the observed magmatic seismic signals in which the frequency content decreases or increases in time step-wisely (in chapter five Fig. 5.9a, one of the observed signals in EEVF which shows such a similar feature is presented too). There, the step-wise decrease in frequency content of the emitted signal is explained as opening of multiple cracks due to a high injection rate of magma into the surrounding rocks and the step-wise increase in frequency content of the signal is explained by closing cracks one after each other. (Aki & Koyanagi, 1981) estimate the corresponding crack size for generating the observed deep tremor signal in Hawaiian volcanos. Based on their kinematic model the dominant period T of the signals generating at the circular cracks is assumed to be equal to $2L/v$ where L is the crack length (diameter) in their model and v is the acoustic wave velocity for magma. They take v equal as 2 kms^{-1} and conclude that the length of the responsible crack (L) for generating the signals with the dominant period of 0.5 s (the typical period for the observed signals in Hawaiian volcanos) will be 500 m. To estimate the thickness of the crack they use the results of their model in calculation of the magma flow rate under the same volcano. They conclude that for the calculated magma flow rate of 700 m^3s^{-1} the thickness of crack must be ~3 mm.

As a unique study in this regard, (D'Auria, et al., 2022) present a correlation between the tomographic images and the source location of the recorded seismic event clusters before, during and after the 85 days eruption phase of the La Palma volcano (Tajogaite) in 2021. They provide evidence in that seismic signals in deep positions near the Moho discontinuity are generated when pressurized magma (inferred from the seismic low velocity anomaly in the tomographic images) is opening its way through the solid rocks (inferred from the seismic high velocity anomaly). There, this intrusion occurred within a narrow width (~1.5 km) vertical structure (dyke form) where active source clusters are distributed for a length of ~5 km in depth. Unfortunately, in their paper one cannot find the other dimension of the intruding area as a 3-dimensional structure. Using a theoretical approach (Shapiro, et al., 2017) assume that the fluid-pressure propagation below volcanoes is governed by the diffusion equation. They use the delay between the observed maximum of the last surge of the deep LF activity and the onset of the Tolbachick eruption (as a five months period) in Kamchatka, Russia to approximately estimate the average hydraulic diffusivity of the feeding system. Then by connecting diffusivity to the permeability of the media and to the properties of the transported fluid they estimate that the average size of the pores, located between the deep (~30 km depth) and the shallow (above 5 km depth) magmatic reservoirs, is in order of a few centimeters. They found it consistent with the possible dimensions of channels filled with the liquid magma in partially molten zones below the volcano.

Based on the spatial distribution of the dikes observed in volcanic fields, (Caricchi, Townsend, Rivalta & Namiki, 2021) point out that, in most of the cases magma ascent does not occur through

the pre-existing faults since fault systems are the consequence of / optimized for shear and not for tensile forces.
Based on observations at 26 worldwide volcanos, including 36 volcanic activity phases, (White & McCausland, 2019) present a forecasting eruption model called “process-based geologic model and the accompanying seismicity prior to magmatic eruptions” which contains four stages. These four stages are marked by numbers in the schematic Fig. 2.10 where the positions of the seismic sources belonging to each stage are marked by red circles.

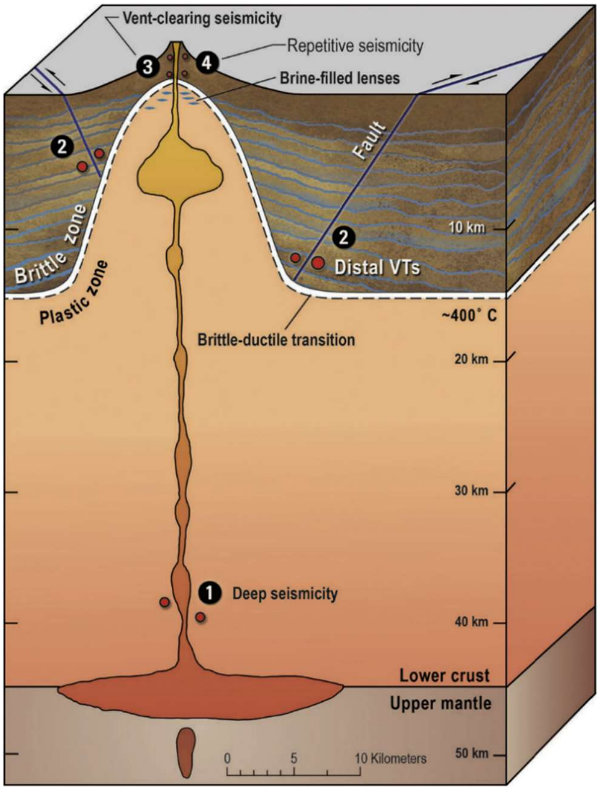

Fig. 2.10 A schematic view of a magmatic zone with a volcano explaining the elements of the model called “process-based geologic model and the accompanying seismicity prior to magmatic eruptions” presented by (White & McCausland, 2019). The numbers indicate each stage of the model beside the corresponding the typical geological element. The red circles indicate the seismic source positions belonging to each stage.

There, as the first stage (stage 1), “aseismic” migration of magma from the uppermost mantle to the lower crust is suggested as one of the possible scenarios. They suggest that in that range of depth the material properties and the high temperature and pressure might prevent generation of seismic waves through fracturing processes (induced brittle failure) and cause the aseismic type of magma migration. However, only in connection with the mantle plumes, the observation of seismic signals emitted from uppermost mantle depth is reported, e. g. for Hawaiian volcanoes (Aki & Koyanagi, 1981) (USGS, 2023), La Palma - Canary Island (Mezcua & Rueda, 2023), Icelandic volcanoes (Greenfield, et al., 2022) and East Eifel Volcanic Field - Germany (Hensch, et al., 2019) which is in contrast with the mentioned scenario suggested by (White & McCausland, 2019). Hence the second scenario of (White & McCausland, 2019) is more likely correct which suggest the waves are attenuated due to the long ray path and/or they are covered by the noise in the region and/or a denser and closer seismological network is required for catching the signals.

b) From the lower crust to the shallow magma reservoir in the upper crust

Based on the (White & McCausland, 2019) model, an increase in the seismic activity in the radial distance between 2 km and 30 km from an eruption site in the volcanic fields is the earliest sign (precursor) denoting a possible eruption at dormant (no activity in the past 20 years or more) volcanoes. This feature is suggested to be true especially for the large explosive eruptions of VEI ≥ 4 (Volcanic Explosivity Index (VEI) ranges from 0 to 8 representing no explosion to a massive catastrophic type of explosion, respectively). They called this kind of seismicity distal VT (Volcano Tectonic) representing the stage 2 of the 4 pre-eruptive to eruptive stages of a volcano and suggest that it occurs in swarm form where it does not contain a mainshock – aftershock pattern like the pattern occurs in typical tectonic type events. They suggest that the intrusion of magma beneath the brittle zone of the crust alters the stress field in the region and triggers induced seismicity on the local pre-existing faults. (White & McCausland, 2019) also suggest that magma transportation within the ductile medium formed around the magma reservoir in the lower crust occurs aseismically (without rupturing process).

The state of the density, viscosity and the volume of magma as the supporting source of heat and pressure is important to determine if the magma is able to pass though the existing stress barriers in the way of migration to the surface. Likelihood of reaching magma to the surface increases for the magma with lower density and viscosity, and for the magma which is supplied by a large volume reservoir. However, in most of the cases not all of these three components are provided at once (Caricchi, Townsend, Rivalta, & Namiki, 2021). Hence, magma reservoirs (magma chambers) are the most common structures located below the volcanic regions on the way of magma ascent.

The accumulated magma in the shallow reservoir in the upper crust undergoes changes due to the drop in the imposing pressure and locating in between cooler rocks. There, some part of the magma which is mainly in contact with the host cool rocks is crystalized in time and forms a relatively impermeable seal. As a consequence of crystallization, the amount of e. g. H_2O and CO_2 molecules (volatiles) increases in the magma. Concentration of such kind of molecules in magma reaches to a point that the melt cannot longer hold all of them and they convert into the gas phase forming bubbles. In petrology this process is called "second boiling". The heat capacity of the magma is decreased by H_2O-rich fluids and drive remelting. Consequences of this process is the increase of the pressure in the magma reservoir and the formation of less viscous and less dense magma which are the important components for describing eruptible/ascendable magma.

c) From destabilized shallow magma reservoir in upper crust to eruption

Injection of magma from deeper positions to the shallow magma reservoir and second boiling are the internal sources providing overpressure for occurrence of tensile failure in the wall rocks of the magma reservoir (reservoir failure). Nevertheless, with time the elasticity of the wall rocks of the long-lasted reservoir undergoes changes due to being in contact with hot materials and chemical alteration by the magma volatiles. The first one increases the resistivity of the wall rocks against rupturing, because the heat increases the capability of the rocks for deformation without fracturing. In other words, in presence of heat rocks lose their elasticity and gain plasticity. Chemical alteration can decrease the resistivity of the wall rocks by converting stiff minerals to the weaker ones. (Caricchi, Townsend, Rivalta, & Namiki, 2021) by referring to (McLeod & Tait, 1999) (Cañón-Tapia, 2019) provide elastic models for the stress around the spherical magma chambers and suggest that for opening a tensile crack at the depth of ~8 km ~400 MPa overpressure is required. However, no evidence supports that magma experiences such an extreme overpressure in that depth. Hence, they conclude that irregularities or weaknesses in the margin of magma chamber or deviation of magma chamber from a spherical shape are the factors which ease formation of fractures in substantially lower level of overpressure.

Magma reservoirs in a critical state can also be destabilized and start volcanic eruption by external triggering mechanisms. (Caricchi, Townsend, Rivalta, & Namiki, 2021) summarize and provide a wide view to this type of triggering mechanisms: loading or unloading, large earthquakes and rainfalls which mostly play a role in small stress variation and/or rock strength. There, climactic eruption and degassing, deglaciation and related erosion, gravitational forces exerted by the sun and moon which modulate stress in the Earth's crust are the examples in connection with *loading or unloading* triggering mechanism. Dynamic stress propagated from *large earthquakes* through the seismic waves can help to initiate crack propagation into the host rock which are close to failure. They suggest that heavy rainfalls change the pore pressure and destabilize volcanic domes by helping in hydrothermal alteration which weakens the minerals and promote dome collapse.

(Dinger, et al., 2019) analytically evaluate the effect of the small stress variation on the volcanic eruption. They model a simplified magmatic system and use the small periodic stress variation generated by the local tides as input and derive a periodical vertical displacement of magma in the conduit. They found that a small stress variation significantly increases the bubble coalescence rate at a depth of several kilometres by up to several multiples of 10%, the process which facilitates separation of gas from magma and enhances volatile degassing. (Girona, Huber, & Caudron, 2018) by monitoring of 13 years volcanic activity of the Ruapehu volcano in New Zealand conclude that the volcano is sensitive to fortnightly tides only when it is close to explode.

When the shallow magma reservoir is destabilized due to the internal and/or external triggering mechanisms, the next phase of volcanic activity (stage 3) begins. (White & McCausland, 2019) point out that "the transition time from the onset of stage 2, distal VT seismicity, to the onset of the stage 3, vent-clearing, may be as little as minutes to six years" by referring to observations by (Nakada, Shimizu, & Ohta, 1999) and (White & McCausland, 2016). (White & McCausland, 2019) introduce stage 3 by vent-clearing seismicity. This stage contains the most variety of the seismic signals throughout the whole 4 stages of the volcanic activity. Events in this stage have shallow depth (<3 km). They mostly are LF events and tremors located in a narrow band in frequency domain. In this stage, VTs and very low frequency events (VLFs) occur occasionally. Occurrence of VLFs is explained by transient pressure variations in the volcanic edifice (Neuberg, 2011) which might be followed by inflation and deflation on the surface. Occurrence of coupled LF events ends this stage where the first LF event is deeper and referred to contained explosion and the second one correlates with an explosion on the surface. Localization of LF events is hard because the P- and S-phase onsets are emergent (White & McCausland, 2019). Hence the shallow

LF events are localized by a large error which reduces the resolution of magma migration path in the seismicity maps.

Indeed stage 3 starts when the relatively impermeable ductile-brittle transition seal, formed around the shallow magma reservoir, is ruptured. The ductile-brittle transition seal is the boundary that separates the hydrostatic pressure regime from a lithostatic pressure regime (Fournier & Dzurisin, 2007) and is made of crystalized minerals in long lasted reservoirs. By rupturing the transition seal magmatic fluids, which already exsolved from the rest of the magma and placed above the reservoir due to the buoyancy, are exposed by a pressure drop. Decompression changes the phase of the liquid to gas. Evaporation and boiling of the fluids thins the seal in time and ease re-rupturing. Magma rising and the interaction of the heat with the hydrothermal system causes non-eruptive subsurface phreatic explosions. Subsurface non-eruptive explosions ease magma ascent by forming vent structures (White & McCausland, 2019).

Following (White & McCausland, 2019) stage 4 is associated with the final magma ascent. It is characterized by repetitive seismicity in which events in time become similar in amplitude and inter-event spacing. When the inter-event spacing reduces it forms tremor-like signals. Events in this stage have the features of LF, hybrid or VT and occur in 2 km or less depth. (White & McCausland, 2019) suggest that long duration repetitive events which persist in time for hours to days/months can be a sign of passive dome extrusion whereas occurrence of non-persistent events with duration of minutes can be a sign for explosive eruption.

(Chouet, 1996) presents a model which explains the features of the LF events while mass transportation condition is also satisfied. He considers a fluid-filled crack / conduit as a resonator which the resonance is excited via an arbitrary initial condition. There, geometry of the crack (such as length, width and the aperture of the crack), physical property of the fluid and solid (such as P-wave velocity, rigidity of solid, acoustic wave velocity, bulk modulus of fluid, and density of the solid and fluid), the pressure fluctuation in time and space and the boundary condition to the crack and its surrounding are introduced as the effective parameters on the resonance characteristics. At the time of his work in year 1996 the triggering mechanism (as he phrased as “the excitation mechanisms of LP events and tremor”) was still unknown until the year 2005 when fault textures in volcanic conduits were discovered. After discovering fault textures in volcanic conduits and performing lab experiments on different composition of magma as the sample, (Tuffen & Dingwell, 2005) (Tuffen, Smith, & Sammonds, 2008) introduce the mechanism which generates seismic signals inside the conduits. Based on their observation fracturing and faulting can happen in the magma body itself, depending on the composition of the magma and even if the magma temperature is 900°C. They prove that the fracturing/faulting mechanism within a magma body is the same mechanism that explains faulting/fracturing in the brittle part of the crust causing common tectonic earthquakes. (Tuffen & Dingwell, 2005) illustrate the different phases of seismic cycles within rising magma (Fig. 2.11). It contains four phases. The first two phases are seismogenic starting by an initial fracture following by stick-slip behavior. The third and fourth phases are aseismic presenting cohesive deformation and complete healing, respectively.

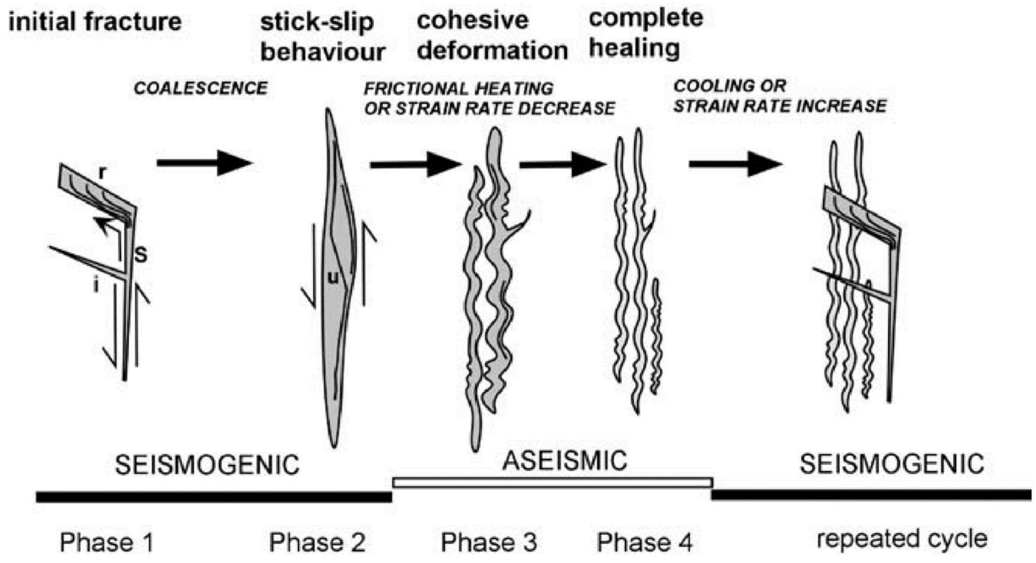

Fig. 2.11 Cartoon illustrating the different phases of seismic cycles within rising magma. S corresponds to a fault vein, i to injection into the vein, r to the reservoir zone, and u to the ultracataclasite zone (Tuffen & Dingwell, 2005)

Monitoring seismicity in volcanic regions reveals the seismically active structure of a volcano. It can provide worthful spatial and temporal information like the geometry of the plumbing system, the speed and migration direction of magma and other worthful information such as number of events in depth which is used for estimation of the magma volume which intruded in each stage of activity or, in over all, the total volume of the moved magma beneath a volcano. Fig. 2.12 is an example of such a worthful information which merged into a cartoon presented by (Hotovec-Ellis, et al., 2018). There, the deep fluid (magma) pathways beneath Mammoth Mountain, California, is well pictured by monitoring of the seismicity in the region. In that study the speed of episodic fluid ascent from the lower to the mid-crust is obtained as the order of kilometers per day. The spatial distribution of the brittle-failure earthquakes denotes the magma chamber border (the yellow area limited to the gray dots in Fig. 2.12) where aseismic type of magmatic activity is expected (Hotovec-Ellis, et al., 2018). One of the interesting features which is revealed also in that study is the downward migration of the events. (Roman & Cashman, 2018) introduce degassing as the responsible mechanism in occurrence of events which migrate downward (from shallower to the deeper position) in the volcanic regions.

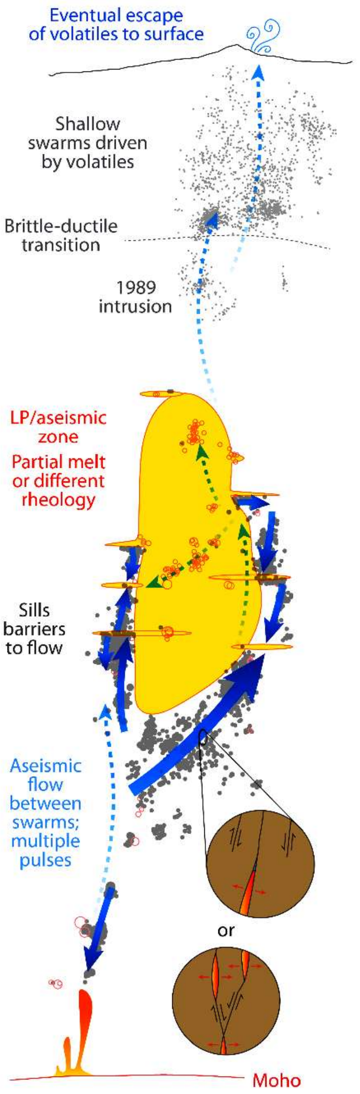

Fig. 2.12 Monitoring seismicity in volcanic region is revealing worthful spatial and temporal information like the geometry of the plumbing system, the speed and migration direction of magma in addition to the number of events per cluster. Here some part of such information is merged by the geological explanations in a cartoon revealing the deep fluid (magma) pathways beneath Mammoth Mountain, California (Hotovec-Ellis, et al., 2018). The gray dots denote the location of stick-slip (brittle-failure) earthquakes with waveforms similar to tectonic earthquakes and the open red circles denote the location of LF events. The earthquake migration (inferred as the fluid migration) direction is marked by the solid blue arrows and the dashed blue arrows indicate the possible aseismic flow interpreted from the gaps between the observed swarms. The yellow area indicates the magma chamber core interpreted from the aseismic zone expanded up to the border of the brittle-failure earthquakes. The insets denote two different possible fracturing explaining different type of observed focal mechanisms in the region.

3 Seismic phase picking and earthquake localization routines

3.1 Picking onsets of seismic phases

The ground motion velocity is recorded by a seismometer and its accompanying devices in an accuracy of some nm s^{-1}. The record (seismogram) contains three components shortly naming as Z, N and E components. Z, N and E components present the ground motion velocity in the vertical, the north-south and the west-east direction of motion in time, respectively.

Some part of the released energy at a seismic source is transported by waves to the recording stations. Emitted waves move particles of the medium (the Earth) in different manners and travel with different speeds. Fig. 3.1 presents a seismogram of a shallow teleseismic event (far distant earthquake) in which the onset of different types of seismic waves are marked with different colors. Some of these waves are generated at the same position of the source and travel though the Earth. These types of waves are called body-waves and are divided into two types of waves itself, the P- (primary) and the S- (secondary) waves (in Fig. 3.1 marked as blue and green areas, respectively). In relation with the direction of the ray-path, the P-waves move the particles longitudinally. P-waves have the highest speed rather than the speed of the other types of waves; hence they are the first motions appear in the records after releasing energy in a seismic source. The S-waves move the particles transversally, in relation with the direction of the ray path and appear in the records after arriving the P-waves. By hitting/passing the P- and S-waves to the Earth's discontinuity layers (layers with different (elastic) properties) they might experience reflection, refraction and conversion to other type of the waves and travel the rest of the path in different direction, type of motion and speed.

The surface waves are generated when the P- and S-waves hit the Earth's surface. Surface waves are divided into two types: the Love and Rayleigh waves. Their speed is less but close to the S-waves speed. Relative to the ray path direction, the Love waves move the particles transversally where the transverse component is along the Earth's surface plane and perpendicular to the ray path direction. The Rayleigh waves move the particles both transversally and longitudinally. The transverse component of the Rayleigh waves is perpendicular to the transverse component presenting the Love wave motion (it is vertical to the Earth's surface and perpendicular to the ray path direction). In Fig. 3.1 onset of the Love and Rayleigh waves are marked by red and yellow area, respectively.

Since the motion of each type of the waves is relative to the ray path direction, conversion of the coordinate system of Z, N and E components to a rotated one (relative to the trajectory of the ray path on the Earth's surface) is the common initial thing that a seismologist needs to do. This is required to distinguish different phases of the waves in the record and therefore better picking the onset of the arrival phases. In Fig. 3.1 the waveform of the teleseismic earthquake in the rotated coordinate system is also presented where T represents the transversal and R the radial components. In this rotated coordinate system, one might pick the onsets of the P and Rayleigh waves from the Z and R components, and onset of the S and Love waves from the T component.

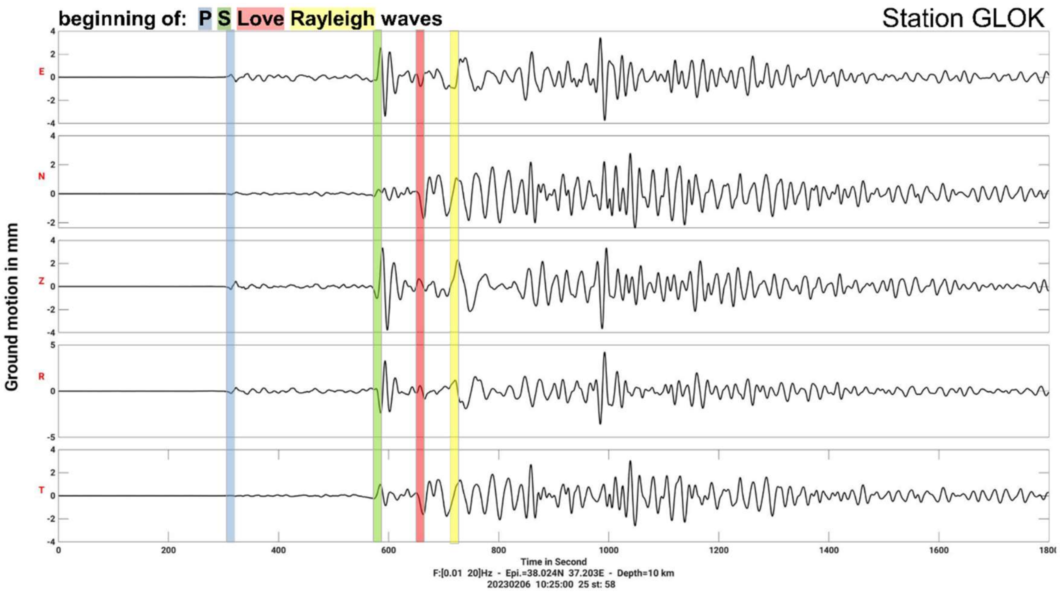

Fig. 3.1 Waveforms of a teleseismic shallow event recorded at the DEEP-TEE network (chap. 4). The red letters E, N, Z, R and T respectively denote the west-east, the north-south, the vertical, the radial and the transversal components. The onsets of different seismic phases are marked by different colors coded on the top of the panel.

Readability of the onset of a phase depends on the SNR, the way that the onset of the phase appears in the record (being an emergent or impulsive phase) and the frequency content of the phase. (Diehl, et al., 2012) provides essential knowledge on how to pick phases of an earthquakes on the records which is the same source that I followed its instructions in picking time onsets. I found it worthful to emphasize here that radiation pattern affects picking procedure when local events are picked using records of a local network. One must be aware that due to this phenomenon the same phase might appear in the records of different stations with totally different features in amplitude form. It must not be a surprise if the same phase in one station appears as a strong impulsive upward phase and in the other station as a weak emergent downward phase.

Fig. 3.2 to Fig. 3.5 present the routine that I applied to pick the direct P and S phases of the LF events in EEVF using the records of the stations at the DEEP-TEE experiment. In these figures the picked onset times of the phases with a low to moderate SNR is presented which demonstrates the typical challenges in picking of LF events in my PhD project. After detecting events using the A6-DFMSD method, which is discussed in the chapter five, for each detection all the available records are first plotted in a wide time window (~35 s), in the typical range of LF events frequency content (1.5 Hz to 10 Hz). Since epicentral location of the LF events are limited to a certain small area (ignoring the small cluster of events in the Neuwied Basin which are found later), the center of the known LF events near the Laacher See Volcano is used as the center of the rotated coordinate system for generating the plots of the waveforms. After a first location, the actual hypocentral parameters of the event are used for rotation of the coordinate system. Also, in these plots the records of the stations are sorted to this hypocenter by distance. This procedure makes the decision on picking phases (even as the very initial step) easer, since the final location of the events is not expected to be far from this preliminary location. Fig 3.2 presents this step.

Then the records with a low SNR are removed from the plots and a wider range of frequency band-pass filter (1 Hz to 45 Hz) is applied to the raw data and records are replotted to check if an unwanted very local manmade activity (like passing a car nearby the station) does not coincide with the P and S phase onsets of any records. In such a case the records of that station are not involved in the further picking procedure. Fig. 3.3 presents this step. Then the records of the selected stations are replotted by the most appropriate frequency range (normally in the range of 1 Hz to 12 Hz). Also, the time window gets shorter and the amplitude is zoomed for the records which allow the highest magnification of the phases (in Fig. 3.4 for the records of the stations OCHT, NICK, DEP10 and GLOK). Afterwards, onset times for P and/or S phases of the zoomed records are picked by a click on the position of the phase on the plots and they receive a quality (readability) weight manually and finally they are saved. In general, the onsets of the P phases are picked on the Z (vertical) component but in some cases where the readability of the phase on the Z component is less than the R (radial) component (e. g. due to the transient higher noise level in the Z component) then the pick is taken from the R component. Onset times of the S phases are taken from the T (transversal) component. When the source of the event has a depth more than twice the epicentral distance of the event, picking the S phase from the R component might be done, if the onset of the S phase on the R component can get a higher readability weight. The reason behind this is the fact that in such a source-station configuration the determination of the transversal and the radial components is more affected by the uncertainty presented in the initial epicentral location parameters of the event. In other words, the ray path of a deep event hits the local station almost vertically and if the station is located above the source, then all directions are located on the surface plane of the Earth can be potentially assumed as the transversal component of the ground motion.

The quality weight is a value between 0 and 3 demonstrating the best to the worst range of the readability of the picks, respectively. In Table 3.1 the picking uncertainty ranges considered in my study are presented according to the different classes of events. I found this classification necessary when I noticed that for example the quality weight 0 in the standard mode of VELEST (Kissling, Ellsworth, Eberhart-Phillips, & Kradolfer, 1994) (the localization program which I used for finding the hypocentral parameters of the events) can even have 100 times more influence than the quality weight 3 on the location solution. Hence, I tried to manually classify events in classes A, B and C and by this way have a control on the influence of the quality weights accepted by VELEST (Kissling, Ellsworth, Eberhart-Phillips, & Kradolfer, 1994) on events in each class. Furthermore later (see chapter six and appendix C), when the hypocentral parameters of the events are planned to pass though the statistical reliability test (jackknifing method), this classification helps to converge the final results more weighted towards the best observation of the picks therefore obtaining a more reliable set of results.

The picks are saved in a format which is ready to use as the input for the localization program VELEST (Kissling, Ellsworth, Eberhart-Phillips, & Kradolfer, 1994). The picks taken from the high SNR records then are used to find the initial hypocentral location of the event after localization by VELEST (Kissling, Ellsworth, Eberhart-Phillips, & Kradolfer, 1994) (the first round of localization).

Table 3.1 Picking uncertainty ranges considered in my study in respect to the quality weights and the event classes

	Uncertainty in s			
	Pick Quality 0 (best)	Pick Quality 1	Pick Quality 2	Pick Quality 3 (worst)
Event Class A	0.01 – 0.05	0.05 – 0.15	0.15 – 0.25	0.25 – 0.4
Event Class B	0.01 – 0.10	0.10 – 0.20	0.20 – 0.30	0.30 – 0.4
Event Class C	0.01 – 0.15	0.15 – 0.25	0.25 – 0.35	0.35 – 0.4

The initial hypocentres taken from the output of VELEST (Kissling, Ellsworth, Eberhart-Phillips, & Kradolfer, 1994) then are used to rotate the coordinate system and sort the records according to the epicentral distance of event. This helps the picking process in which one can then add picks from the rest of the stations with a lower SNR. Fig. 3.5 presents the plots after sorting the traces to the initial hypocenter parameters of the event. Then the readable phases from all the records are zoomed, picked/repicked and saved as the final picking file of the event. Depending on the readability of the phases the mentioned above picking procedure might be repeated once or in some cases two times more to achieve a consistent quality of the picks.

Later the picking files of the events are merged and used e.g. in chapter four by collaborators to generate the KIT5 and KIT6 models, the 1-D P and S wave seismic velocity models for the EEVF including additional pick times from tectonic events. For these models, the picks of the deep events play an effective role in the determination of the velocity models specially regarding the deep layers below the tectonic activity. Also, the same picking files are used later for getting updated hypocentral parameters using the VELEST (Kissling, Ellsworth, Eberhart-Phillips, & Kradolfer, 1994) localization program after determination of the KIT5 and KIT6 models. The updated hypocentral parameters and their corresponding picks are used in another localization program HypoDD (Waldhauser & Ellsworth, 2000) where the relative relocation parameters for each event is calculated. The relative relocations provides a higher resolution image of the structures generating seismic waves.

3.2 Event localization

3.2.1 VELEST (for initial absolute hypocentral parameters of seismic events)

The pick file of an event, coordinates of the recording stations and an approximation of the seismic velocity structure of the region (seismic velocity models) are used to determine the hypocentral parameters (latitude, longitude, depth and the origin time of the source) of the event. Supposing an ideal (unrealistic) form of the problem, in which the exact three-dimensional velocity structure of the region plus the hypocentral parameters of a source are known, then the onset of the arriving phases at the known location of the recording stations can be calculated by the ray tracing method (a forward approach) with the error in the range of the computational limitations in numerical modeling e. g. the size of the model elements (grids).

But there would not be always a one answer as the hypocentral parameters of the source, if the known part of the problem were the exact three-dimensional velocity structure of the region, the

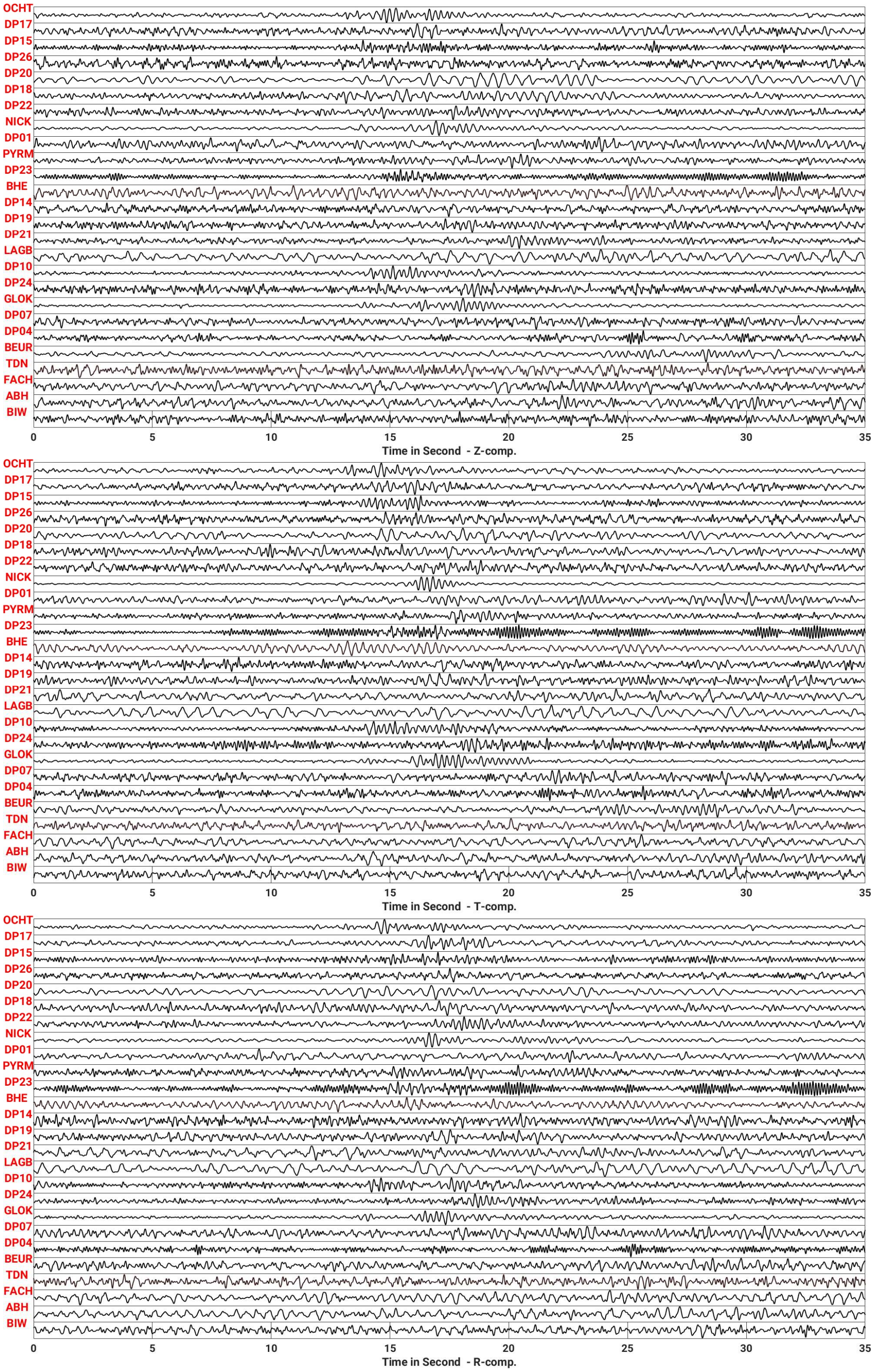

Fig. 3.2 Picking procedure routine part one. For each detection at first a wide window in time (~35 s) in vicinity of the detection is selected and all the available records are filtered and plotted in the frequency range of LF events (1.5 – 10 Hz). Since epicentral locations of LF events are limited to a certain small area, the center of this area is used for the initial coordinate rotation (converting from the Z, N and E coordinate system to the Z, R and T).

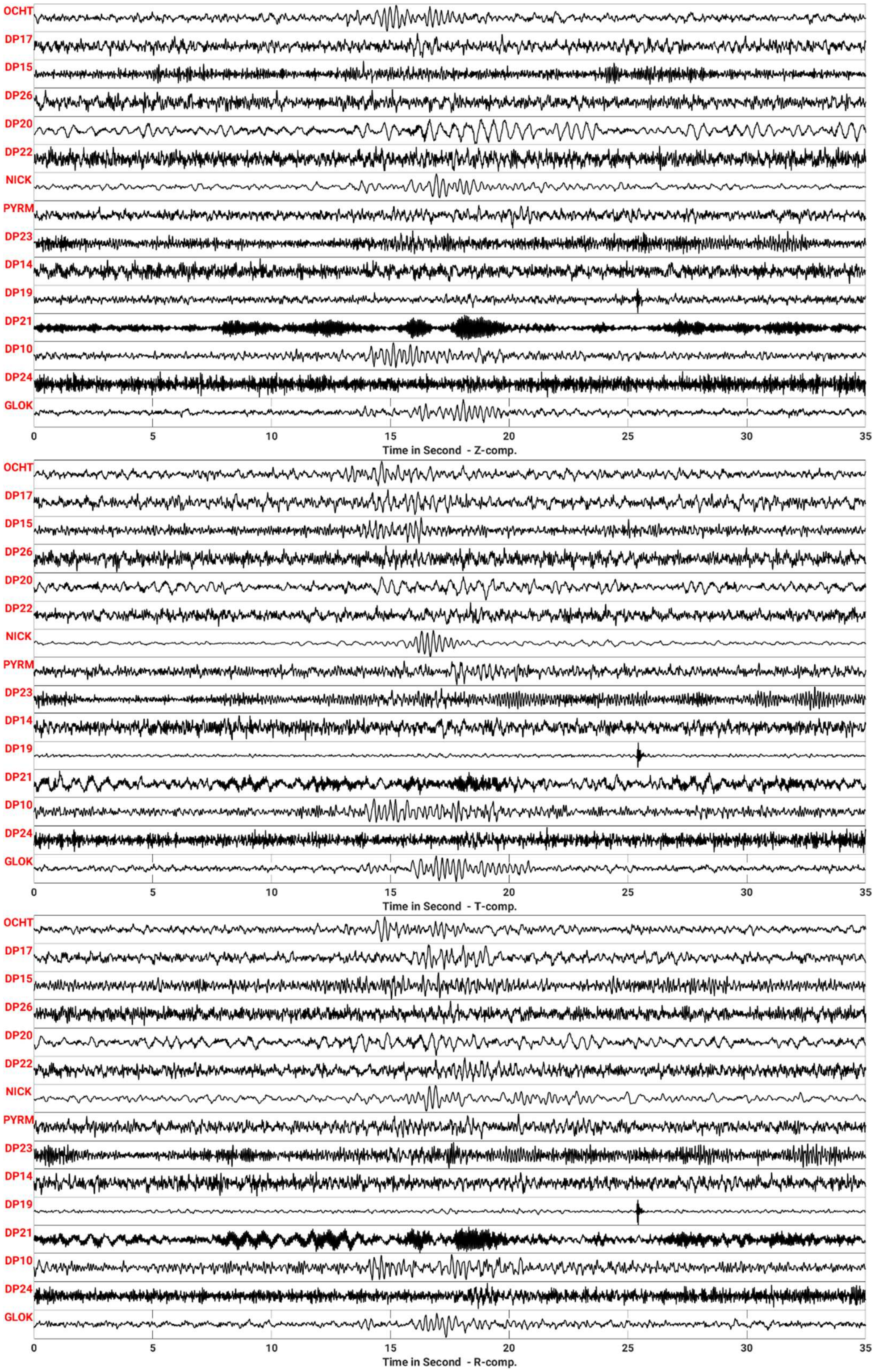

Fig. 3.3 Picking procedure routine part two. The records with the higher SNR are kept and replotted in a wider frequency range (1 – 45 Hz) to check if the onset of P and S phases in any records do not coincide with a very local noise (like passing a car near station). In that case, picking on the records of that station is refrained

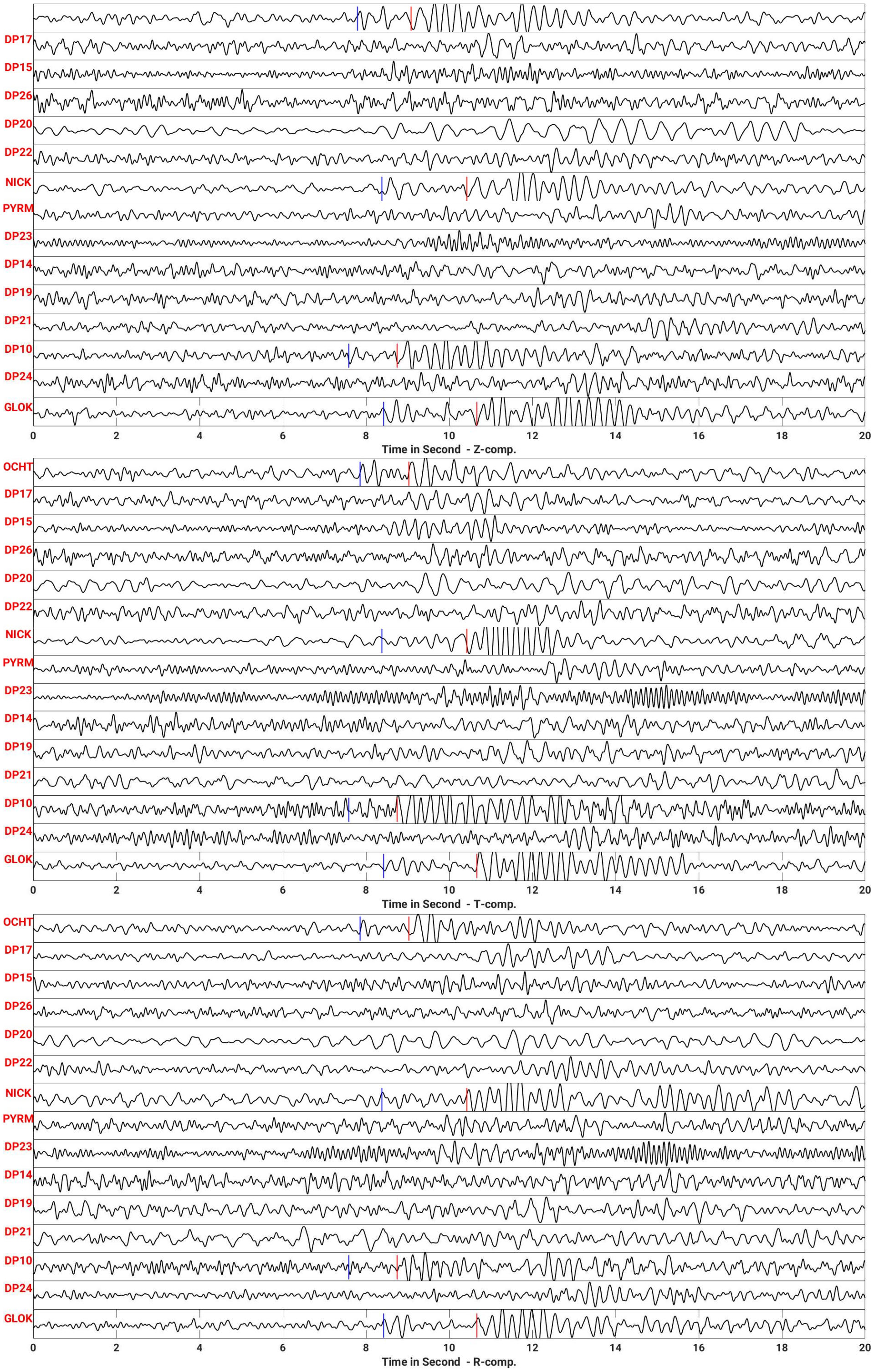

Fig. 3.4 Picking procedure routine part three. The records with the higher SNR are kept and replotted. This time the records are plotted in a shorter time window around the beginning of the signals and filtered within a band pass filter which present the most relative range of frequency to the signals. Amplitude of the records with the highest SNR is magnified (zoomed) and P and/or S phases are picked to get the initial localization parameters of the event. The blue vertical and the red vertical lines denote the onset of the picked P- and S-phases, respectively

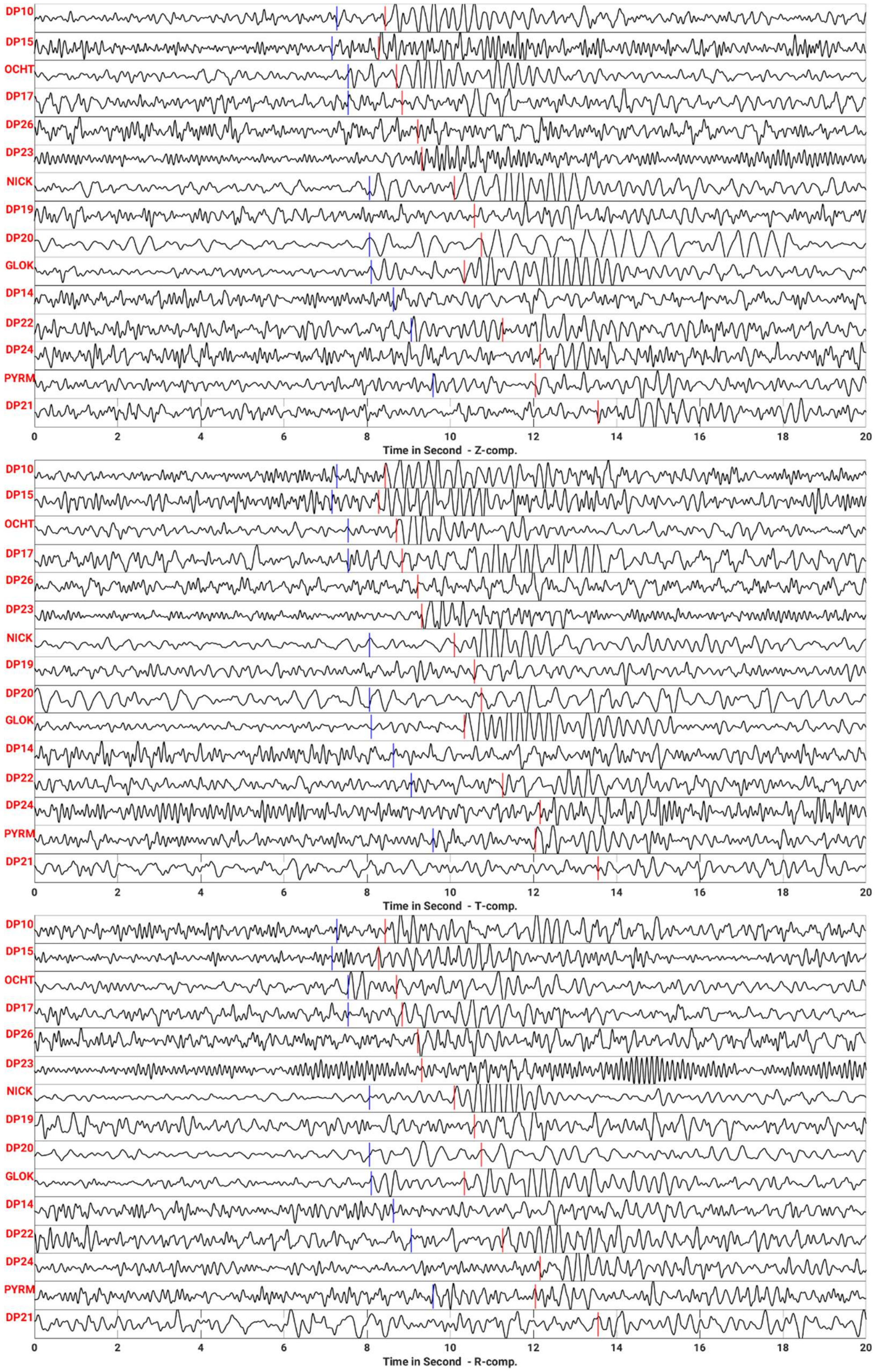

Fig. 3.5 Picking procedure routine part four. After getting the initial hypocentral parameters of the event, the records are sorted by distance to the epicenter of the event and the coordinate system are rotated according to the obtained initial hypocenter parameters. The records are zoomed in amplitude where a phase can be picked. The blue vertical and the red vertical lines denote the onset of the picked P- and S- phases, respectively

onset of the arriving phases of an event recorded at the stations and the location of the recording stations. This type of the problem will face with the complexity of the inverse problems (e. g. facing with several local minima in search of the most matching hypocentral parameters (the global minimum).

Now suppose the only known part of the problem are the onsets of the arriving phases of the events at different recording stations, the location of the recording stations and some estimation regarding the depth-dependent seismic velocity structure of the region (layered seismic velocity models or 1-D seismic velocity models for P-waves and S-waves), then the best answer representing the position of the source of the event is always under a certain amount of uncertainties from the uncertainty in reading the onset times, the velocity approximations in the model and the uncertainty in finding the hypocentral position of the responsible source after facing with several possible solutions in the inversion problem. This is the challenges which we face in seismology while searching for the correct source position (solution).

One of the widely used programs which deals with these challenges is called VELEST (Kissling, Ellsworth, Eberhart-Phillips, & Kradolfer, 1994). This program provides two modes of applications: a) “simultaneous mode” which is able to solve a coupled hypocenter-velocity model problem for local earthquakes, quarry blasts, and shots. b) “single event mode” which is used when only the determination of the hypocentral parameters of the local events is the goal. In the single event mode, the 1-D seismic velocity models and their corresponding “station correction file” (two essential pre-known data) are already supposed to be known.

As it is explained in detail in chapter four, section six, VELEST (Kissling, Ellsworth, Eberhart-Phillips, & Kradolfer, 1994) in simultaneous mode uses the first arrivals of the direct P- and S-wave phases, the coordinates of the recording stations, and different starting velocity models as input to generate the most appropriate 1-D seismic velocity models for the region, the “station correction file” which is a complementary file to the generated velocity models including the effects of the local seismic velocity anomalies (e. g. shallow 3-D heterogeneity and anisotropy) in terms of station delay times and the absolute relocation file of the hypocentral parameters of the input events.

Indeed, supposing a reasonable ranges of values for the initial velocity models, the most appropriate velocity model of a region is the one which leads to the minimum possible misfit between the calculated travel time t_{cal} and the observed travel time t_{obs} at all the stations for all the events used as the input. Using the terms of (Kissling, Ellsworth, Eberhart-Phillips, & Kradolfer, 1994), the observed travel time t_{obs} at a station is a function of the station coordinates s (relative source-receiver positions), the hypocentral parameters h and the velocity field m:

$$t_{obs} = f(s, h, m) \qquad (1)$$

The misfit t_{res} is defined as the difference t_{obs} - t_{cal} and can be approximated by applying a first order Taylor series expansion on the equation (1) resulting:

$$t_{res} = \sum_{k=1}^{4} \frac{\partial f}{\partial h_k} \Delta h_k + \sum_{i=1}^{n} \frac{\partial f}{\partial m_i} \Delta m_i + e \qquad (2)$$

Where Δ presents the differences between the estimated and the true hypocentral and velocity parameters and n is the total number of the velocity parameters. Equation 2 under matrix notation is:

$$t = Hh + Mm + e = Ad + e \quad (3)$$

Where:
t is the vector of the travel time residuals.
H is the matrix of partial derivatives of travel time with respect to hypocentral parameters.
h is the vector of hypocentral parameter adjustments.
M is the matrix of partial derivatives of travel time with respect to model parameters.
m is the vector of model parameter adjustments.
e is the vector of the travel time errors which comes from reading phases (picking step), station coordinates, using a wrong velocity model and hypocentral coordinates, and the errors coming from the linear approximation (can be called the unknown part of error).
A is the matrix of all partial derivatives.
d is the vector of hypocentral and model parameter adjustments.

Following (Thurber, 1981) by ignoring the unknown part of errors e the damped least square solution to the equation 3 is used to avoid the problem of large model perturbation for poorly constrained parameters:

$$d = (A^T A + \lambda^2 I)^{-1} A^T\, t \quad (4)$$

There, λ is the damping parameter and I is the identity matrix. The solution to the problem is searched iteratively where in each step the hypocentre and model parameter adjustments are damped by λ.
In the scope of my work, I used VELEST (Kissling, Ellsworth, Eberhart-Phillips, & Kradolfer, 1994) in single event mode to find the initial absolute hypocentral parameters for the detected and picked events using the 1-D seismic velocity models KIT5 and KIT6 (these models are introduced in chapter four) and their corresponding station correction files.

3.2.2 HypoDD (in search of a finer map of seismicity)

Seismic waves are generated by active seismic sources and seismic sources are limited in space with the geometry of e. g. a fault plane or a volcanic plumbing system. Where the inter-source distances are much smaller than the source-receiver distances and also smaller than the length of the velocity heterogeneities in the region, the ray paths belonging to clustered sources in space are similar along almost the entire path. Therefore, by a very good approximation the observed differences in the travel time of the ray paths emitted from two events with a small inter-source distance can be referred to the spatial offset between the source location of the events. Based on this approximation, (Waldhauser & Ellsworth, 2000) introduce a double-difference earthquake location algorithm called HypoDD which is a powerful method for generating a finer seismicity map. Inputs of this algorithm are: the velocity model of the region, the initial absolute hypocentral parameters of the events, the events phase picks, the station codes and coordinates. It is also designed in a way that it uses a cross-correlation technique for taking the relative travel time differences from similar waveforms, instead of using the observed catalogue picks of events. In the following I introduce HypoDD basics in terms of using picks of the catalogues as the input as the case I used in my work.

Following (Waldhauser & Ellsworth, 2000), the travel time residuals r for an event i can be linearly approximated by the first order Taylor series expansion and related to the perturbations Δm on the four hypocentral parameters for each observation k:

$$\frac{\partial t_k^i}{\partial m} \Delta m^i = r_k^i \tag{5}$$

There

$$r_k^i = (t^{obs} - t^{cal})_k^i \tag{6}$$

Where t^{obs} and t^{cal} are the observed and theoretical travel time, respectively. The perturbation on the hypocentral parameters at event i, includes the perturbation on each of the spatial Δx^i, Δy^i and Δz^i, and temporal $\Delta \tau^i$ hypocentral parameters of the event i (where τ^i is the origin time for the event i).

Supposing the same type of phase pulses emit from two nearby sources indexed by i and j, where locations these sources are far from the recording station / observation point indexed by k, the double difference equation presented by (Waldhauser & Ellsworth, 2000) is defined as:

$$(t_k^i - t_k^j)_{obs} - \left(t_k^i - t_k^j\right)_{cal} = dr_k^{ij} \tag{7}$$

Where dr_k^{ij} presents the time residual between the observed and calculated differential travel time between the two events. Rewriting equation (7) in respect with the equation (5) we have:

$$\frac{\partial t_k^i}{\partial m} \Delta m^i - \frac{\partial t_k^j}{\partial m} \Delta m^j = dr_k^{ij} \tag{8}$$

with an expanded form of:

$$\begin{gathered} \frac{\partial t_k^i}{\partial x} \Delta x^i + \frac{\partial t_k^i}{\partial y} \Delta y^i + \frac{\partial t_k^i}{\partial z} \Delta z^i + \Delta \tau^i \\ - \frac{\partial t_k^j}{\partial x} \Delta x^j - \frac{\partial t_k^j}{\partial y} \Delta y^j - \frac{\partial t_k^j}{\partial z} \Delta z^j - \Delta \tau^j = dr_k^{ij} \end{gathered} \tag{9}$$

The partial derivatives of the travel times t for events i and j, with respect to their locations (x, y, z) and origin times (τ) are calculated for the current hypocenters and the location of the station where the kth phase was recorded. Δx, Δy, Δz, and $\Delta \tau$ are the changes required in the hypocentral parameters to get a better model fit to the data (Waldhauser & Ellsworth, 2000). This change is applied iteretivaly and after each itteration the relocated version of the hypocenter parameters are kept as the current hypocenter to use for the next iteration. For the first iteration HypoDD uses the initial absolute hypocentral parameters provided in the input as the current hypocentral parameters.

The equation (9) gets generalized to include all the hypocentral pairs, all the observations taken at all stations and form a system of linear equations:

$$WGm = Wd \qquad (10)$$

where *G* contains the partial derivatives, m contains the changes in hypocentral parameters (the part which is determined by inversion), d contains the double-differences (following equation 7), and *W* is a diagonal matrix to weight each equation. To have a control on the deviation around the hypocentral parameters, HypoDD may constrain the mean shift of all earthquakes during relocation to zero:

$$\sum_{i=1}^{N} \Delta m_i = 0 \qquad (11)$$

where *N* is the total number of events. This includes the coordinate directions and the origin time of events.

To solve equation (10) in respect with m (determination of the values for the changes in the hypocentral parameters) HypoDD algorithm provides two options: one is the singular value decomposition (SVD) solution and the other one is the conjugate gradient algorithm LSQR (Paige & Saunders, 1982) which solves the problem using a damped least-squares technique. The advantage of using SVD rather than LSQR is that it obtains a reliable error range to each hypocentral parameter by computing proper covariances but on the other hand it is computatinaly expensive and its functuanality depends on the available computing capasity (it is suitable for the small set of data: in the current standard computing system in 2024 it means the data set might include less than ~300 events).

As it is explained in chapter six in detail, I use the SVD solution for relocalization of the events in EEVF where input data is resampled and the reliablity of the final hypocentral parameters are evaluated using a jacknife statistical method (Tichelaar & Ruff, 1989).

3.3 Volcanism in the Eifel

This section summarizes the knowledge on the volcanic activity in the Eifel region following (Schmincke, 2007), the most widely referenced review about studies on Eifel volcanism. Some additional sources are included and their references are given, keeping mind that there are some 200 science articles on this issue (Ritter, pers. comm.).

Volcanism in the Eifel is considered as a part of the Central European Volcanic Fields (CEVF). Volcanic activity in CEVF is geologically young and is divided into a large and a small-scale of activities. The large activity is limited in Tertiary starting about 45 – 10 Ma with a peak at 20 – 15 Ma and the small activity during the Quaternary with the last eruption at ca. 11 ka in Ulmener Maar, Germany. Parallel and in connection with these volcanic activities, the Rhine Graben and the Rhenish Shield uplift started their formation in Early to Middle Tertiary (Eocene to Miocene).

Based on the magma composition, eruption style and distribution of the eruption centers, volcanism on the western Rhenish Shield is divided into two parts called the West and the East Eifel Volcanic Fields (WEVF and EEVF). Both fields are dominantly oriented in NW-SE direction.

Volcanism in the WEVF started <700 kyr forming about 240 volcanoes (Mertes & Schmincke, 1983) (Büchel & Mertes, 1982) covering area of 600 km^2 with the last eruption at 11 ka in the Ulmener Maar. The magma in the WEVF is more mafic (rich in magnesium and iron) rather than the mostly well-evolved and differentiated types of magma in the EEVF. As a consequence of lower viscosity of mafic-type magma, half of the scoria cones in the WEVF produced lava flows, some up to 7 km long (Wartgesberg). Lava flows are fewer and shorter at the scoria cones in the EEVF. Fig. 3.6 is a merged, summarized and modified version of the Figs. in (Büchel & Mertes, 1982) (Schmincke, 2007) presented by (Rausch, Grobéty, & Vonlanthen, 2015). There the major eruption centers of the WEVF and EEVF including the chemical rock compositions of the volcanos are displayed. The inset part of the plot presents the location and expansion of the Rhenish Shield uplift (large light gray area) crossing the Rhine Graben (dotted narrow long area).

In (Rausch, Grobéty, & Vonlanthen, 2015) a self-similarity (fractal dimensions) degree of the volcanic products is used to differentiate eruption style of the volcanoes and the fragmentation processes. There, the large (morphological) and small (textural) self-similarity degree of the juvenile particles taken from three maar deposits in the WEVF and one maar in the EEVF were studied. To do that, thin cross sections of the samples (in order of tens of µm) are imaged using a scanning electron microscopy (SEM) and SEM micro-computed tomography (SEM micro-CT). They conclude that the fragmentation processes in WEVF are governed by the internal volatiles (magmatic origin) in contrast with the fragmentation processes in EEVF which are dominantly influenced by external volatiles (e.g., ground water and surface water). This is compatible with both the geological setting of the studied volcanoes and the chemical composition of the eruption products. Fig. 3.7 presents their schematic models highlighting the differences in volcanic conduits in which magma ascends in the WEVF and EEVF beside a short geological description of the shallow layers. In a recent work by (Eickhoff, Ritter, Hloušek, & Buske, 2024), in relation with petrological data of xenoliths, the amplitude of the reflection coefficient of numerous reversed polarities observed in seismic reflection data are interpreted as the patches of magmatic fluids or partial melt of up to 10% in sills underneath the WEVF. They suggest a part of this volume patches (2%–5%) could be filled with supercritical CO_2 that is found in numerous springs in the region. Due to the limitations in seismic reflection methods for imaging the small-scale vertical structures such as the possible small diameter size conduit, none of the sketched models suggested by (Rausch, Grobéty, & Vonlanthen, 2015) could be mapped by this technique.

Highly fractured and folded, impermeable Devonian rocks are overlain in the EEVF by a low permeable Tertiary clay layer locally containing sandstone and gravel lenses, and in the WEVF by Buntsandstein sediments in local morphological depressions.

Volcanism in the EEVF is younger than in the WEVF and started ~240 kyr after the start of the volcanic activity in the WEVF (so ~460 ka in the EEVF). It contains about 100 volcanoes covering an area of 400 km^2 with the last eruption at 13.006 ± 9 yr ago at the Laacher See Volcano (LSV) (Reinig, et al., 2021). Volcanic activity in EEVF is distinctly episodic "with the period of

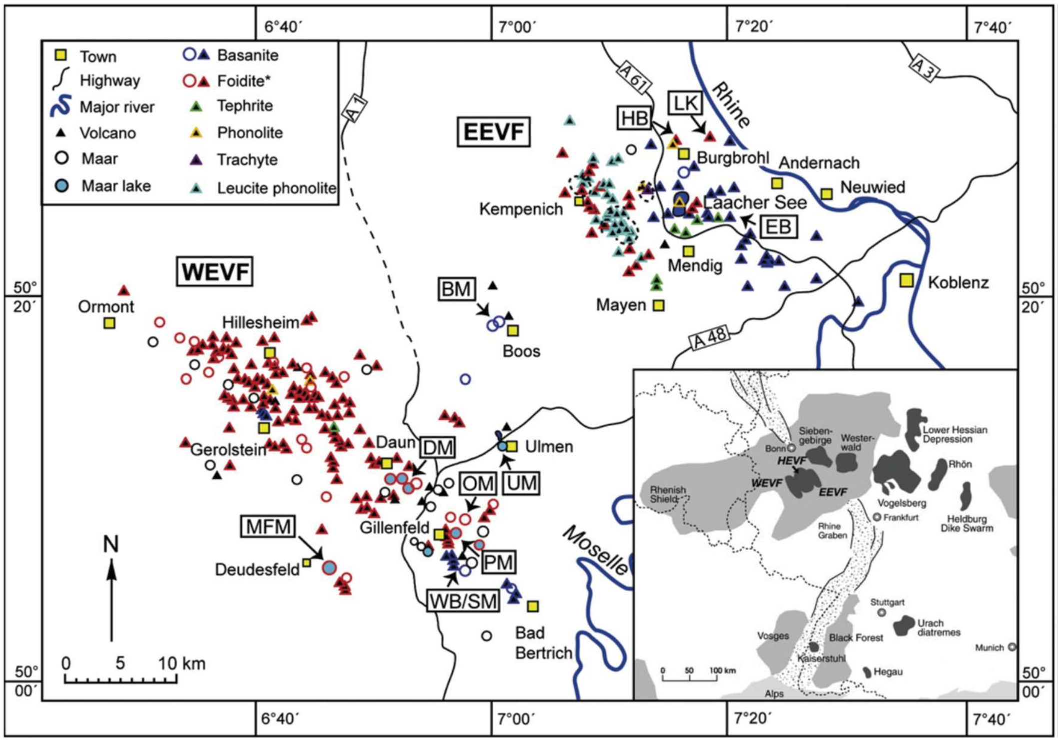

Fig. 3.6 Distribution of volcanoes in the WEVF and EEVF labeled by their chemical rock compositions. The inset part of the plot presents the location and expansion of the Rhenish Shield uplift (large light gray area) crossing the Rhine Graben (dotted narrow long area). MFM: Meerfelder Maar, DM: Dauner Maars, PM: Pulvermaar, OM: Oberwinkler Maar, WB/SM: Wartgesberg/Sprinker Maar, UM: Ulmener Maar, BM: Booser Maars, HB: Herchenberg, LK: Leilenkopf, and EB: Eppelsberg. Modified by (Rausch, Grobéty, & Vonlanthen, 2015) from (Büchel & Mertes, 1982) (Schmincke, 2007).

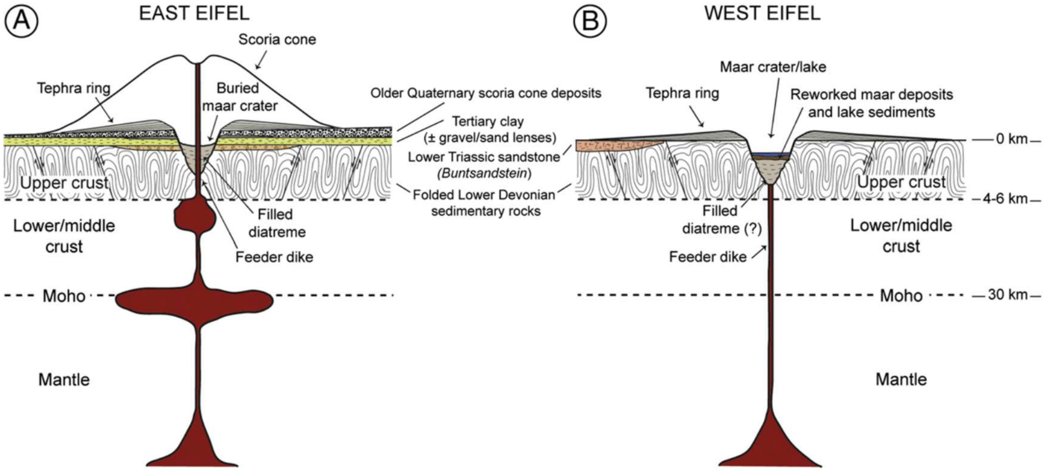

Fig. 3.7 Schematic cross sections for the typical volcanos in the EEVF (A) and the WEVF (B) suggested by (Rausch, Grobéty, & Vonlanthen, 2015) including a short description of the shallow geological layers. Erupted magma in studied typical WEVF volcanoes is transported directly from a deep position (up to upper mantle level), in contrast to erupted magma from the typical volcanos in the EEVF which was accumulated in shallow magma reservoirs long before eruption and interacted with external volatiles e. g. ground water and surface water.

high activity – a few tens of thousands of years - alternating with periods of quiescence lasting 100 kyr to 150 kyr" (Schmincke, 2007). The magma in the EEVF is more phonolitic (an intermediate chemical composition between mafic and felsic) rather than mafic. EEVF includes four major evolved centers of eruptions known as: Kempenich (formed ~ 450 to ~500 ka), Rieden (~430 to ~360 ka), Wehr and Laacher See (younger than ~215 ka) where the youngest one, LSV, experienced the biggest eruption with a volcanic explosivity index of V-VI (the scale ranges between I and VII increasing toward a catastrophic type of explosion). LSV erupted >6 km^3 magma up to 25 km altitude in the atmosphere mostly within a few days. This eruption resulted a layer of tephra recognizable in Central and Northern Europe (up to southern Sweden and northern Italy) which is considered as the most important very late Pleistocene stratigraphic marker bed for relative dating. During the LSV eruption, the Rhine River was dammed by accumulation of tephra and trees. The dam temporarily formed a 20 m deep lake and when it failed due to the water pressure it led to a massive flood traceable at least as far north as Bonn. The depth range of the responsible magma reservoir for the LSV eruption is estimated to have been between 4.6 km and 7.8 km with the temperature ranged between 750 °C and 880 °C (Harms, Gardner, & Schmincke, 2004) (Berndt, Holtz, & Koepke, 2001), using experimental petrological data.

Volcanism in both, EEVF and WEVF, is dormant but not extinct "specially the central and eastern parts of EEVF are geodynamically active" (Schmincke, 2007). This statement is supported by the following measurements, observations and scientific facts: LSV has the highest level of CO_2 release in the entire Eifel (the rate of CO_2 emission is 1000 t/d and 50-100 t/d in the EEVF and WEVF, respectively). The noble gases such as He, Ne and Ar released at LSV have a mantle origin (Giggenbach, Sano, & Schmincke, 1991) (Griesshaber, O'Nions, & Oxburgh, 1992). The springs proximal to LSV have slightly higher temperature (Langguth & Plum, 1984). Regionally for comparison, the brittle/ductile transition in the EEVF is several km shallower signing an elevation of temperature in the crust (Ahorner, 1983). The EEVF is seismically active with both, tectonic and magmatic, sources. The most active fault of the region, the Ochtendung Fault, is located/crosses the EEVF and the typical magmatic type of seismic events are already reported there (Hensch et al., 2019).

Scoria cones are the most typical type of eruption centers of both fields. They are known as the typical landforms in continental intraplate volcanic fields with formation periods of a few weeks to months. Therefore, the formation of a new volcano and/or reactivation of an already formed volcano can happen at any time. Unlike the tectonic type activities which mostly occur in preexisting faults and fractures, volcanoes can be born by opening a new magma path way up from the deeper crust or upper mantle to the surface. This process is always accompanied with several signs of unrest weeks to months prior to the eruption. Therefore, increases in: seismicity, ground water outflow and gas flux, changes in composition of the magmatic gases and surface deformation must be taken as serious signs of a possible eruption. Based on (Schmincke, 2007)'s observations and analysis, new volcanoes will most likely grow in the southern to eastern area of both volcanic fields and in case of reactivation of LSV it would be strongly explosive in presence and interaction of the magma with the water lake in the volcano crater.

4 The DEEP-TEE experiment

In this chapter (and appendix A), the DEEP-TEE experiment (Deep Eifel Earthquakes Project - Tiefe Eifel Erdbeben) as the input dataset of this dissertation is introduced. In connection with the DEEP-TEE dataset my tasks were, fieldwork for installation/servicing the seismological instruments in the EEVF and data analysis for generating sets of the probabilistic power spectral density plots for noise analysis plus the data quality control which helped for a better reconfiguration of the network supporting the detection and localization requirements. In this chapter, the KIT5 and KIT6 seismic velocity models (P- and S-wave) are presented for which my task was providing pick times of P- and S-wave onset from LF events and a catalog of initial absolute hypocentral locations for the deep LF events which increased the reliability of the models specially regarding the deeper velocity layers. There, also I present my picks for one of the relatively well recorded deep LF events.

This chapter entirely published as:
Ritter, J.R.R., Koushesh, K., Schmidt, B. *et al.* Seismological monitoring of magmatic and tectonic earthquakes in the East Eifel Volcanic Field, Germany. *J Seismol* (2024). https://doi.org/10.1007/s10950-024-10257-w

4.1 Abstract

In 2013 there were reports on exceptionally deep earthquakes in ca. 40 km depth below the intraplate East Eifel Volcanic Field, Germany. Due to this observation the regional seismological monitoring network was improved to better explore this unusual seismicity. In order to acquire the necessary instruments, financial resources, and man power, a close partnership was initiated between the local state seismological service and academic research institutions. As an outcome the seismological field experiment called *Deep Eifel Earthquake Project – Tiefe Eifel Erdbeben* (*DEEP-TEE*) was accomplished which measures high-quality ground motion recordings since 2014. These measurements are used to study deep magmatic processes around the Laacher See Volcano (LSV) which was the site of a paroxysmal eruption just 13,079 years ago. As the *DEEP-TEE* network is located in a region with a high cultural noise and loose sediments, a careful site selection was a major task. Here, the network design is described and its recordings are used to determine 1-D seismic velocity models (vp, vs, and vp / vs) with station delay times to relocate the seismic events. The models include a priori information from active seismic experiments, especially in the mantle, to overcome resolution problems. The new velocity models allow to (re)locate the local earthquakes with horizontal and vertical uncertainties of ca. 0.5 km and 2.0 km, respectively. A special highlight of *DEEP-TEE* is the frequent observation of deep low-frequency (<10 Hz) earthquakes whose hypocentres outline an active translithospheric channel, feeding the magmatic-fluid-volatile system underneath the LSV.

4.2 Introduction

The monitoring of active and dormant magmatic and volcanic areas is a fundamental task for hazard analyses and research concerning the understanding of magmatic processes (Pallister and McNutt 2015). The parameters gas composition, gas volume flux, ground temperature, gas temperature, ground deformation, seismicity, gravity changes etc. are basic proxies to describe the current situation of magmatic and volcanic processes, as well as to take decisions on hazard alerts (Pallister and McNutt 2015 and references therein). Especially the observation of seismicity, even deeper than the tectonic brittle zone together with source analyses such as fault plane solutions and moment tensor analysis allow us to recover the location and activity rate of the magmatic plumbing system as well as the state of unrest (McNutt et al. 2015, Paulatto et al. 2022). Besides careful operation by the field team, the quality of such recordings depends on the selection of suitable seismic recording sites. In well-developed and densely populated places, seismic recording is strongly influenced by external sources such as seismic noise from man-made activity, e.g., ground motion emissions from traffic or industry (Trnkoczy et al. 2012). In addition, environmental effects can influence the recording quality: for example, bad coupling of the sensors to the ground due to pyroclastic layers and sediments or a high natural seismic noise level due to water flows, waterfalls, or wind (Bonnefoy-Claudet et al. 2006). Careful planning of a seismological monitoring network needs to minimise such impacts, however, due to given circumstances noise sources cannot always be avoided.

The Eifel is a mountain region in the western part of Germany at the border to Luxembourg and Belgium (Fig. 4.1). Geologically, it is part of the Rhenish Massif composed of Palaeozoic metamorphic rocks (Meyer 2013). The Eifel was strongly uplifted during the Quaternary (Meyer and Stets 2007; Demoulin and Hallot 2009), a process which is still ongoing and unique in Central Europe (Kreemer et al. 2020). Since ca. 700 kyrs the East and West Eifel Volcanic Fields have been active with together ca. 350 eruption sites (Schmincke 2007). In the West Eifel Volcanic Field (WEVF), the last major activity period started about 80 kyrs ago in the SE part (Mertz et al. 2015) and the last eruption occurred at the Ulmener Maar (UM) just ca. 10.900 yrs ago, leaving behind a 400 m wide crater. In the East Eifel Volcanic Field (EEVF) there are four major centres. The last eruption occurred at Laacher See Volcano (LSV) as a climactic event of volcanic explosivity index VI about 13,079±7 years ago (Reinig et al. 2021). LSV ashes were dispersed over wide regions in Europe and the pyroclastic flows even dammed the river Rhine causing major flooding (Park and Schmincke 2020). Today, a similar ash fall event would cause severe damage to infrastructure (Leder et al. 2017) and a closure of air traffic in Central Europe. Petrological data indicate that the upper crustal magma reservoir of LSV had grown for some 10,000 years (Rout and Wörner 2018) before the last eruption. Based on zircon analyses Schmitt et al. (2022) recently determined 63 ka as possible onset of the presence of evolved magma at the top of the crustal magma reservoir. Nowadays gas emissions (Goebel et al. 2015) and deep seismicity (Hensch et al. 2019) indicate that the volcanic activity is in a dormant state. Based on a comprehensive study Schreiber and Jentzsch (2021) come to the conclusion that there is a relatively high probability for future volcanic eruptions in the Eifel.

Active-source seismological studies indicate that the crust of the EEVF is ca. 29-31 km thick and is underlain by a low seismic P-wave velocity anomaly which is interpreted as magmatic underplating zone (Mechie et al. 1983; Dahm et al. 2020). Below this zone, the lithosphere-asthenosphere boundary is located at just 45-50 km depth (Mathar et al. 2006; Seiberlich et al. 2013). The ca. 20-30 km thick upwelling of the asthenosphere is most probably related to a deep reaching mantle plume as found from teleseismic P- and S-wave tomography modelling (Ritter et al. 2001; Keyser et al. 2002). A buoyant mantle plume can also explain the regional uplift, which is the most significant one in Central Europe north of the Alpine orogen (Kreemer et al. 2020; Cloetingh et al. 2022).

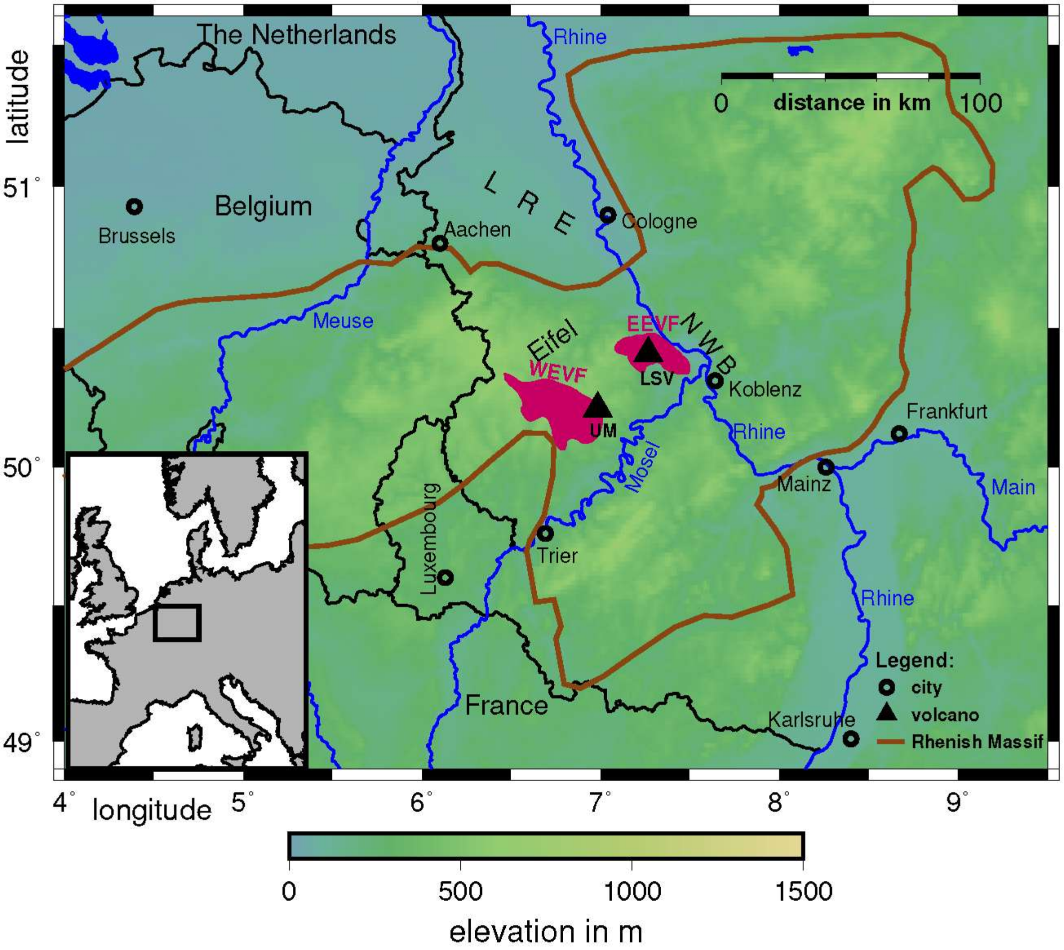

Fig. 4.1 Map of the study region and surroundings. The brown line outlines the Rhenish Massif; WEVF: West Eifel Volcanic Field, EEVF: East Eifel Volcanic Field, UM: Ulmener Maar, LSV: Laacher See Volcano, NWB: Neuwied Basin, LRE: Lower Rhine Embayment. The inset shows the study region within Europe

Local seismicity in the Eifel mountains, including the WEVF and EEVF, is quite low (Hinzen 2003; Weber 2012; Hinzen et al. 2021). Known moderate or damaging earthquakes are related to the rifting processes of the Lower Rhine Embayment about 25 km north of the volcanic fields. Especially in the WEVF, earthquake activity is very low with rare swarm-like events (Weber

2012; Hinzen et al. 2021). Seismicity in the EEVF is more frequent but it is below an intensity related to damage (Leydecker 2011). The most active seismic fault is the Ochtendung Fault Zone (OFZ) (Figs. 4.2) with about 1-2 weak events ($ML < 1$) per week and occasionally felt shocks ($ML < 4$) (Ahorner 1983; Hinzen et al. 2021). Just east of the EEVF some seismicity occurs in the Neuwied Basin (Hinzen 2003). Recently, deep low-frequency (DLF) seismic events related to magmatic processes were described (Hensch et al. 2019) which are the main target of our network presented here. These DLF earthquakes have hypocenters as deep as ca. 45 km, meaning that they occur in the mantle. Their corner frequency increases with depth what is interpreted that the low-frequency content is not a filtering effect along the propagation path (Hensch et al. 2019). Tectonic activity below ca. 20 km depth is unlikely, because it is not observed in Central Europe north of the Alps (BGR Kataloge 2023). The strength profile of regional continental lithosphere is similar as the one proposed by Jackson (2002) with a single seismogenic layer. Tectonic activity in the uppermost mantle is unlikely (nor observed), because the temperature reaches ca. 800-900 °C below the Moho (Witt-Eickschen 2007) and the wet lithology of the metasomatized lower lithosphere (Witt-Eickschen et al. 1998) should not support enough strength for brittle behaviour (Brace and Kohlstedt 1980, Jackson 2002). The low frequency and long coda waveforms of the DLF events can be better explained by magmatic processes (Wassermann 2012) and this is a reasonable assumption due to the Quaternary volcanism (Schmincke 2007).

Seismic monitoring in the Eifel region before 2014 was not specifically tuned towards observing the magmatic processes underneath the EEVF (Fig. 2a). Only weak tectonic activity was known and mainly short-period instrumentation was installed to monitor this region. Microseismic observation has been started since 1976 by the Seismological Station Bensberg of Cologne University (Ahorner 1983) and continues until today (Weber 2012; Stammler et al. 2021). Later, the Geological Service of North Rhine-Westfalia installed seismic stations (TDN, BHE and LOH) in the Eifel volcanic fields to monitor mainly the strong seismicity in the Lower Rhine Embayment (Fig. 1) at hard-rock sites (Pelzing 2008). The State Seismological Service of Rhineland-Palatinate (SSS R-P) started operation in 1998 and extended its network since then including a dense monitoring of the EEVF (see sections 2 and 3 below). Besides these permanent monitoring networks, mobile station deployments were done for passive seismological research projects: Raikes and Bonjer (1983) operated 63 recording stations between 1978 and 1980 across the Rhenish Massif to determine teleseismic travel time residuals. Ochmann (1988) conducted a local teleseismic tomography study around LSV with 14 temporally recording stations in 1985 and 1986. In the framework of the seismological experiment of the Eifel Plume Project about 150 mobile and 100 permanent stations were operated in 1997-1998 with a main focus on the upper mantle structure (GEOFON 1997-1998; Ritter et al. 2000).

In the following we report on the strategy and goals for upgrading of the seismological recording capabilities in the EEVF. This data is used to better detect local tectonic and DLF events as well as locate these events. To improve existing location procedures we determine new local 1-D seismic velocity models with which we relocate the known hypocentre parameters from routine analysis and include new events. Finally, the distribution of the hypocentres is discussed in the context of the established regional geology and magmatism to support hazard analysis.

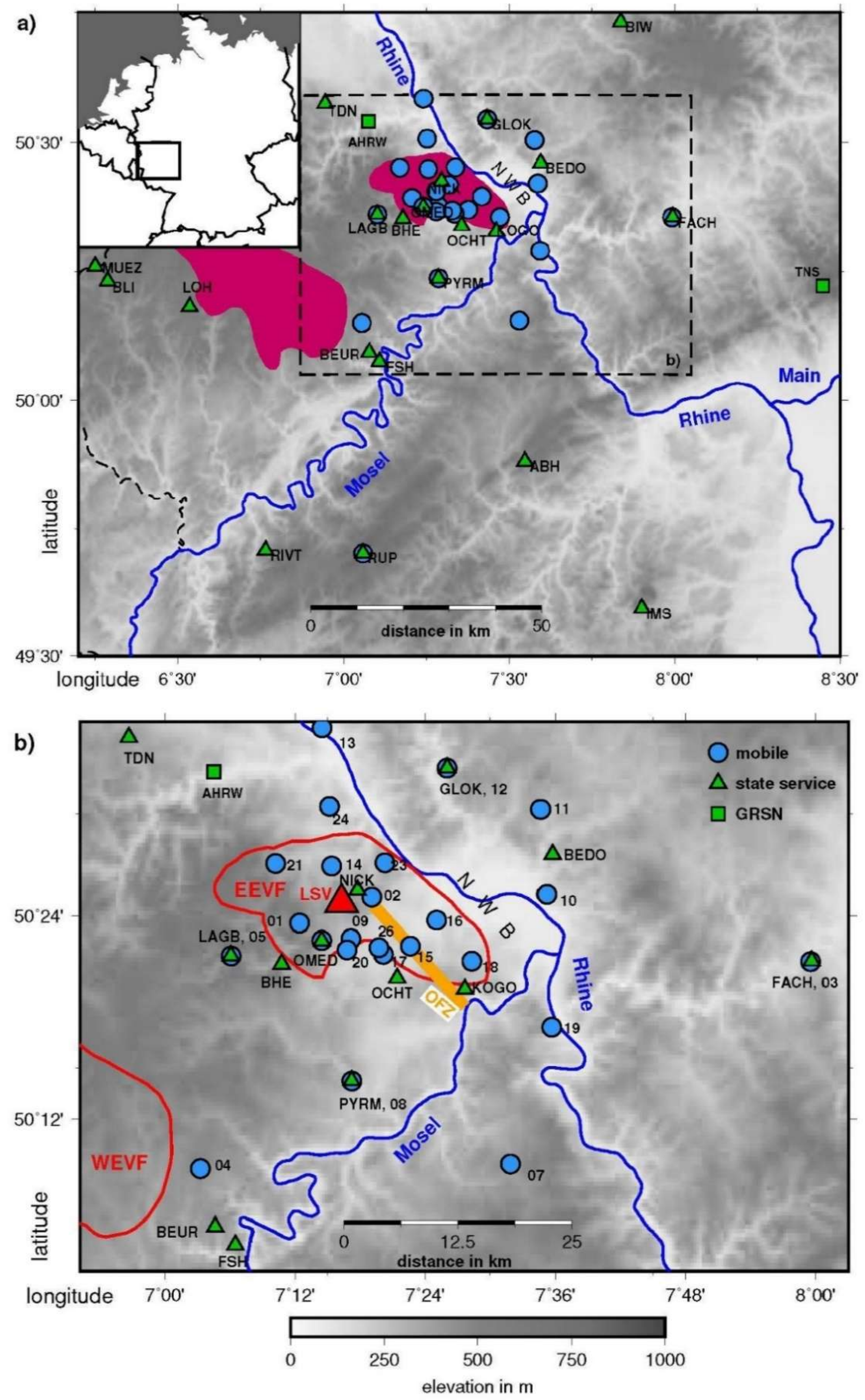

Fig. 4.2 a) Station map of the study region and surroundings. The East and West Eifel Volcanic Fields are indicated in red, NWB: Neuwied Basin. Green triangles are permanent recording stations of different state seismological services, green squares are broadband recording stations of the German Regional Seismic Network. Blue circles are mobile recording stations, b) enhanced view with station codes of mobile stations (DEPXX)

4.3 Monitoring Strategy

Our earthquake monitoring in the EEVF has two main goals: first, events with *ML* > 1 should be detected and located in real time by the SSS R-P; second, events with *ML* > 0 below LSV (DLF events) and along the OFZ should be detected and observed with the help of recordings from mobile stations deployed by the involved research institutions. This effort should help to reliably detect tectonic and magmatic earthquakes for hazard assessment. The joint network is called the *Deep Eifel Earthquake Project – Tiefe Eifel Erdbeben* (*DEEP-TEE*) experiment and is composed of a combination of permanent and mobile seismological recording stations with both, offline and online recording. As the observation of DLF events with frequencies in the range 2-10 Hz is a major goal, only seismometers with a natural frequency of maximum 1 Hz have been deployed. Most seismometers are broadband (Nanometrics Trillium, Streckeisen STS-2) which also cover the frequency range of teleseismic waves and allow the study of deeper mantle structures. All stations from SSS R-P have real time data transmission, whereas most stations from KIT (Karlsruhe Institute of Technology) and GFZ (German Research Center for Geosciences) are operated without online data transmission to save costs and power (station code DEPXX). In addition, mobile phone coverage for data transmission is missing in some remote places in the EEVF.

The backbone of *DEEP-TEE* is the permanent online network of the SSS R-P which operated two stations (OCHT and LAGB) in the EEVF in 2014. It has been upgraded as part of *DEEP-TEE* since then (Fig. 4.2) and has FDSN code LE. In addition, two online stations (BHE and TDN) from the state network in North Rhine-Westfalia (FDSN code NH) were used in 2014 as well as online station AHRW from the German Regional Seismic Network (Stammler et al. 2021) with FDSN code GR. Following the deep events in 2013, the KIT and GFZ installed 13 mobile recording stations in summer 2014 (Fig. 4.2). Ten recording stations were provided from the Geophysical Instrument Pool Potsdam (GIPP at GFZ) for two years and afterwards these were replaced by instruments from the KArlsruhe BroadBand Array (KABBA at KIT). The increase of station numbers with time is illustrated in Fig. 4.3a for the vicinity of the EEVF. At the beginning there were only three permanent short-period stations and the deployment of 13 mobile DEPXX in summer 2014 increased rapidly the recording capacity including a wider frequency band to better record low-frequency signals. Following the removal of the GIPP instruments in summer 2016, the KABBA instruments filled the gaps and since summer 2019 nearly 30 recording stations are available. The FDSN codes for the mobile deployments are 1P (2014-2016) and 9Q (2017-).

The mobile stations were placed in such a way that gaps in the permanent network were filled and that earthquakes as deep as 50 km could be well located. Therefore, a diameter of nearly 100 km was chosen for the *DEEP-TEE* experiment. Azimuthal gaps were closed to allow a good location of the events related to the OFZ (Fig. 4.2). After the occurrence of upper crustal microseismic swarms north of LSV in 2017, additional mobile stations (DEP21, DEP23 and DEP24) were deployed in the northern part of the network.

After a careful analysis of the first low-frequency events (Hensch et al. 2019) and a comparison with similar recordings from other volcanic regions (Wassermann 2012), it was obvious that this low-frequency seismicity is related to ongoing magmatic processes (see introduction). Then, an upgrade of the permanent SSS R-P network became a high priority since 2015. For this reason,

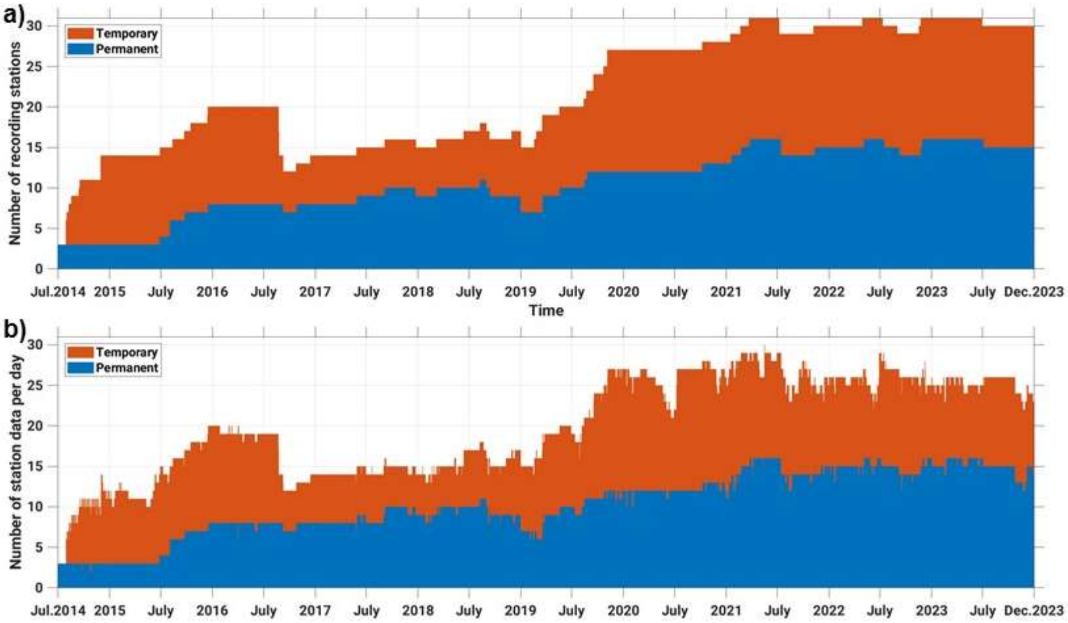

Fig. 4.3 a) Station and b) data availability over time for the DEEP-TEE experiment in the area covered by Fig. 4.2b. The height of the columns represents the sum of permanent (blue) and mobile (orange) stations (a) and the daily station data (b)

we decided to replace the best mobile station sites with permanent ones. Best in this respect means a low-noise environment and/or a suitable position to improve the determination of rapid real-time event parameters based on automated arrival time readings (Greve et al. 1999). In this way, GLOK replaced DEP12, PRYM replaced DEP08, and OMED replaced DEP22 since 2018 (Fig. 4.2b). BEDO was installed in the end of 2020 close to DEP10 which was removed afterwards. To enhance the monitoring directly at LSV, a borehole station (NICK) was installed 80 m underneath the surface on the northeast crater rim of LSV in 2018 to replace DEP02 which was quite noisy. Drilling was necessary to reach solid rock underneath the poorly consolidated volcanic tephra and rocks. In 2020 a mini-array (KOGO) was deployed close to the southern end of the OFZ, consisting of a 3-component central recording station and three surrounding 1-component (vertical) stations. At the end of 2022, within a radius of 40 km from LSV about 28 recording stations contribute to *DEEP-TEE* for monitoring the EEVF.

4.4 Station Selection Criteria and Installation

The finding of suitable recording sites is a challenge in the EEVF. In general, its eastern part is a high noise region with dense settlements, traffic, industry, and agriculture in the Neuwied Basin (Fig. 4.2b). Especially traffic lines are a major problem with two highways (A61 and A49), including large bridges which act as amplifiers for traffic-induced shaking. As the volcanic rocks such as tephra and basalt are widely mined, there are numerous quarries in the region with accompanying blasting activity and heavy traffic. The Neuwied Basin just east of the EEVF is filled with Quaternary sediments which amplify the noise from numerous sources: ships on the river Rhine, railway tracks, major roads, and industrial facilities. In its western part, the EEVF is more rural with agricultural land and forests. Here missing infrastructure (power, telecommunication) is an issue at remote low-noise sites. At several places we could not reach basement rock for a good coupling of the seismometer due to the thick pyroclastic layers.

Appropriate recording sites include gun clubs (few activities in evening hours, e.g., DEP16) which are located outside of villages, cemeteries (DEP07 and DEP20), water reservoirs (without pumping activity, DEP01, 02,04,10,11,12,15,18 and 22) or farms (DEP17 and DEP23). A remote glider airfield (DEP24) also provides a low-noise environment as well as castle ruins (DEP08 and DEP21). Surprisingly, an old 30 m deep, beer cellar (DEP09) in a basalt flow underneath the town of Mendig proved to be a problem for seismic recording: the highway A61 also runs through this basalt flow which carries the strong traffic-induced noise.

Wherever possible, the seismometers are protected against environmental influences by burying them and wrapping them with insulating material (Fig. 4.4). Since 2020 all seismometers are precisely aligned towards north with a gyrocompass (error <0.5° during seismometer orientation) what is more accurate than using a magnetic compass. Comparisons of magnetic and gyrocompass installations found misalignments reaching 15° for the latter. Flexible plastic tubes are used to protect the GPS antenna cables (Fig. 4.4) and seismometer cables against rodents. Recently, three sites were equipped with solar panels to reduce battery and travel costs as non-rechargeable batteries with a high capacity of 175 Ah had to be used. However, solar panels are prone to vandalism and can be installed only at safe places. The mobile recording stations without online data transmission are visited every 5-6 months in order to check the equipment and retrieve the data. The data loss due to technical problems is less than 3% (Fig. 4.3b).

4.5 Noise Analysis and Detection Thresholds

The seismic background noise is a major issue in the EEVF due to the extensive human activities (see section 3). For quality control of our recordings, we calculate noise spectra using the ObsPy routine PPSD (The ObsPy Development Team 2020). The noise spectra are determined as power spectral densities (PSD_{vel}) of the ground motion velocity calculated for 60 minutes long time windows. Fig. 4.5 displays PPSD examples.

For comparison with worldwide ground motion recordings, we add the curves of the global New High and New Low Noise Models (NLNM and NHNM) after Peterson (1993). The average noise level PSD_{vel} at the DEEP-TEE sites ranges between the NLNM and the NHNM (Fig. 4.5). At some sites we find a remarkable difference between a lower noise level at night time and a higher noise level during day time. Such a difference causes a branching of the noise level curves (e.g., DEP14, DEP21, DEP26) in Fig. 4.5. As consequence of the higher noise level during daytime, we hardly find DLF events between ca. 8 am and 4 pm (local time). In addition, during this time interval also quarry blast activity is high causing similar waveforms as DLF events.

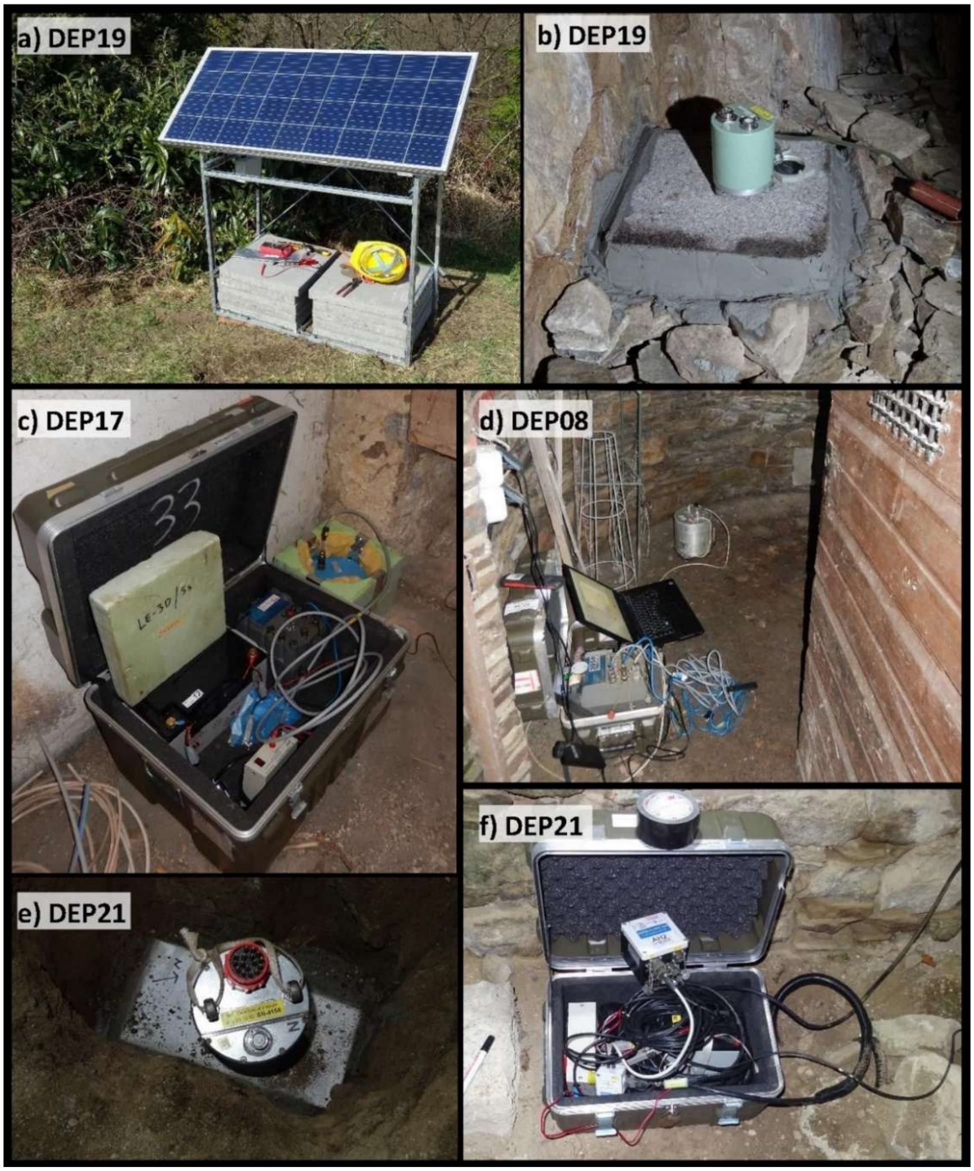

Fig. 4.4 Examples of seismic station installations: a) Solar panel at DEP19, b) Nanometrics Trillium Compact 120 s sensor on a small concrete pier in a small mine at DEP19, c) recording equipment (EarthData PR-24 logger with power supply and a Lennartz 5 s seismometer inside a thermal insulation) at DEP17, d) recording equipment with a MARK 1 s seismometer in the tower of a castle ruin at DEP08, e) Nanometrics Trillium Compact Posthole 20 s sensor on a small concrete pier in the cellar of a castle ruin at DEP21, f) recording equipment (CUBE3 with power supply) at DEP21, the sensor (see e) is buried at the right side of the box

The displayed PSD_{vel} can be used to estimate the approximate resolution threshold of earthquake recordings with regard to the local magnitude ML of events. To relate the amplitude of a signal or earthquake phase with ML we use the standard equation from IASPEI (2013):

$$ML = \log_{10}(A) + 1.11 \log_{10}(R) + 0.00189\, R - 2.09 \qquad (1)$$

with A: maximum horizontal displacement amplitude in nm with response function of a standard Wood-Anderson seismometer, and R: hypocentral distance in km. A in equation (1) is the maximum shear (S-) wave amplitude (As_{max}) or surface wave amplitude (Alg_{max}) of a local earthquake. As we need a clear recording of the compressional (P-) wave to locate earthquakes, we need to estimate a related P-wave amplitude (Ap) value to rate the sensitivity of a station network. To estimate Ap from As we use a relationship of $A_p \sim 0.2\, A_s$, because on average actual measurements of local and regional ground motions often have five times larger shear wave amplitudes than compressional wave amplitudes including source radiation and damping effects. Examples for A_p / A_s can be found in Yavuz et al. (2019) or Shelly et al. (2022). In this way P-phases should not be missed. Furthermore, to be able to identify a compressional wave within a noisy background motion, a signal-to-noise ratio of at least 3 is desired. This means a factor of 0.33 is multiplied to Ap to define an approximate maximum amplitude level for acceptable random ground motion displacements (a_{rms}).

We convert expected average a_{rms} values from the observed ground motion velocity PSD_{vel} (Fig. 4.5) using the equations given in Bormann (1998), e.g.

$$a_{rms} = (PSD_d \cdot f_0)^{1/2} \cdot (2 \cdot (f_u - f_l) / f_0)^{1/2} \qquad (2)$$

with f_0 as central frequency of a signal range which has lower and upper frequency limits of f_l and f_u. PSD_d is the power spectral density of the ground displacement (in m^2/Hz) and can be calculated from

$$PSD_d = PSD_{vel} / (4\, \pi^2 f^2) \qquad (3).$$

In an ideal case we would like to determine a DLF earthquake in the upper mantle with $ML = 0$ in 50 km hypocentral distance (e.g., 40 km depth and 30 km epicentral distance) which has an amplitude As of ca. 1 - 2 nm. Using a central frequency f_0 of 5 Hz with upper and lower limits of $f_u = 9$ Hz and $f_l = 1$ Hz for DLF events (Hensch et al. 2019) a maximum noise displacement amplitude a_{rms} of ca 0.1 nm or PSD_{vel} of ca. -180 dB to -185 dB would be desirable for *DEEP-TEE* sites. Even with low noise conditions during night time this low noise level is hardly fulfilled (Fig. 4.5) and hence we often miss the P-wave of DLF earthquakes, whereas the shear wave trains with higher amplitudes can be observed in many cases.

The PSD_{vel} noise levels between -160 dB and -140 dB at 1-9 Hz, which we find at many DEEP-TEE recording sites in the EEVF, allow us to observe P-wave displacements with SNR ≥ 3 of ~3 nm and ~37 nm, respectively. For DLF events at 40 km depth this corresponds to a minimum ML of ~1.1 and ML of ~2.1 which then can be well located. The quietest recording stations (e.g., DEP04, DEP08 or DEP12 and the permanent stations) reach -170 dB, especially during night, and then $ML \sim 0$ can be reached. Often the long lasting (10-30 s) shear wave trains of DLF events are identified and earlier tiny signals visible in the noise are estimated as P-wave for location. For this, P-wave characteristics are also investigated using polarisation and component product

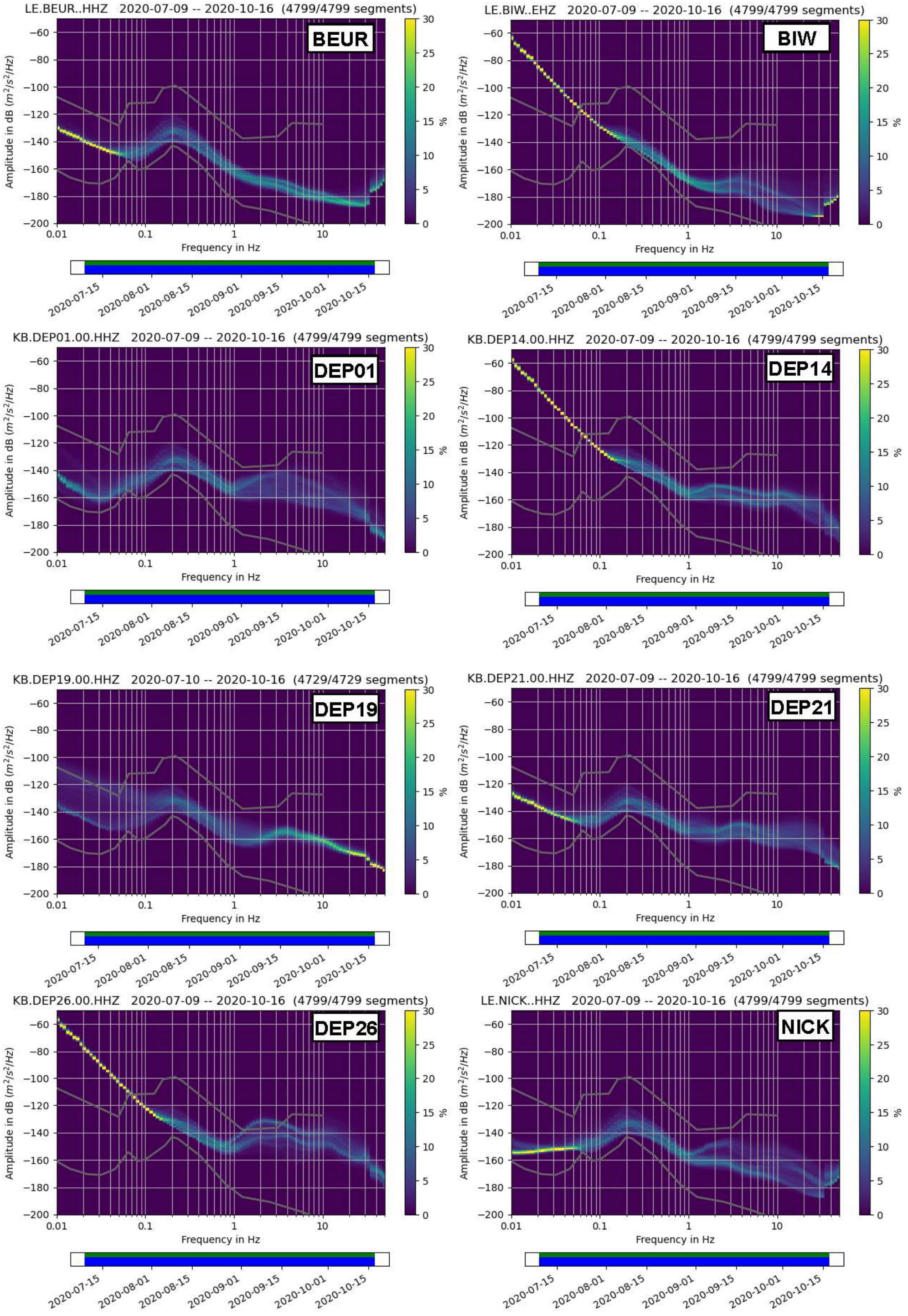

Fig. 4.5 Probabilistic power spectral density of the vertical ground motion velocity at DEEP-TEE sites during summer 2020. The relevant frequency range is between 1 Hz and 20 Hz; here a wider frequency range is plotted as some sensors are broadband (BEUR, DEP01, DEP19, DEP21, NICK). At the time axis, the green line shows data availability (here 100%) and the blue line shows the single PSD measurements that go into the histogram

analyses following Plesinger et al. (1986). Many DLF earthquakes occur at 25-35 km depth and our recording stations directly above these events cannot record clear P-wave signals even at the lower nightly noise levels at ca. -160 dB to -170 dB (Fig. 4.5).

Concerning shallower tectonic earthquakes related to the OFZ, at ca. 15 km depth and up to 20 km hypocentral distance we take a central frequency f_0 of 15 Hz with upper and lower frequency limits of $f_u = 20$ Hz and $f_l = 10$ Hz (see Hensch et al. 2019). If a P-wave signal with $\mathrm{SNR} \geq 3$ should be recorded, theoretically events with $ML \sim 0.2$ (for -160 dB PSD_{vel}) or $ML \sim 1.2$ (for -140 dB PSD_{vel}) should well be observed with DEEP-TEE data including a very good azimuthal coverage. The actual data analysis reveals that events as weak as $ML \sim 0.3$ are regularly detected and located. The noise level at the broadband stations (see BEUR, DEP01, DEP19, DEP21, and NICK in Fig. 4.5) is low enough to conduct structural analyses (receiver functions, SKS-splitting etc.) with teleseismic waves.

4.6 Recording Examples

In Fig. 4.6 we compare waveforms of a DLF event (Fig. 4.6a) and a tectonic earthquake (Fig. 4.6b) of similar magnitude ($ML \sim 1$). Both events occurred during night time and they were recorded with a very good signal-to-noise ratio as far as at least 60 km distance at station ABH (Fig. 4.2a). The DLF event is located at 37 km depth (note the time difference of ca. 5 s between the P- and S-wave close to the epicentre, e.g., at stations OCHT, DEP02 or LAGB). This depth is ca. 7 km below the Moho in the upper mantle. There is a clear difference in the waveforms in Fig. 4.6: the deep magmatic event emitted low-frequency waves of 1-6 Hz which last for about 15-20 s in the epicentral area. In contrast, the tectonic earthquake radiated high-frequency waves (10-20 Hz) within a short-time rupture process. These characteristics can be used to discriminate the different types of events as well as to automatically identify such signals in the continuous data streams. In Fig. A13 the different components and picked P-wave and S-wave onsets are shown. More examples can be found in Hensch et al. (2019) who also discuss the frequency characteristics of the different earthquake types in more detail.

4.7 1-D Seismic Velocity Models (*vp*, *vs*) and Earthquake Relocations

The DEEP-TEE recordings of local earthquakes are used to determine local 1-D seismic P-wave velocity (*vp*) and S-wave velocity (*vs*) models for the EEVF. These seismic velocity versus depth models are the basis for improved hypocentre parameters from relocations relative to standard locations. As database, we use available pick times from permanent recording stations provided by the SSS R-P (Landeserdbebendienst 2018) and we determine additional onset times of seismic phase arrivals in the time series of the mobile DEEP-TEE recording stations. Especially, newly detected DLF events (Koushesh and Ritter accepted) are carefully picked to include ray paths underneath the tectonic seismogenic zone which reaches down to ca. 17.5 km depth.

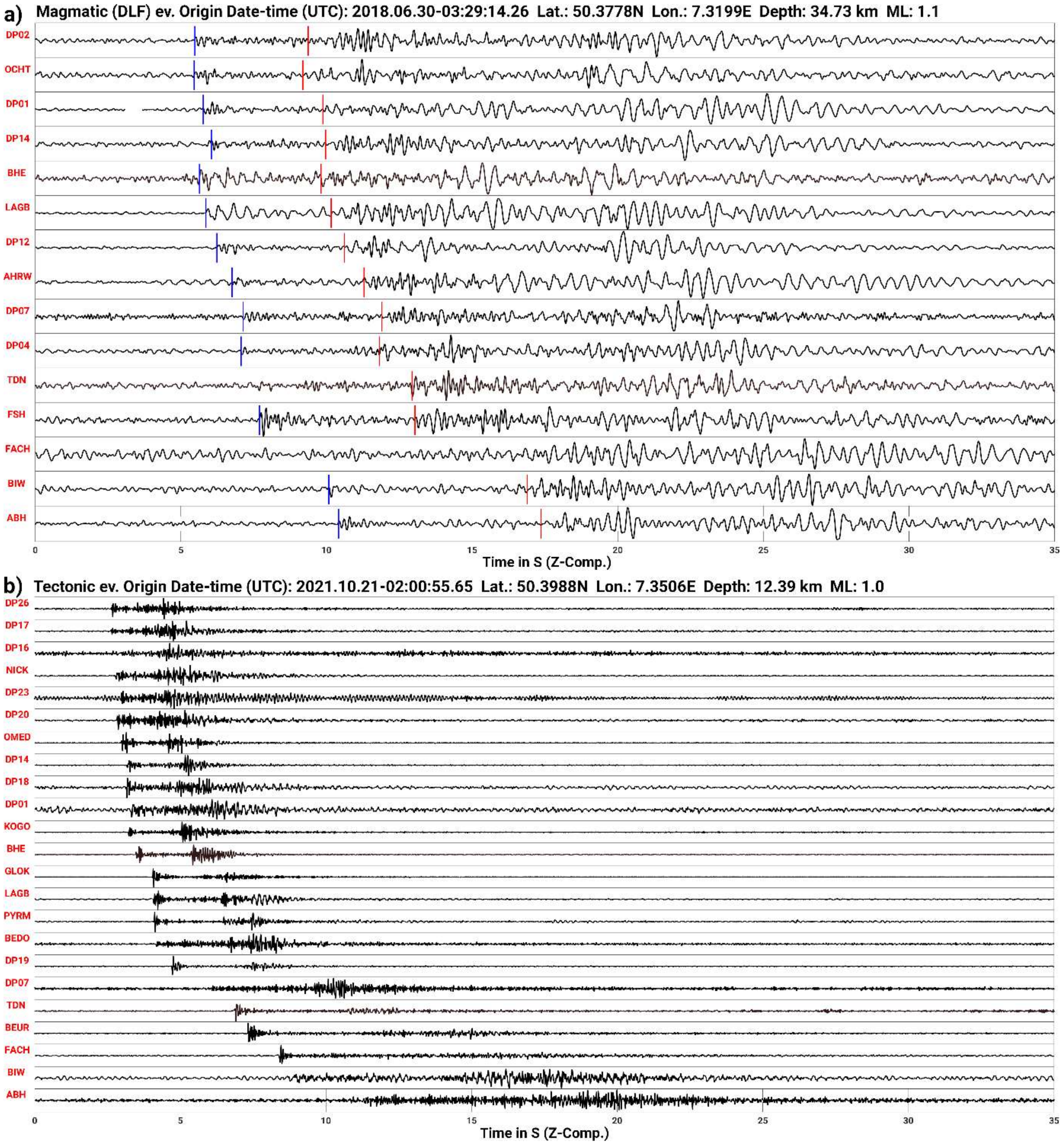

Fig. 4.6 Recordings of two different types of earthquakes in the East Eifel Volcanic Field, a) the source is a deep low-frequency event at about 35 km depth with long-lasting waveforms. P-wave (blue) and S-wave onsets (red) are marked, b) a tectonic event from the Ochtendung Fault Zone at about 12 km depth with high-frequency waves of short duration. The displayed vertical ground motion amplitudes are trace-normalised and the seismograms are ordered by distance from top to bottom. See Fig. A13 for for horizontal component recordings of the DLV event

As inversion method we apply the VELEST routine (Kissling et al. 1994, 1995) which is stable and well tested. The input parameters for VELEST are the arrival times of the direct seismic P- and S-wave phases, station coordinates, and different starting velocity models. As output, we receive minimum 1-D velocity models, refined hypocentral parameters and individual station delay times for the seismic stations, which take into account local seismic velocity anomalies such as 3-D heterogeneity and anisotropy. In addition, one gets statistical information on the inversion calculation, e.g., the root mean square (RMS) values of the travel time residuals.

4.7.1 Input Data

In total, our event catalogue contains 1762 regional events, which are composed of 1475 events from bulletin files in the years 2010-2021 (Landeserdbebendienst 2018), 319 DLF and 1135 tectonic events in the years 2014-2021 and 155 DLF and 547 tectonic events in the years 2018-2021 when most DEEP-TEE stations were recording (Fig. 4.3). The velocity model is confined to the region around the EEVF, because we want to concentrate on the DLF events and the seismicity of the OFZ. Therefore, recordings from events are chosen from an area which is restricted to 6.81 °E < longitude < 8.13 °E and 50.0 °N < latitude < 50.75 °N. A maximum epicentral distance of ca. 80 km to the centre of the network and a maximum azimuthal observational gap of 180° is allowed; only few events at the borders have a gap of 160°-180°, mostly it is much less. The event selection criteria reduce the amount of input events for VELEST to 1325 events.
Phase picking of first P- and S-wave arrivals is done manually following the criteria in Diehl et al. (2012). To account for different accuracies of the time readings of the phase arrivals, we use a quality weighting scheme. This scheme is based on the following quality classes: a high quality (quality class 0) means that the maximum uncertainty for the picking time of a phase is $\Delta t \leq 0.05$ s. A lower quality (quality class 1) is for an uncertainty of 0.05 s $< \Delta t \leq$ 0.1 s. Uncertainties of 0.1 s $< \Delta t \leq$ 0.2 s are rated as quality class 2. Larger uncertainties are rated as quality class 3 (0.2 s $< \Delta t \leq$ 0.4 s) and quality class 4 ($\Delta t >$ 0.4 s) which are both not used for the further analysis steps. After this quality ranking, 2598 P-wave and 3491 S-wave arrival times are available for the inversion (Table A5).
The distributions of the travel time residuals are displayed in Fig. 4.7 for quality classes 0, 1, and 2, separately for P-wave arrivals (Fig. 4.7 a-c) and S-wave arrivals (Fig. 4.7 d-f). The theoretical travel times are calculated with the existing local reference velocity model by Ahorner (1983), see Fig. A1 in the supplement. The distributions in Fig. 4.7 are close to Gaussian distributions and, as expected from the quality ranking of the picking procedure, the residuals increase from quality class 0 to quality class 2 (the statistical numbers are given in Fig. 4.7). In general, the residuals are quite small, less than 0.5 s, indicating that the Ahorner model (1983) is one possible appropriate reference or starting model for further inversions with VELEST.
Fig. 4.8 shows the depth distribution of the events from which the arrival times (qualities 0-2) are picked and which we use as three input data sets VI1-V3 (Table A5) for VELEST. VI1 contains P-wave picks with at least 8 picks from 201 events with a hypocentral depth $d <$ 17.5 km and at least 6 picks from events with $d >$ 17.5 km, altogether 2049 picks. VI2 contains S-wave picks with the same criteria as VI1 for P-waves, altogether 3038 picks from 320 events. VI3 is composed of pick times from 382 events with at least 8 P- or 8 S-wave picks for $d <$ 17.5 km and 6 P- or 6 S-wave picks for $d >$ 17.5 km (2598 P- and 3491 S-wave picks). Most picked phases are from earthquakes in the upper crustal seismogenic zone (<17.5 km depth), especially from earthquakes of the OFZ. All deeper phases are from DLF events with more uncertain arrival times due to a lower signal-to-noise ratio and the more emergent DLF waveforms compared to the impulsive waveforms of tectonic ruptures. A special feature in Fig. 4.8 is the higher number of S-phases

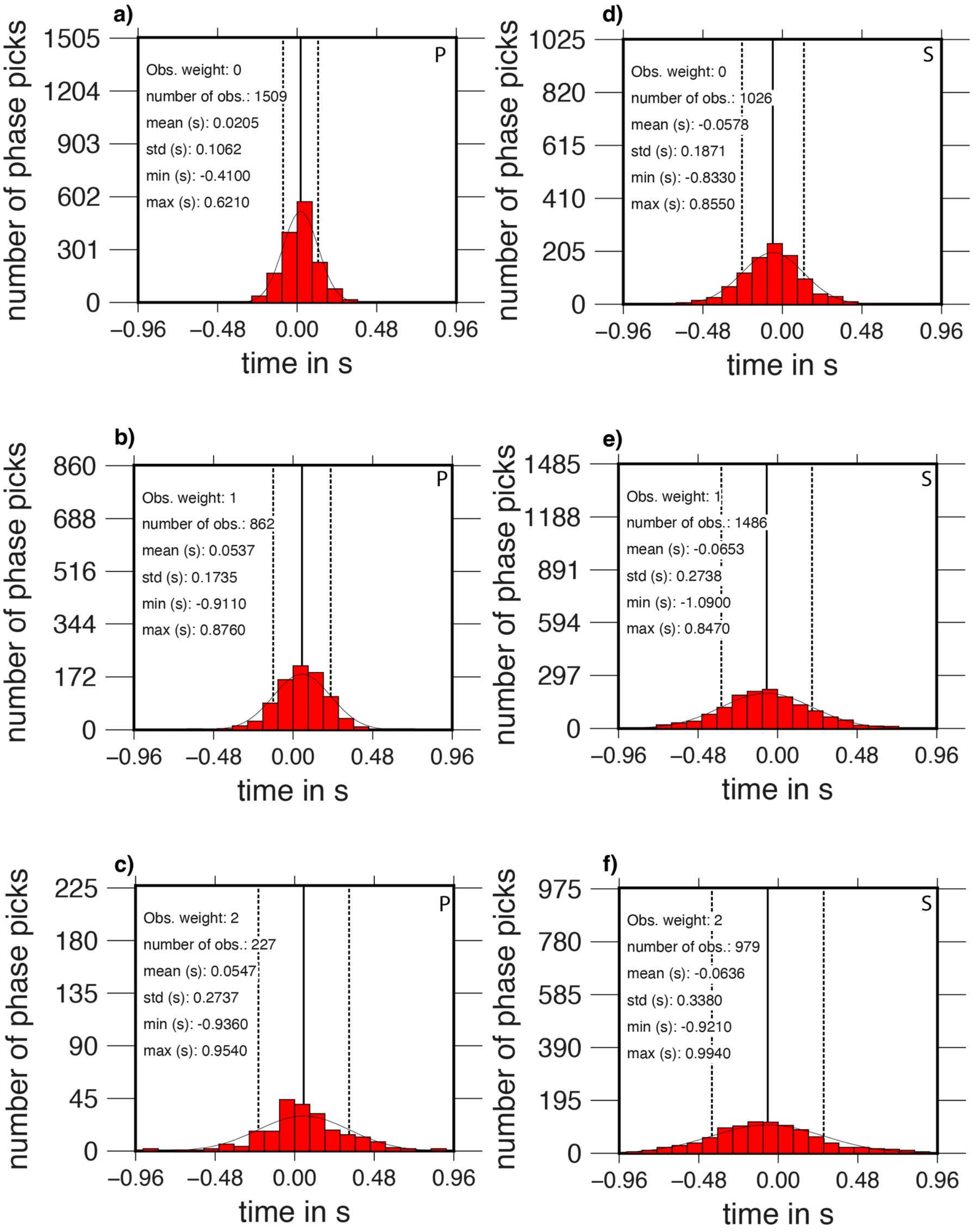

Fig. 4.7 Statistics of travel time residuals used as input data for the VELEST inversion. As reference the Ahorner (1983) *vp* and *vs* models (Fig. A1) are used. a) - c) P-wave data for qualities 0, 1, and 2; d) – f) S-wave data for quality classes 0, 1, and 2

relative to P-phases for events below the seismogenic zone; numbers are given in Table A5. Typically, in seismological studies the amount of data from P-phases is higher than the number of S-phases. However, in our case, the P-phases of the DLF events are often not visible or quite uncertain, whereas the S-wavetrains with higher amplitudes are better visible (see section 4). Hence, *vs* is better constrained in the lower layers compared to *vp*. This point is described below in more details, because it strongly influences the inversion process.

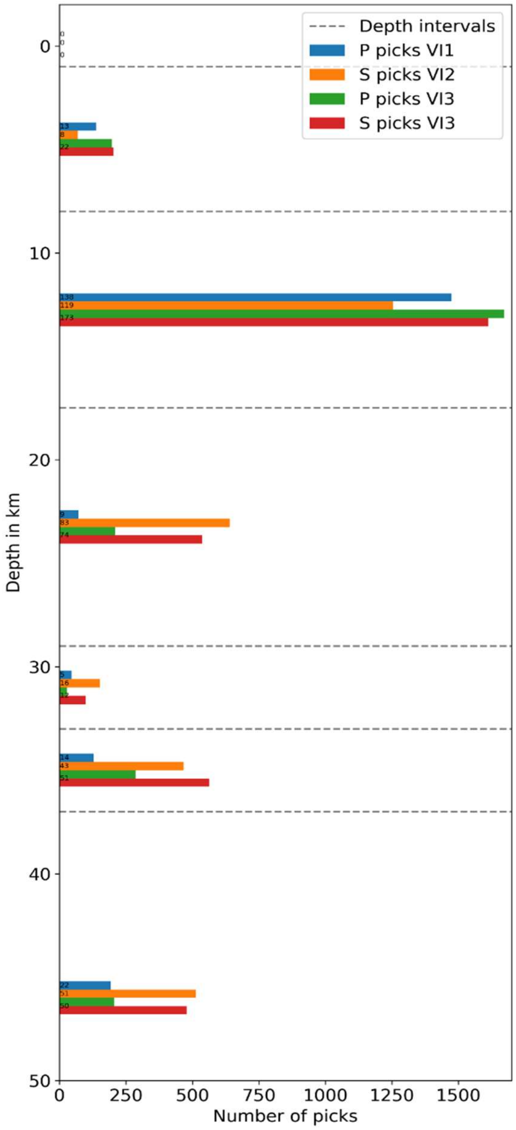

Fig. 4.8 Distribution of the hypocentre depths of picked seismic phases used for the inversions with VELEST. Blue and orange bars show P- and S-phase counts, respectively, if only P-phases or only S-phases are used for separately determined *vp* and *vs* models using input VI1 and VI2 (Tab. S5). Green and red bars show P- and S-phase counts, respectively, if both, P- and S-phases, are simultaneously used for the inversion with input VI3 (Tab. S5). The dotted lines indicate the main layers in the study region. The exact numbers of phase picks are given in Table A5

We use the permanent station OCHT (Fig. 4.2b) as reference station for our model, because it is close to the centre of the network in the EEVF and it was available from the start of the experiment. Therefore, station OCHT is also one of the stations with most determined phase arrival times.

A Wadati diagram (Fig. 4.9) is plotted to retrieve the *vp / vs* values as additional *a priori* information from the dataset. The Wadati diagram indicates a relatively low *vp / vs* which seems to increase with depth: 1.62 for events in the upper crust, 1.68 for events in the lower crust, and 1.68 for events in the uppermost mantle (standard deviations are less than 0.01). These values are averages along the complete ray path from the source to the receiver. Thus, the actual *vp / vs* value may be higher in the deeper layers, as rays from these layers have to traverse the upper crust. The Ahorner model (1983) has a *vp / vs* value of 1.69 in the crust and 1.70 in the uppermost mantle (Table A1); both values are below 1.73, the value for a standard elastic body.

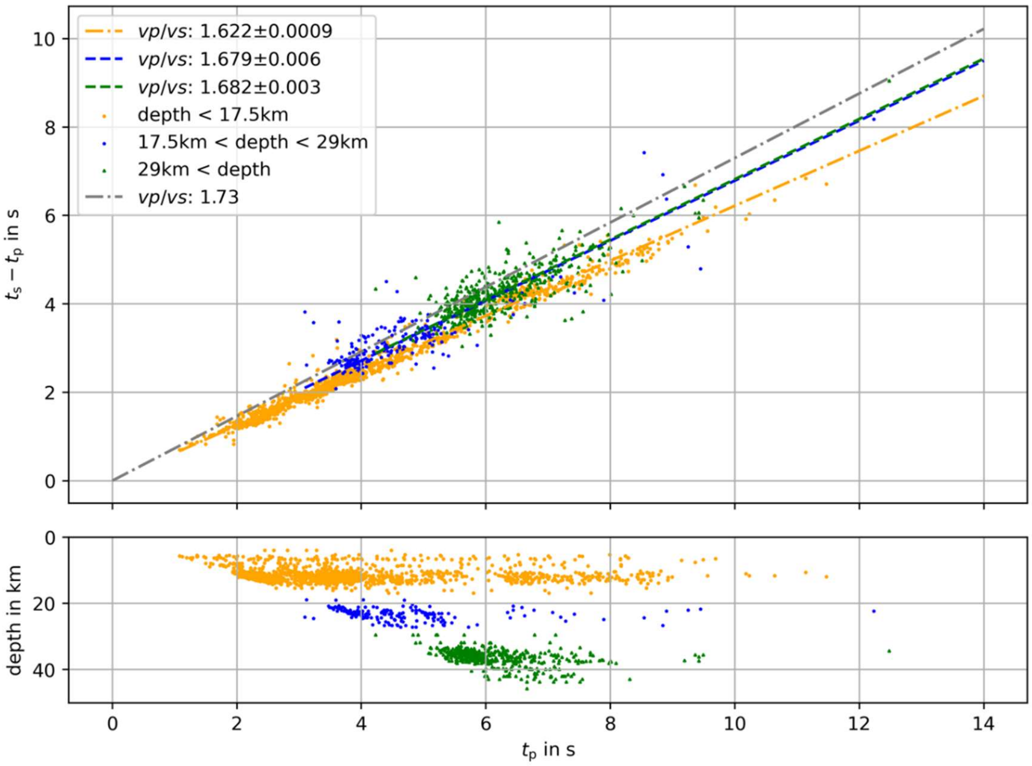

Fig. 4.9 Wadati diagram with arrival time data of 373 events in the study region. The origin time is taken from a relocation of the events using the *vp* and *vs* models from Ahorner (1983), see Tab. S1. The gray line represents a *vp / vs* of 1.73 as expected for a standard elastic body with a Poisson's ratio of 0.5. The dashed lines are fitted *vp / vs* values (Marquardt-Levenberg regression) for events at different hypocentral depths of 0-17.5 km (upper crust, orange), 17.5-29 km (lower crust, blue) and 29-45 km (uppermost mantle, green). The arrival times indicate a decreased *vp / vs* value at depth which slightly increases from 1.62 to 1.68 with depth. The given uncertainties are 1-σ ranges

We use three different starting models and perturbations of each of these as input models for VELEST to probe the model space and find an appropriate layering. We use the seismic velocity structures from two previous studies in the region. The Ahorner model (1983), see Fig. A1 and Table A1, was determined using earthquake data from the western Rhenish Massif region. Here the resolution with depth is restricted to the distribution of the earthquake data, which consist of events with a maximum depth of ca. 17.5 km (Ahorner 1983). The model by Mechie et al. (1983), see Fig. A1 and Table A2, is from an active-source seismic-refraction experiment and we take the model part at the EEVF which has a Moho depth of ca. 29 km. This model has a better depth resolution as Ahorner (1983) due to the deep reaching ray paths of the long refraction seismic profile. The third model is a very simple model with one layer in the crust and one layer in the mantle only plus a thin near-surface layer after Eickhoff (2022) (Fig. A3).

4.7.2 Inversion Strategy

The seismic velocities of the starting models are perturbed 20 times within a range of ±20% to obtain the input models for VELEST, indicated as grey lines in Fig. A2 and Fig. A3. The random velocity perturbations are tested to avoid a dependence of the inversion solution on the starting model. The number, thicknesses, and depths of the layers are varied based on the starting models. For the inversion with VELEST we apply a staggered inversion scheme. First, we invert four times for the velocity models and hypocentre locations. The output velocity models are iteratively used as input for the next inversion run. One inversion run consists of up to 10 iteration steps. During the inversion process we allow the inversion for low-velocity layers, after the first inversion run, if VELEST tries to introduce a low-velocity zone in the first run. Second, after we found a stable velocity structure, a final run inverts for the velocity models, hypocentre locations, and station delay times (again 10 iteration steps). Afterwards we analyse the resolution of the velocity models. Layers which do not converge, due to a lack of earthquakes within the layer, too few hits per layer, an overall short ray length within the layer, or which are too thin, are combined with other layers or are set to seismic velocity values using *a priori* information from active-source experiments. Such layers are damped in the next modelling step. Furthermore, layers with equal velocities are combined to one layer. Afterwards, a final inversion is conducted for station delay times only.

4.7.3 Test runs / Probing the model space and resolution

To probe the model space and the model resolution we inverted for *vp* and *vs* separately using the three previously described starting models (Ahorner 1983, Mechie et al. 1983 and the simple three-layer model) and the catalogues VI1 and VI2 as input (Table A5). The input data of the quality classes 0, 1, and 2 (Fig. 4.7) are assigned weights of 1.0, 0.5, and 0.25. We recognized that the uppermost layer (down to 1 km depth) is poorly constrained, because the inversion models do not converge and/or result in unrealistic seismic velocities. An explanation for this instability may be the short horizontal ray lengths and missing events inside the first layer (Table A5). To account for this problem, we fix *vp* to 5.0 km/s in the first layer based on an averaged shallow regional *vp* model of Eickhoff (2022) and a *vp / vs* of 1.65 from the Wadati diagram in all following runs, independent of the starting model. Furthermore, below the Moho (29 km depth), the *vp* is too low and *vp / vs* does not fit to the values of the Wadati diagram) in the uppermost mantle. This is due to the low numbers of events and phases (Table A5), especially for P-waves for which there is only a low number of P-picks from the DLF events (Fig. 4.8). Thus, we invert with joint P- and S-data (input VI3) with an equal weighting of P- and S-picks, as our catalogue contains more S-picks than P-picks, especially in the lower crust and uppermost mantle. All described inversion results below are the result from joint *vp* and *vs* inversion using catalogue VI3 as input, if not stated otherwise. After the inversion (four times inversion for velocity and hypocentres and one run for velocity, hypocentres and station delay times) with our three different starting models, we analyse the output models concerning their RMS, their convergence of the input models and the resulting velocities.

The output RMS values using Ahorner (1983) and Mechie et al. (1983), as well as the two-layer model as input models are quite similar. The output models with the best fit (minimum RMS) have all a very similar RMS value of 0.114-0.119 s (Table A6).

The resulting models after Ahorner (1983) and Mechie et al. (1983) have a similar velocity structure (Fig. A2). The minimum 1-D VELEST models contain a reduction of *vp* and *vs* in the lower crust compared to the upper crust. Below the Moho (29 km depth), we observe that the models are poorly constraint due to the low numbers of events and phases (Table A5), especially for P-waves. Minimum 1-D models with the Ahorner (1983) model as starting model, which have one layer in the mantle (half space), converge to low seismic velocities, especially for *vp* with just 7.03 km/s (Fig. A2b, Table A1B). Using the finer-layered mantle model from Mechie et al. (1983) the inversion results vary, indicating a resolution problem, again especially for P-waves (Fig. A2 d) due to the low number of rays (Table A5). As we cannot resolve the velocity step at the Moho, especially for *vp*, we fix the velocity increase at 29 km depth using the seismic refraction model of Mechie et al. (1983) as *a priori* information in the following models. We use the long-range seismic refraction model of Mechie et al. (1983) as the depth resolution of this model for the lower crust and upper mantle is better constraint than the one of Ahorner (1983) which has only upper crustal earthquake sources and short epicentral distances.

The simpler starting model with only three layers (near-surface, crust and mantle, Fig. A3 and Table A3) was tested to find averages for *vp* and *vs*. Using different starting seismic velocities, the results converge to *vs* = 3.54 km/s and *vp* = 5.80 km/s in the crust and *vs* = 4.21 km/s and *vp* = 6.67 km/s in the uppermost mantle. The average crustal *vp / vs* of 1.64 is quite close to the results in the Wadati diagram (Fig. 4.9). However, the average mantle *vp / vs* of 1.58 (Fig. A3, Table A3) does not coincide with the Wadati diagram, indicating a too low *vp* due to resolution problems.

4.7.4 Models KIT5 and KIT6

a) KIT5

Based on the resolution and results of the previous inversions we defined a new starting model for another inversion. We use the *vp* structure from Mechie et al. (1983) as starting point but include more *a priori* information. First, we keep the first layer fixed like before with a *vp* of 5 km/s after Eickhoff (2022) and a *vp / vs* of 1.65 from the Wadati diagram. Second, we combine layers in the upper crust based on their similar velocities and to simplify the model according to the resolution capabilities of VI3. This results in two layers instead of six layers as in the Mechie et al. (1983) model in the upper crust. The lower boundary of the upper crust is fixed at 17.5 km depth according to the maximum hypocentral depth of the tectonic earthquake hypocenters and the assumption that the brittle zone coincides with the upper crust. Anyway, variations of ca. ±2 km of this boundary do not significantly change the inversion results, what is learnt from the results of the previous inversion runs. In Mechie et al. (1983) the boundary between lower and upper crust is in 15 km depth, whereas in Ahorner (1983) it is in 19 km depth (Table A1 and A2). Both inversion results have similar velocity structures in the crust and a similar RMS (Fig. A2). The deeper layers are kept according to the model of Mechie et al. (1983). For this reason, the starting models for KIT5 contain five layers in the upper mantle, because the Mechie et al. (1983) model has a complex structure there, including a low-velocity zone (LVZ) with a gradient. As the Mechie et al. (1983) model does not contain *vs*, the starting values for *vs* in KIT5 are determined from a range of different *vp / vs* values to generate a *vs* gradient.

After the inversion process the *vs* structure in the crust converges well and even in the mantle the *vs* model range is small (Fig. A4). There are two LVZs in the lower crust and upper mantle. The variation of the *vp* structure of KIT5 is also small in the crust, but more variable in the mantle. In the mantle *vp* has a tendency to unrealistically low values. There are still difficulties in resolving the complicated thin layered structure below the Moho, but we observe a tendency to the model by Mechie et al. (1983) in the KIT5 *vs* layer structure. To better constrain *vp* in KIT5 we fix the velocities below 29 km depth following the seismic refraction model of Mechie et al. (1983), see Fig. A1, and a *vp / vs* which is adapted to melt and volatiles as suggested by Dahm et al. (2020). In this depth, the subparallel and subvertical ray distribution of our data does not allow to properly determine the fine upper mantle layering or the velocity step related with the Moho, even so the hypocentres are as deep as ca. 45 km. After fixing the velocity structure in the upper mantle we conduct a final inversion run for station delay times only. The resulting lowest RMS deteriorates marginally to 0.115 s (Table A6).

The best model with the lowest RMS (Table A4 and Fig. 4.11) has low *vp / vs* in the crust and higher *vp / vs* in the mantle. Synthetic Wadati diagrams are given in Fig. A5 and their *vp / vs* values in Table A7. These values, which are averages along the complete ray paths from the source to the mantle, have a similar trend as the observed values with increasing *vp / vs* for deeper hypocenters (Fig. 4.9).

b) KIT6

As all previous inversions indicate a problem to resolve the thin-layered velocity structure in the upper mantle, especially for *vp*, we further simplify the input model of KIT5. This is done to keep all resolvable information in the mantle with our input data. We select a simpler mantle structure with only three layers. As *a priori* information the seismic velocities in the first layer, the Moho depth from Mechie et al. (1983), and the thickness of the upper crust (brittle zone) are kept, like for KIT5. In the following, we describe the results of the inversion for *vp* and *vs* separately as well as the joint inversion for both.

After the inversion the *vs* values converge quite well (Fig. 4.10a and 10c) for different starting models. If only S-wave data are used (VI2), there is a LVZ in the crust with a small *vs* reduction. If P- and S-wave data are jointly inverted (VI3), then *vs* is clearly reduced in the lower crust and there appears a LVZ in the upper mantle which is recovered for all input models. These results agree well with the Mechie et al. (1983) model and the Dahm et al. (2020) model, which also contain a LVZ in the lower crust and in the upper mantle. The *vp* results of the inversion are not well resolved (Fig. 4.10a and 10d) in the mantle. The *vp* result below the Moho contains a gradual increase in velocity with very low velocities in the mantle and no velocity step as in the model by Mechie et al. (1983), which may not be resolvable due the small number of P-phases in this depth range. Furthermore, the expected reduction of *vp* below the Moho may also contribute to this problem. Also, the resulting *vp / vs* value of the separate *vp* and *vs* inversions does not fit the observations of our data from the Wadati diagram (Fig. 4.9). These arguments lead to the conclusion to better use the result of the joint *vp* and *vs* inversion. As the resolution of *vp* is low in the mantle, we fix *vp* to a simplified *vp* structure after Mechie et al. (1983) which includes a LVZ (Fig. 4.11). The *vs* model is not damped in the mantle and the velocities are the ones determined by the previous inversion runs. Finally, we conduct the last inversion step for station delay times only, with fixed *vp* in the mantle.

The resulting lowest RMS values insignificantly vary between 0.114 s and 0.116 s for the KIT6 modelling procedure. The 1-D KIT6 model in Fig. 4.11 well recovers the *vp / vs* values in the Wadati diagram (Fig. A6 and Table A7). This outcome may give a faint preference for final model KIT6 over final model KIT5 in Fig. 4.11. Inversion model KIT6 has also three layers less than KIT5, so an overfitting is better avoided. However, we note that the model parameter resolution is influenced by the implemented *a priori* information for both solutions. As both models achieve a similar low RMS, both can be treated as *pari passu* as long as no further deep-reaching seismic refraction models are available for the EEVF.

4.7.5 Station delay times

The determined station delay times are presented for the 1-D models KIT5 in Fig. A7 and Table A8, and for KIT6 in Fig. 4.12 and Table A9. For both models station OCHT is used as reference station and the distribution as well as values of the station terms are very similar. Hence, we only describe Fig. 4.12. The P-wave station delay times (Fig. 4.12b) are quite low in the centre of the recording network (<0.2 s) and seem to have a positive NW-SE trend and a negative NE-SW

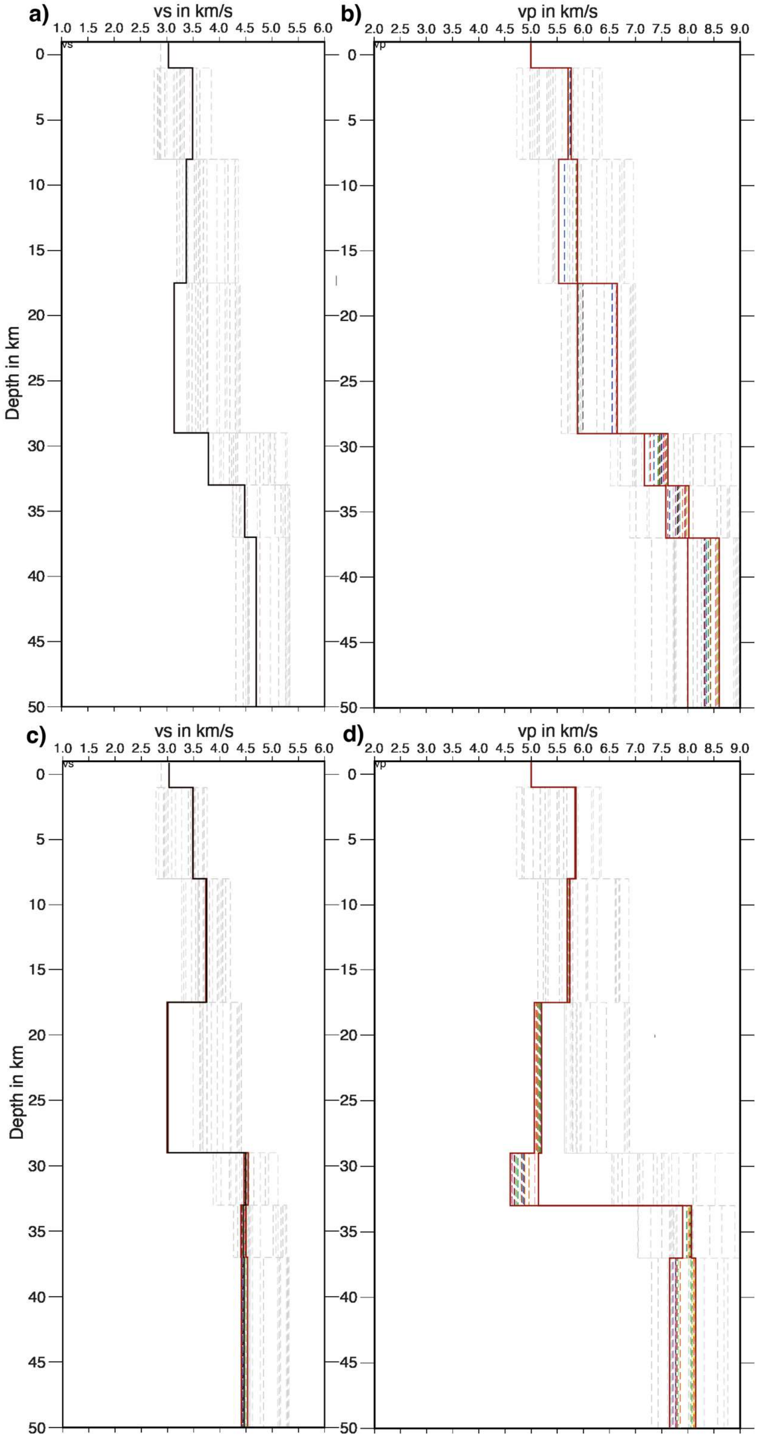

Fig. 4.10 1-D seismic velocity inversion models for KIT6. Gray lines are 21 perturbed input models, colored models are the related inversion results. a) *vs* model from S-wave travel times only (VI1), b) *vp* model from P-wave travel times only (VI2), c) *vs* model from combined P- and S-wave travel times (VI3), d) *vp* model from combined P- and S-wave travel times (VI3)

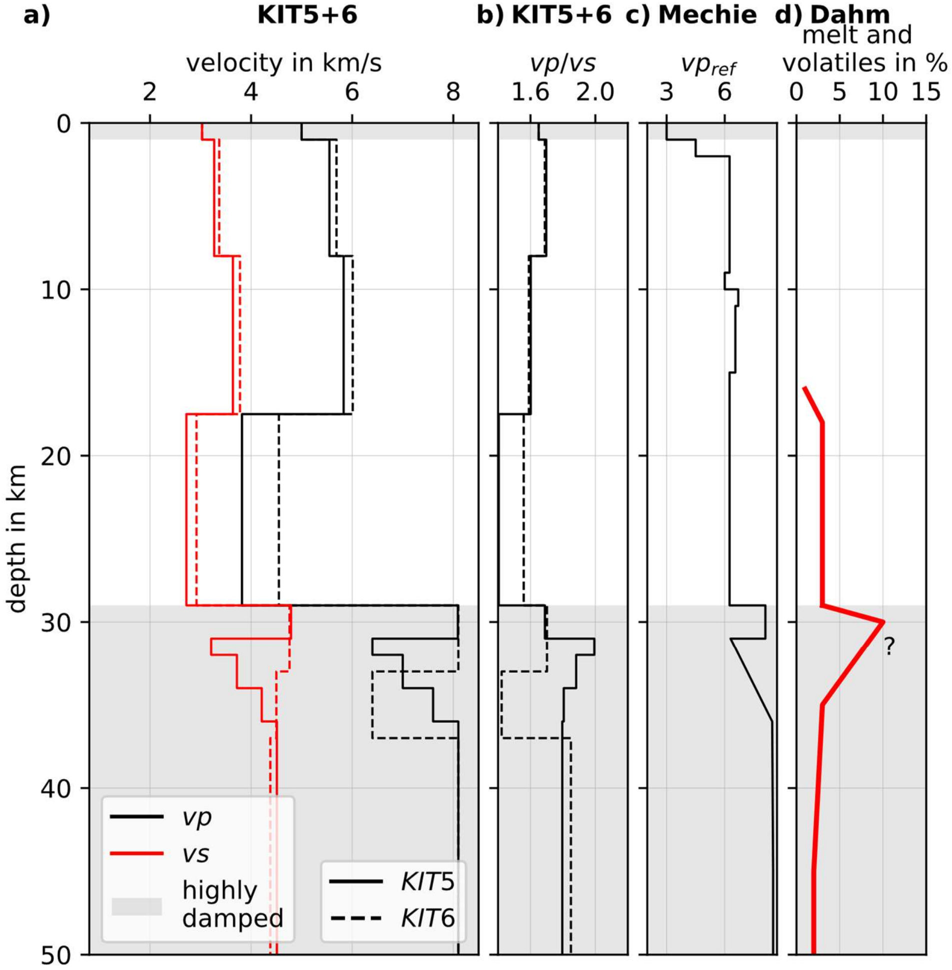

Fig. 4.11 a) 1-D seismic *vp* and *vs* models KIT5 (solid lines) and KIT6 (dashed lines), b) *vp* / *vs*, c) *vp* model after Mechie et al. (1983) in the EEVF, d) proposed melt and volatile distribution from Dahm et al. (2020). Gray shaded areas indicate depth ranges with poor resolution where *vs* and *vp* inversion is partly damped and thus based on *a priori* information (see text)

Table 4.1 1-D seismic layer model KIT6

depth in km	*vs* in km s^{-1}	*vp* in km s^{-1}	*vp* / *vs*
-0.9 – 1.0	3.03	5.00	1.65
1.0 – 8.0	3.37	5.69	1.69
8.0 – 17.5	3.78	6.01	1.59
17.5 – 29.0	2.92	4.55	1.56
29.0 – 33.0	4.76	8.10	1.70
33.0 – 37.0	4.50	6.40	1.42
> 37.0	4.38	8.10	1.85

trend relative to OCHT. A similar pattern is observed for the S-wave station delays (Fig. 4.12a) with slightly higher delay time values compared to the P-wave values. Such an azimuth-dependent pattern may be due to anisotropy, however, the positive delays towards NW may also reflect low seismic velocity in the crust related with the main volcanic centres of the EEVF. At depth there could be still hot magma reservoirs which have a lifetime of several 10,000 years (Schmitt et al. 2022). Overall, the small delay time values of KIT6 in the center of the network (Fig. 4.12) are interpreted as a hint that the related 1-D *vp* and *vs* models do well represent the seismic structure below the EEVF. The same holds for the delay times of model KIT5 with its similarly small delay time values.

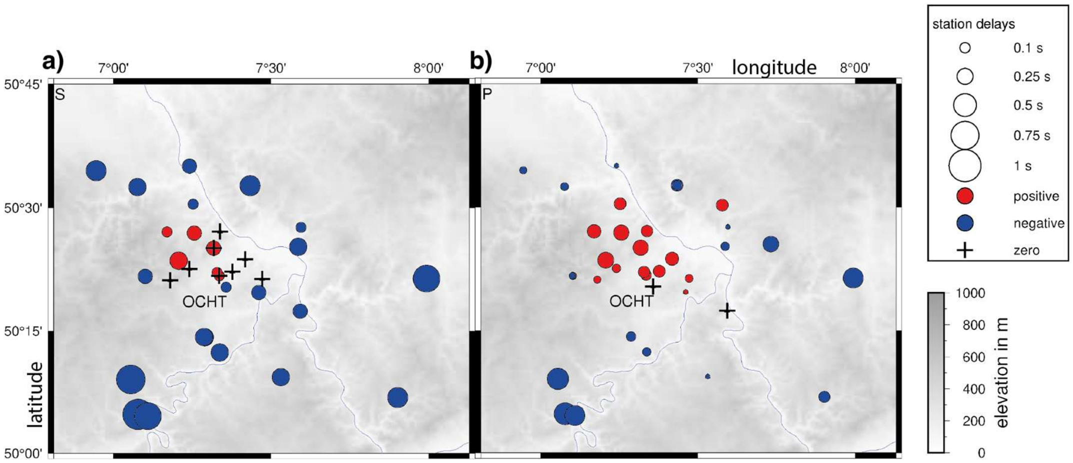

Fig 12 Station delay times of the 1-D model KIT6 and the DEEP-TEE network. a) S-waves, b) P-waves. Station OCHT is the reference station

4.7.6 Stability test

To evaluate the stability of the minimum 1-D *vp* and *vs* models KIT5 and KIT6 we conducted shift tests (Kissling et al. 1995) for which we randomly perturbed the input hypocentres in space by up to 0.1° horizontally and by up to 5 km in depth (Figs. A9 – A12). During the inversion runs the velocity model is not damped.

As result of the shift tests, we find that the relocated events differ by less than ca. 2 km in depth and less than ca. 500 m in latitude and longitude relative to our best hypocentre solutions (Fig. A11). The shift tests recover well the sharp line of events along the OFZ, which is aligned NW-SE. The DLF events are shifted back into a channel-like structure underneath the Laacher See Volcano, indicating a clearly confined region of their occurrence. Likewise, the unusual depth of up to ca. 45 km for the DLF events is retrieved by the shift tests. The seismic velocities remain stable, except for the first and second layers, as well as the uppermost mantle layer (Fig. A12). The former can be explained, as previously described, by short horizontal ray lengths in these layers. The Moho region cannot be resolved, due to the complicated structure, enclosed by two LVZs. These three layers are also the ones with the smallest event numbers. Hence the inclusion of the *a priori* information is necessary to fix the velocity models below the crust.

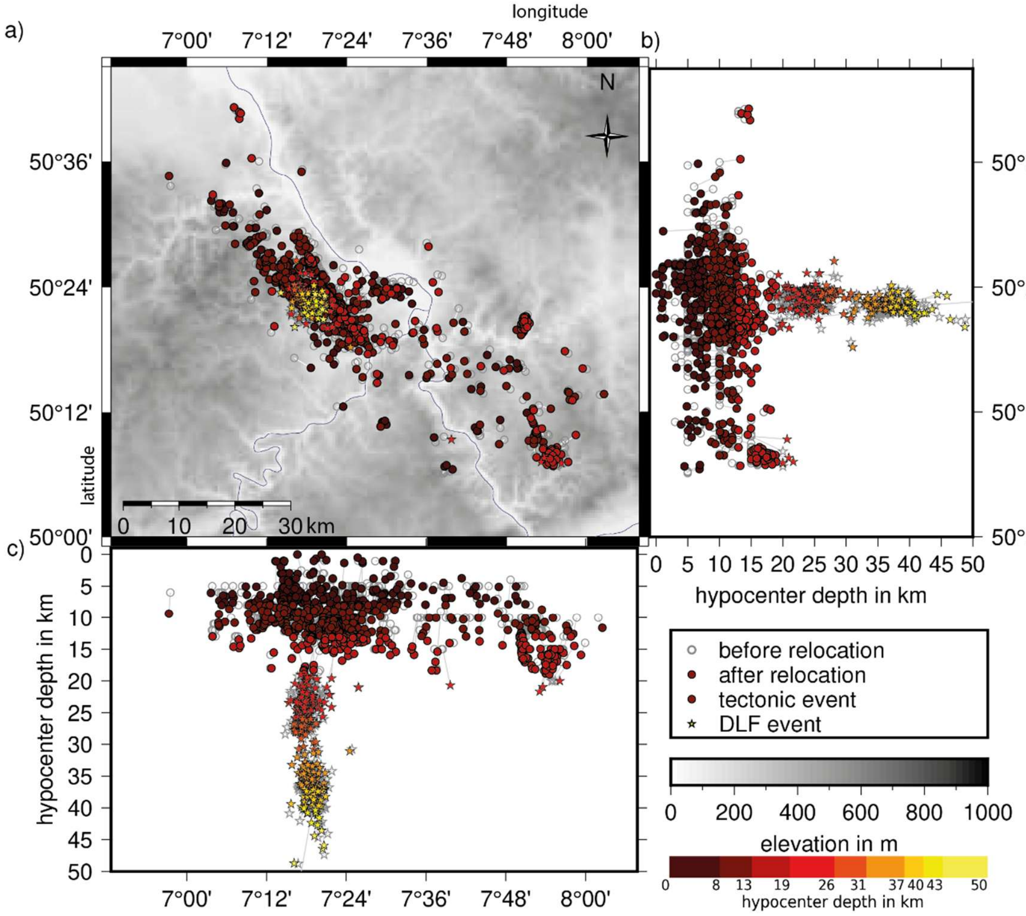

Fig. 4.13 Relocation result for the 1325 input events using the 1-D *vp* and *vs* models KIT6 (Fig. 4.11) incl. station delay times from Fig. 4.12. The starting hypocentres are from the bulletins of the state seismological service and from own preliminary locations, especially for DLF events. Circles show tectonic events, stars indicate DLF events; colour indicates hypocentral depth with a color scale adjusted to Hensch et al. (2019)

4.7.7 Relocation of event catalog

The relocation result with the 1-D model KIT6 in Fig. 4.13 displays a clearer picture of the seismicity distribution compared to the routine event locations. The earthquakes along the OFZ are more closely together and outline a sharp active fault with NW-SE strike (Fig. 4.13). The hypocentres of the tectonic events (dots) are as deep as ca. 17-18 km which corresponds to the depth range of the seismogenic zone typical for Germany (BGR Kataloge 2023). The distribution of the DLF seismicity (stars in Fig. 4.13) seems to be confined to a less than 10 km wide zone just SE of LSV as found in Hensch et al. (2019). This zone steeply crosses the crust and the lower lithosphere and reaches the asthenosphere at about 45 km depth (Mathar et al. 2006; Seiberlich et al. 2013).

4.8 Discussion and Preliminary Results

The *DEEP-TEE* experiment provides valuable seismological data which confirm the occurrence of unusually deep earthquakes in the upper mantle underneath the EEVF in the midst of Central Europe, as first described by Stange et al. (2014) and Hensch et al. (2019). The earthquake catalog of the University of Cologne, earthquake station Bensberg, reported an event in the mantle at already in September 2011 (http://www.seismo.uni-koeln.de/catalog/2011.htm). Such intra-plate seismicity in the lithospheric mantle is seldomly observed and due to its spatial coincidence, we argue for a strong causal relationship with the dormant volcanic field in the East Eifel.

To improve the event locations in the EEVF, we invert the picked P-wave and S-wave phase arrival times for 1-D *vp* and *vs* models KIT5 and KIT6 (Fig. 4.11) including station delay times (Fig. A7 and Fig. 4.12). Both, KIT5 and KIT6, equally well fit the input data. KIT5 and KIT6 consist of an upper crust with increasing seismic velocities with depth and a LVZ in the lower crust. As the ray distribution does not allow a unique solution for *vp* and *vs* below the Moho, we add a priori information after Mechie et al. (1983) and Dahm et al. (2020). The differences between KIT5 and KIT6 are small, however, we slightly prefer KIT6, because it has fewer layers and, therefore, better avoids an overfitting of the data. This is in accordance with the often used principle of Occom's razor (De Groot-Hedlin and Constable 1990).

The two LVZs can be explained with partial melt and volatiles in the lower crust and upper mantle (Fig. 4.11d, Dahm et al. 2020). A depth-dependent low *vp / vs* is observed in the data (Fig. 4.9) and this is reproduced with the models KIT5 and KIT6. The low *vp / vs* could be a hint for volcanic gas in the upper crust (Dvorkin et al. 1999) which is consistent with the observation of volcanic gas emissions at the surface (Bräuer et al. 2013; Goepel et al. 2015). The P- and S-wave station delay times reveal a positive NW-SE and a negative NE-SW trend. The positive delays towards NW hint to lower seismic velocities in the crust in the area of the volcanic centres of the EEVF relative to the seismic velocities in KIT5 and KIT6. This is another indicator for increased temperature and/or melt and volatiles in the crust (Paulatto et al. 2022 and references therein). For an improved petrophysical interpretation a 3-D velocity model including *vp / vs* is necessary to discriminate between temperature, melt, fluids and gases.

The systematic analysis of the low frequency events between 2014 and 2018 revealed that they have deeper hypocentres (about 8-45 km depth) than the known tectonic crustal seismicity (mainly 5-17 km depth) with higher frequency waves (Hensch et al. 2019). In addition, Hensch et al. (2019) observe a slight increase of the corner frequency of the DLF events with depth and, therefore, argue that the low-frequency content is not a filter effect along the propagation path between source and receiver. The waveforms of the DLF events are similar to recordings from other active volcanic regions world-wide and, therefore, they are interpreted as signals related to ongoing deep magmatic processes. Combining the recordings from permanent and mobile seismological stations allows us now to well locate many events below the Moho (Fig. 4.13). The refined locations of the ca. 200 DLF events ($ML < 1.5$) between 2014 and 2021 using the local *vp* and *vs* models KIT5 and KIT6 visualise a nearly continuous depth distribution of the DLV events. This distribution seems to represent a translithospheric magmatic channel southeast of Laacher

See Volcano (Fig. 4.13) which may be related with a very slow refilling of crustal magma reservoirs with melt and/or volatiles (Koushesh et al. in prep). During the time period 2014-2021 there is no systematic temporal or spatial migration of the DLF events. Perhaps such migrations may occur at longer time scales which cannot be resolved yet.

Tectonic activity is limited to the upper ca. 17 km depth, in accordance with a regional model in which strength resides in one layer (Jackson 2002, Jackson et al. 2021). This behaviour should be modelled in more details, using the numerous temperature and lithology data from the Eifel region. The continual tectonic activity at the Ochtendung Fault Zone (OFZ) can be used to image its actual fault plane (Fig. 4.13 and Fig. A8). A preliminary model proposes a near-vertical fault which is active between ca. 5 km and 15 km depth (Föst et al. 2022) and will be complemented with fault plane solutions. The occurrence of swarm-like shallow activity in the north of LSV (Hensch et al. 2019) is not yet analysed in detail, but the DEEP-TEE data may help in the future to outline possible fluid pathways at depth in this area. The many different seismic signals in the EEVF require more studies to better understand the ongoing magmatic and tectonic processes and its consequences, including a robust hazard analysis. Therefore, we will continue the operation of the *DEEP-TEE* experiment. There are also other ongoing seismic experiments in the EEVF. In 2020/2021 a ca. 4.5 km long line of 17 recording stations was running ca. 8 km southeast of LSV to study the OFZ. During June 2021 additional 200 instruments were placed on this line at 5 m distances during an active source experiment with an accelerated drop weight which was dropped at 25 m shot distances (Houpt et al. 2022). For an additional high-resolution study, a large-N seismological network recorded between summer 2022 and summer 2023 (Dahm et al. 2022a,b) which will hopefully add more data to resolve the crustal structure underneath the EEVF in hitherto unprecedented resolution.

4.9 Conclusions

The seismological *DEEP-TEE* experiment is a significant contribution to monitor the dormant magmatic-volcanic system of the Laacher See Volcano and the East Eifel Volcanic Field. Despite problems with high cultural seismic noise, a sensitive recording network was installed which records local events with magnitudes below *ML* 1 in the uppermost mantle. The new seismic velocity models (*vp*, *vs*, *vp / vs*) including stations correction terms allow us to well locate these events what is the basis for geodynamic and magmatic studies. The determined low-seismic velocity in the lower crust and upper mantle is interpreted as signs for volatiles or melt. The located deep low-frequency events outline a narrow 3-D structure (Fig. 4.13). This structure reaches downwards some 15 km underneath the Moho representing the deepest seismicity in Central Europe. It is interpreted as a translithospheric magmatic channel which may feed a crustal magma reservoir from as deep as the asthenosphere or rather the top of the low velocity anomaly related with the Eifel plume (Mathar et al. 2006; Seiberlich et al. 2013). Based on petrological analysis of the rock material that was brought to the surface during the last eruption of the LSV, the lifetime of such a crustal reservoir may last some 10,000 years (Rout and Wörner 2018; Schmitt et al. 2022) before the occurrence of another eruption in the far future.

5 Detector A6-DFMSD

In this chapter (and appendix B), a robust detection algorithm (detection algorithm A6-DFMSD) is presented which I developed in accordance with the DEEP-TEE dataset properties and the goal of the project; detection of the seismic signals which do not have the common ordinary characteristics of the tectonic type events but also detection of the diverse set of signals in connection with magmatism. There, a diverse set of seismic signals is presented which A6-DFMSD could detect within the relatively moderate noise level dataset of the DEEP-TEE.

This chapter entirely published as:
Koushesh, K., Ritter, J.R.R. An adaptive 6-dimensional floating-search multi-station seismic-event detector (A6-DFMSD) and its application to low-frequency earthquakes in the East Eifel Volcanic Field, Germany. *J Appl. Volcanol.* 13, 9 (2024). https://doi.org/10.1186/s13617-024-00147-8

5.1 Abstract

We introduce a seismic event detector that applies signal analysis in the time and frequency domains. Signals are searched for with matching coincidences at neighbouring recording stations in space and time. No a priori waveform information is needed for the Adaptive 6-Dimensional Floating-search Multi-station Seismic-event Detector (A6-DFMSD). It combines a short / long time average algorithm (STA/LTA), frequency range selection, energy envelope matching, and backprojection techniques to find a robust detection model. As a challenging test example, the new detector is tuned and applied to a dataset with five months of microearthquake ($ML < 2$) recordings in the East Eifel Volcanic Field (EEVF), Germany. There, both magmatic and tectonic earthquakes occur in a depth range between 3 km and 43 km. A6-DFMSD detected 4.3 times as many events as were already known and it discovered a previously unknown event cluster. After manual localization and classification of the events, we show that A6-DFMSD finds events of different origins: tectonic, magmatic, atmospheric, and anthropogenic. In particular, low-frequency (LF) earthquakes of magmatic origin with a complicated waveform coda are very well identified. We suggest that seismological networks monitoring local seismicity in similar target zones would benefit from the use of A6-DFMSD to allow the detection of a wide range of different seismic signals.

5.2 Introduction

Volcanic regions are known for a wide variety of seismic signals emitted from different sources connected with or activated by magmatism, tectonic stresses, and rock-fall processes (Sherburn et al. 1998, Neuberg 2011, Wassermann 2012, Naofumi et al. 2013). These signals substantially differ in frequency content and waveform compared to tectonic earthquake signals, and they can be emitted from a very shallow source position (like rock-fall events or magma oscillations in a crater) to very deep regions even from below the Moho discontinuity due to magma movements near initial melting processes. Thereby they cover a wide range of source intensities and activity rates (Ratdomopurbo and Poupinet 2000, Hidayat et al. 2000, Stroujkova and Malin 2001, Cusano et al. 2013, Malfante et al. 2018).

One of the challenging issues in this regard is the detection of very weak signals and microseismic events (local magnitude $ML < 1$) in volcanic regions. Detection of the weak signals becomes even more challenging when we consider the two following common scenarios: (a) region of the study is newly covered by a local seismological network (b) the detection of new types of seismic sources (unknown waveforms) becomes a special goal for the local seismological monitoring.

In both cases, there is no a priori information specifying the target waveform characteristics to search for. On the other hand, the state-of-the-art high-performance seismic event detectors, like the template matching method (Ross et al. 2019), supervised machine learning methods (Perol et al. 2018), or some of the unsupervised machine learning methods (Yoon et al. 2015) need a priori estimates regarding the target waveform characteristics for training the algorithms.

In this work, first, we introduce a new detection routine in MATLAB called Adaptive 6-Dimensional Floating-search Multi-station Seismic-event Detector (A6-DFMSD) which does not require a priori knowledge of the target waveforms. To search for matching detections at neighbouring recording stations, it uses a homogeneous or, in the best cases, a 1-D layered velocity model, to find a detection model. Second, we evaluate the performance of A6-DFMSD by analysing a challenging seismological dataset. The test dataset includes five months of continuous recordings from the East Eifel Volcanic Field (EEVF), Germany, where earthquake signals of both tectonic and magmatic origins have been reported (Hensch et al. 2019). Subsequently, we manually pick the identified phases, localize and classify the detected events and compare them with the published event catalogues of two local seismological surveys (state seismological service of Rhineland-Palatinate and Bensberg Observatory, University of Cologne) that monitor seismic activity in the region. We also compare our results with an internal event list provided by Hensch et al. (2019) which is focused on deep low-frequency (DLF) events in the EEVF. A comparison of the performance is provided regarding the detection of DLF events with the same test dataset between A6-DFMSD and the STA/LTA method (Allen 1978, Trnkoczy 2009) after tuning its parameters to DLF events.

Previous seismological and geodynamic studies on the EEVF (Fig. 5.1) suggested a deep-seated mantle plume system (Ritter et al. 2001, Ritter 2007, Kreemer et al. 2020) and a long-lived magma chamber beneath the Laacher See volcano (Wörner and Wright 1984, Schmitt et al. 2010) where the last big eruption occurred about 13 ky ago (Schmincke et al. 1983; Reinig et al. 2021). After the detection of the first two DLF events at depths of 40 km and 43 km on 18th and 22nd in Sep.

2013 (Stange et al. 2014), monitoring of the seismicity in the EEVF became an important scientific subject. To investigate microseismic activity in the region more closely, especially regarding DLF events, several temporal seismic stations were installed in between the few existing permanent stations in the region. This seismological experiment is called Deep Eifel Earthquakes Project - Tiefe Eifel Erdbeben (DEEP-TEE) and started in July 2014 (Ritter et al. submitted. Up to now, the DEEP-TEE seismic dataset contains almost ten years of continuous seismic records (more than 2.4 terabytes in volume) and the network has been reconfigured and continuously improved to achieve an optimum configuration regarding detection and location of seismic events.

Detection of LF events is more challenging than detection of tectonic events, because of their waveform complexity, diversity and often low signal-to-noise ratio. Although the observation of LF waveforms in records from volcanic areas can be related to the strong attenuation of the signals in the subsurface (Bean et al. 2014), this is not the case for the deep LF (DLF) events observed in EEVF. Here the corner frequency of the deeper LF events is often higher than for the shallower LF events (Hensch et al. 2019). This observation of higher frequencies from larger depths indicates that the unusual low frequencies of DLF earthquakes are not caused by any filter effects between source and receiver, e.g., due to shallow low velocity zones such as fluid reservoirs (Hensch et al. 2019). Anyhow, we use the frequency content as parameter for the detection.

In volcanic regions, the origin of LF events has been attributed to the growth and possibly resonance of fluid-filled cavities (Aki et al. 1977; Aki and Koyanagi 1981). Further modelling and numerical studies are reported in Neuberg et al. (2000). Waveform characteristics and spectral content of these signals depend on the source geometry, the location where the crack nucleates, and the acoustic properties of the fluid or embedding rocks. As a consequence, waveforms of these signals are more complex than those from purely tectonic sources. LF events in the EEVF occur in a wide depth range from ca. 8-43 km, whereas tectonic events in this region have only a source depth between ca. 3-15 km (Hensch et al. 2019). Below, we label as DLF those LF events whose sources are below the Moho (deeper than 29 km). The wide depth range spanned by the LF events in the EEVF influences and increases the waveform diversity: there is a large variability in S-P phase arrival times and often the phases (specially the P-phases) are strongly attenuated. Another factor, which is important regarding detection of the LF events, is the low magnitude of the events. In the EEVF the known LF events have very weak magnitudes between 0.4 *ML* and 1.3 *ML*, except for two events with 1.7 *ML* and 1.8 *ML*. The related low-amplitude phases make the detection harder, especially during the day time when anthropogenic noise level increases strongly in the EEVF. Due to this background, the idea behind A6- DFMSD is to develop a robust search method which can cope with a wide frequency band, waveform diversity, and low phase amplitudes without the need for a priori waveform information.

In the next section, we explain the technical side of the method A6-DFMSD in accordance with the flow diagram in Fig. 5.2. Later in the discussion section we expand on the advantages, limitations and the capabilities of the method. A user manual of the detector is also provided besides the codes in GitHub (https://github.com/Koushesh/A6-DFMSD/tree/master) as the supplementary file to explain more details. Since the codes are written in MATLAB, Signal Processing and

Statistics Toolboxes are required to be installed in advance. The abbreviations used in this paper are listed alphabetically in Table 5.1.

5.3 Method and parametrization

A6-DFMSD method and its philosophy are explained in the following subsections and Fig. 5.2:
- Input Parameters
- Configuration of the Detection Model (CDM step)
- Detection Field preparation (DF preparation)
- Single Station Detection (SSD step)
- Multi-Station Detection (MSD step).

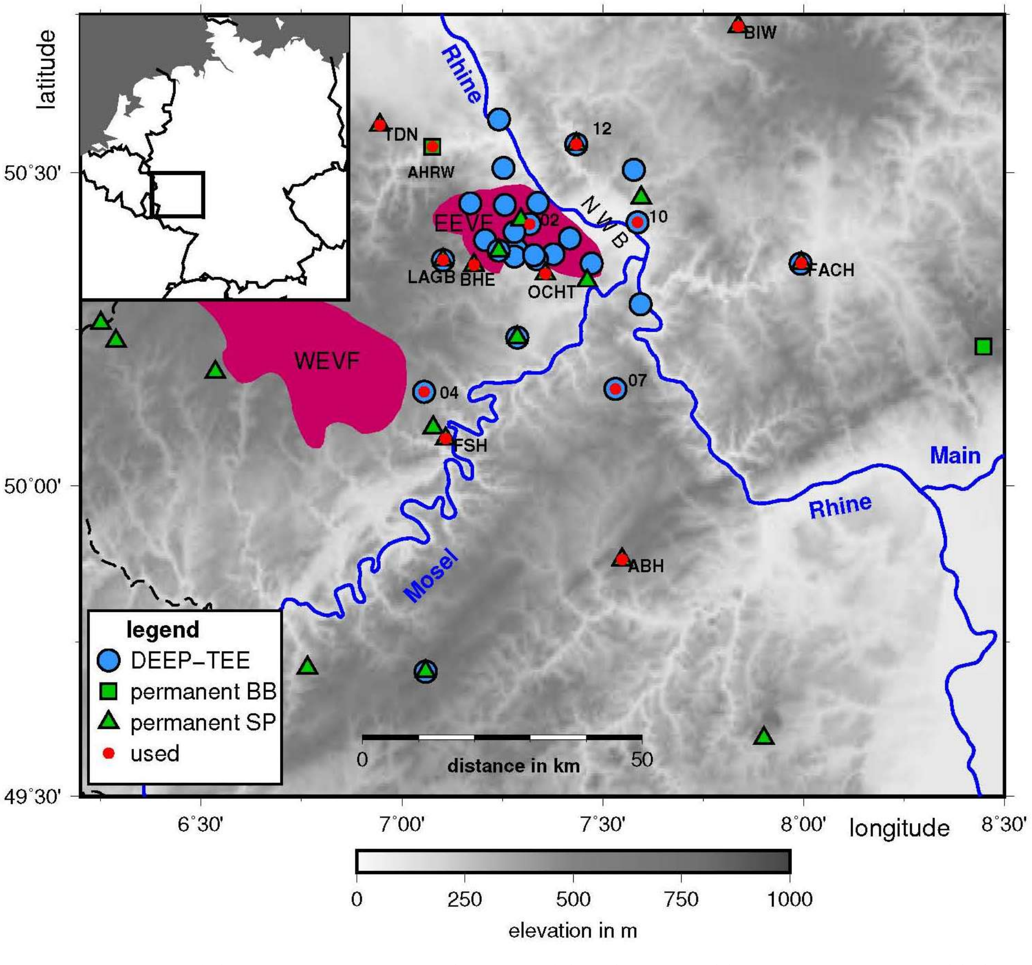

Fig. 5.1 Location of the Quaternary East and West Eifel Volcanic Fields (EEVF, WEVF, reddish areas) with the seismological stations of the DEEP-TEE experiment. Green symbols indicate permanent recording stations (BB: broadband, SP: short-period), blue symbols are temporary stations; a red dot indicates stations used in this study. NWB: Neuwied Basin. The inset shows the position of the study region (square) in Germany

5.3.1 Input parameters

A6-DFMSD is designed to detect the seismic signals which originate from a predefined seismic target zone (e.g., a volcanic field) and which are recorded by a local seismological network. For this reason, in addition to the three continuous seismic velocity records (Z: vertical, N: north-south, E: east-west), the following information is needed to construct a detection model:
(a) coordinates and codes of the seismological stations,
(b) a simple (homogeneous or layered) 1-D P- and/or S-wave seismic velocity model,
(c) a center location, a radius length for a target area, an upper and a lower depth for determining the event locations inside the target area. These data define a cylindric geometry of the target zone.

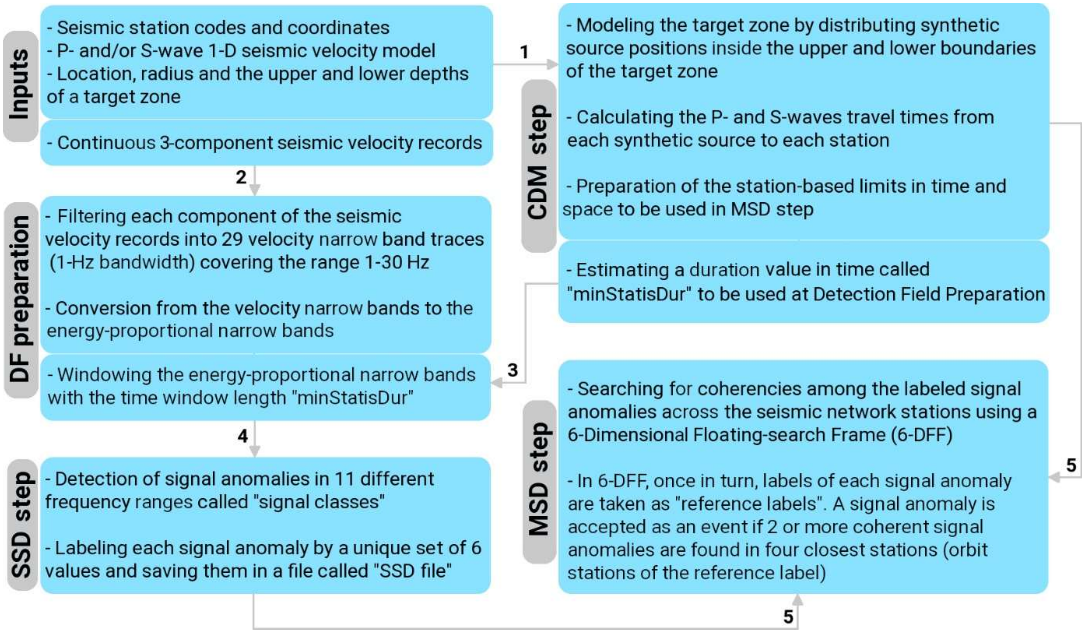

Fig. 5.2 Overview on the major steps of A6-DFMSD: Inputs, Configuration of the Detection Model (CDM step), Detection Field preparation (DF preparation), Single Station Detection (SSD step), and Multi-Station Detection (MSD step)

5.3.2 Configuration of Detection Model (CDM step)

A6-DFMSD uses the input information to construct a model and generates some outputs which later are used in DF preparation and MSD steps. The CDM step consists of the following sub-steps:
(a) Defining the upper and lower sides of a seismic target zone: synthetic source positions are distributed inside the circular bottom and top sides of a cylindric target zone, to cover the shortest and the longest raypaths. Fig. 5.3a provides an exemplary top view of distributed synthetic source positions which are the same as in the application of this study (see section 3).
(b) Calculating the P- and S-phase travel times (T_p and T_s, respectively) for each individual combination of the synthetic sources and the recording stations: the local 1-D seismic P- and S-wave

seismic velocity models, the synthetic source positions, the positions of the seismological stations and Snell's law are used for the ray path approximation.

(c) Obtaining sets of time limits for the search of detection coherencies based on the potential travel times between the recording stations and possible source locations: these time limits are used in the MSD step when the seismic signals, which originate from the target zone, are discriminated from signals with source locations outside the target zone. In this part, A6-DFMSD calculates the relative difference in arrival time of the seismic phases between each pair of stations considering each synthetic source. Figs. 5.3b and c, visualize these (exact-) time limits in dark blue and dark red bars for recording stations DEP02 and ABH, respectively. There, the light blue and light red bars indicate the exact-time limits after rounding up in respect with the window length "minStatisDur" explained in the second next paragraph (sub-step (e)). The detector takes the rounded-time limits instead of the exact-time limits while searching coherencies. This prevents to miss the detection of the events at the edges of the time limits.

(d) For each station, the four closest stations are determined: this information is used to limit the search for coherencies in space in the MSD step. Fig. 5.4a shows how the stations are grouped for the test example in this study.

(e) Estimation of an optimum time window (called "minStatisDur") for windowing seismic traces: minStatisDur is obtained by a statistical approach to estimate the typical half signal duration of the microearthquakes which are supposed to occur inside the target zone and are recorded at the seismological network.

Table 5.1 The alphabetically sorted abbreviation list

Abbreviation	Meaning
6-DFF	6-Dimensional Floating-search Frame
A6-DFMSD	Adaptive 6-Dimensional Floating-search Multi-station Seismic-event Detector
CDM	Configuration of the Detection Model
DEEP-TEE	Deep Eifel Earthquakes Project - Tiefe Eifel Erdbeben
DF	Detection Field
DLF	Deep Low-Frequency
EEVF	East Eifel Volcanic Field
LF	Low-Frequency
MSD	Multi-Station Detection
SSD	Single Station Detection
STA/LTA	Short Time Average/Long Time Average amplitude

5.3.3 Detection Field Preparation (DF preparation)

In A6-DFMSD, the distribution of recorded energy around the signal anomalies is taken as an attribute for searching coherencies. This is especially helpful to search for frequency-dependent signals, e.g., such as LF magmatic tremor. This part provides basic information to analyse the distribution of the recorded energy in different frequency ranges (here called signal classes). Such frequency-dependent signal classes are helpful for the detection of different type of signals with different frequency contents observed in volcanic regions (Chouet 1988, Neuberg 2011, Naofumi et al. 2013). For this purpose, each component of the continuous velocity records is decomposed into 29 narrow frequency bands (with a width of 1-Hz in our application) spanning the frequency range 1-30 Hz (Figs. 5.5b, c and d). We verify that choosing a narrower band width than 1-Hz adds artifacts to the data specially to the lower frequency part. Choosing a wider band width reduces the sensitivity of the method in extracting features of the signal anomalies. Following equation 1, the narrow-band seismic velocity traces are then converted to energy-proportional (E^*) narrow band traces. There, for each sample i of each narrow band j (with j running from 1 to 29) E^* is obtained by the summation:

$$E^*_{j,i} = Z^2_{j,i} + N^2_{j,i} + E^2_{j,i} \qquad (1)$$

where Z, N and E are seismic velocity records of the three components of ground motion (Fig. 5.5e). The energy-proportional narrow bands are the unified measures of the ground motion. With this summation the whole recordable energy of the signals in each frequency band is taken into account. This prevents to miss the detection of polarized seismic signals.

In the next step, the energy-proportional narrow bands (E^*_j) are windowed (Fig. 5.5f). By windowing, we mean partitioning the data with a constant window length (routine minStatisDur) in the time domain and then taking the mean value of each partition for further analysis. The value

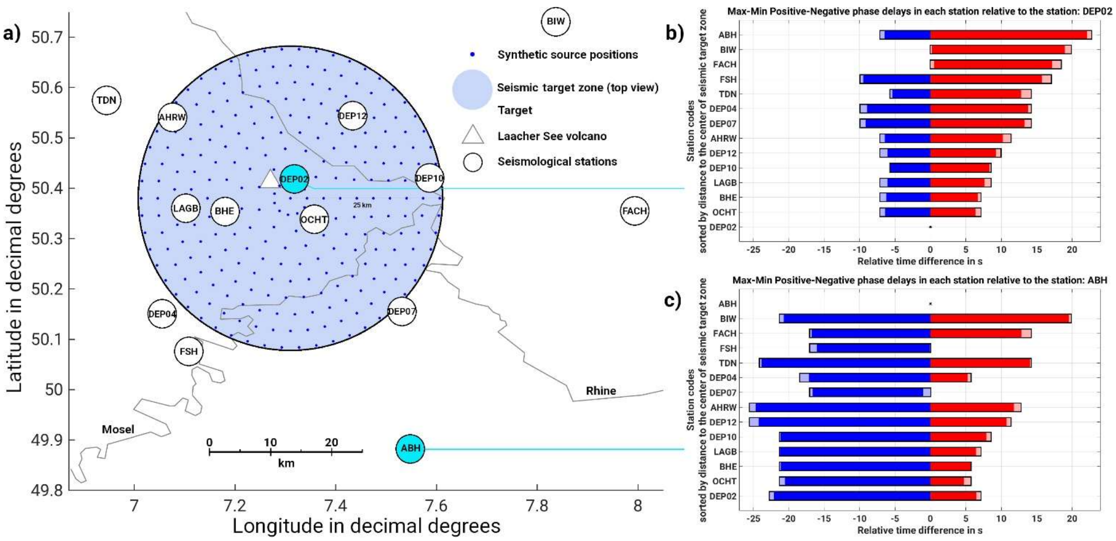

Fig. 5.3 Configuration of a detection model (CDM step) in association with the test example in the EEVF (Fig. 5.1). a) station locations and top view of the seismic target zone considered in this study. Each small blue dot is considered as a seismic source and the travel times for the first P- and S- phase arrivals are calculated for each source-station pair. b) subset of calculations to find the station-wise detection limits in the time domain. It is indicated how long before (in light blue) and/or after (in light red) the detection of a seismic phase at station DEP02 the routine searches for coherent seismic signals in the records of the other stations. c) the same b), but here the time differences are obtained relative to the recording station ABH. Note: in b) and c) the dark blue and dark red bars denote the exact-time limits, and the light blue and light red bars indicate the exact-time limits after rounding up in respect with the window length "minStatisDur"

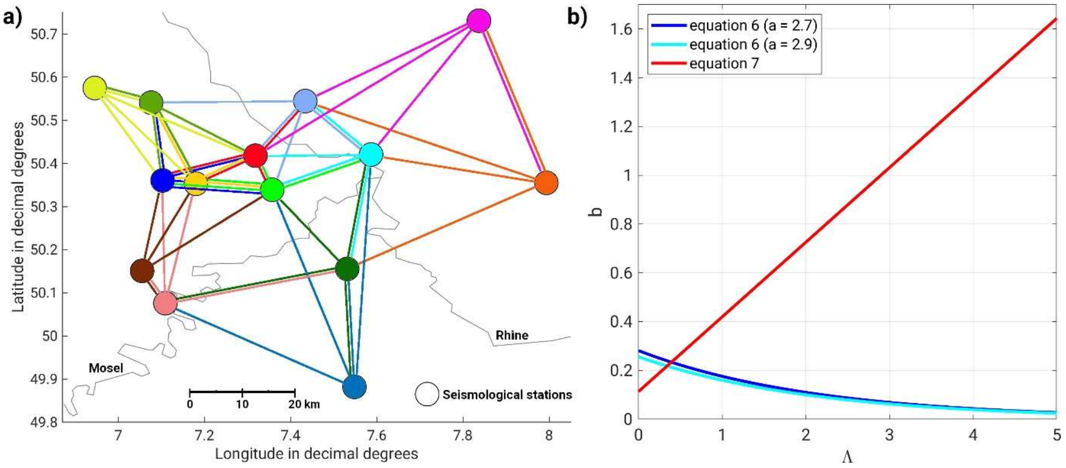

Fig. 5.4 a) Station locations and their mutual relationships while searching and connecting coherent signals in the Multi-Station Detection step (MSD step). For each station, the coherency search is limited to a radial distance in which only the four closest stations are involved. Here, each station is plotted with a specific color and the corresponding four nearest stations are linked to it with the same color, b) during the MSD step, vicinities for the coherency search for the variation coefficient of the DFs are determined using empirical equations (6) and (7). Here this relationship is plotted in blue (dark and light) for equation (6), and in red for equation (7). The dark blue line shows this relationship while searching for tectonic and volcano-tectonic events (signal classes higher than 3) in the shallower zone (3-30 km depth), and the light blue line shows this relationship for the detection of possible events in the deeper zone (30-50 km depth). The red line indicates this relationship while searching for LF events (signal classes less than 4, see section 2.4) in both seismic target zones

for ”minStatisDur” is obtained in the CDM step (see section 2.2). As results of this procedure, we obtain 29 windowed energy-proportional narrow bands called Detection Fields (DFs). The DF of each narrow band is indexed by j (DF_j).

5.3.4 Single Station Detection (SSD step)

For each recording station, signal anomalies are detected independently in different frequency ranges called signal classes. Each signal class is defined by two values denoting the upper and lower corner frequency of a desired frequency range in Hz. Depending on the corner frequencies of the signal classes, each signal class contains a bunch of certain DFs (Fig. 5.5f). A signal anomaly is detected when the signal to noise ratios exceed certain thresholds at all the DFs of a signal class. Similar to the STA/LTA (short / long time average amplitude) algorithm (Allen 1978), the threshold values vary depending on the amplitude value of each sample. For each sample i of a DF, a threshold is defined by the mean value of the amplitudes of the three samples before sample i (reference samples or noise part) plus the absolute mean deviation of the amplitudes of the reference samples multiplied by 0.7 (an empirical constant). This empirical constant can be varied to adjust the sensitivity of the detection.

As an example, in Fig. 5.5g, the detection of a signal anomaly in a signal class is presented (signal class 6 among the total 11 predefined signal classes). Based on the detector logic, sample i (red dot) is detected as a signal anomaly, because the amplitude values at sample i have a higher value than the defined thresholds (blue dashed lines) at all DFs of the signal class. In Fig. 5.5 the reference samples are shown by the green dots right before the sample i.

For each signal anomaly, which is detected in a signal class, a unique set of six parameter values is saved as the labels of the signal anomaly. These six parameter values are:

- station code: implicitly, the latitude and longitude of the station location
- sample number (i) of the detection point: representing the detection time
- signal class (*n*): which is defined by the upper corner (j_2) and the lower corner (j_1) of a frequency range in Hz
- variation coefficient (Λ) of the DFs at the detection point i in the signal class *n*: this is obtained from equation 2 and implicitly represents the distribution status of the recorded energy at the point of detection in the corresponding signal class. Λ is indeed equal to standard deviation of the DFs amplitudes in the signal class *n* at the detection point i, divided by mean value of the DFs amplitudes (μ) in the same signal class *n* and at the same detection point i. The $\mu_{n,i}$ used in equation 2 is obtained by equation 3.

$$\Lambda_{n,i} = \frac{\sqrt{\frac{1}{j_2 - j_1 + 1} \sum_{j=j_1}^{j_2} \left(DF_{j,i} - \mu_{n,i}\right)^2}}{\mu_{n,i}} \tag{2}$$

$$\mu_{n,i} = \frac{1}{j_2 - j_1 + 1} \sum_{j=j_1}^{j_2} DF_{j,i} \tag{3}$$

- a value called "sigClasPower (Γ)": which implicitly represents the amplitude ratio of the recorded energy in the signal class *n* at the detection point i relative to the reference samples (noise part). Γ is obtained from equation 4. It is equal to the result of the division of two values: the numerator is the mean value of the DFs amplitudes in the signal class *n* at the detection point i ($\mu_{n,i}$) minus the mean value of the DFs amplitudes of the reference samples (in Fig. 5.5h, this is equal to the length of the red line), and the denominator is the mean absolute deviation of the mean values of the DFs amplitudes of the reference samples (in Fig. 5.5h, this is equal to the length of the blue line). $M_{n,i}$ which is used in equation 4, is obtained by equation 5 and is equal to the average of the mean value of the DFs amplitudes of the reference samples of detection point i in the signal class *n*.

$$\Gamma_{n,i} = \frac{\mu_{n,i} - M_{n,i}}{\frac{1}{3} \sum_{i=i-3}^{i-1} \mu_{n,i} - M_{n,i} \vee} \tag{4}$$

$$M_{n,i} = \frac{1}{3} \sum_{i=i-3}^{i-1} \mu_{n,i} \tag{5}$$

5.3.5 Multi-Station Detection (MSD step)

A signal anomaly detected at a station is listed as an event only if a certain number of coherent signal anomalies are found at other stations. This is similar to the phase association part in other known techniques. Here searching coherent signal anomalies is done by applying a 6-Dimensional Floating-search Frame (6-DFF). Depending on the labels of each signal anomaly (the unique set of six values), 6-DFF sets specific search ranges and limits accordingly. In this way, labels of each signal anomaly are taken as reference, based on the content of the reference labels (we use the phrase ”reference labels” to indicate labels of the signal anomaly which are taken as reference):

a) the coherency search in space is limited to the four closest stations (called ”orbit stations”). This supports the principle that the direct waves of the local events arrive earlier at stations closer to the source than at the more distant ones. As a result of applying such a coherency search limit in space, the number of false detections was remarkably reduced in our tests.

b) the coherency search in time is limited to a certain time window around the time sample in the reference label. The time window limits are unique and differ from station to station depending on the relative position of the reference and orbit stations in relation with the position of the target zone. The time and space limits, which are applied in this step, are already determined in the CDM step.

c) the coherency search in a signal class is limited to the corresponding signal class of the reference label.

d) the coherency search in *sigClasPower* (*Γ*) is limited to the labels having a *sigClasPower* value more than 2.

e) the coherency search with a variation coefficient (*Λ*) for DFs is limited to a border value around the variation coefficient of the DFs of the reference label. This border value (*b*) is obtained by empirical equations (6) and (7):

$$b = 1.6^{-(\Lambda + a)} \tag{6}$$

$$b = c \times \Lambda + d \tag{7}$$

a in equation 6 is a constant which can take a minimum value of 2.7. Following our test runs to minimize the ratio of false detections to the total number of detections, we found values 2.7 and 2.9 are suitable choices for a when the upper border of the target zones is 3 km depth and 30 km depth, respectively. The parameters c and d in equation 7 are constant values and after trial and error, we found the best values to be 0.306 and 0.113, respectively, to minimize the ratio of false detections to the total number of detections. This may differ for other applications.

In equation 6, the coherency search gets a wider border when Λ at the reference label has smaller values. In contrast, in equation 7 the coherency search gets a wider border when Λ at the reference label has bigger values. The borders determined by equation 6 are suitable for the detection of the signals which have less fluctuations in the amplitude of their frequency spectra around their dominant frequencies. This was the case for tectonic-type events in our study. In contrast, the

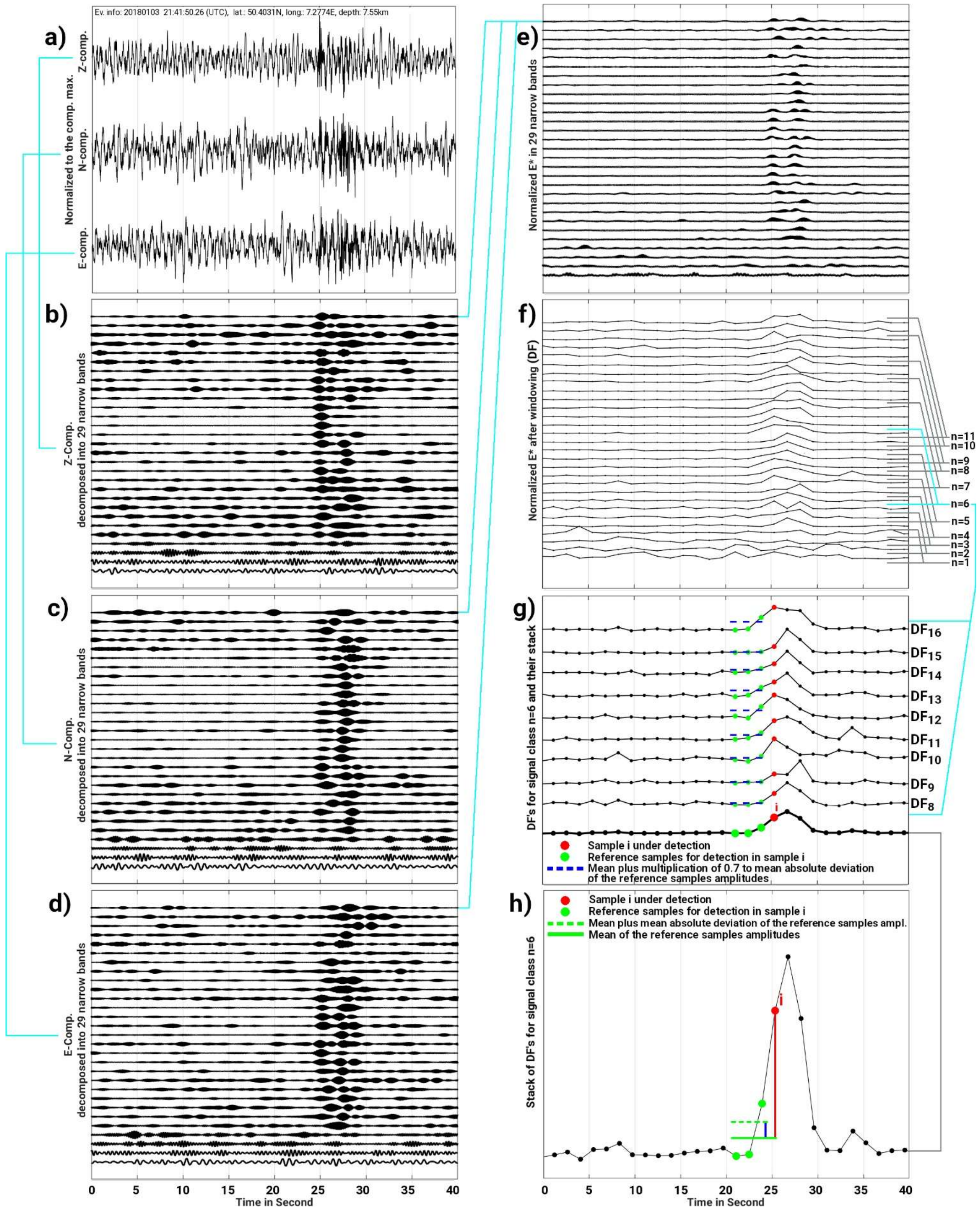

Fig. 5.5 Examples for Detection Field preparation (DF preparation) and Single Station Detection step (SSD step). a) three-component band-pass filtered (1-30 Hz) ground motion velocity of a microearthquake recorded at station AHRW, b), c), and d) decomposition of each component Z, N, and E by filtering with 29 1-Hz-wide frequency bands, e) conversion of the ground motion velocity in each frequency band into energy-proportional narrow bands following equation (1), f) traces in e) are windowed to prepare the Detection Fields (DFs) g) detection status of a signal anomaly at the sample i in the signal class n = 6 is shown. The red dot (sample i) is detected as a signal anomaly because the amplitude values at sample i have a higher value than the specific thresholds defined by reference samples (three green dots). The bold line is the stack of DFs of the signal class 6 (DFs from DF_8 to DF_{16}), h) close-up view of the stacked trace in g).

Value of sigClasPower ($\Gamma_{6,i}$) at sample i in signal class n = 6 can be illustrated as ratio of the length of the red line to the blue line. The technique used for detecting signal anomalies (g and h) is partly similar to the STA/LTA method with a very sharp criterium (window length in the LTA part is only three times longer than in the STA part)

borders determined by equation 7 are suitable for detection of the signals which have large fluctuations in the amplitude of their frequency spectra around their dominant frequencies, like LF type events.

Further explanations are provided in the supplementary file (section 1.5.2: equations 6 and 7 and, Figs. B5 and B6). Fig. 5.4b shows the relationship between b and Λ while detecting events in different signal classes in the differently defined seismic target zones in our test example.

Following a) – e), if two or more coherent signal anomalies are found at other stations (while passing through all the above 6-DFF conditions), the routine accepts the referenced signal anomaly as an event which originated from the seismic target zone. It is then written into the detection list. The detection list contains the following information regarding each detection:

- date, arrival time and duration of the event in UTC
- codes of the stations having coherent labels
- the signal class of the reference label.

While manually checking the detection outputs, the two latter information helps users to select events based on their dominant frequency content and/or based on the stations where the signal of the event was detected.

5.4 Test example and results

We apply the A6-DFMSD routine to study a period with microseismicity in the EEVF (Fig. 5.1). We select 5 months (October 1, 2017 - February 28, 2018) of continuous seismic records of the DEEP-TEE recording stations. In this time period, the recording equipment consisted of four broad-band STS2 (120 s) sensors and one short period Lennartz 3-D (1 s) at the mobile recording stations. At the permanent stations one Nanometrics sensor (Trillium Compact 120 s), one STS2, and seven short period sensors (1 s) including Mark L4 and LE3-D sensors were used. There were strongly varying noise conditions, because of traffic and industrial activity (Ritter et al. submitted. Table 5.2 lists the properties of the DEEP-TEE recording stations in more details plus the missing data status for each station within the five-month long selected time period.

To assess the performance of A6-DFMSD regarding the detection of DLF events, we compare the results of A6-DFMSD with the results of the STA/LTA routine (Allen 1978). The events detected by both methods are checked by a visual inspection of the waveforms, then they are manually localized and classified (as DLF, tectonic etc.) according to their waveform properties. We use the minimum 1-D layered velocity models KIT5 for *vp* and *vs* (Ritter et al. revised) and the routine VELEST (Kissling et al. 1994) to localize the events with at least six picked seismic phases. To check whether the events detected with A6-DFMSD are newly discovered events (or not) in comparison with the published local seismicity catalogues, we also cross-check each event with the event catalogues provided by the state seismological service of Rhineland-Palatinate (2023) and Bensberg Observatory, University of Cologne (2023). Both institutions regularly monitor and report seismic activity in the study region.

Table 5.2 The DEEP-TEE recording stations used in this study. The column indicated by “Missing” gives the number of the days without data. The column indicated by STA/LTA marks the stations used in STA/LTA test by a “+” and the not used by a “-“.

Network Station code	Lat. in degrees	Lon. in degrees	Elev. in m	Sensor type	Sampling rate in Hz	Missing Data in days	STA/ LTA
KB.DEP02	50.4181	7.3181	310	STS-2 120 s	100	0	+
KB.DEP04	50.1509	7.0550	455	STS-2 120 s	100	0	+
KB.DEP07	50.1556	7.5312	428	LE-3D 1 s	100	0	+
KB.DEP10	50.4208	7.5865	164	STS-2 120 s	100	0	-
KB.DEP12	50.5447	7.4337	295	STS-2 120 s	100	0	+
LE.OCHT	50.3387	7.3575	140	LE-3D 1 s	100	0	+
LE.LAGB	50.3608	7.1007	372	Trillium 120 s	100	0	+
LE.FSH	50.0760	7.1090	350	LE-3D 1 s	100	59	-
LE.ABH	49.8820	7.5480	618	Mark L4 1 s	100	0	-
LE.FACH	50.3563	7.9938	110	LE-3D 1 s	100	0	-
LE.BIW	50.7308	7.8373	310	LE-3D 1 s	100	23	-
GR.AHRW	50.5419	7.0760	180	STS-2 120 s	100	17	+
NH.BHE	50.3530	7.1800	290	Mark L4 1 s	200	0	+
NH.TDN	50.5750	6.9450	350	Mark L4 1 s	200	0	-

In addition, an internal event list from Hensch et al. (2019) is used which specifically lists DLF earthquakes of magmatic origin. Since A6-DFMSD is configured to detect events from a certain seismic target region, we summarize the final results in association with this target region. In the two following sections, we explain how the parameters for both A6-DFMSD and STA/LTA method are chosen, afterwards we explain the summarized results in Tables 4 and 5, where A6-DFMSD is compared with the three local seismicity catalogues and with STA/LTA results, respectively.

5.4.1 A6-DFMSD parameter setting

Concerning the variety of the observed signals in the EEVF (Hensch et al. 2019), we adapt the control file of A6-DFMSD to search for a wide range of signals. It covers the frequency ranges typical for the observed DLF events (ca. 1-8 Hz) and of the tectonic microseismic events (>10 Hz) by considering eleven frequency ranges as a part of the search limits (eleven signal classes). The lower and higher frequency borders of these eleven signal classes (1 - 11) are: [1 5] Hz, [2 7] Hz, [3 9] Hz, [4 11] Hz, [6 14] Hz, [8 17] Hz, [10 20] Hz, [12 23] Hz, [13 25] Hz, [15 28] Hz, and [16 30] Hz. We set the centre of the seismic target region to the midpoint between the epicentral area of the 75 reported DLF events (Hensch et al., 2019) and the centre of the Laacher See crater (Fig. 5.1), with a radius of 25 km (Fig. 5.3 a). The control file parameters are adjusted to search for events which possibly occur in two different depth zones: zone 1 is limited between 3 km and 30 km depth and zone 2 is limited between 30 km and 50 km depth.

5.4.2 STA/LTA parameter setting

The STA/LTA parameters are tuned to reach the most appropriate performance regarding the detection of the DLF events, because these are the main goal of our research study. In this regard, concerning the seismic noise conditions, at first, we select the eight quietest and closest recording stations to the target region out of the total of 14 available stations in the DEEP-TEE dataset. The noise level conditions were determined with a probabilistic power spectral density analysis (Ritter et al. revised). Since the DLF events of the EEVF have a dominant frequency range of 1-8 Hz (Hensch et al. 2019), we filter the recordings in the same frequency range with a band-pass filter before using STA/LTA detector. Then, as input for STA/LTA, the band-passed filtered records of each station are converted to the energy-proportional records using equation 1. The results of the station-wise STA/LTA detections are then collected into one detection list and compared within a 7 s time window for coincident detection. We choose a time length of 7 s in accordance with the observation of the typical DLF events in EEVF. After testing different sets of STA/LTA parameters, we select the most appropriate ones (Table 5.3) for which the number of false detections reaches a minimum while none of the DLF events is missed which are listed in the outputs of A6-DFMSD and in the local seismicity catalogues.

Table 5.3 STA/LTA parameters for detecting DLF events

Parameter	**Choice**
STA window length in s	2
LTA window length in s	15
Triggering STA/LTA threshold	2
Detriggering STA/LTA threshold	1.5
Time window for clustering events for an integrated detection list in s	7

5.4.3 Detection summary

Table 5.4 shows the results of A6-DFMSD in comparison with the merged three local seismicity catalogues (see above). We provide two sets of results for comparison. One is generated in a high sensitive mode and another one in a low sensitive mode for the detection of DLF events. In the high sensitive mode, we select a subset of the events in the detection lists that are detected by at least six stations out of a total of 14 stations. In the low sensitive mode, we select a subset of the events in the detection lists that are detected by at least seven stations out of 14 stations. For both modes, while searching DLF events within the detection lists of A6-DFMSD, we only select the event list corresponding to the target depth of 30-50 km (zone 2) and the events whose initial frequency classes are labelled between 1 and 3, covering the frequency range 1-9 Hz. To select tectonic events and possibly volcano-tectonic events, we take detections from both depth zones, 3-30 km and 30-50 km. Since volcano-tectonic type of events had never been reported in EEVF, we find it worthful searching this type of event in both ranges of depths in target region. To account for the higher frequencies of tectonic and possibly volcano-tectonic earthquakes compared to magmatic events (Hensch et al. 2019) we selected the detections with initial frequency classes between 4 and 11, covering the frequency range 4-30 Hz. In addition, we select that part of the detection lists in which the events are detected by at least five stations out of 14 stations. This selection, which is the result of some trial-and-error testing, controls the efficiency of the work regarding the ratio of false detections to the total number of detections. The outputs are analysed into two main categories: events inside and events outside of the target region.

As summarized in Table 5.4 and as far as the information of the public event catalogues allows, in general A6-DFMSD detects about 4 times more natural events which can be classified by their source type as DLF, tectonic and volcano-tectonic events. In section 3.4, we explain the characteristics of each type of the observed events in more detail. Comparing detection results of the high sensitive mode with the low sensitive mode shows a minor difference in quantity. Relative to the low sensitive mode we get 13% more events and 33% more false detections in the high sensitive mode.

With DLF event detection as a target, the low sensitive mode misses one DLF event which might be important for observatories. In Figs. 5.6a and b, seismicity maps of the target region are plotted before and after applying A6-DFMSD. Numbers of both, tectonic and DLF events, increase using A6-DFMSD. Especially, the increase of detected DLF events is important, since they are hard to find and their occurrence is a unique feature in Central Europe especially below the Moho at more than 29-30 km depth (Hensch et al. 2019). In addition, a new cluster of tectonic activity appears which has not been reported yet. This cluster of events is located around 50.3 °N, 7.3 °E (close to the village Polch) and it is highlighted by an orange circle in the map (Fig. 5.6b).

Table 5.4 Comparing the events in a merged list of three local seismicity catalogues with the detection results of A6-DFMSD. Here, A6-DFMSD is adjusted to detect all type of events.

	Event Type	**Merged 3-Catalogues**	**A6-DFMSD**	
			high sensitive mode	low sensitive mode
Inside the target region	DLF	3	13	12
	quarry blast	--	111	107
	tectonic	85	364	364
	volcano-tectonic	0	1	1
Outside the target region	quarry blast or tectonic	not comparable	1153	1046
Number of false detections		--	606	456
Total number of detections		--	2248	1986
Ratio of false detections to total number of detections		--	27%	23%

In Table 5.5, we compare the results of A6-DFMSD with the STA/LTA method. Here, we focus on the performance of the methods in detection of DLF events. For each method we provide two sets of outputs: the high sensitive and the low sensitive sets. For comparison of the methods, first, we investigate which output sets are generated in a higher efficiency and then compare the most efficient sets with each other. For the STA/LTA method, the first output set (A) is the high sensitive set and includes the events that are detected at least by five stations out of the eight chosen stations. The second output set (B) is the low sensitive set and includes the events that are detected by at least by six stations out of the eight chosen stations. For A6-DFMSD, the first output set (A′) is the high sensitive set and includes the events that are detected at least by six stations out of all the 14 available stations. The second output set (B′) is the low sensitive set and includes the events that are detected by at least seven stations out of all the 14 available stations. Similar to Table 5.4, we select the events from the A6- DFMSD detection list which are generated for the target depth of 30-50 km and events whose initial frequency classes are labelled between 1 and 3, covering the frequency range of 1-9 Hz.

Comparison of set A with set B: considering the goal of detection, which is on DLF events inside the seismic target zone, the major difference is in connection with the number of tectonic events (as unwanted type of detected event) and number of false detections. The results show that the high sensitive set (set A) includes 1.8 times more tectonic events along with 8.1 times more false detections relative to the low sensitive set (set B). This suggests that the low sensitive mode detects DLF events in a more efficient way using STA/LTA.

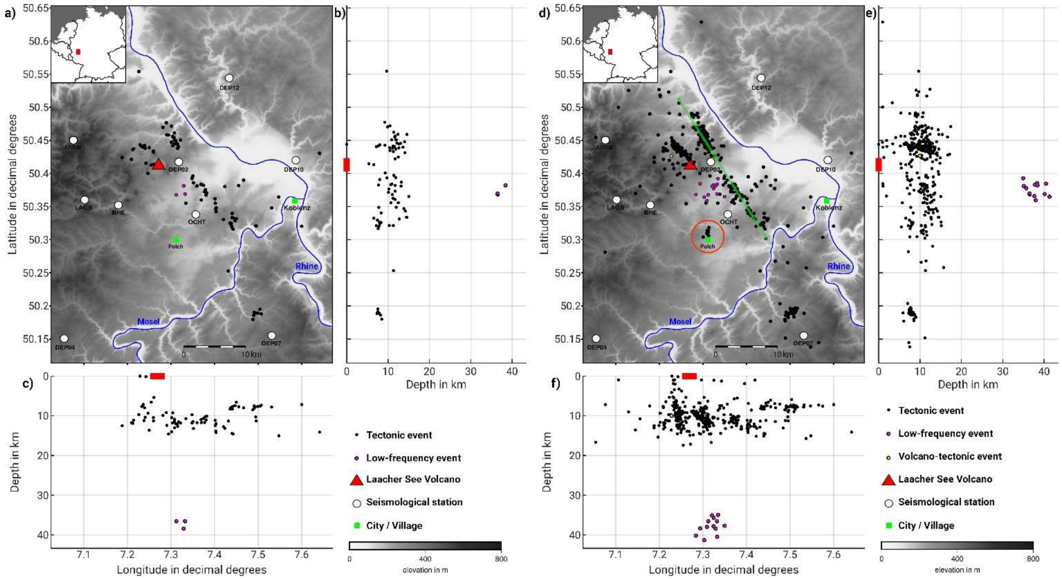

Fig. 5.6 Seismicity map of the East Eifel Volcanic Field (EEVF) for the period between 1 Oct. 2017 and 28 Feb. 2018. a), b) and c) hypocenters of 88 microearthquakes known before applying A6-DFMSD. These events are already listed at least by one of the local seismological services: state seismological service of Rhineland-Palatinate (2023), Bensberg Observatory, University of Cologne (2023) or by Hensch et al. (2019). d), e) and f) hypocenters of 378 microearthquakes detected after applying A6-DFMSD. The green line shows the trend of the active Ochtendung fault zone, and the orange circle indicates the location of a newly discovered seismic cluster near the village Polch. Note: ten new DLF events (in purple) were discovered in the uppermost mantle

Table 5.5 Comparing the detection results of STA/LTA with A6-DFMSD. Parameters of both methods are adjusted for detecting DLF events. Set A: detections by at least five out of eight chosen stations, set B: detections by at least six out of eight chosen stations, set A´: detections by at least six out of 14 available stations, set B´: detections by at least seven out of 14 available stations

	Event Type	**STA/LTA**		**A6-DFMSD**	
		set A	set B	set A´	set B´
Inside the target region	DLF	13	12	13	12
	quarry blast	101	84	98	94
	tectonic	81	46	3	3
	Volcano-tectonic	0	0	0	0
Outside the target region	quarry blast or tectonic	836	354	829	722
Number of false detections		840	103	227	80
Total number of detections		1871	599	1170	911
Ratio of false detections to total number of detections		45%	17%	19%	9%

Comparison of set A´ with set B´: with the same criterium used for comparison of set A with set B, the only major difference between sets A´ and B´ is concerning the number of false detections. The high sensitive set (set A´) includes 2.8 times more false detections relative to the low sensitive set (set B´). This suggests that the low sensitive mode detects DLF events in a more efficient way using A6-DFMSD.

Comparison of set B with set B´: in both sets the same number of DLF events are detected. Set B, generated by STA/LTA, contains 1.3 times more false detections than set B´ generated by A6-DFMSD. Although the goal of both methods is the detection of DLF events, in set B 46 tectonic events are found which is 15.3 times more than in set B´. This shows how the designed automatic classification by A6-DFMSD filters out irrelevant types of events, as far as the dominant frequency of the events is located in a specific band of the frequency spectra. The total number of quarry blasts inside the target region in set B (84) and set B´ (94) is in the same order for both methods but the number of quarry blast / tectonic events outside the target region is 2 times more in set B´ compared to set B. Since these types of events have similar characteristics with DLF events, partly in the time domain (waveforms) and mostly in the frequency domain, an increase in detection of them is reasonable and predictable. This may be interpreted as higher sensitivity for detection of DLF events by A6-DFMSD in comparison with STA/LTA. Comparing the ratio of false detections to the total number of detections indicates that A6-DFMSD with set B´ (9%) is 1.9 times more efficient than STA/LTA with set B (17%), with respect to detection of all meaningful type of events (even while both methods are tuned for the detection of DLF events of a certain seismic target zone). 52% of false detections in set B and 23% of false detections in set B´ are multiple detections of same event (false positives).

5.4.4 Event classification

In the framework of the test example and in accordance with the definitions by Malfante et al. (2018), Wassermann (2012) and Neuberg (2011), we manually classify the detected natural microseismic events of the seismic target region. Fig. 5.7 summarizes the typical events detected during the five months of analysis by providing records of the vertical components of the events plus their corresponding spectrograms. Below in the discussion section, we present more observations regarding a diverse set of signals detected by A6-DFMSD while applying it on the DEEP-TEE dataset within a longer time period than for the test example.

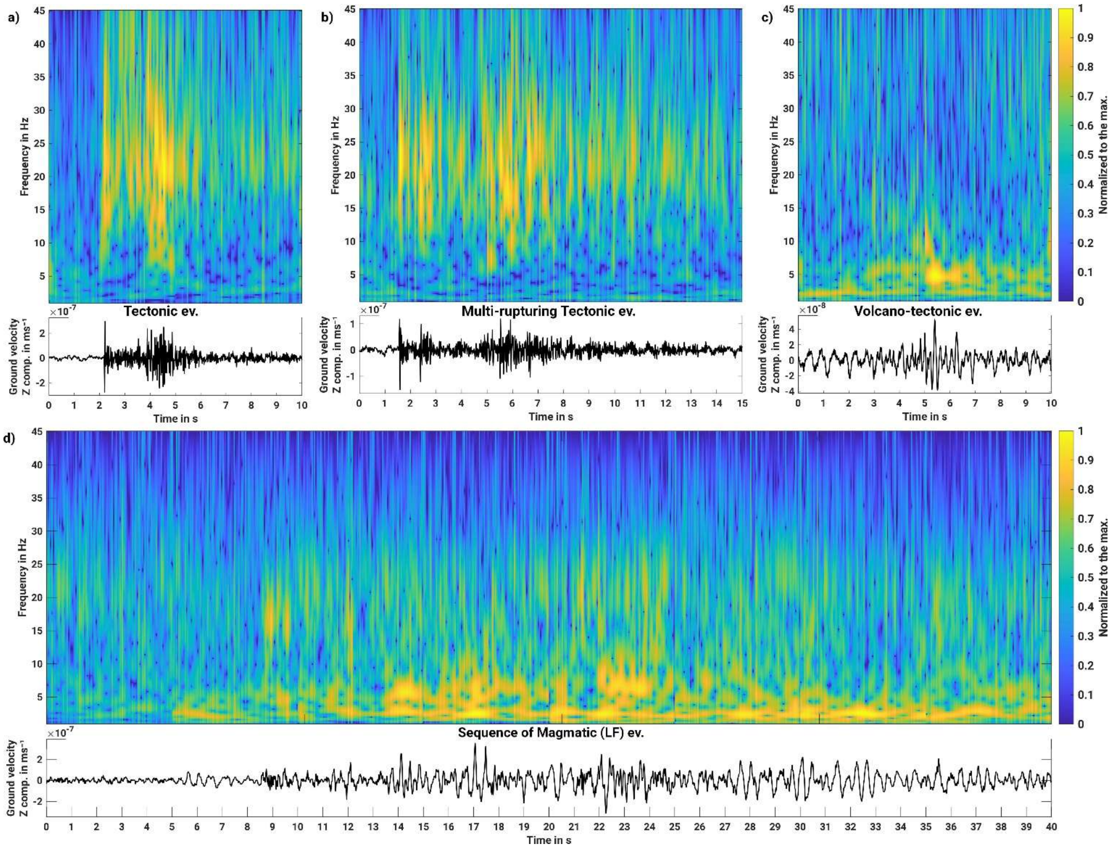

Fig. 5.7 Waveform examples (ground motion velocity, vertical component) and their corresponding spectrogram, a) tectonic event, record since 2018-01-31T22:48:27.00 UTC at DEP12, b) multi-rupturing tectonic event, record since 2018-01-06T23:09:21.50 UTC at DEP12, c) volcano-tectonic event, record since 2018-02-18T02:01:46.00 UTC at LAGB, and d) low-frequency (LF) event, record since 2017-10-16T22:02:34.00 UTC at DEP12. All events occurred inside the seismic target region between 1 Oct. 2017 and 28 Feb. 2018

Tectonic events: the frequency content in the ground motion velocity records of these signals is limited between 5 Hz and 40 Hz. The waveforms contain clear P- and S-phases highly affected by the double couple source mechanisms. As a general property, the duration of the signals and dominant frequency content in this event class are controlled by the magnitude of the event. A larger magnitude leads to a wider frequency content including lower frequencies and a longer duration of the signal. In some cases, we observed a longer signal duration of the tectonic events which is not only controlled by the magnitude but also by the source activity rate. In such cases, several tectonic-type events occurred within a short time window in such a way that phases of the first event are partly or completely covered by the phases of the second event and so on. The detected microseismic tectonic events, within the five months study period, had a minimum signal duration of less than 10 s at the surface considering the closest recording station to the epicentre ~5 km (Fig. 5.7a and b).

Volcano-tectonic events: the frequency content in the velocity records of this type of signals is limited between 4 Hz and 15 Hz. The waveforms contain clear P- and S-phases affected by a kind of radiation pattern (observations from different station-source back azimuths show different phase amplitudes and polarity). It is noticeable that, within the time period of the test example, only one event (Fig. 5.7c) could be found in this class. The observation of only a single volcano-tectonic (VT) event is in the contrast with the definition suggested by Wassermann (2012), where deep VT events are characterized by their frequent occurrence as swarms. The source of our VT event is located at a depth of 9.4 km with an epicentre close to the one of the CO_2 gas emission points (Gal et al. 2011) in the region. The minimum signal duration recorded on the surface is less than 10 s. This event was only detected by A6-DFMSD and was not listed in the three local seismological catalogues.

Low-Frequency events (LF): in general, LF events in the EEVF are quite diverse and their frequency content is mostly between 1 Hz and 10 Hz. However, the higher frequency part of the signals has much smaller amplitudes than the lower frequency part. For this reason, we assign the LF class to this type of signals rather than other existing defined classes (e.g., hybrid). Most of the LF events are characterized by emergent phase arrivals and a much longer coda compared to the tectonic earthquake recordings, that is possibly due to the source mechanism of oscillating fluids in a crack (e.g., Chouet 1988, Neuberg et al. 2000). Except for a few sequences with a high source activity rate and hence overlapping waveforms, S-waves are well identifiable for the remaining LF events. Sometimes unusually deep hypocentres are found down to more than 40 km depth, which is well below the brittle-ductile transition at ca. 15 km depth (see depth distribution of the tectonic events Fig. 5.6). Therefore, ts - tp differential arrival times are longer than for tectonic events and P-waves of LF events are often attenuated along the long ray path. Within the test example time period, we detected six sequences of DLF events including overall 13 events. In comparison only one of these sequences with three events had already been listed in the catalogues of the local observatories. In Fig. 5.7d, a waveform example of the typical DLF events detected within the time period of the test example is plotted. It shows the occurrence of a sequence with several sub-events.

5.4.5 Computational aspects

For the test example, the computational time for detection for each day (24 h of continuous recordings) takes ca. 75 minutes on a standard PC (using one core CPU - 3.3 GHz system) with on average 14 recording stations involved for each day. Each station has three-component records with a sample rate of 100 Hz, except for two stations BHE and TDN with a sample rate of 200

Hz. Detection is done simultaneously for searching events in two seismic target zones with different depth ranges. The signals were searched in eleven frequency classes. Since our A6-DFMSD code in MATLAB is not yet written in parallel form, there is a potential for speeding up the detector in future works. The most time-consuming part of detection is the SSD step, specifically where the signal anomalies are detected and labelled for each signal class. Beside rewriting the code in a parallel form, considering pre-allocation memories for the defined arrays and reducing the number of nested loops could further optimize the code.

5.5 Discussion

Detection of very weak earthquake signals ($ML < 1$) is a challenging issue in the presence of background seismic noise. A6-DFMSD routine provides a new way to detect signals emitted from a certain target region by analysing the records of the seismic stations located not only inside the target region, but also outside the target region where possibly the noise level is lower. A special feature is the high sensitivity for signal frequency that can be advantageous, if a specific frequency range characterises a type of seismic waves – a typical case in volcanic environments. As it was tested and explained in Table 5.5, the routine can filter out unwanted types of events (tectonic events, in test example) while preferring, e.g., magmatic DLF events (Tables 4 and 5). The main detection restriction in this configuration is the level of signal amplitude which is influenced by the source strength and seismic attenuation characterising the study region. In our study, we used A6-DFMSD with seismic records obtained up to 50 km away from the seismic target centre for events with magnitudes below $ML \sim 1$.

From station to station, the recorded waveforms of a single event vary. This issue becomes evident when near-by seismicity is monitored by a local network, because the source mechanism (radiation pattern) might play a more effective role in comparison with the medium properties and site conditions (site effects). A6-DFMSD is designed to cope with these circumstances by applying two techniques: one applied in the frequency domain and the other in the time domain. In the frequency domain, it calculates the variation coefficient of DFs of the signal, which is a stable criterion for the signals recorded at different stations and emitted from the same source. In this domain, the range of coherency acceptance for the variation coefficient of DFs is individually determined depending on the intensity of the variation coefficient of DFs of each event. In the time domain, it calculates sets of station-wise time limits while searching for coherencies across stations. These time limits are unique for each pair of recording stations and vary depending on the position of each pair of stations relative to the position of the defined target zone, thus searching for a wave front. These time limits are chosen wide enough to include the P- and S-phase pulses. This spread in time allows the detector to decide whether the detected pulses are also observed at neighbouring stations and whether the signals are connected to the same source in the seismic target zone or not. This is done by considering both P- and S-phases into the decision process. By this means, the detector can recognize that the detected pulses are connected to the same event, even if the emitted signal from a source located in the seismic target zone is affected by a strong radiation pattern for which, for example, at one station only the P-phase is detectable and at the other station only the S-phase.

The goal of A6-DFMSD is to not miss the events occurring inside a predefined target region, however, ~50% of our detections belong to distant sources (sources located outside the target region) when the detection of LF events is the goal. This happens because far-distant events have similar signal characteristics, partly in the time domain (waveforms) and mostly in the frequency domain compared with the signals of LF events. These far-distant signals arrive at the network almost simultaneously due to their steep incidence angles and contain lower frequencies as their higher frequency parts are lost due to attenuation.

As a result of the detection mechanism in A6-DFMSD, detection of relatively weak events is enhanced in the regions where the seismological network is denser. If the seismological network is close to cities or industrial regions, the denser part of the network has the main role in detection of incoherent events due to human activities (traffic, industry). To reduce number of the false or human-made (unwanted) events in the detection list we recommend to not use data of the stations with an interstation distance of less than ~2 km to avoid coherent noise signals. For regions, where a 1-D layered seismic velocity model is not yet determined, users can take a 1-D homogenous seismic or a simple 1-D layered seismic velocity model obtained from regions with a similar geology. The output of the detector provides an initial information about the dominant frequency of the detected events which is very useful when searching for a specific type of signal (for example DLF events as in the test example).

To use A6-DFMSD for other targets, beside adding the input information (see section 2.1) to the control file of the detector, only the following parameters might require some adjustments (for more details see the supplementary file). Similar to the role of the detection threshold in STA/LTA, in A6-DFMSD the parameter sigClasPower controls the sensitivity of the detection in respect with the signal to noise ratio. Higher values for sigClasPower lead to an elimination of weak signal anomalies. On the other hand, lower values than 2 add more incoherent detections. A coherency search in space is limited to a certain number of orbit stations, however, the latter may be adjusted. Therefore, if coherent signal anomalies are found with a minimum number of X stations out of Y orbit stations, this leads to a detection. By increasing the number of Y, while keeping a fixed value for X, a larger radius in space (wider area) is used for finding coherent signal anomalies. This change increases a chance of detecting events which are coherent in their signal properties. By increasing the number of X, while keeping a fixed value for Y, the coherency search performs with a more restricted condition and this leads to the elimination of weaker events. This happens, e.g., due to the wave propagation attenuation which can damp weak signals at larger distances. Indeed, one should always consider that the detection of signals from weak events is limited to a certain hypocentral distance (Li et al. 2020) which might be less than the dynamic search radius defined by the selection of the value Y and the actual station distribution. The values for X and Y are set in the control file as parameters “minLocSearCohStNum” and “maxLocSearStNum”, respectively. We recommend to select the values for these two parameters with a ratio of minLocSearCohStNum to maxLocSearStNum between 0.6 and 0.7. Search vicinities around the variation coefficient of DF signal anomalies are determined by empirical equations (6) and (7). These equations were obtained by testing different sets of values and relationships (see also supplementary material with examples, section 1.5.2 Figs. B5 and B6). Further tries with more datasets may provide an improved performance of the detection. The rest of the parameters introduced in this method are fixed parameters and independent of the target. Changing their values might require an updated regularization step which can lead to changes in the choice of the other adjustable parameters.

The variation coefficient of DFs is a dimensionless value. If the amplitude of the seismic records is multiplied by a value, it does not change the value of the variation coefficient of DFs. Therefore, even records measured at stations located on very different site conditions (where the recorded amplitudes are amplified by some factors due to the site effect) still can be used as input for the detector. We assign this as a stabilising property which becomes important while searching for the correlation between signal anomalies at different stations.

One of the interesting aspects of the detector is the detection of a sequence of events in which the coda of the first event is partly or mostly covered by the phases of the second event and so on. Figs. 5.7 (b and d), Figs. 5.8 (e and j) and Figs. 5.9 (a and b) present waveform examples of these type of events with both magmatic and tectonic origins. The recorded waveforms of such sequences are affected by the source activity rate. Such kind of events are typically missed using methods like waveform matching. A6-DFMSD can successfully detect such swarm-like events (or multi-rupture sources). This demonstrates the capability of the method, e.g., for the detection of the tremor-like magmatic signals. Like for the STA/LTA method, such a kind of sequences is also listed as one event but with a difference: A6-DFMSD provides a value in the detection list that gives the time duration between the detection of the first detected phase of the first event in the sequence and the last detected phase of the last event in the sequence, in a network-wide scale. Single events in the detection list have a relatively short time duration (in our test example with an average time duration value of ~11 s) whereas sequences of events (including also events outside of the target region, e.g. regional or teleseismic events) have a longer time duration. Hence, one can use this average time duration as a criterium and split the events of the detection list into two groups: the one which mostly contains of single events and the other one which contains sequences of events or events outside the target region. Of course, the average time duration of single events is a function of the network geometry (network diameter), size of the target region (diameter and depth of the target region) and the relative position of the centre of the target region and the centre of the network stations.

In the detection summary (Table 4), we presented a part of the detection output which is generated based on coherent findings at five or more stations in the EEVF. There, we did not take into account the remaining events detected by less than five stations, because the ratio of false detections to the total number of detections increases too much. One suggestion to prevent an increase in false detections is reducing the radius of the target region. Thus, defining a large target region increases the ratio of false detections to the total number of detections. In this study we considered a radius of 25 km for the target region. As result of applying a smaller radius (for example 10 km), the time-window search for finding coherencies is shortened. Consequently, the search with a shorter time-window reduces the chance of the occurrence of false coherent coincidences due to noise signals.

A6-DFMSD can detect a wide range of different signal types. Figs. 5.8 and 9 present the capability of detecting diverse waveforms. These two figures summarize some typical waveform examples of different event types which were detected by A6-DFMSD in the EEVF, not only within the five-month period of the test example, but also since starting the DEEP-TEE project in July 2014.

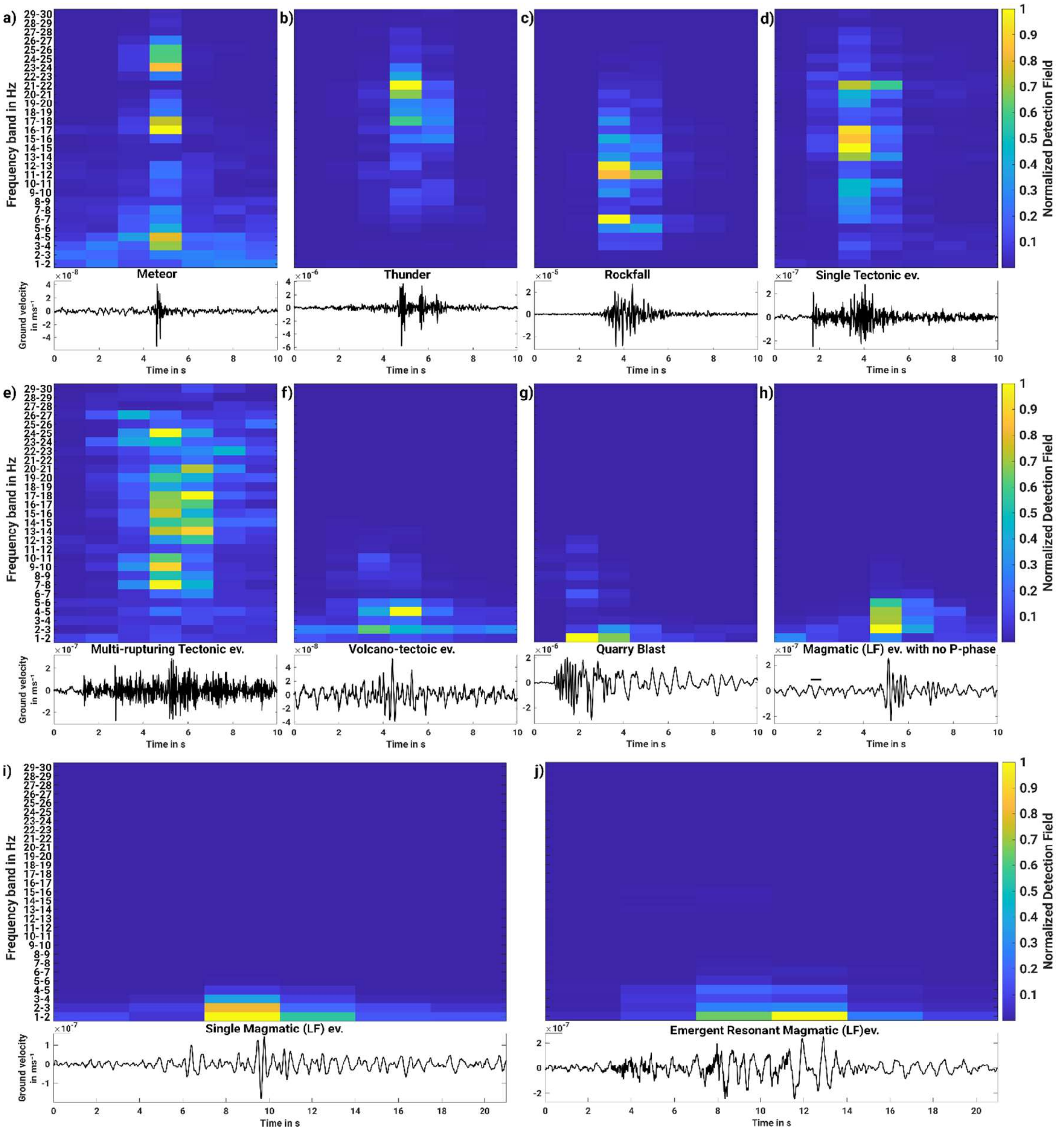

Fig. 5.8 Waveform examples (ground motion velocity, vertical component) along with their corresponding detection fields (windowed energy-proportional narrow bands, similar to Fig. 5.5f, but as spectrogram) for different event types detected by A6-DFMSD in the EEVF. Records in the subplots are in UTC since: a) 2016-08-08T00:06:54.50 at DEP12, b) 2015-08-10T19:55:19.00 at DEP02, c) 2020-10-20T02:20:06.50 at OF09, d) 2018-01-31T22:48:27.50 at DEP12, e) 2020-07-03T05:48:03.00 at GLOK, f) 2018-02-18T02:01:46.00 at LAGB, g) 2020-10-05T09:18:24.00 at OCHT, h) 2017-06-06T19:22:06.00 at LAGB, i) 2017-06-04T20:36:32.00 at LAGB, and j) 2018-04-28T02:44:58.00 at DEP12

In Fig. 5.8, atmospheric signals are presented under the labels “Thunder” and “Meteor”. We identified several hundreds of thunders and even some bursts of meteors around our seismological station network (Eickhoff et al. 2024). The location of these type of signals, up to tens of kilometers high in the atmosphere, is verified by source location using a sound velocity model of the atmosphere (Kirtskhalia 2012).

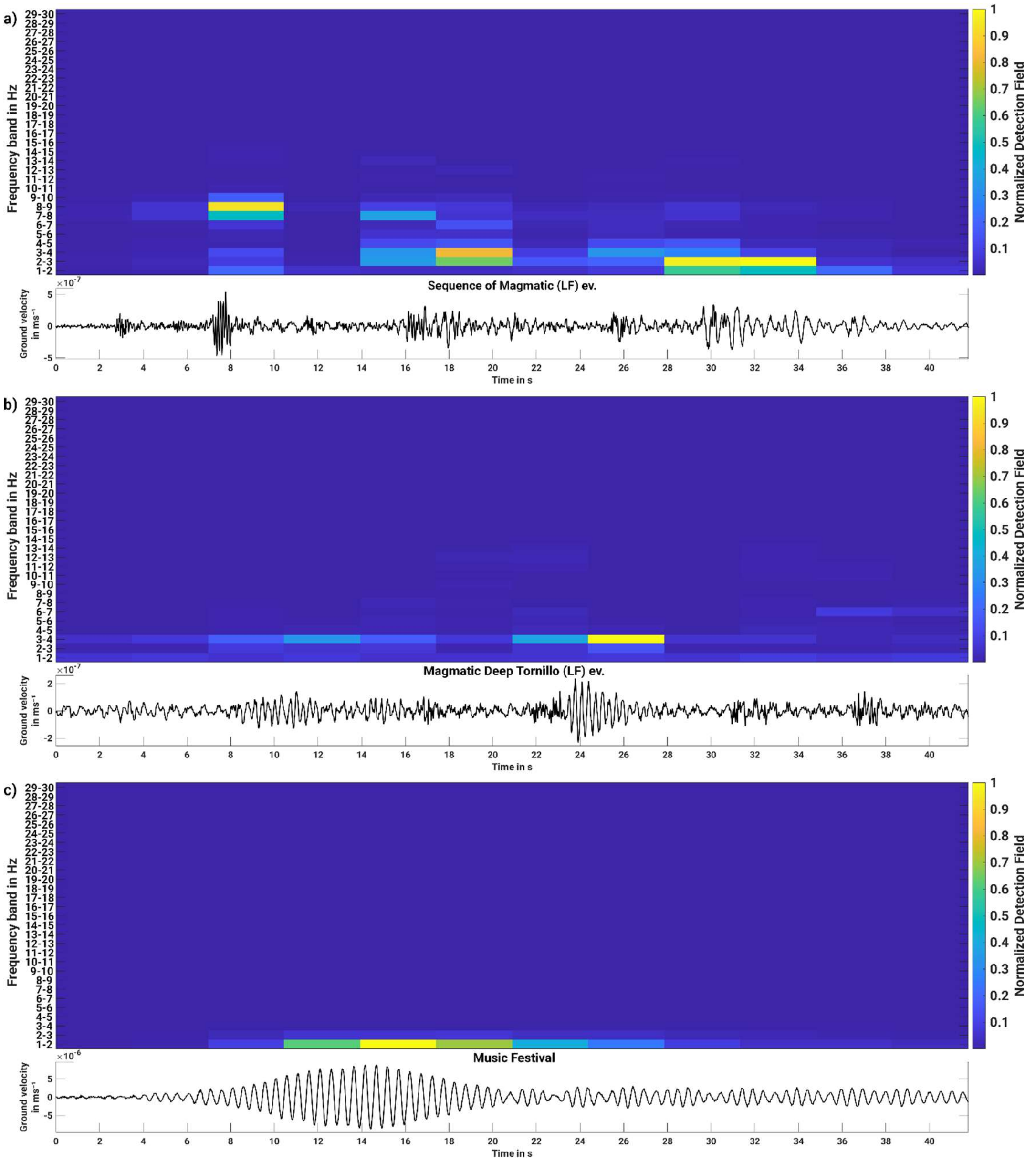
a) Sequence of Magmatic (LF) ev.

b) Magmatic Deep Tornillo (LF) ev.

c) Music Festival

Fig. 5.9 Waveform examples (ground motion velocity, vertical component) along with their corresponding detection fields (windowed energy-proportional narrow bands, similar to Fig. 5.5f, but as spectrogram) for different event types detected by A6-DFMSD in the EEVF. Note: the signal from the music festival is similar to magmatic tornillo-shaped LF events (see e.g., Wassermann, 2012). Records in the subplots are in UTC since: a) 2019-08-07T21:13:44.20 at GLOK, b) 2019-04-08T20:08:05.00 at DEP08 and c) 2015-06-05T21:10:45.00 at DEP09

Quarry blast signals are the most common and often strongest anthropogenic signals. In Fig. 5.8, one example is presented under the label “Quarry blast”. In our study, detection of quarry blast signals is limited to day-time (7:15 – 15:15 UTC). Since the frequency content of the quarry blasts totally overlaps with the frequency content of the LF events, they are the most frequent detections during day-time (see explanation of the Table 4 and Table 5 for more details). This type of the events is also labelled by the frequency classes 1 to 3 in the detection lists, similar to the label setting of the LF evens. For this reason, the current version of A6-DFMSD is not completely able to distinguish the LF events from quarry blasts. We note that up to a radius of 100 km from the centre of the target region in the EEVF, we could identify the locations of 424 open mines using Google Maps. This demonstrates the challenging conditions regarding the detection of LF events in our target region where anthropogenic noise is very high. Another anthropogenic signal that is interesting from the detection point of view are some sets of long-lasting signals emitted from a music festival hold in May 2015 in the EEVF, called *Rock am Ring* (Fig. 5.9 the signal labelled by “Music festival”). These signals are prominent in the frequency band 1-5 Hz, with a high peak at 2 Hz. Both, the waveform and the frequency content are similar to volcanic tremor (e.g., Wassermann 2012), however the shallow hypocentre, the location and the origin time are coincident with the *Rock am Ring* festival and, therefore, excluding a magmatic origin. The signal labelled by “Rockfall” in Fig. 5.8 is detected during midnight (local time) with a shallow (~0.1 km depth) source position, matching with the location of a big open mine in the region. The waveform characteristics of this event do not match with the waveforms of the other type of observed events in the region. Since blasting in the mines is limited to day time, falling rocks at midnight inside the open mine is the most reasonable scenario explaining the detected observed signal.

The most ordinary type of the LF signals observed in EEVF is shown in Fig. 5.8 with the label “Single Magmatic ev.”. Relative to the other waveforms of the observed LF signals in EEVF, this type of signals has a shorter duration. Their occurrence is not limited in a certain depth location. Depending on the relative source-station position, noise level and magnitude of the event, the P-phase might not be seen in the records. One example of this kind of observed signal is labelled by “Magmatic ev. with no P phase” in Fig. 5.8. There, the expected P-phase arrival time is marked by a “-“ after localization of the event with the useable picked phases taken at the DEEP-TEE network stations. Among the detected signals of the LF events in the EEVF, there are some signals that provide evidence for the occurrence of resonance (in Fig. 5.8, “Emergent Resonant Magmatic ev.”). This type of signals starts with a small amplitude, comparable with the background noise, and then the lower frequency part of the signal is gradually increasing over time at all the network stations. This type of event occurs in a shallow position (~10 km depth). In Fig. 5.9 two of the most interesting types of the long-lasting magmatic signals are presented, too. The source of both events is located deeply below the Moho at ~39 km and ~33 km depth, respectively. The first one is a sequence of events in which the frequency content of the events decreases in time (Fig. 5.9a). This characteristic of the sequence is well illustrated in the detection fields plotted below the signal. The observation of such kind of signals was already reported by Aki et al. (1977) from Kilauea volcano, Hawaii. Aki and Koyanagi (1981) modelled the mechanical mechanism as magmatic intrusions, explaining the characteristics of the signal. The second example in Fig. 5.9b is a pulse-like signal very similar to long-lasting magmatic LF events which sometimes are called tornillos. The related detection fields of this event illustrate the partly mono-chromatic frequency behaviour. This example shows, even if these signals are characterised by a lower amplitude than other higher frequency signals, the frequency domain part of A6-DFMSD will facilitate their detection.

5.6 Conclusion and outlook

We introduce a new seismic event detector (A6-DFMSD) which is able to detect local (micro-) seismic events occurring inside an arbitrary target zone in the presence of a moderate to high local seismic noise level. It is sensitive to the energy increase in the continuous ground motion in the frequency and time domains and it does not require a priori knowledge of the waveform characteristics of the searched events. Station coordinates, location and cylindric geometry of a seismic target zone and an approximate simple 1-D (homogeneous or layered) seismic velocity model of the region are the only input that is required to apply A6-DFMSD on a seismic dataset.

To evaluate the method, we selected 5 months of continuous seismic records in the East Eifel Volcanic Field (EEVF), Germany, which is a challenging test example, because a) different types of seismic sources (with magmatic and tectonic origins) have already been identified (Hensch et al. 2019) and b) there is a high cultural noise level in the records. All the detected events were manually checked by visual inspection of the waveforms, localized and classified. Results were then compared with a merged list of three local seismicity catalogues (Table 4) and also with the results of STA/LTA tuned for detection of DLF events (Table 5). In comparison with the merged list of three local seismicity catalogues and regarding the detection of all type of natural source events (e.g., DLF, tectonic and volcano-tectonic), A6-DFMSD detected 4.3 times more events without missing any tectonic or DLF event.

In comparison with the results of STA/LTA tuned for detection of DLF events, A6-DFMSD and STA/LTA, both, detected the same number of DLF events. However, the STA/LTA results included 3.7 and 1.3 times more false detections in comparison with A6-DFMSD where the high sensitive event lists (set A and set A´) and the low sensitive event lists (set B and set B´) are taken into consideration, respectively (Table 5). It is noteworthy that STA/LTA results included 27 and 15.3 times more tectonic type events than A6-DFMSD (comparing set A with set A´, and set B with set B´, respectively), although for both methods the detection of DLF events was the goal. This comparison shows that besides the task of detection, A6-DFMSD can successfully separate events concerning their frequency content. In this regard, the separation of quarry blasts from LF events still remains as an unsolved issue, due to the fact that quarry blasts and LF events are characterised by very similar features in frequency domain.

Based on the detection mechanisms implemented in A6-DFMSD, the following cases are the most recommended targets for applying the method:

a) regions which are newly covered by a local seismological network (or, when the local seismological network is still under development), especially, if no local waveforms are known,

b) detection of new types of seismic sources with unknown waveforms,

c) if waveform matching detection methods are planned but reference waveforms are not yet identified.

In the latter case (c), A6-DFMSD is recommended as a pre-detection step. In this case, A6-DFMSD provides a diverse set of waveforms as inputs for waveform matching detection methods and prevents these methods from missing events in their blind spots.
All coding is currently done in one MATLAB program. However, users are free to connect optional routines. For example, users may integrate the TauP Toolkit for the travel time calculation as well. Similarly, a preferred location routine can be added to the detection part.

6 An active translithospheric magmatic channel in Central Europe

In this chapter (and appendix C), a high-resolution 3-D image of the seismically active magmatic sources in the East Eifel Volcanic Field (EEVF) is presented. Here, I present the following subjects: a summary in number of detected events and the strategies which I applied to eliminate the outliers after event localization steps, the most repeating values as the final hypocentral parameters of the events obtained through a jackknifing cross-validation test, the event migration in time and depth and the frequency index of the three types of events: LF, tectonic and quarry blasts for comparison. In addition, an estimation to the amount of the moved magma volume within the time period July 2014 – December 2022 beneath the EEVF is presented based on the modified model of Aki et al. (1977) and Aki and Koyanagi (1981). This chapter is prepared for submission Nature Geoscience together with co-authors.

6.1 Abstract

Conceptual models of intraplate volcanism contain a melt source in the asthenosphere which injects primitive magma into the lower lithosphere from where shallower crustal magma reservoirs are fed. Some melts may reach the surface within a few days, others may reside in the reservoirs, differentiate chemically and erupt as evolved magma. The pathways of these melts are poorly known as well as the physical processes how melt penetrates through a thick lithospheric plate. Here we present the image of a translithospheric magmatic channel below the Eifel in Central Europe based on seismological observations of signals from as deep as 45 km at the transition to the asthenosphere. These pulses are emitted from a 5 - 8 km wide zone and interpreted as magmatic injections due to overpressure. The channel is located close to Laacher See Volcano, where a paroxysmal eruption occurred 13.000 years ago. Presently there seems to be a slow refilling of crustal magma reservoirs at a rate of about 3,500 m^3 per year. The dense population and infrastructure in the region result in a relatively high volcanic risk, although the hazard is only moderate due to the long residence times of the melts inside the crust.

6.2 Imaging magma transfer through the continental lithosphere

Compared to interplate volcanism at plate boundaries and intraplate volcanism on relatively thin oceanic lithosphere, continental intraplate volcanism is by far less abundant on Earth (Global Volcanism Program, 2024). This is due to the less vigorous mantle dynamics generating melt sources below continents and the low melt generation at high ambient pressure below the 60 – 200 km thick continental lithosphere (McKenzie and Bickle, 1988) which can also act as blockage against rising melts from the asthenosphere. Ball et al. (2021) find a correlation of continental volcanism with thin (<100 km) continental lithosphere and low shear wave velocity in the upper mantle. Different models for subcontinental magma generation (Conrad et al., 2011) and magma ascent (Ribe, 1987; Schmeling et al., 2019) have been proposed (Fig. 6.1b), however these processes have rarely been observed. E.g., analyses of earthquake swarms allowed to image the rise of magmatic fluids through the crust below Mammoth Mountain (Hotovec-Ellis et al., 2018) or Lake Tahoe (Smith et al., 2004) in the US. Delineating the continuous subvertical rise of melt and magmatic fluids in the lower lithosphere and asthenosphere was yet only possible at plate boundaries by detecting resistivity anomalies (McGary et al., 2014) and seismic perturbations (Haberland & Rietbrock, 2001; White et al., 2019) or underneath intraoceanic locations such as Hawaii (Aki & Koyanagi, 1981) or Mayotte (Foix et al., 2021).

In the intracontinental setting of the Eifel region, Germany (Fig. 6.1a), an upper mantle plume thinned the lower lithosphere and the lithosphere-asthenosphere boundary (LAB) is found at *c.* 45-50 km depth (Mathar et al., 2007; Seiberlich et al., 2013). There decompressional melting in the asthenosphere, partly enhanced by fluids from earlier metasomatic phases (Stosch & Lugmair, 1986, Rummel et al., 2018), produces basanitic and foiditic melts which formed two volcanic fields (Schmincke, 2007). Reports on two deep (40 - 43 km) seismic events near the Laacher See Volcano (LSV) in the East Eifel Volcanic Field (EEVF) (Stange et al., 2014) initiated the installation of a dense seismic recording network (Ritter et al., 2024) and about 80 deep low-frequency (LF) events were described in four clusters at 8-43 km depth (Hensch et al., 2019).

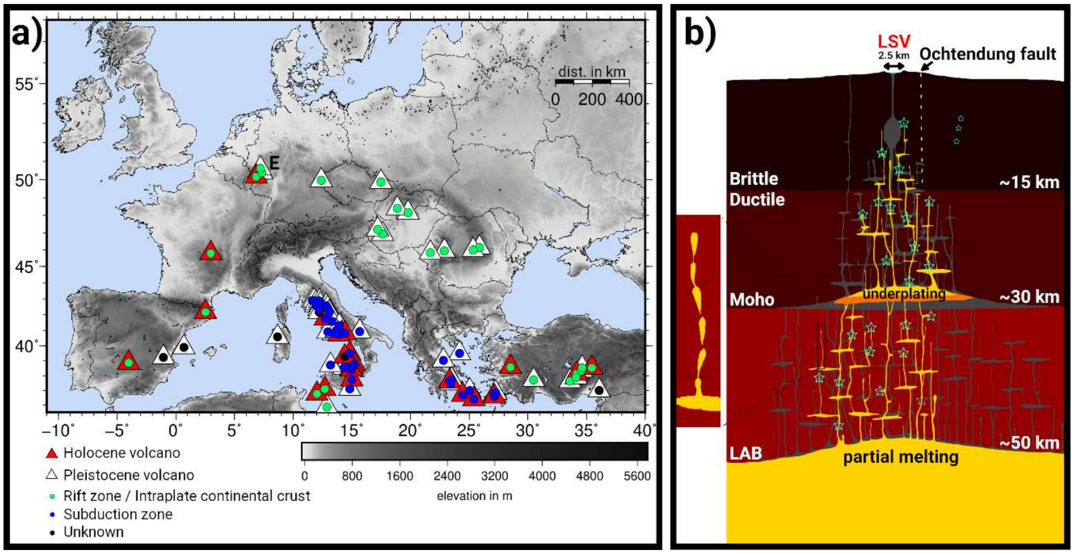

Fig. 6.1 | Quaternary volcanism in Europe and scheme for rising magma. a, the intra-plate volcanism in the Eifel (E) is the northernmost in Europe where most volcanoes are in the south within subduction zone settings, source (GVP, 2024). **b,** schematic illustration of magma rise from the upper mantle across the lithosphere-asthenosphere boundary (LAB) to the surface at an intracontinental setting such as the EEVF. A complex network is formed from cooled and hot sills and dikes. In the brittle upper crust, tectonic events can occur along discrete shear planes such as the Ochtendung Fault, left: buoyant rise of fluids under overpressure causes micro-earthquakes which crack the lithosphere for melt movement (after Aki & Koyanagi, 1981).

6.3 Observation and identification of magmatic events

The recorded seismic signals in the EEVF are mainly excited from three sources: quarry blasts, tectonic rupture and magmatic pulses. Their different frequency content can be used for discrimination (Figure 2a): the tectonic low-magnitude ($ML < 2$) events have typical frequencies of 10 - 30 Hz, the quarry blast recordings are dominant at 1 - 5 Hz due to their surface wave part and the LF magmatic events ($ML < 2$) occur at mostly at 2 - 8 Hz. The frequency index (Buurman & West, 2010) can be used to highlight these differences (Figure 2b) and assist the event identification. The detection of the LF events is done using frequency characteristics (see methods and Koushesh & Ritter, 2024), but many detections also include quarry blasts due to the overlapping frequency content. The latter are excluded by hand based on waveform appearance or hypocentral depth which is close to zero for quarry blasts. Due to the numerous quarry blasts and the high anthropogenic seismic noise during daytime, which covers the low-amplitude LF signals, we limit our search between 3:15 pm and 7:15 am (UTC) during night time.

The detection finds 462 DLF events between July 2014 and Dec 2022 of which 435 were identified as LF events and 332 of these could be located (Supplementary Information) due to the following criteria: the waveform, especially the long coda, is similar to known LF signals (Hensch et al., 2019) and the depth of the events is more than 4 km. Preliminary hypocentral parameters are calculated using VELEST (Kissling et al., 1995) with a local seismic velocity model and station correction terms (Ritter et al., 2024).

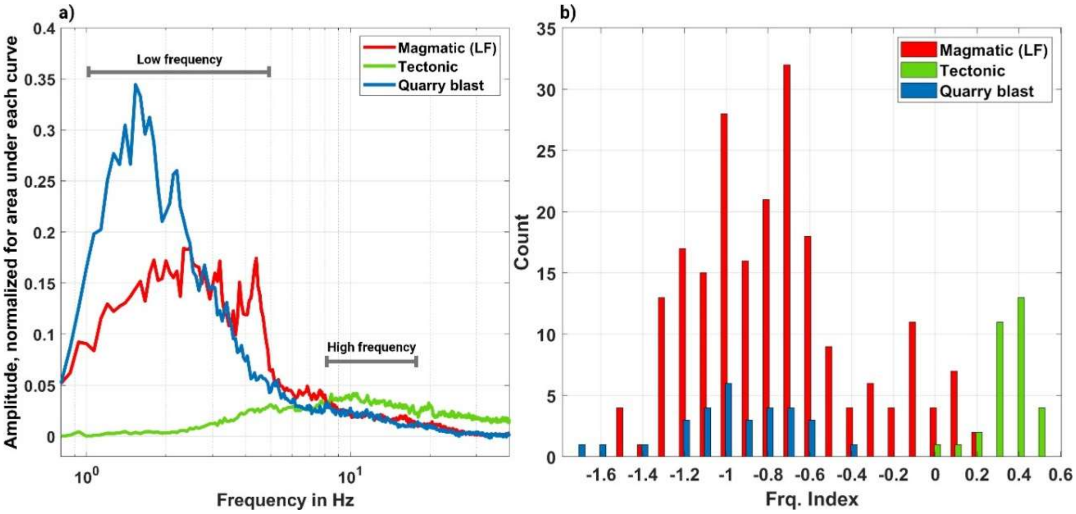

Fig. 6.2 | Frequency spectra and frequency index of seismic signals. **a**, average spectra for 30 tectonic, 30 quarry blast and 200 LF events. **b**, Frequency index values are well below 0 for magmatic LF events and selected quarry blasts. For tectonic earthquakes the positive values indicate a systematically higher frequency content.

6.4 3-D image of a translithospheric channel

To outline the structure and size of the 3-D source volume of the LF events, we relocate these together with the 203 strongest tectonic events of the region (0.8 < *ML* < 2.8, LGB, 2024) to determine relative hypocenters (Waldhauser & Ellsworth, 2000, see methods) (Figure 3). The tectonic events are added as cross-check, because a sharp line of epicenters is expected and indeed recovered for the well-known NW-SE striking Ochtendung Fault Zone (Ahorner, 1984; Ritter et al., 2024). Relative uncertainties of the hypocentre locations are on the order of 166 m –189 m and 171 m respectively for lat. lon. and depth (taking the median values for the errors), see Supplementary Information A. The LF events occur inside two main structures: a shallow (5 - 10 km depth) small cluster with 35 events ca. 8 – 10 km NW of Koblenz in the Neuwied Basin and a main group which stretches along 7 - 45 km depth SE of the Laacher See Caldera. Compared to (Hensch et al., 2019) the main group is more continuous in depth and near-vertical. Depth intervals with low LF activity at 15 – 20 km and 30 – 32 km could be due to the limited observation time and filled in the future. The lateral extension of the magmatic LF events delineates a 5 km (SW-NE) by 8 km (NW-SE) wide zone and their 3-D appearance looks like a vertical channel.

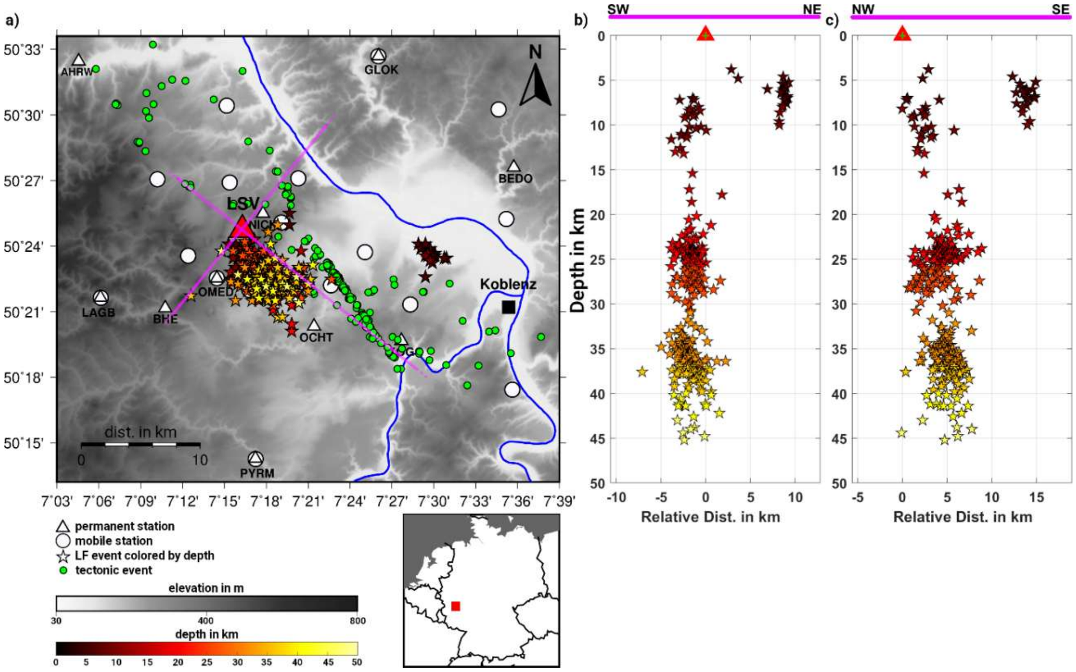

Fig. 6.3 | Locations of seismic events in the East Eifel Volcanic Field. **a**, epicentres of LF events (stars) and tectonic earthquakes (green dots). The Laacher See Volcano (LSV) is indicated as red triangle. **b**, southwest-northeast cross section with hypocenter distribution of low frequency events. **c** northwest-southeast cross section. These relative locations highlight the spatial clustering of the events. The centre of the coordinate system is the centre of the LSV. The map shows the location within Germany.

6.5 Discussion

The c. 45 km deep bottom of the channel coincides with the upper limit for models of the LAB (Mathar et al., 2007; Seiberlich et al., 2013), therefore, for the first time a magmatic channel through the entire continental lithosphere is recovered.

The LF signals can be explained with a pulse-like opening of cracks with a subsequent flow of a fluid into the opening as proposed by (Aki et al., 1977 and Aki & Koyangi, 1981), see Additional Information B. In the West Eifel Volcanic Field such a mechanism of a flow of magma batches due to overpressure is known from veins in xenoliths (Witt-Eickschen et al., 2003; Shaw et al., 2005). Using the relationships given in (Aki et al., 1977 and Aki & Koyangi, 1981), the volume of involved fluid can be calculated to get a rough quantitative estimate of the ongoing magmatic processes. E.g. assuming melt and a LF event with $ML = 1.6$ at 10.4 km depth, the recorded amplitudes can be excited by a volume of c. 350 m^3. To estimate the moved volume during our analysis period 2014 – 2022 we calculate a cumulative volume of about 29,400 m^3 what is equivalent to a cube with 31 m side length (Fig. 6.4). We note that this estimate has a significant uncertainty (see Additional Information B), however, it provides an order of magnitude for the ongoing magmatic processes.

The related average yearly flow of 3,500 m^3/yr is less than the estimate of (Thomlinson et al., 2020) who propose a flow rate of 20,000 – 100,000 m^3/yr for a period of 20 kyr before the eruption of LSV at 13 ka. Our estimate of 3,500 m^3/yr has two implications: (1) if this volume would be completely added to the area of the channel width (5 km by 8 km), then a vertical displacement rate of just 0.1 mm/yr could be expected. The cumulative displacement over 10 yr could be resolved using long-term measurements, (2) the residence time of melts in the crustal reservoir before the eruption of LSV 13 kyr ago was on the order of 24-50 kyr (Rout and Wörner, 2020; Schmidt et al., 2024); assuming a melt refill of 3,500 m^3/yr since the last eruption would result in 0.045 km^3 accumulated melt what is about one hundredth of the melt-equivalent material which erupted during the 13 ka paroxysm. Low melt flow rates could also result in cooling and solidifying of a large portion of the magma in the lithosphere without further involvement in volcanic surface processes. Hence, a similar eruption as the LSV paroxysm seems to be unlikely at present. However, taking into account the dense population in the area, the volcanic risk even for a small-scale eruption should not be underrated (Mani et al., 2021) and needs further research activities to test our results.

Methods

Detection

Signals from seismic events can automatically be identified by STA/LTA detectors (short-term average divided by long-term average signal level), cross-correlation, and artificial intelligence (Allen 1978, Trnkoczy 2009) (Ross et al. 2019) (Perol et al. 2018) (Yoon et al. 2015). The DLF events in the EEVF are characterized by low local magnitudes ($ML < 2$), large depth ranges, a high background noise and hence a very low signal-to-ratio (SNR often less than 2-3) (Ritter et al., 2024). This hampers STA/LTA and the waveform cross correlation for detection. Thus, a

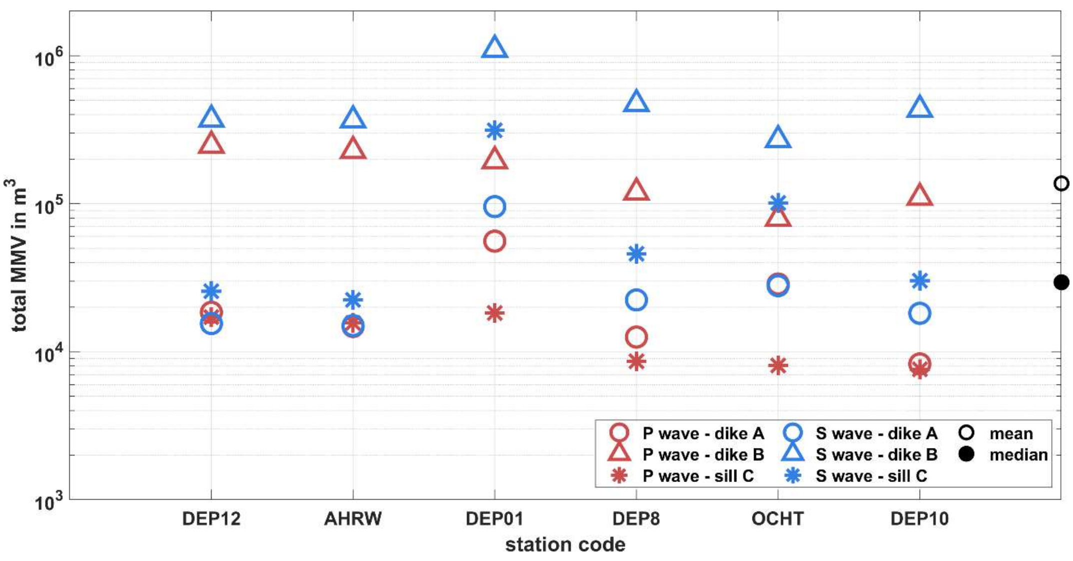

Fig. 6.4 | Estimation of the moved magma volume during 2014-2022 inside the translithospheric channel below the East Eifel Volcanic Field. Several scenarios with different dike and sill geometries (coded as symbola) are accounted for together with P- and S-wave amplitude measurements from six seismic stations (colour). The mean value of 2.94 10^4 m^3 has an uncertainty range of 10^4 to 3 10^5 m^3.

multi-step detection (Koushesh and Ritter, 2024) was applied to enhance the tiny signals by computing the energy of the ground motion (Fig. C.3.1 in Supplementary Information C) and filtering in narrow frequency bands to take care of the frequency characteristics (Fig. 6.2). Afterwards a STA/LTA is applied and signal detections are compared across neighbouring recording stations to avoid local noise peaks. The time window for this correlation is limited to seismic arrivals which originate in a predefined volume at depth which is taken from Hensch et al. (2019) and correspond to the lithospheric column underneath the EEVF. Due to the signal similarity between DLF events and quarry blasts, hundreds of the latter are determined. These occur during day time (see additional information) when there is also an increased anthropogenic noise level which masks DLF events. Therefore, we restricted the search for DLF events to 15:15 to 07:15 UTC time.

Arrival time picking

The picking of the P- and S-phase arrival times is quite difficult because of a low SNR and mostly emergent waveforms. Thus, picking is done by hand with the help of visual correlation between recordings at neighbouring recording stations, record sections and component products (Plesinger et al., 1996). According to the visibility and signal-to-noise ratio of the phases, the events are classified manually into quality classes A, B and, C. These are described in details in Supplementary Information A.

Hypocenter determination

For an accurate hypocenter determination, local 1-D P-wave and S-wave velocity models (KIT6, Ritter et al., 2024) were derived using VELEST (Kissling, 1995). To account for unresolved local site effects such as 3-D seismic velocity heterogeneities and anisotropy, P- and S-wave station correction terms were determined and applied. The correction terms are small close to the center of the network (<0.2 s and <0.3 s for P- and S-waves, respectively) and increase for recording sites at the edges of the station network (<0.7 s and <1 s for P- and S-waves, respectively). The absolute hypocenter locations have uncertainties of *c*. 2 km vertically and 0.5 km horizontally (Ritter et al., 2024).

Relative hypocenter determination

To improve the spatial resolution between the hypocenters, the relative relocation algorithm HypoDD (Waldhauser & Ellsworth, 2000) is applied. As input the absolute location parameters of the events, their weighted arrival times, and the 1-D P- and S-wave velocity models KIT6 (Ritter et al., 2024) are used. In HypoDD the singular value decomposition (SVD) is selected to solve the inversion problem and to obtain the relocation error values together with relocated hypocenter parameters. Spatial linking of events is limited to a maximum distance of 8 km (parameter WDCT), the residual threshold in time (parameter WRCT) is set to 0.4 s through 15 iteration steps (parameter NITER). We randomly resample the input data with the jackknife method (Tichelaar and Ruff 1989) to generate 100 input data subsets. For each subset, we randomly select 80% of the events in class A, 60% of the events in class B, and 40% of the events in class C resulting in a total number of 181 events in each subset for the jackknife selections. Fig. C.1.1b indicates how many times each event is involved into this random selection. Afterwards HypoDD is applied in SVD solution mode to each subset with the following set of parameter values: WDCT = 10, WRCT = 0.4 and NITER = 15. Fig. C.1.1c shows the relocation status for each event after passing this procedure. Out of 332 involved events, 43 one do not find enough links with neighbouring earthquakes and these are removed. The jackknife results are used to estimate the uncertainty of the relative locations what is shown in Fig. C.1.4.

Melt volume estimation

We use a mechanical model based on a ‘chain of cracks connected by narrow channels’ (Fig. C.2.1) as originally suggested and formulated by Aki et al. (1977) and Aki and Koyanagi (1981). Hereby the measured seismic amplitudes are used to estimate the fluid or melt volume. The assumption is that a fluid with overpressure inside a crack causes a tensile failure which allows a fluid flow. During this rock failure, tremor-like seismic waves are excited. We apply this formalism with input parameters adjusted to the Eifel case and their variations are used to determine uncertainty ranges.

7 Summary and outlook

The Quaternary East Eifel Volcanic Field (EEVF) is seismically active. Unlike the tectonic type activities which mostly occur at pre-existing faults and fractures, volcanoes can be born by opening a new magma pathway up from the deeper crust or upper mantle to the surface (Caricchi, Townsend, Rivalta, & Namiki, 2021) (Schmincke, 2007) (White & McCausland, 2019) (Rausch, Grobéty, & Vonlanthen, 2015). Scoria cones are the most typical type of eruption centers in both, the East and West Eifel Volcanic Fields (EEVF, WEVF) (Schmincke, 2007) (Büchel & Mertes, 1982). These types of volcanoes are known for formation periods of a few weeks to some months. Therefore, the formation of a new volcano and/or reactivation of an already formed volcano can happen at any time in EEVF.

Fortunately, ascending magma is always accompanied by several signs of unrest weeks to months prior to the eruption. The earliest sign for a possible eruption, “the occurrence of deep LF events”, is already registered in the EEVF (Hensch, et al., 2019). Based on the noise analysis, the DEEP-TEE dataset introduced in this thesis is sensitive enough to capture detectable and localizable signals of LF events with ML >1, even when the source is located in depths of ~40-50 km, so much below the Moho (~29 km) in the uppermost mantle. This sensitivity is despite the fact that the EEVF is seismically quite noisy due to human activity with the main sources such as transportation by railways, highways and on the Rhine River. Recording seismic activity in volcanic regions is an appropriate way for monitoring magmatic activity and the prediction of a possible eruption. Therefore, recording and monitoring changes in seismic activity must continue specially in the EEVF where the life of ~265,000 people in a radius of less than 20 km to the centre of the LF events would be directly influenced by the impact of a starting volcanic eruption.

In total 462 pulses of LF events were detected, after applying the developed detection algorithm (A6-DFMSD) presented in this work to the seismic records of the DEEP-TEE experiment. 103 of them were the inter-sequence pulses of LF events which could not be directly located due to overlapping waveforms but their locations were reasonably estimated to be the same as the located events in these sequences. Waveforms and seismic phases from 27 events could hardly be picked and their obtained locations using the VELEST location program is not stable and reliable. The remaining 332 LF pulses could be located using VELEST and 289 events could reliably be relocated by HypoDD (a relative relocation algorithm) after passing the jackknife validity test to the relocation results. Plotting these relative hypocentres of 289 LF events provides a reliable 3-D image of the fine structure of the seismically active part of the currently active plumbing system of the Laacher See Volcano (LSV) which is presented in Fig. 6.3. It is schematically modelled in Fig. 6.1b with other corresponding geological and geophysical elements in the EEVF. The main structure, as seen in the plots, is interpreted as a wide zone of dike intrusions with melt and magmatic fluids into the whole lithosphere from a depth of ~45 km in the upper mantle up to ~6 km depth beneath the EEVF. In addition, the discovery of the small cluster of LF events, ~12 km to the east of the center of the main cluster in the Neuwied Basin, is of interest for hazard assessment, due to being closer to the more populated part of the region. The LF events in this cluster have a shallow depth range of ~4 km to 10 km and they are interpreted as sources of gas release in the

Neuwied Basin (Berberich, Berberich, & Ellison, 2019) (Bräuer, Kämpf, Niedermann, & Strauch, 2013). Their connection to the main structure is still an open topic for future studies.
The latest remarkable seismic activity of the magmatic processes occurred in Nov. and Dec. 2021 including two large sequences and one small sequence of LF events (Fig. 7.1). Only within one month 45 well locatable LF events and 103 non-locatable inter-sequence events were detected and (partly) located well below the Moho in a depth range of 33 km to 40 km. Some signals of the LF events in these sequences have a wider range of frequency towards higher frequencies from 1 Hz to even 22 Hz. Indeed, a third of the detected LF pulses (148 out of 462) belong to this one-month long, sub-Moho activity. Due to the high rate of magma intrusion within these sequences of events, the high frequency part of these events might have a relation with the specific occurrence of more vigorous types of opening cracks for transporting magma. This phenomenon remains an open topic for further future investigations.

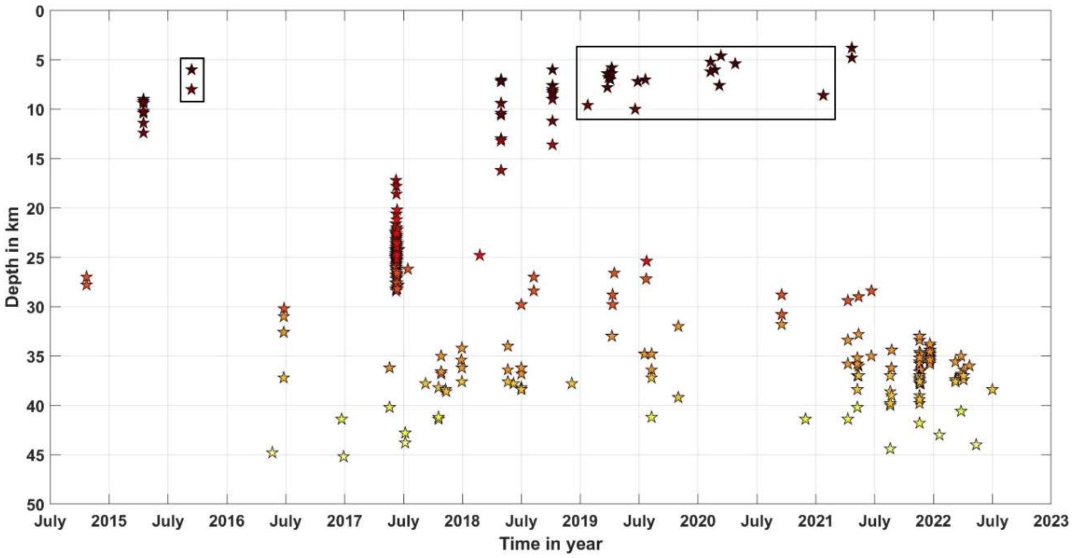

Fig. 7.1 Depth migration of the LF events in time. The two boxes indicate the events which occurred in the eastern cluster in the region (the Neuwied Basin cluster), see map in Fig. 6.3.

For estimation of the moved magma volume (MMV) through the lithosphere beneath the EEVF, I used a model called “a chain of cracks connected with narrow channels” presented by Aki et al. (1977) and Aki and Koyanagi (1981). I added a correction to the calculation of the RMS of the far-field waveform of the P- and S-waves radiated from the source, a jerky crack opening, described there (Fig. 8 in Aki and Koyanagi (1981)). The sensitivity of the model to its input parameters tested by using a reasonable range of values of each parameter while keeping the other parameter values fixed at reasonable values (Table C.2.2 column 2, Appendix C), and amplitude measurements taken from station DEP12. This test showed that the model of melt volume is most sensitive to a) the magma movement direction relative to the station, b) the duration of magma intrusion per event and c) amplitude of the pulses, respectively. The final result for the value of MMV is based on twelve well-observed peak-to-peak amplitude measurements, three extreme scenarios representing the known possible magma intrusion geometries and the reasonable values for the model parameters presented in table C.2.2 column 3 in Appendix C. This estimation resulted in a MMV of ~2.9 10^4 m^3 equivalent to a cube with ca. 31 m side length when the median of the all the estimations is taken, within the time period July 2014 – December 2022. Since the distribution of the 36 estimations is not Gaussian (Fig. 6.4), the uncertainty range of the distribution cannot be simply taken as the first standard deviation. Therefore, as a robust estimation, the uncertainty is deduced from the variation of the data points (Fig. 6.4). This gives a range of 1 10^4 – 3 10^5 m^3 for the melt volume which seems to be a reasonable value in the context of petrological studies on the EEVF (Tomlinson, Smith, & Menzies, Chemical zoning and open system processes in the Laacher See magmatic system, 2020). For a better estimation of the uncertainty range, one might first measure more high-quality amplitude data and then fit the distribution to a representing function for a statistical analysis. This issue remains as an open topic, in addition to adding more data points from new measurements, to the distribution of MMV values.

The detection algorithm (A6-DFMSD) presented in this work has proved its ability in detection and initial frequency-based event-classification of a wide type of signals with different origins: tectonic, magmatic, atmospheric, and anthropogenic. However, due to the presence of a large similarity between the seismic signals of the LF events and quarry blasts, mostly in frequency and partly in time domain (Fig. 6.2a and b), using the detection list of A6-DFMSD for the day time period (7:15 – 15:15 UTC) for searching LF events is not recommended for the regions like EEVF, where up to a radius of 100 km from the centre of LF events there are 424 open mines (sources for quarry blasts). Therefore, searching LF events in an efficient way during day time remains an open topic for future research. Then once the actual number of the LF events during day time, for the same time period (July 2014 – December 2022) is obtained, one can update the MMV estimation presented here to calculate a better estimation of the MMV beneath the EEVF.

Acknowledgement

It was a long journey.

I want to thank you Joachim (my supervisor) that you never left me alone in this scientific journey. I learned a lot from you. I would like to thank you Fatemeh (my wife) for your patience and understanding in this journey.

I want to thank Andreas Rietbrock for his critical and constructive perspective which developed my understanding. Guido Drexlin, I want to thank you here. I could concentrate better after our meeting in Sep. 2024. Here, I want to say thank you to Thomas Bohlen. I was motivated better after our conversation in Nov. 2024. Thomas Forbriger, I would like also to thank you here. Your comments in the meetings have always improved my understanding.

I want to thank you people: Sarah, Dario, Yvonne, Jan-Phillip, Marie, Felix, Rune, Annika, Hans, Caroline, Laura, Michael, Toni, Andreas, Julian, Miriam, Mike, Benedikt, Adam, Leon, Felix and Werner in our institute for keeping our GPI a good place for developing ideas.

I would like to thank Thomas Nadolny, Thomas Hertweck and Michael Frietsch for your IT supports and Kerstin Dick for your kindly administrative supports during my long journey. I hope i did not forget anybody, forgive me in that case .. :-)

Nick you were 20 months old ..

8 Bibliography

Ahorner, L. (1983). Historical Seismicity and Present-Day Microearthquake Activity of the Rhenish Massif, Central Europe. In K. Fuchs, K. von Gehlen, H. Mälzer, H. Murawski, & A. Semmel, Plateau Uplift (pp. 198-221). Berlin, Heidelberg: Springer Berlin Heidelberg.

Allen RV (1978) Automatic earthquake recognition and timing from single traces. Bulletin of the Seismological Society of America 68 1521-1532, doi:10.1785/bssa0680051521.

Aki, K., & Koyanagi, R. (1981). Deep volcanic tremor and magma ascent mechanism under Kilauea, Hawaii. Journal of Geophysical research 86, 7095–7109.

Aki, K., Fehler, M., & Das, S. (1977). Source mechanism of volcanic tremor: fluid-driven crack models and their application to the 1963 Kilauea eruption. J Volcanol Geoth Res 2, 259–287.

Ball, P.W., White, N.J., Maclennan, J. et al. Global influence of mantle temperature and plate thickness on intraplate volcanism. Nat Commun 12, 2045 (2021). https://doi.org/10.1038/s41467-021-22323-9

Bean CJ, De Barros L, Lokmer I, Métaxian J-P, O' Brien G, Murphy S (2014) Long-period seismicity in the shallow volcanic edifice formed from slow-rupture earthquakes. Nature Geoscience 7:71-75.

Bensberg Observatory, University of Cologne (2023) http://www.seismo.uni-koeln.de/events/index.htm. Accessed 17 Apr. 2023.

Berberich, G. M., Berberich, M. B., & Ellison, A. M. (2019). First Identification of Periodic Degassing Rhythms in Three Mineral Springs of the East Eifel Volcanic Field (EEVF, Germany). Geosciences 9(4), 189.

Berndt, J., Holtz, F., & Koepke, J. (2001). Experimental constraints on storage conditions in the chemically zoned phonolitic magma chamber of the Laacher See volcano. Contributions to Mineralogy and Petrology 140, 469-486.

BGR Kataloge, 2023. https://www.bgr.bund.de/DE/Themen/Erdbeben-Gefaehrdungsanalysen/Seismologie/Seismologie/Erdbebenauswertung/Erdbebenkataloge/Kataloge_Bulletins/kataloge_bulletins_node.html. Accessed 01. Sept. 2023

Bond, D. P., & Wignall, P. B. (2014). Large igneous provinces and mass extinctions: An update. In G. Keller, & A. C. Kerr, Volcanism, Impacts, and Mass Extinctions: Causes and Effects. Geological Society of America.

Bonnefoy-Claudet S, Cotton F, Bard, P-Y (2006) The nature of noise wavefield and its applications for site effects studies - A literature review. Earth Science Reviews 79:205–227. https://doi.org/10.1016/j.earscirev.2006.07.004

Bormann P (1998) Conversion and comparability of data presentations on seismic background noise. J Seismol 2:37–45. https://doi.org/10.1023/A:1009780205669

Brace W F, Kohlstedt D L (1980) Limits on lithospheric stress imposed by laboratory experiments. J Geophys Res 85(B11): 6248–6252. doi:10.1029/JB085iB11p06248

Bräuer, K., Kämpf, H., Niedermann, S., & Strauch, G. (2013). Indications for the existence of different magmatic reservoirs beneath the Eifel area (Germany): A multi-isotope (C, N, He, Ne, Ar) approach. Chemical Geology, 356, 193-208.

Buurman, H., West, M.E., 2010. Seismic precursors to volcanic explosions during the 2006 eruption of Augustine Volcano. In: Power, J.A., Coombs, M.L., and Freymueller, J.T., editors, The 2006 eruption of Augustine Volcano, Alaska, U.S. Geological Survey Professional Paper 1769, 41-57, https://pubs.usgs.gov/pp/1769/

Büchel, G., & Mertes, H. (1982). Die Eruptionszentren des Westeifeler Vulkanfeldes. Zeitschrift der Deutschen Geologischen Gesellschaft 133, 409 - 429.

Cañón-Tapia, E. (2019). Influence of angularities on magma tapping processes. Journal of Volcanology and Geothermal Research, 140-156.

Caricchi, L., Townsend, M., Rivalta, E., & Namiki, A. (2021). The build- up and triggers of volcanic eruptions. Nat Rev Earth Environ 2, 458–476.

Chouet BA (1988) Resonance of a fluid-driven crack: Radiation properties and implications for the source of long-period events and harmonic tremor. J Geophys Res 93:4373-4400.

Chouet, B. A. (1996). Long-period volcano seismicity: its source and use in eruption forecasting. Nature 380, 309-316.

Clapham, M., & Renne, P. (2019). Flood Basalts and Mass Extinctions. Annual Review of Earth and Planetary Sciences 47, 275-303.

Cloetingh S, Koptev A, Lavecchia, A, Kovács IJ, Beekman F (2022) Fingerprinting secondary mantle plumes. Earth Planet Sci Lett 597: 117819. https://doi.org/10.1016/j.epsl.2022.117819

Conrad, C.P., Bianco, T.A., Smith, E.I., Wessel P., 2011. Patterns of intraplate volcanism controlled by asthenospheric shear. Nature Geosci 4, 317–321 (2011). https://doi.org/10.1038/ngeo1111

Cusano P, Petrosino S, Bianco F, Del Pezzo E (2013) The first long period earthquake detected in the background seismicity at Mt. Vesuvius. Annals of Geophysics 56, 4, S0440 doi:10.4401/ag-6447.

Dahm T, Stiller M, Mechie J, Heimann S, Hensch M, Woith, H., Schmidt B, Gabriel G, Weber M (2020) Seismological and geophysical signatures of the deep crustal magma systems of the Cenozoic volcanic fields beneath the Eifel, Germany. Geochemistry, Geophysics, Geosystems, 21:e2020GC009062. https://doi.org/10.1029/2020GC009062

Dahm T, Milkereit C, Isken M, Cesca S, Yuan X, Sens-Schönfelder C, Tilmann F, Pilz M, Cotton F, Woith H, Krawczyk C, Haberland C, Hensch M, Schmidt B, Endrun-Knapmeyer B, Meier T, de Siena L, van Camp M, Lecocq T, Oth A (2022a) Ein seismologisches Großexperiment zur Untersuchung magmatischer Prozesse unter der Eifel. Jahrestagung Deutsche Geophysikalische Gesellschaft, Tagungsband (Proceedings), Munich, PS-G.05, p 211

Dahm T et al. (2022b) Vulkanseismologisches Experiment in der Eifel. https://www.gfz-potsdam.de/sektion/erdbeben-und-vulkanphysik/projekte/eifel-vulkanseismologisches-experiment/. Accessed 19 September 2024

D’Auria, L., Koulakov, I., Prudencio, J., Cabrera-Pérez, I., Ibáñez, J. M., Barrancos, J., García-Hernández, R., Martínez van Dorth, D., Padilla, G. D., Przeor, M., Ortega, V., Hernández, P., Peréz, N. M. (2022). Rapid magma ascent beneath La Palma revealed by seismic tomography. Scientific Reports 12, 17654.

Dannberg, J. (2016). Dynamics of mantle plumes: Linking scales and coupling physics (Dissertation). Potsdam: Universität Potsdam.

De Groot-Hedlin C, Constable SC (1990) OCCAM's inversion to generate smooth, two-dimensional models from magnetotelluric data. Geophysics 55: 1613-1624. 10.1190/1.1442813

Demoulin A, Hallot E (2009) Shape and amount of the Quaternary uplift of the western Rhenish shield and the Ardennes (western Europe). Tectonophysics 474:696–708

Diehl T, Kissling E, Bormann P (2012) Tutorial for consistent phase picking at local to regional distances. In: Bormann P (Ed.) New Manual of Seismological Observatory Practice 2 (NMSOP-2. Deutsches GeoForschungsZentrum GFZ Potsdam, 1-21. https://doi.org/10.2312/GFZ.NMSOP-2_IS_11.4

Dinger, F., Bredemeyer, S., Arellano, S., Bobrowski, N., Platt, U., & Wagner, T. (2019). On the link between Earth tides and volcanic degassing. Solid Earth 10, 225-240.

Dvorkin J, Mavko G, Nur A (1999) Overpressure detection from compressional- and shear-wave data. Geophys Res Lett 26(22):3417-3420. https://doi.org/10.1029/1999GL008382

Eickhoff D (2022) Abbildung der Krustenstruktur im Bereich der Eifel durch Reprozessierung der tiefenseismischen Profile DEKORP87-1A/1B. University of Freiberg, Master thesis, 94 pp

Eickhoff D, Föst J-P, Ostermeier R, Koushesh M, Ritter JRR (2024) Estimating a meteoroid’s trajectory using seismic data: a case study of the November 2017 meteoroid over Germany. Proceedings of the International Meteor Conference Redu, Belgium, 2023, 143-145, ISBN 978-2-87355-036-3.

Eickhoff, D., Ritter, J. R., Hloušek, F., & Buske, S. (2024). Seismic Reflection Imaging of Fluid-Filled Sills in the West Eifel Volcanic Field, Germany. Geophysical Research Letters 51, e2024GL111425.

Foix, O., Aiken, C., Saurel, J.-M., Feuillet, N., Jorry, S.J., Rinnert, E., Thinon, I., 2021. Offshore Mayotte volcanic plumbing revealed by local passive tomography. J. Volcanology and Geothermal Research, 420, 107395. https://doi.org/10.1016/j.jvolgeores.2021.107395.

Föst J-P, Bühler J, Koushesh K, Mader S, Ritter J, Hensch M, Schmidt B (2022) New 1-D Seismic Velocity Models and Hypocentres in the East Eifel Volcanic Field. Jahrestagung Deutsche Geophysikalische Gesellschaft, Tagungsband, Munich, PS-C.28, p 141, https://dgg2022.dgg-tagung.de/app/download/12293129598/DGG2022_Tagungsband.pdf?t=1646410568. Accessed 7 Oct. 2022.

Fournier, R. O., & Dzurisin, D. (2007). Hydrothermal systems and volcano geochemistry. In Volcano Deformation: Geodetic Monitoring Techniques (pp. 323-341). Berlin Heidelberg: Springer .

French, S., & Romanowicz, B. (2015). Broad plumes rooted at the base of the Earth's mantle beneath major hotspots. Nature 525, 95–99.

Gal F, Brach M, Braibant G, Jouin F, Michel K (2011) CO2 escapes in the Laacher See region, East Eifel, Germany: application of natural analogue onshore and offshore geochemical monitoring. International Journal of Greenhouse Gas Control 5:1099-1118.

GEOFON (1997-1998) The XE Seismic Network, 1997–1998. https://geofon.gfz-potsdam.de/waveform/archive/network.php?ncode=XE&year=1997. Accessed 19 September 2024

Giggenbach, W. F., Sano, Y., & Schmincke, H. U. (1991). CO2-rich gases from Lakes Nyos and Monoun, Cameroon; Laacher See, Germany; Dieng, Indonesia, and Mt. Gambier, Australia—variations on a common theme. Journal of Volcanology and Geothermal Research, 311-323.

Girona, T., Huber, C., & Caudron, C. (2018). Sensitivity to lunar cycles prior to the 2007 eruption of Ruapehu volcano. Scientific Reports 8, 1476.

Global Volcanism Program, 2024. [Database] Volcanoes of the World (v. 5.2.4; 21 Oct 2024). Distributed by Smithsonian Institution, compiled by Venzke, E. https://doi.org/10.5479/si.GVP.VOTW5-2024.5.2

Goepel A, Lonschinski M, Viereck L, Büchel G, Kukowski N (2015) Volcano-tectonic structures and CO2-degassing patterns in the Laacher See basin, Germany. Int J Earth Sci 104:1483–1495. https://doi.org/10.1007/s00531-014-1133-3

Greenfield, T., Winder, T., Rawlinson, N., Maclennan, J., White, R. S., Ágústsdóttir, T., Bacon, C. A., Brandsdóttir, B., Eibl, E. P. S., Glastonbury-Southern, E., Gudnason, E. Á., Hersir, G. P., Horálek, J. (2022). Deep long period seismicity preceding and during the 2021 Fagradalsfjall eruption, Iceland. Bulletin of Volcanology 84, 101.

Greve A, Stange S, & Brüstle W (1999) Datenerfassung und –verarbeitung im Erdbebendienst. Landesamt Geol Rohst Bergb Baden–Württ, Freiburg i. Br., Informationen 11: 25–32 https://www.google.com/url?sa=t&source=web&rct=j&opi=89978449&url=https://produkte.lgrb-bw.de/docPool/c223_data.pdf&ved=2ahUKEwjlyfXj6IGHAxVA3gIHHaR7ACIQFnoECBEQAQ&usg=AOvVaw1Wq2gRfq6S8aBPuNNc7TeG Accessed 28 June 2024

Griesshaber, E., O'Nions, R. K., & Oxburgh, E. R. (1992). Helium and carbon isotope systematics in crustal fluids from the Eifel, the Rhine Graben and Black Forest, F.R.G. Chemical Geology 99(4), 213-235.

Haberland, C., and A. Rietbrock (2001), Attenuation tomography in the western central Andes: A detailed insight into the structure of a magmatic arc, J. Geophys. Res., 106(B6), 11151–11167, doi:10.1029/2000JB900472.

Harms, E., Gardner, J. E., & Schmincke, H.-U. (2004). Phase equilibria of the Lower Laacher See Tephra (East Eifel, Germany): constraints on pre-eruptive storage conditions of a phonolitic magma reservoir. Journal of Volcanology and Geothermal Research 134, 125 - 138.

Hensch, M., Dahm, T., Ritter, J., Heimann, S., Schmidt, B., Stange, S., & Lehmann, K. (2019). Deep low-frequency earthquakes reveal ongoing magmatic recharge beneath Laacher See Volcano (Eifel, Germany). Geophysical Journal International 216(3), 2025-2036.

Hidayat D, Voight B, Langston C, Ratdomopurbo A, Ebeling C (2000) Broadband seismic experiment at Merapi Volcano, Java, Indonesia: very-long-period pulses embedded in multiphase earthquakes. Journal of Volcanology and Geothermal Research 100:215-231.

Hinzen K-G (2003) Stress field in the Northern Rhine area, Central Europe, from earthquake fault plane solutions. Tectonophysics 377:325-356. https://doi.org/10.1016/j.tecto.2003.10.004

Hinzen K-G, Reamer SK, Fleischer C (2021) Seismicity in the Northern Rhine Area (1995–2018). J Seismol 25:351–367. https://doi.org/10.1007/s10950-020-09976-7

Hotovec-Ellis, A. J., Shelly, D. R., Hill, D. P., Pitt, A. M., Dawson, P. B., & Chouet, B. A. (2018). Deep fluid pathways beneath Mammoth Mountain, California, illuminated by migrating earthquake swarms. Science advances 4(8), 2375-2548.

Houpt L, Frietsch M, Rietbrock A, Ryberg T, Haberland C, Ritter J, Schmidt B, Reicherter K, Hertweck T (2022) The active Ochtendung Fault Zone Seismic Experiment – shallow refraction tomography in the East Eifel Volcanic Field, Germany. European Geosciences Union, General Assembly, EGU22-9800, https://doi.org/10.5194/egusphere-egu22-9800. Accessed 01 December 2022

Jackson J (2002) Strength of the lithosphere. GSA Today 12(9): 4-10.

Jackson J, McKenzie D, Priestley K (2021) Relations between earthquake distributions, geological history, tectonics and rheology on the continents. Phil Trans R Soc A 379: 20190412. https://doi.org/10.1098/rsta.2019.0412

Kenneth D. Smith et al. Evidence for Deep Magma Injection Beneath Lake Tahoe, Nevada-California.Science305,1277-1280(2004).DOI:10.1126/science.1101304

Keyser M, Ritter J R R, Jordan M (2002) 3D shear-wave velocity structure of the Eifel plume, Earth planet Sci Lett 203:59–82

Kirtskhalia VG (2012) Speed of sound in atmosphere of the earth, Open Journal of Acoustics 2:80-85.

Kissling, E., Ellsworth, W. L., Eberhart-Phillips, & Kradolfer, U. (1994). Initial reference models in local earthquake tomography. journal of geophysical research 99(B10), 19635-19646.

Kissling, E., Kradolfer, U., & Maurer, H. (1995). VELEST user''s guide-short introduction. Institute of Geophysics, ETH Zuerich.

Koppers, A. A., Becker, T. W., Jackson, M. G., Konrad, K., Müller, R. D., Romanowicz, B., Steinberger, B., Whittaker, J. M. (2021). Mantle plumes and their role in Earth processes. Nature Reviews Earth & Environment 2, 382-401.

Koushesh, K. and Ritter, J.R.R. (2024). An adaptive 6-dimensional floating-search multi-station seismic-event detector (A6-DFMSD) and its application to low-frequency earthquakes in the East Eifel Volcanic Field, Germany. J. Applied Volcanology, 13:9, https://doi.org/10.1186/s13617-024-00147-8

Kreemer C, Blewitt G, Davis PM (2020) Geodetic evidence for a buoyant mantle plume beneath the Eifel volcanic area, NW Europe. Geophysical Journal International 222:1316–1332. https://doi.org/10.1093/gji/ggaa227

Kumagai, H. (2009). Volcano Seismic Signals, Source Quantification of. In R. A. Meyers, Encyclopedia of Complexity and Systems Science (pp. 9899-9932). New York, NY: Springer New York.

Landeserdbebendienst, 2018. Bulletin Files, Az. 4784//21_8714, Az. 4784//19_12333. https://erdbeben.led-bw.de/ Accessed 19 September 2024

Langguth, H. R., & Plum, H. (1984). Untersuchung der Mineral- und Thermalquellen der Eifel auf geothermische Indikationen. Karlsruhe: Fachinformationszentrum Energie, Physik, Mathematik Karlsruhe, https://books.google.de/books?id=lKAzPwAACAAJ.

IASPEI (2013) Summary of Magnitude Working Group recommendations on standard procedures for determining earthquake magnitudes from digital data. http://www.iaspei.org/commissions/CSOI/Summary_WG_recommendations_20130327.pdf. Accessed 01 December 2022

Leder J, Wenzel F, Daniell JE, Gottschämmer E (2017) Loss of residential buildings in the event of a re-awakening of the Laacher See Volcano (Germany). J Volcanol. Geotherm Res 337:111–123. http://dx.doi.org/10.1016/j.jvolgeores.2017.02.019

Leydecker G (2011) Erdbebenkatalog für Deutschland mit Randgebieten für die Jahre 800 bis 2008. Geologisches Jahrbuch Reihe E 59, Schweitzerbart, Stuttgart, 198 pp. ISBN 978-3-510-95989-1

LGB, 2024. https://www.lgb-rlp.de/de/fachthemen/landeserdbebendienst-rheinland-pfalz/erdbebenereignisse-lokal.html (last access 25 Dec. 2024)

Li L, Tan J, Schwarz B, Staněk F, Poiata N, Shi P, Diekmann L, Eisner L, Gajewski D (2020) Recent Advances and Challenges of Waveform-Based Seismic Location Methods at Multiple Scales. Reviews of Geophysics, 58, e2019RG000667. https://doi.org/10.1029/2019RG000667

Malfante, M., Dalla Mura, M., Metaxian, J. -P., Mars, J. I., Macedo, O., & Inza, A. (2018). Machine Learning for Volcano-Seismic Signals: Challenges and Perspectives. IEEE Signal Processing Magazine 35(2), 20-30.

Mani, L., Tzachor, A. & Cole, P., 2021. Global catastrophic risk from lower magnitude volcanic eruptions. Nat Commun 12, 4756. https://doi.org/10.1038/s41467-021-25021-8

Mathar J P, Ritter J R R, Friederich W (2006) Surface waves image the top of the Eifel plume. Geophys J Int 164(2):377–382. https://doi.org/10.1111/j.1365-246X.2006.02835.x

McGary, R., Evans, R., Wannamaker, P. et al. Pathway from subducting slab to surface for melt and fluids beneath Mount Rainier. Nature 511, 338–340 (2014). https://doi.org/10.1038/nature13493

McKenzie, D. & Bickle, M. J. The volume and composition of melt generated by extension of the lithosphere. J. Petrol. 29, 625–679 (1988).

McLeod, P., & Tait, S. (1999). The growth of dykes from magma chambers. Journal of Volcanology and Geothermal Research, 231-245.

McNutt SR, Thompson G, Johnson J, De Angelis S, Fee D (2015) Seismic and infrasonic monitoring. In: Sigurdsson H, Houghton B, McNutt SR, Rymer H, Stix J (eds.) The Encyclopedia of Volcanoes. Academic Press, London, pp 1071-1099. http://dx.doi.org/10.1016/B978-0-12-385938-9.00063-8

Mechie J, Prodehl C, Fuchs K (1983) The long-range seismic refraction experiment in the Rhenish Massif. In: Fuchs K, von Gehlen K, Mälzer H, Murawski H, Semmel A (eds.) Plateau Uplift, Springer, Berlin, pp 261–274

Menand, T. (2011). Physical controls and depth of emplacement of igneous bodies: A review. Tectonophysics 500, 11-19.

Mertes, H., & Schmincke, H. -U. (1983). Age Distribution of Volcanoes in the West-Eifel. Jahrbuch für Geologie und Paläontologie 166, 260-293.

Mertz DF, Löhnertz W, Nomaded, S, Pereira A, Prelevića D, Renne PR (2015) Temporal–spatial evolution of low-SiO2 volcanism in the Pleistocene West Eifel volcanic field (West Germany) and relationship to upwelling asthenosphere. J Geodyn 88:59–79. http://dx.doi.org/10.1016/j.jog.2015.04.002

Meyer W (2013) Geologie der Eifel. 4th edition, Schweizerbart'sche Verlagsbuchhandlung, Stuttgart, 704 pp

Meyer W, Stets J (2007) Quaternary uplift in the Eifel Area. In Ritter J R, Christensen U R (eds.) Mantle Plumes — A Multidisciplinary Approach, Springer, Heidelberg pp 369–378

Mezcua, J., & Rueda, J. (2023). Seismic swarms and earthquake activity b-value related to the September 19, 2021, La Palma volcano eruption in Cumbre Vieja, Canary Islands (Spain). Bulletin of Volcanology 85, 32.

Nakada, S., Shimizu, H., & Ohta, K. (1999). Overview of the 1990–1995 eruption at Unzen Volcano. Journal of Volcanology and Geothermal Research 89, 1-22.

Naofumi A, Kazuaki O, Satoshi I (2013) Tectonic, volcanic, and semi-volcanic deep low-frequency earthquakes in western Japan. Tectonophysics 600:27-40.

Neuberg J, Luckett R, Baptie B, Olsen K (2000) Models of tremor and low-frequency earthquake swarms on Montserrat. Journal of Volcanology and Geothermal Research 101:83-104.

Neuberg, J. (2011). Earthquakes, Volcanogenic. Encyclopedia of Earth Sciences Series, 261-269. doi:10.1007/978-90-481-8702-7_159

Nicol, N., & Albrecht, R. (2007). Wissenschaftliche Arbeiten schreiben mit Word 2007. München: Addison-Wesley Verlag.

Nielsen, S. G., & Marschall, H. R. (2017). Geochemical evidence for mélange melting in global arcs. Science Advances 3(4), e1602402.

Ochmann N (1988) Tomographische Analyse der Krustenstruktur unter dem Laacher-See-Vulkan mit Hilfe von teleseismischen Laufzeitresiduen. Dissertation, RWTH Aachen 106pp

Paige, C. C., & Saunders, M. A. (1982). LSQR: Sparse linear equations and least squares problems. ACM Transactions on Mathematical Software, 195-209.

Pallister J, Mc Nutt SR (2015) Synthesis of volcano monitoring. In: Sigurdsson H, Houghton B, McNutt SR, Rymer H, Stix J (eds) The Encyclopedia of Volcanoes. Academic Press, London, pp 1151-1171. http://dx.doi.org/10.1016/B978-0-12-385938-9.00066-3

Park C, Schmincke H-U (2020) Multistage damming of the Rhine River by tephra fallout during the 12,900 BP Plinian Laacher See Eruption (Germany). Syn-eruptive Rhine damming I. J Volcanol Geotherm Res 389, 106688. https://doi.org/10.1016/j.jvolgeores.2019.106688

Paulatto M, Hooft EEE, Chrapkiewicz K, Heath B, Toomey DR and Morgan JV (2022) Advances in seismic imaging of magma and crystal mush. Front Earth Sci 10:970131. doi: 10.3389/feart.2022.970131

Pelzing R (2008) Erdbeben in Nordrhein-Westfalen. Geologischer Dienst NRW, Krefeld, ISBN 978-3-86029-971-5

Perol T, Gharbi M, Denolle M (2018) Convolutional neural network for earthquake detection and location. Science Advances 4 (2), doi:10.1126/sciadv.1700578.

Peterson J (1993) Observations and modeling of seismic background noise. U.S. Geological Survey, Open-File report 93-322, 95 pp

Plesinger, A., Hellweg, M., & Seidl, D. (1986). Interactive high-resolution polarization analysis of broad-band seismograms. J geophysics 59, 129-139.

Raikes S, Bonjer K-P (1983) Large-scale mantle heterogeneity beneath the Rhenish Massif and its vicinity from teleseismic P-residuals measurements. In: Fuchs K, von Gehlen K, Mälzer H, Murawski H, Semmel A (eds.) Plateau Uplift, Springer, Berlin, pp 315-331

Rausch, J., Grobéty, B., & Vonlanthen, P. (2015). Eifel maars: Quantitative shape characterization of juvenile ash particles (Eifel Volcanic Field, Germany). Journal of Volcanology and Geothermal Research 291, 86-100.

Ratdomopurbo A, Poupinet G (2000) An overview of the seismicity of merapi volcano (java, indonesia), 1983-1994. Journal of Volcanology and Geothermal Research 100:193-214.

Reinig F, Wacker L, Jöris O, Oppenheimer C, Guidobaldi G, Nievergelt D, Adolphi F, Cherubini P, Engels S, Esper J, Land A, Lane C, Pfanz H, Remmele S, Sigl M, Sookdeo A, Büntgen U. (2021). Precise date for the Laacher See eruption synchronizes the Younger Dryas. Nature 595(7865), 66-69.

Ribe, N.M., 1987. Theory of melt segregation - a review. Journal of Volcanology and Geothermal Research, 33 (1987) 241-253.

Ritter JRR, Schmidt B, Haberland C, Weber M (2014) DEEP TEE. GFZ Data Services (other / seismic network), https://geofon.gfz-potsdam.de/doi/network/1P/2014. Accessed 19 September 2024

Ritter J R R, Achauer U, Christensen U R, Eifel Plume Team, (2000) The teleseismic tomography experiment in the Eifel Region, Central Europe: design and first results. Seismol Res Lett 71:437–443

Ritter J R R, Jordan M, Christensen U R, Achauer U (2001) A mantle plume below the Eifel volcanic fields, Germany. Earth planet Sci Lett 186:7–14

Ritter, J. (2007). The Seismic Signature of the Eifel Plume. In J. Ritter, & U. (. Christensen, Mantle Plumes: A Multidisciplinary Approach (pp. 379-404). Berlin, Heidelberg: Springer.

Ritter, J.R.R., Koushesh, K., Schmidt, B., Bühler, J., Föst, J.-P., Hensch, M. and Mader, S., 2024. Seismological monitoring of magmatic and tectonic earthquakes in the East Eifel Volcanic Field, Germany. J. Seismology, https://doi.org/10.1007/s10950-024-10257-w.

Roman, D., & Cashman, K. (2018). Top–Down Precursory Volcanic Seismicity: Implications for 'Stealth' Magma Ascent and Long-Term Eruption Forecasting. Front. Earth Sci 6, 124.

Ross ZE, Trugman DT, Hauksson E, Shearer PM (2019) Searching for hidden earthquakes in Southern California. Science 364:767-771.

Rout SS, Wörner G (2018) Zoning and exsolution in alkali feldspars from Laacher See volcano (Western Germany): constraints on temperature history prior to eruption. Contrib Mineral Petrol 173:95. https://doi.org/10.1007/s00410-018-1522-x

Rout, S.S., Wörner, G., 2020. Constraints on the pre-eruptive magmatic history of the Quaternary Laacher See volcano (Germany). Contrib Mineral Petrol 175, 73. https://doi.org/10.1007/s00410-020-01710-3

Rummel, L., Kaus, B.J.P., White, R.W., Mertz D.F., Yang, J., Baumann, T.S., 2018. Coupled petrological-geodynamical modeling of a compositionally heterogeneous mantle plume.Tectonophysics, 723, 242-260. https://doi.org/10.1016/j.tecto.2017.12.022.

Schmeling, H., Marquart, G., Weinberg, R., Wallner, H., Modelling melting and melt segregation by two-phase flow: new insights into the dynamics of magmatic systems in the continental crust, Geophysical Journal International, Volume 217, Issue 1, April 2019, Pages 422–450, https://doi.org/10.1093/gji/ggz029

Schmidt, S., Hertwig, A., Cionoiu, K., Schäfer, C., Schmitt, A.K., 2024. Petrologically controlled oxygen isotopic classification of cogenetic magmatic and metamorphic sapphire from Quaternary volcanic fields in the Eifel, Germany. Contrib Mineral Petrol 179, 55.. https://doi.org/10.1007/s00410-024-02136-x

Schmincke H-U, Lorenz V, Seck HA (1983) The Quarternary Eifel volcanic fields. In: Fuchs K, Gehlen KV, Mälzer H, Murawski H, Semmel A: Plateau uplift. The Rhenish Shield — a case history, 139-151, Springer, Berlin, Heidelberg, New York, Tokyo.

Schmincke, H. (2007). The Quaternary volcanic fields of the East and West Eifel (Germany). . In J. Ritter, & U. Christensen, Mantle Plumes. Berlin, Heidelberg: Springer.

Schmitt AK, Wetzel F, Cooper KM, Zou H, Wörner G (2010) Magmatic longevity of Laacher See volcano (Eifel, Germany) indicated by U-Th dating of intrusive carbonatites. J Petrol 51:1053-1085.

Schmitt FH, Schmitt AK, Gerdes A, Harvey JC (2022) Magma accumulation underneath Laacher See volcano from detrital zircon in modern streams. J Geol Society 180. https://doi.org/10.1144/jgs2022-064

Schreiber U, Jentzsch G (2021) Vulkanische Gefährdung in Deutschland. BGE-Vergabenummer: SEVGV3T-19-04-OI. https://www.bge.de/fileadmin/user_upload/Standortsuche/Forschung/Bericht_-_Vulkanische_Gefaehrdung_in_Deutschland_barrierefrei.pdf. Accessed 19 September 2024

Schwarz, M. (2020). Detektion und Clusteranalyse von Mikroerdbeben mit Kreuzkorrelations-Untersuchungen im Vulkanfeld der Osteifel. Karlsruhe : Karlsruhe Institute of Technology, Master Thesis.

Seiberlich C A, Ritter J R R, Wawerzinek B (2013) Topography of the lithosphere-asthenosphere boundary below the Upper Rhine Graben Rift and the volcanic Eifel region, Central Europe. Tectonophysics 603:222–236. https://doi.org/10.1016/j.tecto.2013.05.034

Shapiro, N. M., Droznin, D. V., Droznina, S. Y., Senyukov, S. L., Gusev, A. A., & Gordeev, E. I. (2017). Deep and shallow long-period volcanic seismicity linked by fluid-pressure transfer. Nature Geoscience 10, 442-445.

Shaw, C.S.J., Eyzaguirre, J., Fryerm B., Gagnon, J., 2005. Regional variations in the mineralogy of metasomatic assemblages in mantle xenoliths from the West Eifel Volcanic Field, Germany. J. Petrol., 46(5), 945–972, https://doi.org/10.1093/petrology/egi006

Shaw C.S.J., Lebert, B.S., Woodland, A.B., 2018. Thermodynamic modelling of mantle–melt interaction evidenced by veined wehrlite xenoliths from the Rockeskyllerkopf Volcanic Complex, West Eifel Volcanic Field, Germany. J. Petrol., 59(1), 59–86, https://doi:10.1093/petrology/egy018

Shaw, C.S.J. & Woodland, A. B., 2012. The role of magma mixing in the petrogenesis of mafic alkaline lavas, Rockeskyllerkopf Volcanic Complex, West Eifel, Germany. Bull Volcanol (2012) 74:359–376, DOI 10.1007/s00445-011-0532-6

Shelly D R, Skoumal R J, Hardebeck J L (2022) S/P amplitude ratios derived from single-component seismograms and their potential use in constraining focal mechanisms for microearthquake Sequences. The Seismic Record 2(2): 118–126. doi: 10.1785/0320220002

Sherburn S, Scott BJ, Nishi Y, Sugihara M (1998) Seismicity at white island volcano, new zealand: a revised classification and inferences about source mechanism. Journal of Volcanology and Geothermal Research 83:287-312.

Siebert, L., Cottrell, E., Venzke, E., & Andrews, B. (2015). Chapter 12 - Earth's Volcanoes and Their Eruptions: An Overview. In H. Sigurdsson, The Encyclopedia of Volcanoes (Second Edition) (pp. 239-255). Amsterdam: Academic Press.

Stammler K, Bischoff M, Brüstle A, Ceranna L, Donner S, Fischer K, Gaebler P, Friederich W, Funke S, Hartmann G, Homuth B, Knapmeyer-Endrun B, Korn M, Megies T, Pilger C, Plenefisch T, Pustal I, Rappsilber I, Schmidt B, Sonnabend L, Stange S, Wassermann J, Wegler U (2021) German seismic and infrasound networks contributing to the

European Integrated Data Archive (EIDA). Seismol Res Lett 92: 1854–1875. https://doi.org/10.1785/0220200401

Stange, S., Kurrle, D., Dahm, T., Hinzen, K.-G., Lehmann, K., Ritter, J.R.R., Schmidt, B., 2014. Subkrustale Seismizität in der Osteifel. Jahrestagung Deutsche Geophysikalische Gesellschaft, Tagungsband (Proceedings), Karlsruhe, SO-5.002, p 231, https://www.dgg-2014.de/downloads/DGG_Tagungsband.pdf. last access 05 January 2025

State seismological service of Rhineland-Palatinate (2023). https://www.lgb-rlp.de/de/fachthemen-des-amtes/landeserdbebendienst-rheinland-pfalz/. Accessed 3 Nov. 2023.

Stosch, H.-G., Lugmair G.W., 1986. Trace element and Sr and Nd isotope geochemistry of peridotite xenoliths from the Eifel (West Germany) and their bearing on the evolution of the subcontinental lithosphere. Earth and Planetary Science Letters, 80, 281-298, https://doi.org/10.1016/0012-821X(86)90111-1

Stroujkova A, Malin P (2001) Multiple ruptures for long valley microearthquakes: a link to volcanic tremor. Journal of Volcanology and Geothermal Research 106:123-143.

Survey, B. G. (n.d.). Earth hazards. Retrieved 10 2024, from https://www.bgs.ac.uk/discovering-geology/earth-hazards/volcanoes/

The ObsPy Development Team (2020) ObsPy Tutorial Release 1.2.0. https://docs.obspy.org. Accessed 19 September 2024

Trnkoczy A (2009) Understanding and parameter setting of STA/LTA trigger algorithm. – In: Bormann P (ed) New Mannual of Seismological Observatory Practice (NMSOP), Potsdam, Deutsches GeoForschungsZentrum GFZ, 1:20.

Thurber, C. H. (1981). Earth structure and earthquake locations in the Coyote Lake area, central California. Massachusetts: Massachusetts Institute of Technology, PhD Thesis.

Tichelaar, B. W., & Ruff, L. J. (1989). How good are our best models? Jackknifing, bootstrapping, and earthquake depth. Eos, Transactions American Geophysical Union 70(20), 593-606.

Tomlinson, E. L., Smith, V. C., & Menzies, M. A. (2020). Chemical zoning and open system processes in the Laacher See magmatic system. Contributions to Mineralogy and Petrology 19.

Tuffen, H., & Dingwell, D. (2005). Fault textures in volcanic conduits: evidence for seismic trigger mechanisms during silicic eruptions. Bulletin of Volcanology, 370-387.

Tuffen, H., Smith, R., & Sammonds, P. R. (2008). Evidence for seismogenic fracture of silicic magma. Nature, 511-514.

Turcotte, D. L. (1987). Physics of magma segregation processes. In B. O. Mysen, Magmatic Processes: Physicochemical Principles. The Geochemical Society, Special Publication No.1,.

USGS. (2023, Dec. 7). About Earthquakes in Hawaii (Hawaiian Volcano Observatory). Retrieved from https://www.usgs.gov/observatories/hvo/science/about-earthquakes-hawaii

Waldhauser, F. (2001). hypoDD-A Program to Compute Double-Difference Hypocenter Locations. USGS Publications Warehouse.

Waldhauser, F., & Ellsworth, W. L. (2000). A Double-difference Earthquake location algorithm: Method and application to the Northern Hayward Fault, California. Bulletin of the Seismological Society of America 90, 1353-1368.

Wassermann J (2012) Volcano Seismology. - In: Bormann P. (ed) New Manual of Seismological Observatory Practice 2 (NMSOP-2), Potsdam: Deutsches GeoForschungsZentrum GFZ, 1-77. https://doi.org/10.2312/GFZ.NMSOP-2_ch13. Accessed 3 Nov. 2023.

Weber K (2012) Erdbeben in der Eifel und dem Neuwieder Becken. In: Viereck L (ed) Einblicke - vom Gestern zum Heute, 25 Jahre DVG, Mendig, pp 84-94

Wessel P, Luis JF, Uieda L, Scharroo R, Wobbe F, Smith WHF, Tian D (2019) The generic mapping tools version 6. Geochem Geophys Geosyst 20:5556-5564. https://doi.org/10.1029/2019GC008515

Westaway, R. (1993). Forces associated with mantle plumes. Earth and Planetary Science Letters, 119 , 331-348.

White, L. T., Rawlinson, N., Lister, G. S., Waldhauser, F., Hejrani, B., Thompson, D. A., Tanner, D., Macpherson, C. G., Tkalčić, H., Morgan, J. P. (2019). Earth's deepest earthquake swarms track fluid ascent beneath nascent arc volcanoes. Earth and Planetary Science Letters 521, 25-36.

White, R., & McCausland, W. (2016). Volcano-tectonic earthquakes: A new tool for estimating intrusive volumes and forecasting eruptions. Journal of Volcanology and Geothermal Research 309, 139–155.

White, R. A., & McCausland, W. A. (2019). A process-based model of pre-eruption seismicity patterns and its use for eruption forecasting at dormant stratovolcanoes. Journal of Volcanology and Geothermal Research 382, 267-297.

Witt-Eickschen G, Kaminsky W, Kramm U, Harte B (1998) The nature of young vein metasomatism in the Lithosphere of the West Eifel (Germany): Geochemical and Isotopic Constraints from composite mantle xenoliths from the Meerfelder Maar. J Petrology 39: 155–185. https://doi.org/10.1093/petroj/39.1.155

Witt-Eickschen, G., Seck, H.A., Mezger, K., Eggins, S.M., Altherr, R., 2003. Lithospheric mantle evolution beneath the Eifel (Germany): constraints from Sr–Nd–Pb Isotopes and trace element abundances in spinel peridotite and pyroxenite xenoliths. J. Petrol., 44(6), 1077–1095, https://doi.org/10.1093/petrology/44.6.1077

Witt-Eickschen G (2007) Thermal and geochemical evolution of the shallow subcontinental lithospheric mantle beneath the Eifel: constraints from mantle xenoliths, a review. In: Ritter JRR, Christensen UR (eds) Mantle Plumes. Springer, Berlin, pp 323–337. https://link.springer.com/chapter/10.1007/978-3-540-68046-8_9

Wörner G, Wright TL (1984) Evidence for magma mixing within the Laacher See magma chamber (East Eifel, Germany). Journal of Volcanology and Geothermal Research 22:301-327.

Yavuz E, Sertçelik F, Livaoğlu H, Woith H, Lühr B-G (2019) Discrimination of quarry blasts from tectonic events in the Armutlu Peninsula, Turkey. J Seismol 23:59–76. https://doi.org/10.1007/s10950-018-9793-2

Yoon CE, O'Reilly O, Bergen KJ, and Beroza GC (2015) Earthquake detection through computationally efficient similarity search. Science Advances 1 (11) doi:10.1126/sciadv.1501057.

Appendix A: for chapter four (the DEEP-TEE experiment)

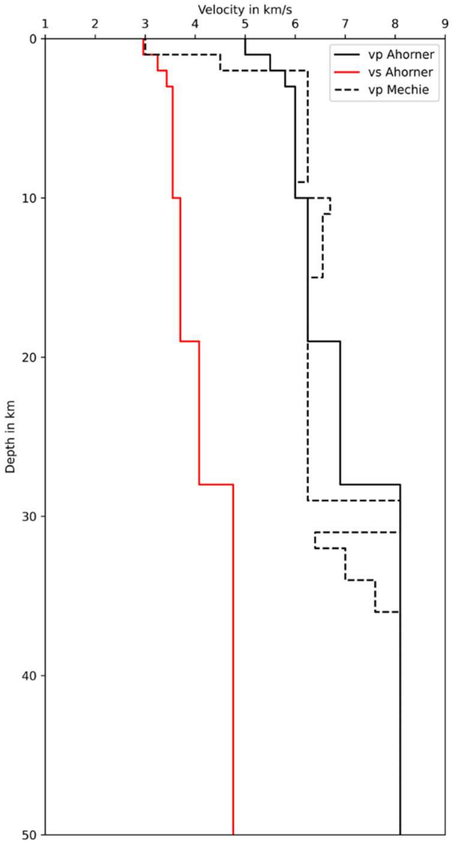

Fig. A1 Starting seismic velocity models for the inversion with VELEST (Kissling 1994; Kissling et al. 1995). The seismic *vp* and *vs* velocity models from Ahorner (1983) are shown with solid lines. These were determined with earthquake recordings from the Rhenish Shield region. Note, here the Moho of the Ahorner model is shifted to 28 km depth as found in active source models, whereas in the original Ahorner model it is at 31 km depth. The model (only *vp*) from Mechie et al. (1983) was determined from a seismic refraction experiment from Paris to the Harz Mountains. The long deep-sounding profile allowed to recover sub-Moho *vp* information. Here we show *vp*(*z*) as dashed line for the region of the East Eifel Volcanic Field. A special feature is the low-velocity layer with a *vp* gradient about 3 km below the Moho. Layers and seismic velocities are listed in Tables A1 and A2

Table A1a 1-D seismic layer model from Ahorner (1983). Note, here the Moho is at 28 km depth as found in active source models, whereas in the original Ahorner model it is at 31 km depth

depth in km	*vs* in km s^{-1}	*vp* in km s^{-1}	*vp* / *vs*
-0.9 - 1.0	2.96	5.00	1.69
1.0 - 2.0	3.25	5.50	1.69
2.0 - 3.0	3.43	5.80	1.69
3.0 - 10.0	3.55	6.00	1.69
10.0 - 19.0	3.70	6.25	1.69
19.0 - 28.0	4.08	6.90	1.69
>28.0	4.76	8.10	1.70

Table A1b Inversion result for 1-D seismic layer model based on the Ahorner (1983) model as starting model

depth in km	*vs* in km s^{-1}	*vp* in km s^{-1}	*vp* / *vs*
-0.9 - 1.0	3.03	5.00	1.65
1.0 - 2.0	2.58	5.77	2.24
2.0 - 3.0	2.57	5.81	2.26
3.0 - 10.0	3.61	5.86	1.62
10.0 - 19.0	3.69	5.27	1.43
19.0 - 28.0	2.98	5.39	1.81
>28.0	4.52	7.03	1.56

Table A2 1-D seismic layer model (*vp*) from Mechie et al. (1983). The values for the starting model are taken from the 2-D model in the region of the East Eifel Volcanic Field. *vs* is calculated with a constant *vp* / *vs* of 1.72. Below 36 km depth there is a half space with *vp* = 8.1 km/s. 1-D model results are from the inversion with the lowest RMS and VELEST input data VI3 (Table A5)

depth in km	starting model *vp* in km s^{-1}	starting model *vp* / *vs*	1-D inversion model *vs* in km s^{-1}	1-D inversion model *vp* in km s^{-1}	1-D inversion model *vp* / *vs*
-0.9 - 1.0	3.00	1.72	3.03	5.00	1.65
1.0 - 2.0	4.50	1.72	3.56	4.57	1.28
2.0 - 8.0	6.25	1.72	3.23	5.69	1.76
8.0 - 9.0	6.25	1.72	3.63	6.00	1.65
9.0 - 10.0	6.00	1.72	3.84	6.02	1.57
10.0 - 11.0	6.70	1.72	3.84	6.21	1.62
11.0 - 15.0	6.55	1.72	3.84	5.77	1.50
15.0 - 29.0	6.25	1.72	3.20	5.30	1.66
29.0 - 31.0	8.10	1.72	4.42	5.43	1.23
31.0 - 32.0	6.40	1.72	4.62	6.70	1.45
32.0 - 34.0	7.00	1.72	4.83	6.98	1.45
34.0 - 36.0	7.60	1.72	4.02	8.29	2.06
>36.0	8.10	1.72	4.55	7.66	1.68

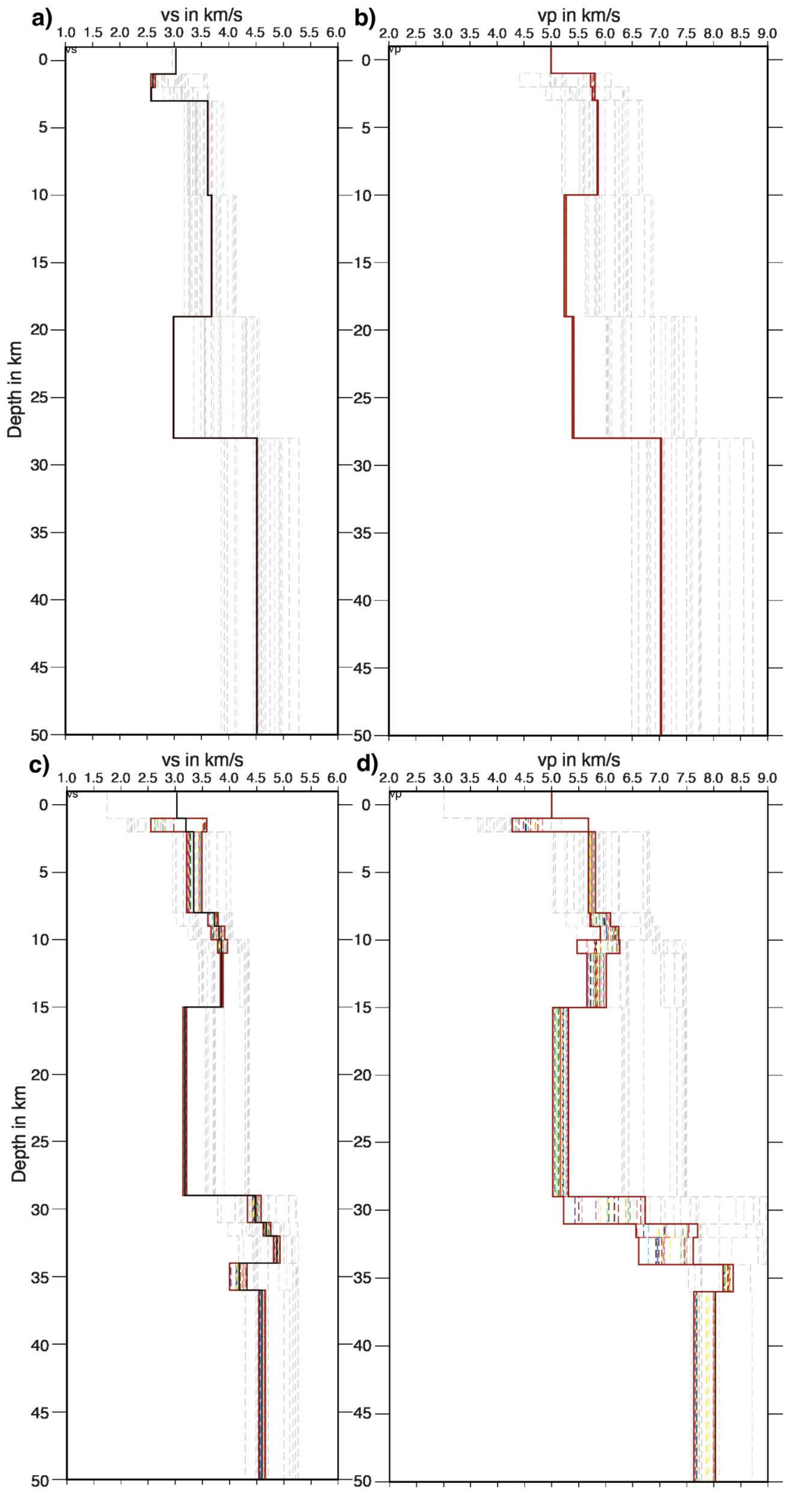

Fig. A2 1-D seismic velocity models from inversion tests. Grey lines show the starting model and 20 perturbed input models which vary by up to 20 percent relative to the starting models in Tables A1 and A2. Coloured models are the related inversion results. a) *vs* and b) *vp* input models and results for the layering after Ahorner et al. (1983); c) *vs* and d) *vp* input models and results for the layering after Mechie et al. (1983), the *vs* input velocities for c) were calculated with a *vp / vs* ratio of 1.72

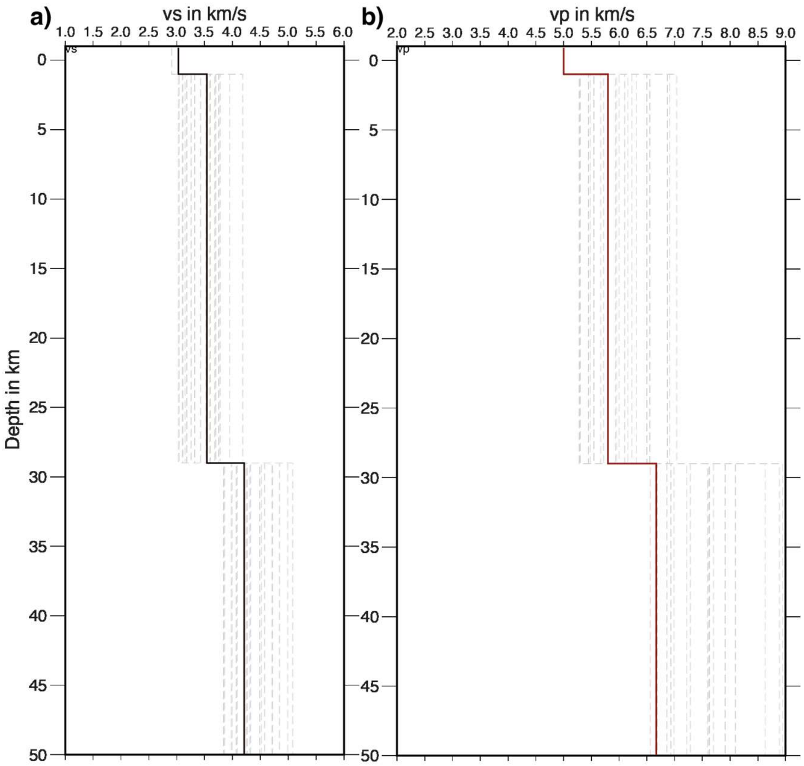

Fig. A3 Seismic velocity models from inversion tests with a simple three-layer structure of the crust and upper mantle. Grey lines are the starting model plus 20 perturbed input models which vary by up to 20 percent relative to the starting model velocity in Table A3. Coloured models are the related 1-D inversion results. a) *vs* models and b) *vp* models. As input the P- and S-wave data from input VI3 (Table A5) was used

Table A3 1-D seismic model for the simple three-layer model for inversion tests with constant *vp* and *vs* in the crust and upper mantle (Fig. A3). The uppermost layer is taken from Eickhoff (2022)

depth in km	*vs* in km s^{-1}	*vp* in km s^{-1}	*vp* / *vs*
-0.9 – 1.0	3.03	5.00	1.65
1.0 – 29.0	3.54	5.80	1.64
>29.0	4.21	6.67	1.58

Table A4 1-D seismic layer model KIT5. The uppermost layer is taken from Eickhoff (2022)

depth in km	*vs* in km s^{-1}	*vp* in km s^{-1}	*vp* / *vs*
-0.9 - 1.0	3.03	5.00	1.65
1.0 - 8.0	3.27	5.55	1.68
8.0 - 17.5	3.64	5.83	1.58
17.5 - 29.0	2.72	3.82	1.69
29.0 - 31.0	4.79	8.09	1.70
31.0 - 32.0	3.21	6.40	2.00
32.0 - 34.0	3.72	7.00	1.89
34.0 - 36.0	4.21	7.60	1.81
>36.0	4.51	8.10	1.80

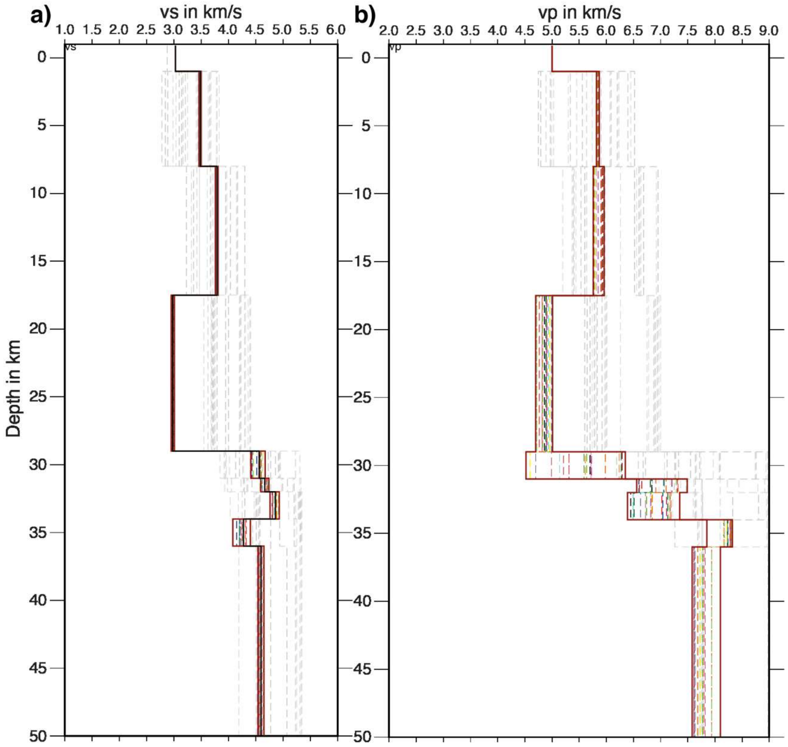

Fig. A4 1-D seismic velocity models for inversion tests with model KIT5. Grey lines are 21 perturbed input models which vary by up to 20 percent relative to the starting model. Coloured models show the related inversion results. a) *vs* and b) *vp* models. As input the P- and S-wave data from input VI3 (Table A5) was used

Table A5 Number of seismic P-wave and S-wave phases from hypocenters inside a specific layer in model KIT6. VELEST input 1 (VI1): minimum 8 P-phases per event above 17.5 km depth plus 6 P-phases per event below 17.5 km depth. VELEST input 2 (VI2): minimum 8 S-phases per event above 17.5 km depth and minimum 6 S-phases per event below 17.5 km depth. VELEST input 3 (VI3): 8 P- or 8 S-phases per event above 17.5 km depth and minimum 6 P- or 6 S-phases per event below 17.5 km depth. VI1, VI2, and VI3 contain phases from 201, 320, and 382 different events, respectively. The event and phase distributions are nearly identical for model KIT5

Layer number	Depth in km	Description	VI1, no. of P-phases	VI2, no. of S-phases	VI3, no. of P-phases	VI3, no. of S-phases
1	-0.9 – 1.0	near-surface	0	0	0	0
2	1.0 – 8.0	upper crust 1	137	70	197	203
3	8.0 - 17.5	upper crust 2	1474	1255	1672	1612
4	17.5 - 29.0	lower crust	72	641	210	537
5	29.0 - 33.0	Moho region	45	152	28	98
6	33.0 - 37.0	underplating region	128	467	286	563
7	>37.0	upper mantle	193	513	205	478
		sum:	2049	3098	2598	3491

Table A6 RMS of 1-D layer models for different VELEST inversions. The trial models contain different numbers of layers. Note: the final RMS values are quite similar after the inversion incl. station corrections

Model name	number of layers	min RMS in s
Ahorner	7	0.115
Mechie	13	0.114
3 layers	3	0.119
KIT5	9	0.115
KIT6	7	0.115

Table A7 vp / vs values from Wadati diagrams. Three values are calculated with Marquardt-Levenberg regression for each diagram (Fig. 4.9, Fig. A5, and Fig. A6) depending on the hypocentral depth of the events that generated the picked or calculated phases; vp / vs_{obs} is from the observed data with hypocenters determined with the Ahorner velocity model (Fig. A1), vp / vs_{KIT5} and vp / vs_{KIT6} are from synthetic data calculated with hypocenters and velocity structures determined with the 1-D KIT5 and KIT6 models, respectively (Fig. 4.11)

depth of phase origin in km	vp / vs_{obs}	vp / vs_{KIT5}	vp / vs_{KIT6}
< 17.5	1.62	1.63	1.62
17.5 – 29	1.68	1.59	1.61
>29	1.68	1.69	1.63

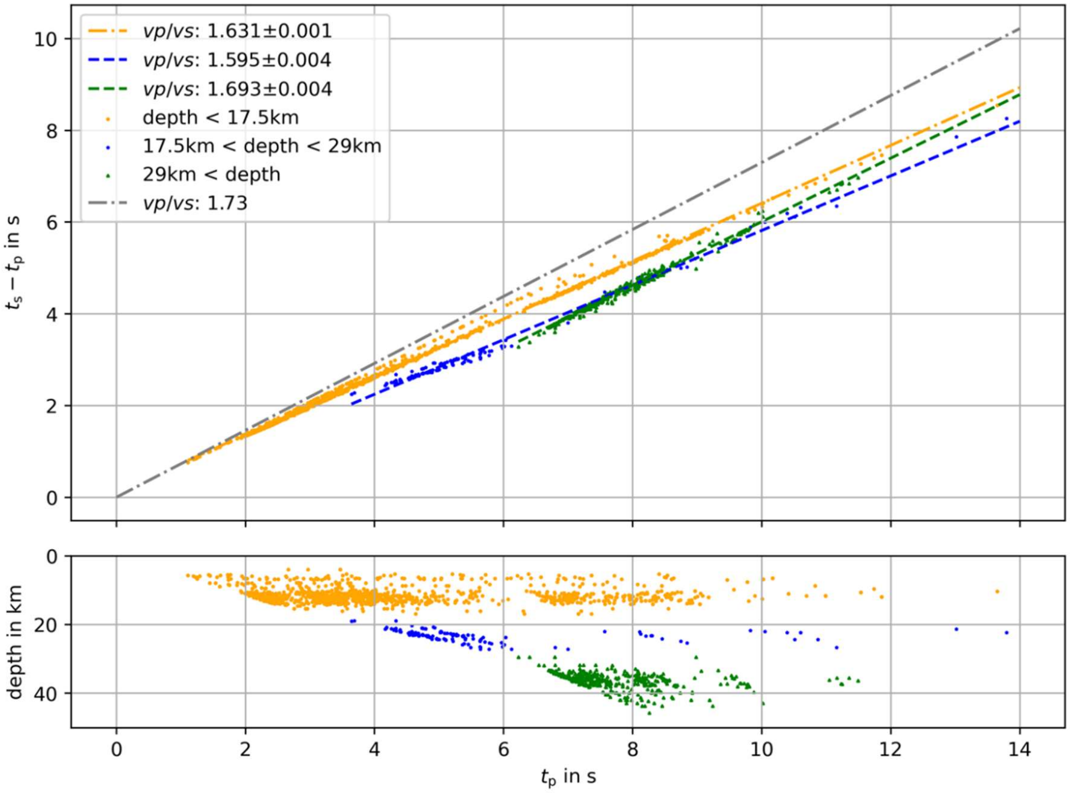

Fig. A5 Synthetic Wadati diagram for 1-D model KIT5 (Fig. A4 and Table A4) with fitted vp / vs values and their 1-σ uncertainties. Underneath the lower crust the structure is fixed for P-waves based on the model by Mechie et al. (1983), see Fig. A1 and Table A2. The vp / vs value of 1.73 is plotted as reference to a standard elastic body with a Poisson's ratio 0.5

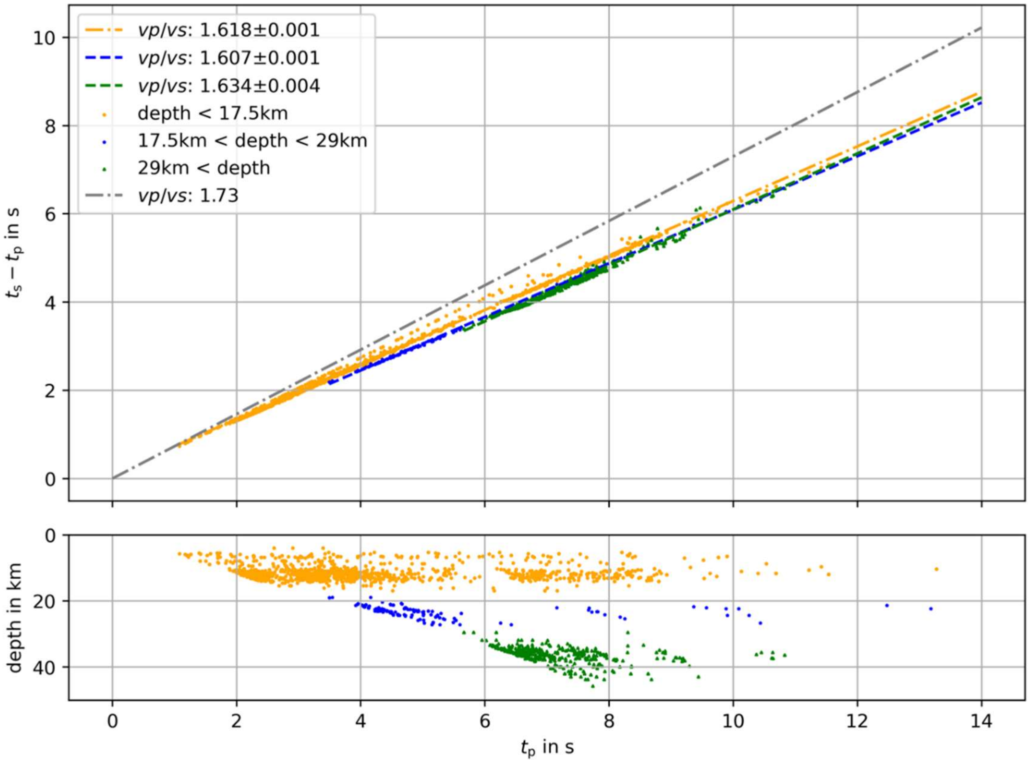

Fig. A6 Synthetic Wadati diagram for 1-D model KIT6 (Fig. 4.11) with fitted *vp / vs* values and their 1-σ uncertainties. Underneath the lower crust the structure is fixed for P-waves based on the model by Mechie et al. (1983), *vs* is determined by inversion. The *vp / vs* value of 1.73 is plotted as reference to a standard elastic body with a Poisson's ratio of 0.5

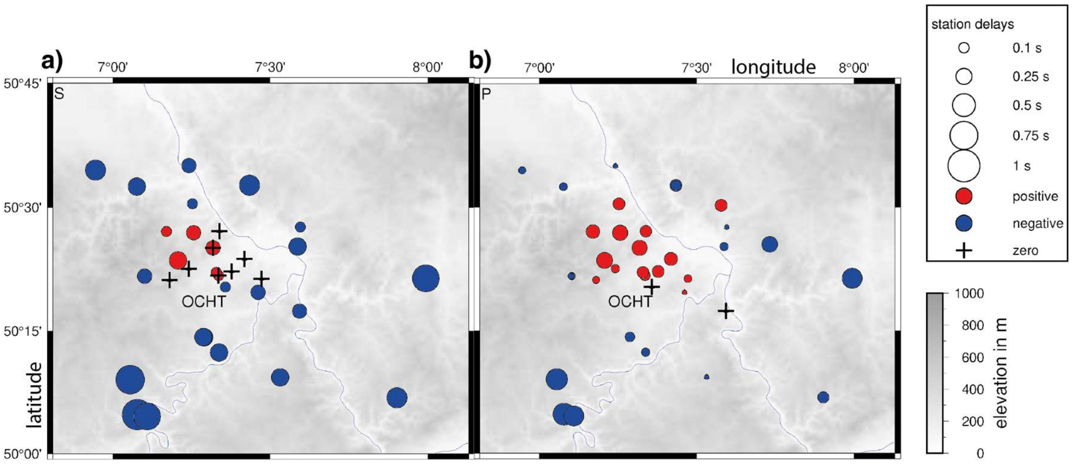

Fig. A7 Station delay times for 1-D model KIT5 (Fig. A4) and the DEEP-TEE network. a) S-waves, b) P-waves. Station OCHT is the reference station. The pattern of the stations-wise delay time distribution is very similar to the one of model KIT6 (Fig. 4.12). Note the positive delays which are concentrated in the East Eifel Volcanic Field. These may outline a zone of reduced seismic velocity due to elevated temperature or an increased fluid and volatile content related to the magmatic processes

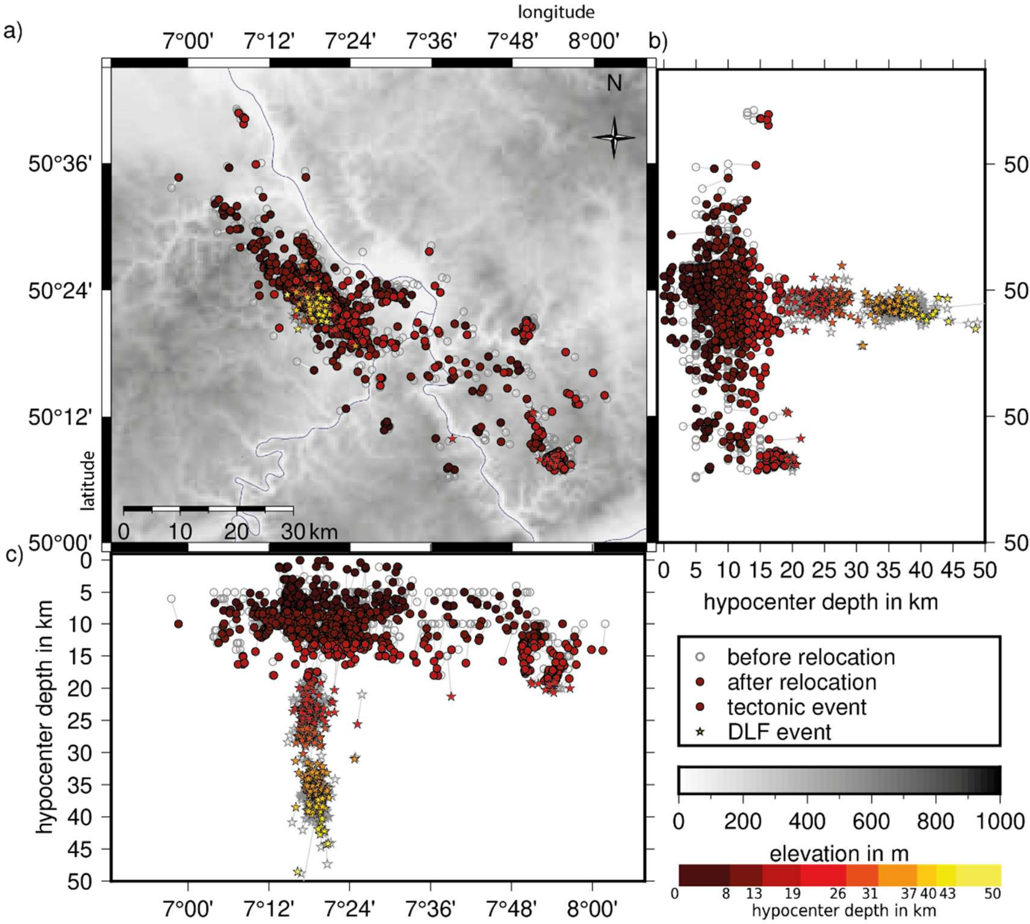

Fig. A8 Relocation result for the 1325 input events using the 1D *vp* and *vs* models KIT5 (Fig. A4) incl. station delay times from Fig. A7. The starting hypocentres (open symbols) are from the bulletins of the state seismological service and from own preliminary locations, especially for DLF events. Circles show tectonic events, stars indicate DLF events; colour indicates hypocentral depth with a colour scale adjusted to Hensch et al. (2019)

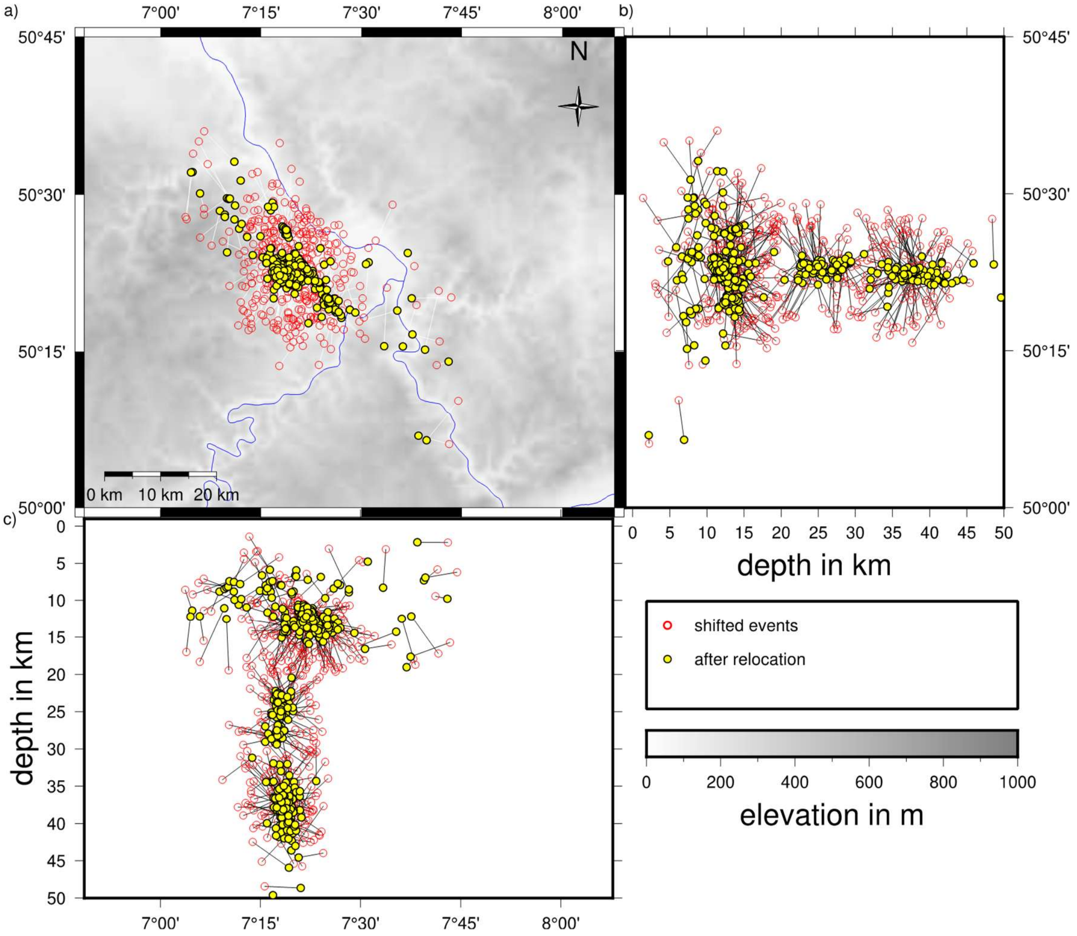

Fig. A9 Shift test with 382 randomly shifted hypocenters (perturbed start locations are given as red open circles) to check the stability of the location solution with 1-D velocity model KIT6. The randomly shifted events (red) are well relocated (yellow circles) what can be seen for example by the clear NW-SE alignment of the earthquakes along the Ochtendung Fault Zone, the narrow zone of the events below 20 km depth, and the small differences to the KIT6 solution in Figs. A11 and A12

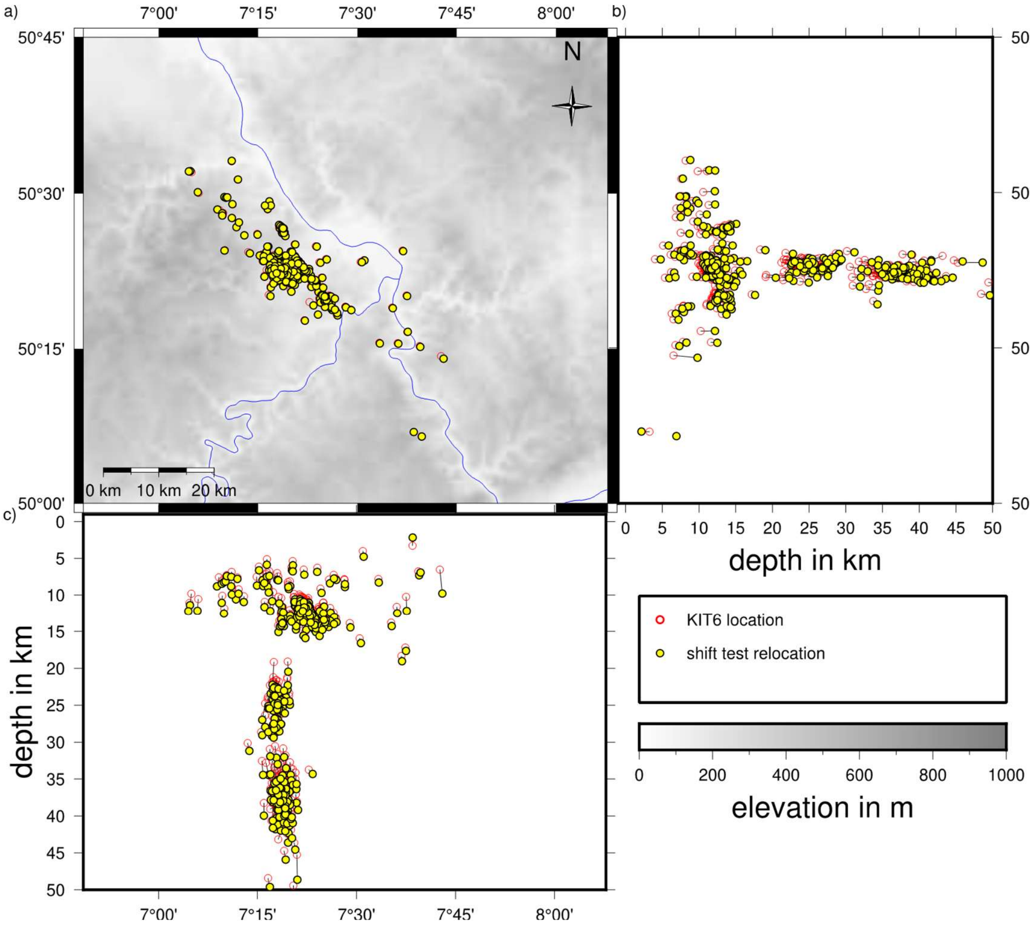

Fig. A10 Shift test with 382 randomly shifted hypocenters to check the stability of the location solution with the 1-D velocity model KIT6. The comparison of the final KIT6 hypocenters (red, see also Fig. 4.13) with the relocations of the shift test (yellow) indicate mostly lateral differences of less than 0.5 km and vertical differences of less than 2 km. These differences are also plotted in Fig. A11

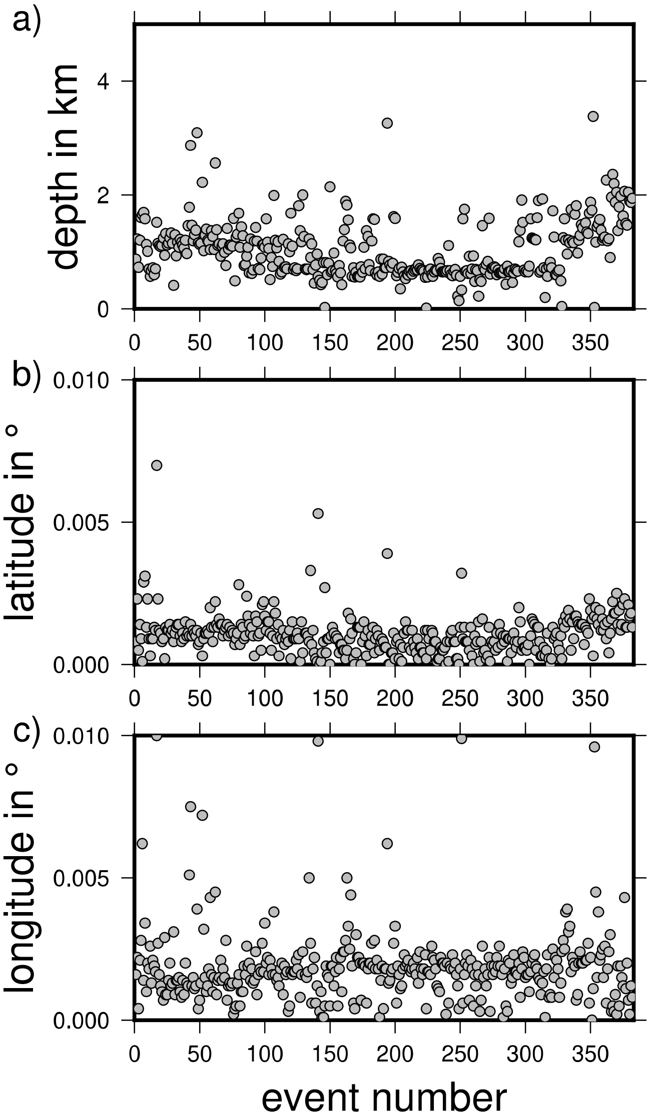

Fig. A11 Shift test result for 382 randomly shifted hypocenters (Fig. A10) to check the stability of the location solution with the 1-D velocity model KIT6. The plotted values are the differences in hypocenter locations between the well-located events based on velocity model KIT6 and the shift test result; a) depth, b) latitude, and c) longitude. The typical differences in distance are less than 2 km in depth and less than 500 m in latitude and longitude

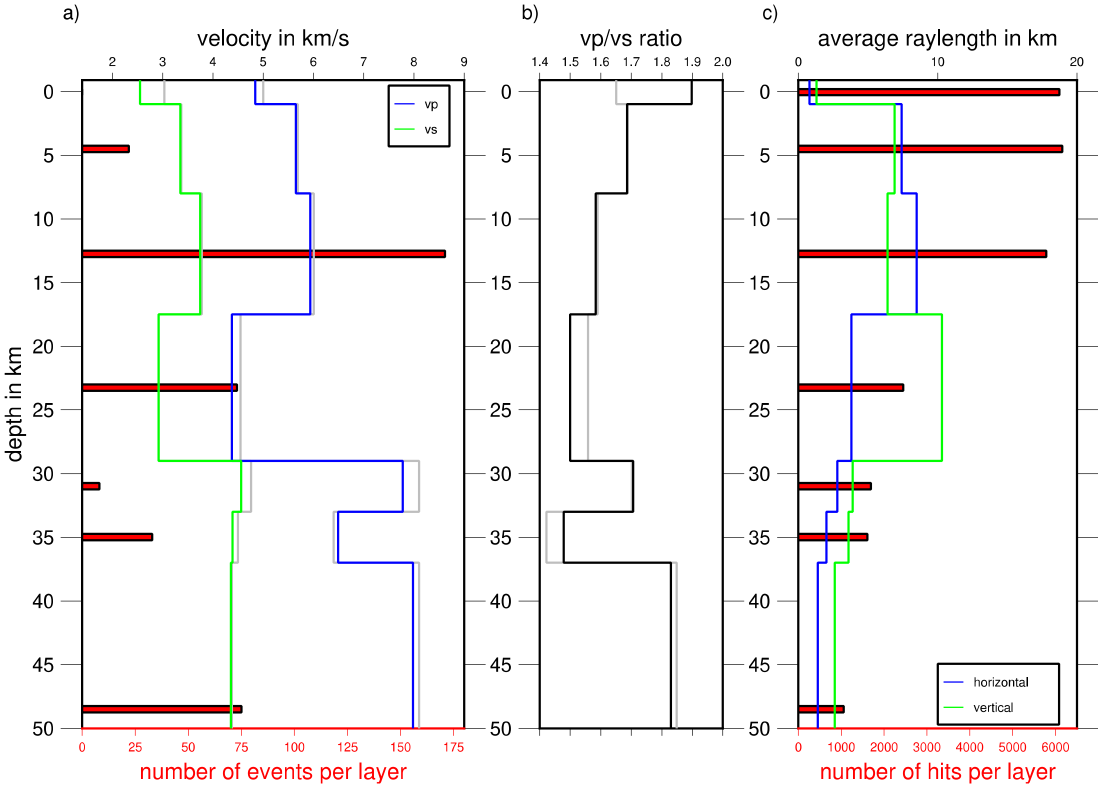

Fig. A12 Details for the model KIT6. a) *vp* (blue) and *vs* (green) from the shift test inversion as well as KIT6 (grey) together with the number of events, b) *vp / vs* for the shift test result (black) and KIT6 (grey), c) information on the number of seismic rays per layer

➔ Caption of the next page's figure

Fig. A13 Waveforms of a deep low-frequency event which is located in ca. 37 km depth. The event occurred on 30th June 2018 at 03:29 (UT, local time 05:29 a.m.). The blue and red marks indicate the onsets of the P-waves and S-waves, respectively. P-wave onsets are picked on the vertical component (a), S-wave onsets are picked preferentially on the transverse component (c). For comparison all pick marks are also shown on the other components. Note that the P-wave with its near-vertical incidence angle is only visible on the vertical component (a) whereas the S-wave and its long coda are visible on the vertical (a), radial (b), and transverse (c) components. The waveforms are filtered from 1.5-10 Hz and amplitudes are trace-normalised

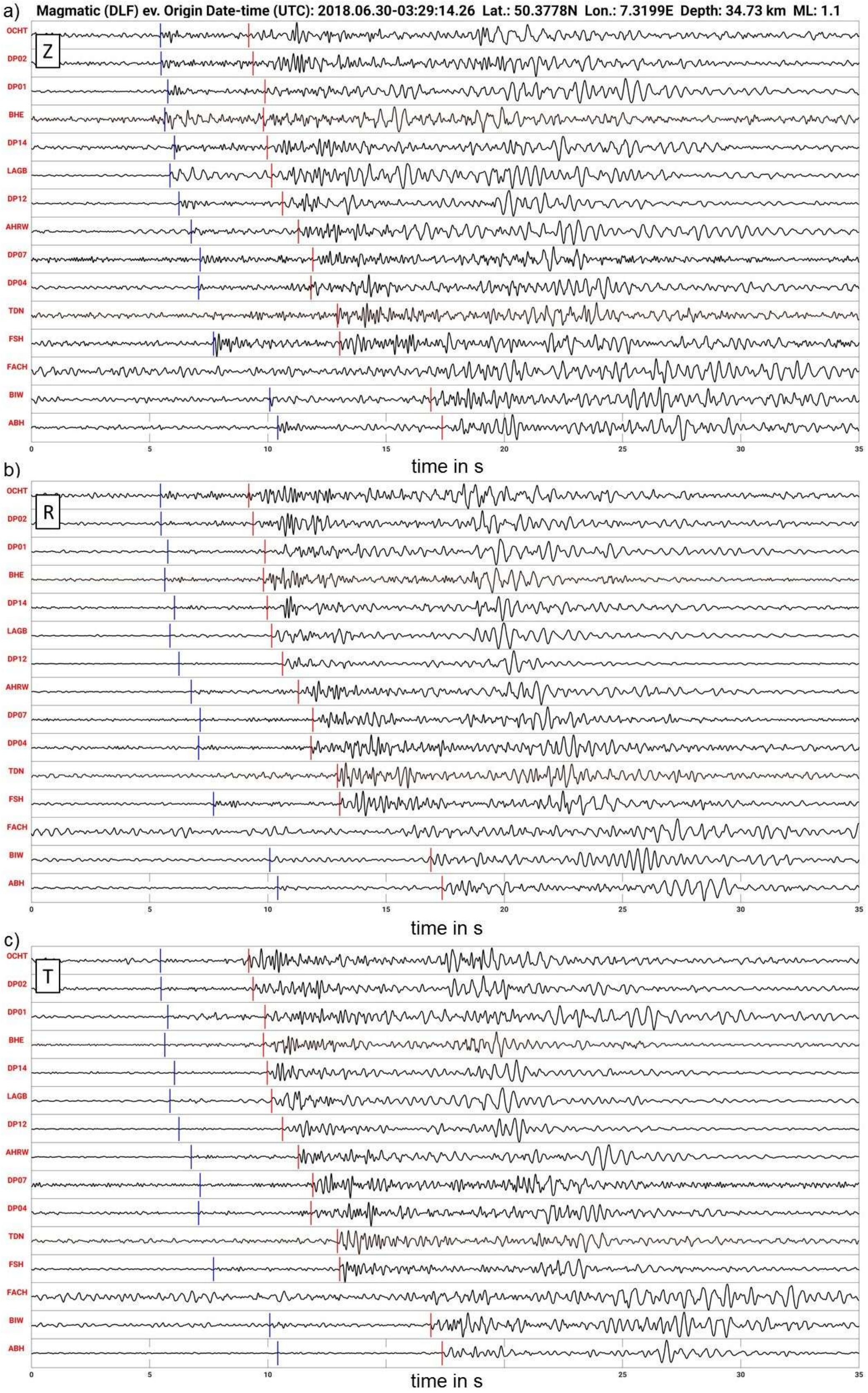
a)
Magmatic (DLF) ev. Origin Date-time (UTC): 2018.06.30-03:29:14.26 Lat.: 50.3778N Lon.: 7.3199E Depth: 34.73 km ML: 1.1
Z
OCHT
DP02
DP01
BHE
DP14
LAGB
DP12
AHRW
DP07
DP04
TDN
FSH
FACH
BIW
ABH
0
5
10
15
20
25
30
35
time in s
b)
R
OCHT
DP02
DP01
BHE
DP14
LAGB
DP12
AHRW
DP07
DP04
TDN
FSH
FACH
BIW
ABH
0
5
10
15
20
25
30
35
time in s
c)
T
OCHT
DP02
DP01
BHE
DP14
LAGB
DP12
AHRW
DP07
DP04
TDN
FSH
FACH
BIW
ABH
0
5
10
25
30
35
time in s

Table A8 Station correction (delay time) terms for P- and S-waves in seconds for 1-D model KIT5 (see also Fig. A7)

station code	P wave delay in s	S wave delay in s
AHRW	-0.06	-0.35
BEDO	-0.02	-0.16
BEUR	-0.47	-0.92
BHE	0.05	-0.07
DEP01	0.25	0.31
DEP02	0.10	0.00
DEP03	0.00	-0.29
DEP04	-0.44	-0.80
DEP05	0.05	-0.16
DEP06	-0.47	-0.48
DEP07	-0.02	-0.34
DEP08	-0.05	-0.35
DEP09	0.46	0.58
DEP10	-0.07	-0.34
DEP11	0.14	-0.38
DEP12	-0.14	-0.46
DEP13	-0.02	-0.22
DEP14	0.23	0.25
DEP15	0.14	0.04
DEP16	0.17	0.09
DEP17	0.10	0.17
DEP18	0.06	0.01
DEP19	0.00	-0.27
DEP20	0.00	0.28
DEP21	0.18	0.18
DEP22	0.00	0.13
DEP23	0.13	-0.13
DEP24	0.14	-0.02
DEP26	0.13	-0.12
FACH	-0.39	0.13
FSH	-0.39	-0.75
GLOK	-0.09	-0.77
KOGO	0.02	-0.45
LAGB	-0.04	-0.28
NAST	-0.04	-0.23
NICK	0.23	-0.40
OCHT	0.00	0.23
OMED	0.07	-0.17
PYRM	-0.09	-0.08
STB	0.01	-0.38
TDN	-0.05	-0.42
WBS	-0.16	-0.52

Table A9 Station correction (delay time) terms for P- and S-waves in seconds for 1-D model KIT6, see also Fig. 12

station code	P wave delay in s	S wave delay in s
AHRW	0.01	-0.15
BEDO	0.02	-0.03
BEUR	-0.35	-0.62
BHE	0.06	0.01
DEP01	0.26	0.38
DEP02	0.10	0.06
DEP03	0.00	0.11
DEP04	-0.34	-0.55
DEP05	0.08	-0.04
DEP06	-0.33	0.04
DEP07	0.05	-0.12
DEP08	-0.01	-0.24
DEP09	0.46	0.65
DEP10	-0.04	-0.22
DEP11	0.18	-0.22
DEP12	-0.09	-0.34
DEP13	0.05	-0.07
DEP14	0.24	0.32
DEP15	0.12	0.08
DEP16	0.17	0.11
DEP17	0.09	0.21
DEP18	0.07	0.08
DEP19	0.00	-0.13
DEP20	0.00	0.34
DEP21	0.21	0.22
DEP22	0.00	-0.06
DEP23	0.12	0.12
DEP24	0.17	0.04
DEP26	0.11	-0.01
FACH	-0.23	0.16
FSH	-0.28	-0.41
GLOK	-0.06	-0.49
KOGO	0.02	-0.33
LAGB	-0.01	-0.21
NAST	0.10	-0.12
NICK	0.22	-0.06
OCHT	0.00	0.27
OMED	0.06	-0.11
PYRM	-0.06	-0.03
STB	0.15	-0.27
TDN	0.06	-0.13
WBS	0.01	-0.13

Appendix A: for chapter four (the DEEP-TEE experiment)

Appendix B: for chapter five (Detector A6-DFMSD)

1 METHOD

The core idea of the detector approach is to find signals emitted from a certain seismic target zone. No a priori knowledge about the waveforms is required, however, narrow frequency bands can be used to tune the search algorithm This is important in volcanic areas where different kinds of seismic events occur: tectonic, magmatic, mono-frequent etc. events.
We define and determine the limits that separate the target part of the dataset from the rest. These limits are in six dimensions and they are determined by:
a) time,
b) space (two dimensions),
c) frequency (as “signal class”),
d) variation coefficient of recorded energy *, and
e) signal to noise power (as “sigClasPower”).
These parameters are described in the sub-sections below when they appear.

Users of A6-DFMSD first need to adjust the program’s control-file (Parameters) including the modeling and detection parameters (see Table B1 for a short description), then first execute the code part called "fromSingl2multi6obspyBased" and afterwards the part “multiPartMastStBackwardTimSel4". The role of the parameters for detection are explained step by step while explaining A6-DFMSD in its five major steps:

- Inputs
- Configuration of the Detection Model (CDM step)
- Detection Field preparation (DF preparation)
- Single Station Detection (SSD step)
- Multi Station Detection (MSD step).

An overview of these five steps is presented in Fig. B1 in a flow diagram. In the following, at first, we describe how a detection model is built in accordance with the control-file parameters, and how the model helps to find sets of station-based limits. Afterwards, we describe the application of the obtained limits through the detection by giving examples.

1.1 Inputs

In addition to the continuous three-components seismic velocity records, A6-DFMSD requires the following information to establish a detection model, accordingly:
- seismic stations codes and coordinates: stored as ”stInfo”,
- simple 1-D seismic P- and/or S-wave velocity models: stored as ”velS” and ”velP”, respectively, and
- a target zone expressed by a geographical center location stored as ”targCen”, a radius length stored as ”targRadi”, an upper depth limit stored as ”targDep1” and a lower depth limit stored as ”targDep2”. All lengths are in kilometers.
This information is given by the users in the control-file.
Before using the detector, the seismic records of each day of for each station should be converted into a Q-file format (https://www.seismic-handler.org/wiki/ShmDocMenuFileReadq) and saved

in the same folder of the codes of the detector with the specific naming format: XXXXyyyymmdd. For example, seismic data of the day February 1, 2023 of the station code LAGB must be saved by the name LAGB20230201 and the seismic data of the station ABH for the same day by the name ABH 20230201. Note - if the station code has less than four characters, this gap must be filled with blanks.

1.2 Configuration of the Detection Model (CDM step)

1.2.1 Building up the synthetic seismic source positions on the upper and lower surfaces of the target zone

According to the control-file values, the seismic target zone has a cylindric shape as geometry, defined by the parameters: ”targCen”, ”targRadi”, ”targDep1” and ”targDep2” (center, radius, upper depth boundary, lower depth boundary).

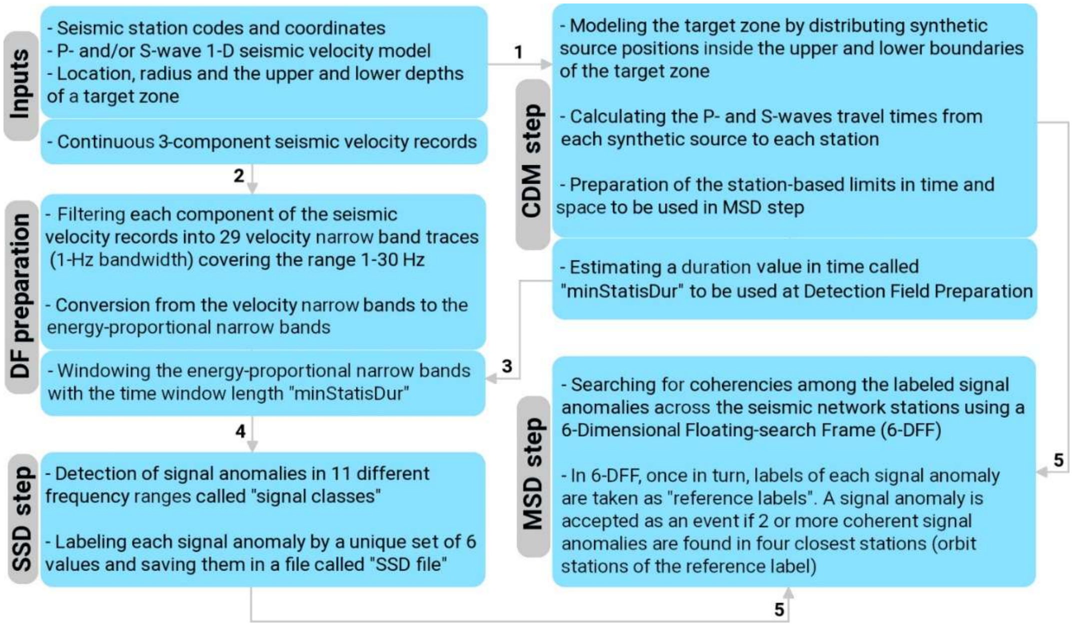

Fig. B1 Overview on the major steps of A6-DFMSD: Inputs, Configuration of the Detection Model (CDM step), Detection Field preparation (DF preparation), Single Station Detection (SSD step), and Multi-Station Detection (MSD step)

Then the program determines and sorts synthetic source positions on both, the upper and lower disk-shape surfaces of the target zone, by considering a uniform distance between the synthetic sources. The distance value is set in the control-file by the variable called ”minSor2SorDis”. In accordance with the test example of the program and its control-file values, Fig. B2a shows a top view of the sorted synthetic source positions for the case of the East Eifel Volcanic Field (EEVF), where the target zone has a radius of 25 km.

1.2.2 P- and S- phase travel-time calculation

The seismic velocity model of the seismic target zone (”velS” and ”velP”) and the stations coordinates of the seismic network (”stInfo”) plus applying Snell’s law, enable us to calculate the synthetic arrival times of the P phases (Tp) and the S phases (Ts) which are emitted from each synthetic source and recorded at each station. The results of this calculation are used in following steps.

1.2.3 Calculation of the typical minimum signal duration

Depending on the relative position of each pair of a synthetic source and a recording station, we calculate and assign a waveform duration to each pair. In this part, the program finds the typical half minimum signal duration, potentially recordable at the seismic network stations. For this calculation, the program considers only the synthetic sources located on the upper depth position of the target zone and traces the rays that emit from the synthetic sources to all the stations listed in stInfo. Afterwards, for all the pairs of sources and stations the $Ts - Tp$ values are calculated. The geometric-mean value minus the geometric standard deviation value of all the calculated $Ts - Tp$ values is saved in a variable called ”minStatisDur”. If we assume that the duration of an earthquake signal is at least twice longer than the time difference between its Ts and Tp, then the value, which is saved as minStatisDur, is a good approximation for representing the typical half minimum signal duration of the events that occurs on the upper depth position of the target zone and is potentially recorded by the seismic network stations. Below in section 1.3, the value of minStatisDur is used as a duration in time to window the record traces.

1.2.4 Calculation of the station-based relative phase-delay differences

The results of this part provide time limits specified for each station for several usages.

After this calculation, we know for example: how long before or/and after the detection of a phase x (can be a P-phase or a S-phase) at station A, another phase y (also can be a P-phase or a S-phase) should be expected at station B, if the source of both phases is the same source and located somewhere inside the seismic target zone. This is needed for the coincident detection of an event at several stations to minimize false detections due to locally emitted noise signals. Figs. B2b and c visually explain the role of this calculation for the detection and the phase-delay differences relative to station example DEP02 and also relative to station example ABH. The relative time differences are calculated and plotted, respectively.

For all the synthetic sources the following calculation is done: we take into account the Ts values at each station pair (for example stations A and B) and compare these with each other, assuming the Ts values are the S-phase travel times emitted from the same synthetic source position, recorded at stations A and B. If the Ts value at station B (BTs) is bigger than the Ts value at station A (ATs), we allocate the value of BTs to a MATLAB array called ”positivPhasDelayMax” and the value of $BTs - ATs$ to a MATLAB array called ”positivPhasDelayMin”. And, in addition, if the ATs value is bigger than the BTs value, we allocate the value of $ATs - BTp$ to a MATLAB array called ”negativPhasDelayMax” and the value of $ATs - BTs$ to a MATLAB array called ”negativPhasDelayMin”. Here, the ATp and BTp values are the P-phase travel time values emitted from the same synthetic source position and recorded at stations A and B, respectively. In the corresponding MATLAB codes arrays are built called ”positivPhasDelayMax”, ”positivPhasDelayMin”, ”positivPhasDelayMax”, and ”negativPhasDelayMin”.In the MATLAB arrays, the row, column, and slice indeces represent station A, station B and source number I, respectively.

Considering all the stations listed in the stInfo in the control-file, such kind of calculation is done for all possible pairs of stations and synthetic sources, and the results are stored in the same arrays with unique indeces as described. To find the maximum possible positive-phase-delay between each unique pair of stations, we determine the maximum value of the slices elements in the array ”positivPhasDelayMax” and build up a new array called ”maxPositivPhasDelayMax”. This array in its slice has only one value connected to each pair station. The rows and columns of the new MATLAB array have the same index configuration as the root array ”positivPhasDelayMax”. The same is done with the row, column and slice elements of the ”negativPhasDelayMax” and the results are saved in the array ”maxNegativPhasDelayMax”. On the other hand, to find the lower limits in the positive delays connected to each pair of station, we find the minimum value of the slice elements of the array ”positivPhasDelayMin” and build up a new array called ”minPositivPhasDelayMin”. This array in its slice has only one value connected to each pair of stations. The rows and columns of the new array have the same index configuration as the root array ”positivPhasDelayMin”. The same is done with the row, column and slice elements of the ”negativPhasDelayMin” and the results are saved in the array ”minNegativPhasDelayMin”.

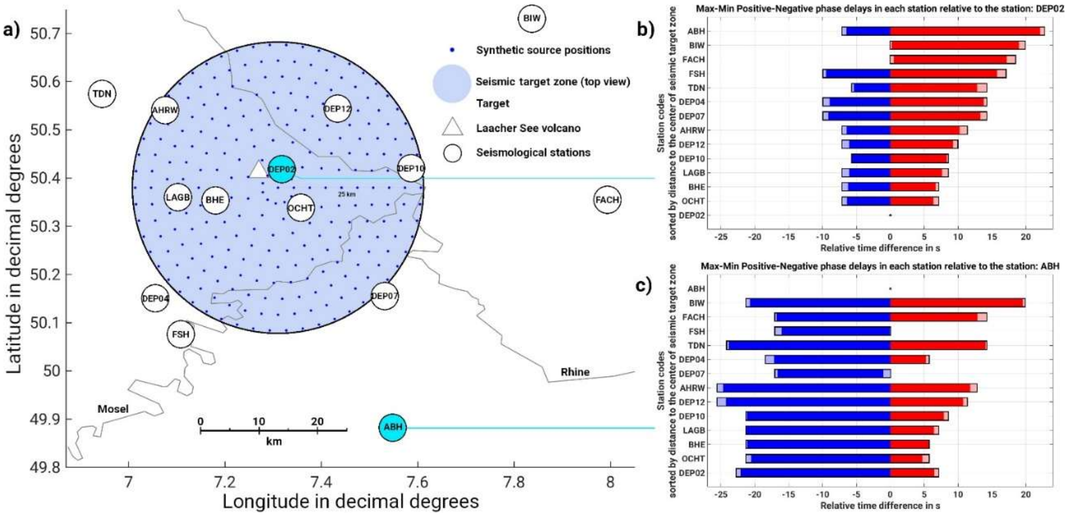

Fig. B2 Configuration of a detection model (at CDM step) in association with the test example in the EEVF. a) seismological station locations plus the top view of the seismic target zone considered in this study. In the CDM step each small blue dot is considered as a potential seismic source and the travel times for the first P- and S- phase arrivals are calculated for each source-station pair based on the input 1D seismic velocity model. b) subset of calculations in the CDM step to find the station-wise detection limits in the time domain. It is indicated how long before (in light blue) and/or after (in light red) the detection of a seismic phase at station DEP02 the routine searches for coherent seismic signals in the records of the other stations. c) the same b), but here the time differences are obtained relative to the recording station ABH. Note: in b) and c) the dark blue and dark red denote the exact time limits, and the light blue and light red indicate the time limits after involving time windowing (discretization) into the detection model

1.2.5 Calculation of the station-based typical negative phase delay for the local search

Results of this part are used in the MSD step section 1.5.4, where the program builds up a Global (net-wide) Detection list (GD-list) out of the Local Detection list (LD-list). The LD-list is indeed the result of the detection through the local coherency search and is built by writing information (date, time and signal class) of each detected event on separated lines in a text list. For building up the GD-list out of the LD-list (which is a kind of time clustering task), we need to know the maximum acceptable time difference between the declared events in the LD-list for clustering. The maximum acceptable time differences for clustering of the events in the LD-list should be obtained in a way that if, for example, for one event several detections are assigned in the LD-list, finally only one event is written in the GD-list. Also, this maximum acceptable time difference should be determined in a way that none of the events, which possibly occur inside the target zone, is omitted during clustering process.

To execute the above points, we do the following calculations: for each recording station X which contributes in the MSD step (section 1.5), first, we identify the four nearest stations to station X which are called the ”orbit stations” (see Fig. B3). Suppose these four nearest stations to the station X are Y1, Y2, Y3, and Y4 (we call them Yi). Then for each Yi, we calculate the mean plus the standard deviation value of the slice elements (which are relative phase-arrival time-differences between each station pair as explained above) in ”negativPhasDelayMax” which correspond to the station X and stations Yi. The resulting value is allocated to a new array called ”meanStdNegativPhasDelayMax”, in which the row index points to station X and the column index to station Yi . When the calculation is finished for all stations Yi, we find the mean and its standard value of the elements in the array ”meanStdNegativPhasDelayMax”, in which the row points to the station X and the columns to the stations Yi. The result is stored in a one dimensional matrix called ”netDelay”, whose row index relates to station X. By applying the same operation to all stations, which contribute in MSD step, netDelay takes the values that specifically belong to each station.

1.3 Detection Field Preparation (DF preparation)

As shown in the examples in Fig. B4a, b, c, and d, for each station, each seismogram component is at first decomposed into 29 1-Hz wide (narrow-) bands. Before filtering, seismograms are demeaned and detrend and after filtering one minute of the beginning and one minute of the end of the records are cut to remove the filtering artifacts. The upper and lower corner frequencies in Hz are listed in control-file as ”monoBanList” and the order of tapering which we use is 3 in the frequency domain using the MATLAB signal processing toolbox. They cover the frequency range between 1 Hz and 30 Hz. Then correspondingly for each record sample i of each narrow-band j, a conversion proportional to the kinetic energy (called energy-proportional or E^*) is obtained (Fig. B3e) according to the following equation:

$$E^*_{j,i} = Z^2_{j,i} + N^2_{j,i} + E^2_{j,i} \tag{1}$$

where *Z*, *N* and *E* are the seismic velocity records for each component in e.g., m/s. Afterwards, the energy-proportional narrow bands (E^*_j) are windowed (Fig. B4f) by the window length of minStatisDur.

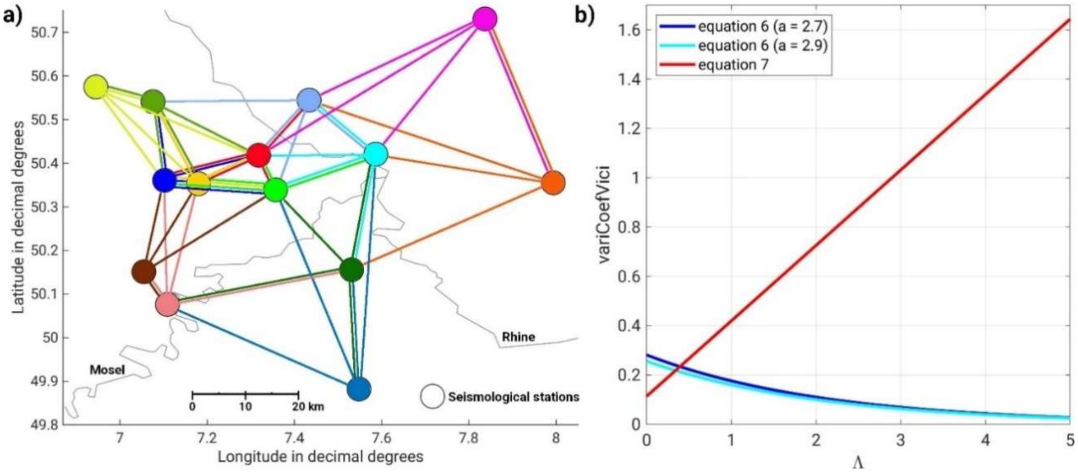

Fig. B3 a) Locations of recording stations and their relation with each other while searching and connecting coherent signals in the Multi-Station Detection step (MSD step). For each station, the search is limited to a radial distance in which only the four closest stations are involved. Here, each station is plotted with a specific color and the corresponding four nearest stations are linked by a line with the same color as the station, b) in MSD step, coherency search vicinities for the variation coefficient of DFs are obtained using empirical equations (6) and (7). Here this relationship is depicted in blue (dark and light) for equation (6), and in red for equation (7). The dark blue line shows this relationship when the goal is to search for tectonic and volcano-tectonic events (signal classes higher than 3) in the shallower zone (3-30 km depth), and the light blue line shows this relationship for possible tectonic and volcano-tectonic events in the deeper zone (30-50 km depth). The red line shows this relationship when searching for LF events (signal classes less than 4) in both seismic target zones

Windowing of the E^*_j traces is done when the mean value of the samples in each window is written in a new array called DFj (Detection Field of the band j). By this means, we efficiently mask/smooth traces to prevent redundant time-consuming operations in the next steps. Note: the number and width of the frequency bands may be chosen differently for other applications, e.g., for very low frequency events with f << 1 Hz.

1.4 Single Station Detection (SSD step)

During the SSD step, signal anomalies are detected and labeled with a unique set of six values which represent the properties of the signal anomalies.

1.4.1 Signal Anomaly Detection and Labeling

The tasks of the detection program in this part are:

- picking the signal anomalies in the detection field (DF) of each individual station,
- labeling their features, and
- saving the featues in a list.

Signal anomalies are independently detected in different frequency ranges called signal classes. In our example 11 signal classes are chosen (Fig. B4f). Each signal class is defined by two values denoting the upper and lower corner frequency of the signal class in Hz. For each signal class a Short Time Average (STA) amplitude to Long Time Average (LTA) amplitude ratio is determined with all DFs, which are within the upper and lower corner frequencies of the signal class. This leads to the detection criterion. A signal anomaly is detected, if all DFs within a signal class reach to the sample that has amplitude values higher than the mean value of the three previous sample amplitudes plus a multiplication of 0.7 (an empirical constant) to their mean absolute deviation. As an example, in Fig. B4g, a signal anomaly detection in signal class $n = 6$ is presented. The signal class $n = 6$ includes the DFs that are indexed from 8 to 16. In the example, the red dot (at sample i) is found as a signal anomaly, because at all DFs the amplitude values at sample i have a higher value than the mean plus a multiplication with 0.7 to the mean absolute deviation of the reference samples (shown as three green dots right before the sample i in the DFs). For each signal anomaly, which is detected in a signal class, a unique set of 6 values are saved as labels of the signal anomaly in a file called ”SSD file”. These six values are:

- the station code (implicitly, the latitude and longitude of the station location),
- the sample number of the detection point (i) representing the detection time,
- the signal class (n) which is defined by the upper border (j_2) and the lower border (j_1), and
- a value called ”variation coefficient of DFs (Λ)” which is obtained by equation (2) and represents the energy* distribution status at the point of detection in the corresponding signal class. The value of Λ is indeed the standard deviation of the DF amplitudes located in the signal class n at the sample of detection i divided by the mean value of the DF amplitudes (μ) located at the same signal class n and at the same sample of detection i. The term $\mu_{n,i}$ used in equation (2) is obtained by equation (3).

$$\Lambda_{n,i} = \frac{\sqrt{\frac{1}{j_2 - j_1 + 1}\sum_{j=j_1}^{j_2}(DF_{j,i} - \mu_{n,i})^2}}{\mu_{n,i}} \tag{2}$$

$$\mu_{n,i} = \frac{1}{j_2 - j_1 + 1}\sum_{j=j_1}^{j_2} DF_{j,i} \tag{3}$$

- a value called ”sigClasPower (Γ)” which is obtained by equation (4) and represents the amplitude level of energy* in the signal class at the detection point sample relative to the 3 previous samples just before the detection point sample (Fig. B4g). This value is equal to the result of the following division operation: the numerator is the mean value of the DF amplitudes of the signal class n at the detection point i ($\mu_{n,i}$) minus the mean value of the DF amplitudes located three samples right before the samples at the detection point (in Fig. B4h, this is equal to the length of the red line). The denominator is the mean absolute deviation of the mean values of the DF amplitudes for the three samples right before the sample at the detection point (in Fig. B4h, this is equal to the length of the blue line). The term $M_{n,i}$, which is used in the equation (4), is obtained by equation (5) and it is equal to the mean value of the mean value of the DF amplitudes three samples right before the sample of detection i in the signal class n.

$$\Gamma_{n,i} = \frac{\mu_{n,i} - M_{n,i}}{\frac{1}{3}\sum_{i=i-3}^{i-1}\mu_{n,i} - M_{n,i}} \tag{4}$$

$$M_{n,i} = \frac{1}{3}\sum_{i=i-3}^{i-1} \mu_{n,i} \tag{5}$$

When the single station detection for one station is finished, the results are stored in a file with a unique name including the date and station code called SSD-file. Then it continues to find signals at the remaining stations listed in stInfo.

1.5 Multi Station Detection (MSD step)

During the MSD step the saved SSD-files of all the stations are loaded and the coherent signals are searched by applying a 6-Dimensional Floating-search Frame (6-DFF). To increase the reliability of the final detection list, before doing a global (net-wide) search, the program follows two strategies simultaneously:

1- In the 6-DFF, the search for coherent signals is limited within a certain radial distance (called local search distance) in which only the four closest stations relative to each station are involved in the search (see Fig. B3a). This radius differs from station to station depending on the network configuration and it is adjusted dynamically according to the location of each station in the seismic network. This strategy avoids the identification of coincident non-relevant signals (noise etc.) by the detection procedure. For example, the signals detected at the stations located at the two opposite edges of the network can be connected to each other, only if coherent signals at the stations, which are geographically located in between these two stations, were detected, too. This procedure make use of the wave propagation properties of direct seismic waves that waves arrive earlier at the stations closer to the source than at the more distant stations.

2- Local searches are done in two steps. During the first step, only those stations are involved that are characterized by a relatively low level of noise. The output of this step provides a list of events that is called ”confident list”. During the second step, the stations with a moderate level of noise are added in 6-DFF. In this step, the 6-DFF uses the time search limits only around the time points listed as events in the confident list. We explain more details about the station categorization regarding the level of noise, and the mechanism of the search in the following sections.

➔ Next page: **Fig. B4** Examples for Detection Field preparation and Single Station Detection (SSD step). a) three-component band-pass filtered (1-30 Hz) ground motion velocity of a microearthquake recorded at station AHRW, b), c), and d) decomposition of each component Z, N, and E by filtering with 29 1-Hz width frequency bands, e) conversion of the ground motion velocity in each frequency band into energy-proportional narrow bands (E^*) following equation (1), f) the traces from e) are windowed using the window length of ”minStatisDur” to prepare the Detection Fields (DFs) g) the detection status of a signal anomaly at the sample i in signal class *n* = 6 is shown; the red dot (sample i) is found as a signal anomaly because at all DFs located in signal class 6 the amplitude values at sample i have a higher value than the mean plus a multiplication with 0.7 to the mean absolute deviation of the reference samples (shown as three green dots right before the sample i in the DFs). The bold line is the stack of the DFs located in this signal class (DFs from DF_8 to DF_{16}), h) close-up view of the stacked trace in g). The stored value of $\Gamma_{6,i}$ for the signal anomaly at sample i in signal class *n* = 6 is equal to the ratio of the length of the red line to the blue line. The technique used for detecting signal anomalies (g and h) is similar to the STA/LTA method with a very sharp criterium (here we suppose that the window length in the LTA part is only 3 times longer than in the STA part)

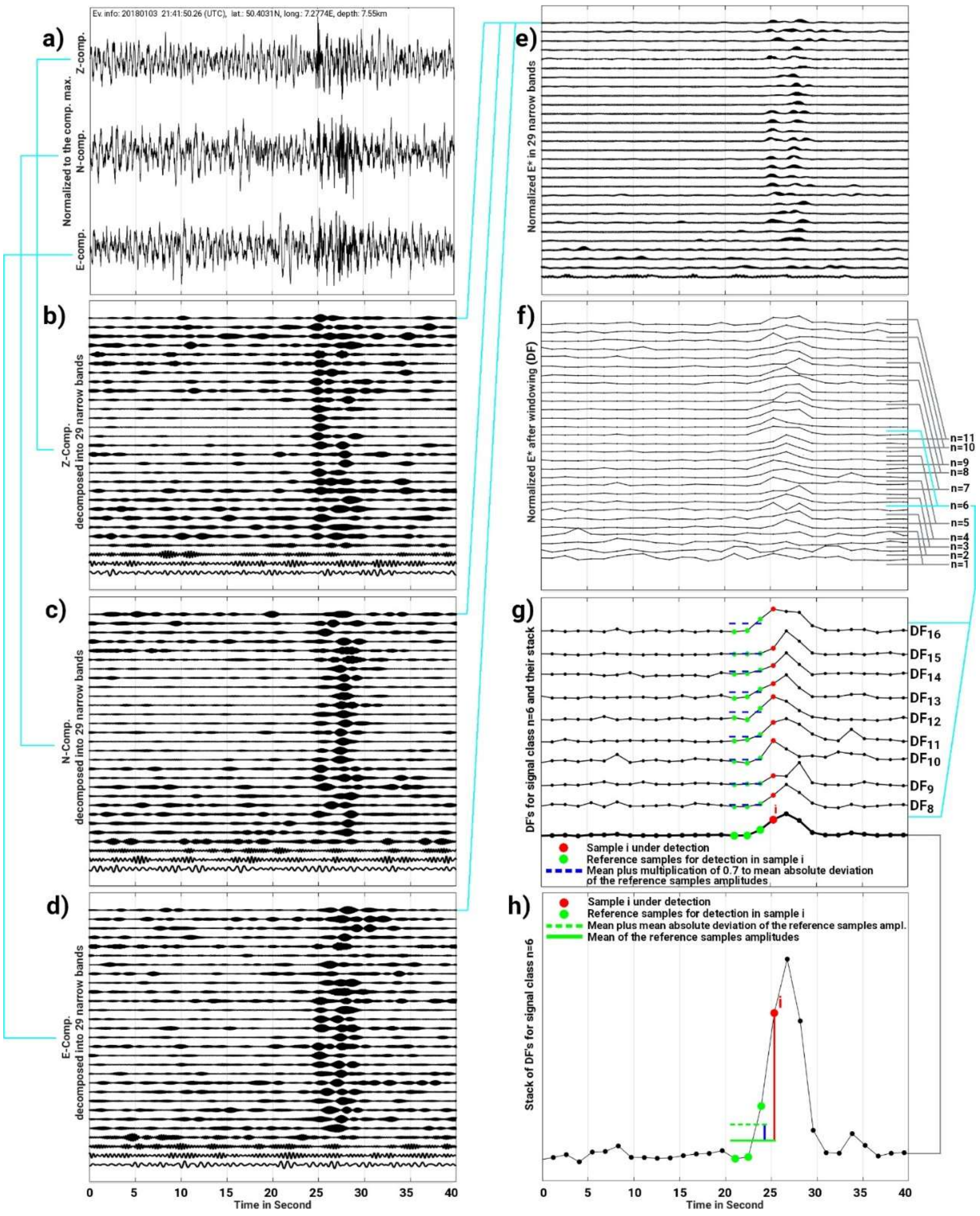

1.5.1 Station categorization

Before applying 6-DFF on the saved labeled signal anomalies, based on the number of detected signal anomalies in SSD-files, the program categorizes stations into three categories: removSt (removed stations), mastSt (master stations) and seconSt (secondary stations).

removSt are the stations whose number of detected signal anomalies in their SSD-files exceeds from a certain predefined level (this level is written at the control-file as ”maxEvPerDay” and we set it to 600 which means the maximum acceptable number of events per day for the records of each station is 600). The sites of these stations are very noisy or there are possible instrument failures (e.g.s the recording instruments generate pulses that make the records useless). As a part of data quality control, the program does not involve SSD-file of these stations into the search process.

mastSt are the stations located at the sites experiencing a relatively low level of transient noise. SSD-files of these stations have a relatively low number of signal anomalies. The confident list of events is generated using only these stations during the first step of the local search. Optionally, users of the program can force the detector to keep specific stations in the list of mastSt by adding their codes in the parameter called ”morImpoSt” in the control-file. This option is useful, if the location of a station (e.g. being close to the known active seismic sources) is more important than any possibly bad effect due to an increased noise level of the station.

seconSt are the stations with a moderate transient noise level. The information saved in the SSD-file of these stations are used only during the second step of the local search. Optionally, users of the program can force the detector to keep specific stations in the list of seconSt by adding their codes in the parameter called ”lesImpoSt”in the control-file. This option is useful when users want to reduce the influence of some stations to contribute in the detection process, due to a priori knowledge regarding, e.g., the noise conditions at those stations.

The separation of mastSt and seconSt is determined by using a simple statistical approach regarding the number of detected signals in all SSD-files. After loading all the saved SSD-files, the program sorts the stations according to the number of signal anomalies in the SSD-files of each station. Then it selects the stations whose number of signal anomalies is between the top 70% and 90% number of signal anomalies. Afterwards, it considers the rate of change in the number of detected signal anomalies among the selected stations. It finds the point where a relatively clear change of numbers of signal anomalies happens. The stations with a higher number of detected signal anomalies than the point of clear change are listed as the seconSt and the stations with a lower number are listed as mastSt.

1.5.2 The first step of the Local Search (LS-1)

The SSD-file of each station is a matrix with six columns, containing the detection information for each signal anomaly such as the time sample, the latitude and longitude of the station, the signal class, the variation coefficient of DFs in the signal class and the signal class power (as described in SSD step). In this part, the program focuses only on SSD-files of the mastSt to provide the confident list of events. For each mastSt, each row (line) of the corresponding SSD matrix can be listed as an event, if at least one of the four nearest mastSt in the vicinity also has a line in its SSD-file that satisfies the specific conditions of the 6-DFF. For example, suppose the mastSt are stations A, B, C, D, and E. Consider the program takes the first line of SSD-file of the station A as reference label. It searches in the lines of the SSD-file of the station B to find which of the following conditions are satisfied:

1- station B should be a member of the four nearest mastSt to station A

2a- time sample in station B <= time sample in station A + maxPositivPhasDelayMax(A,B)

2b- time sample in station A - maxNegativPhasDelayMax(A,B) <= time sample in station B

3- signal class in station A = signal class in station B

4a- variation coefficient of DFs in station B <= variation coefficient of DFs in station A + variCoefVici

4b- variation coefficient of DFs in station A – variCoefVici <= variation coefficient of DFs in station B

5- signal class power in both stations A and B >= sigClas2NoisTher

Here ”sigClas2NoisTher” takes its value from the control-file as the predefined minimum limit. The sigClas2NoisTher enables the program to eliminate the weak signal anomalies for which their relative amplitudes are less than a certain limit. Those signal anomalies are prevented from being involved into the detection.

If all the above five conditions logically become true, the program adds one to a counter variable, then it continues the search with station C (later, D and E) by applying the same procedure. If the counter has a value of 2 or more after searching with stations C, D, and E, the program writes the first line of SSD-file of station A into a new matrix called ”confEvList” as a confident list of events. This process is done for all the lines at SSD-file of stations A, B, C, D, and E. After building up the new array of ”confEvList”, the program continues with the second step of the local search.

The value of variCoefVici in the above conditions is determined by empirical equations (6) and (7).

$$\text{variCoefVici} = 1.6^{-(\Lambda+a)} \tag{6}$$

a is a constant which can take a minimum value of 2.7. Following our trial error tests concerning the ratio of false detections to total number of detections, we found values 2.7 and 2.9 are suitable choices for *a* when the upper border of the target zones is set to 3 km depth and 30 km depth, respectively. Fig. B3b shows the relationship between variCoefVici and Λ while detecting events in different signal classes in different defined seismic target zones in our test example. In the control file of detector, the constant variable *a* is renamed to “*variCoefViciEffectFactor”* for having clearer code. Note *a* may change for other application and possibly should be testedas outlined above.

Note: In the main manuscript on the detector variCoefVici is called b for simplicity.

$$\text{variCoefVici} = 0.306 \times \Lambda + 0.113 \tag{7}$$

In equation (6), the coherency search gets a wider border when Λ at the reference label has smaller values. In contrast, in equation (7) the coherency search gets a wider border when Λ at the reference label has bigger values. The borders determined by equation (6) are suitable for the detection of the signals which show less fluctuations in the amplitude of their frequency spectra around their dominant frequencies, like tectonic type events. In contrast, the borders determined by equation (7) are suitable for the detection of signals which show large fluctuations in the amplitude of their frequency spectra around their dominant frequencies. This occurs for example for LF type seismic events and their signals.

Figs. B5 and B6 respectively present the effect of equations (6) and (7) on the determination of *variCoefVici*. In Figs. B5a and S6a normalized spectral amplitudes are presented from typical tectonic and LF microearthquakes in the EEVF, respectively. In A6-DFMSD, the spectral amplitude of the events represents DFs of the events, especially when the spectrum is windowed with the window length of 1 Hz.

In Figs. B5 and S6, the borders of 11 frequency classes are highlighted by coloured dashed lines in which each colour indicates borders of a signal class. In Figs. B5b and S6b the value of Λ for each signal class is plotted. Correspondingly, the value of *variCoefVici* for each signal class in connection with Λ is plotted in Figs. B5c and S6c. In Figs. B5b and B6b maximum and minimum values of Λ are marked. As it is shown in Fig. B5a, where the spectral amplitude experiences the most fluctuation (at signal class 1) the smallest value is selected for *variCoefVici* (Fig. B5c) to reduce the sensitivity of the coherency search in this signal class. In contrast, where the spectral amplitude experiences the least fluctuations (at signal class 6) the largest value is selected for *variCoefVici* (Fig. B5c) to increase the sensitivity of the coherency search in this signal class. In Fig. B6a, where the spectral amplitude experiences the most fluctuation (at signal class 3) the largest value is selected for *variCoefVici* (Fig. B6c) to increase the sensitivity of the coherency search in this signal class. In contrast, where the spectral amplitude experiences the least fluctuations (at signal class 7) the smallest value is selected for *variCoefVici* (Fig. B6c) to reduce the sensitivity of the coherency search in this signal class.

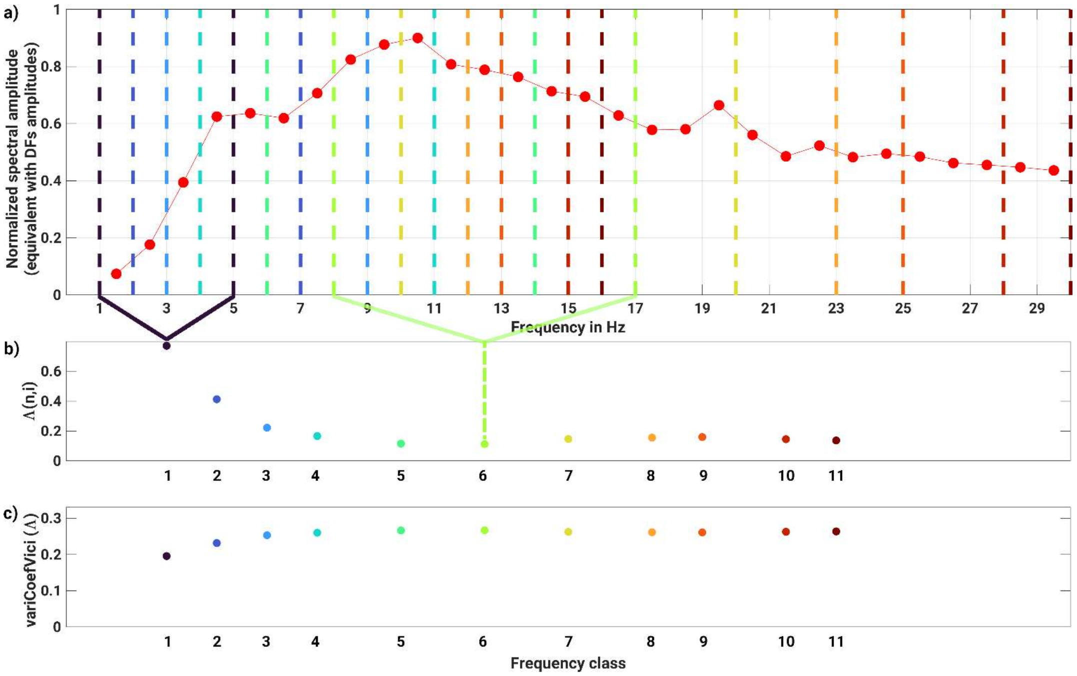

Fig. B5 Effect of equation (6) on the determination of *variCoefVici*. a) normalized spectral amplitude of a typical tectonic microearthquake in EEVF and borders of defined signal classes. Borders of signal classes are marked by coloured dashed lines. Each colour represents one signal class. b) value of Λ obtained for each signal class is plotted. c) *variCoefVici* obtained for each signal class in connection with corresponding Λ is plotted. Signal classes having max. and min. values of Λ are selected and marked to demonstrate extreme effects of using equation (6)

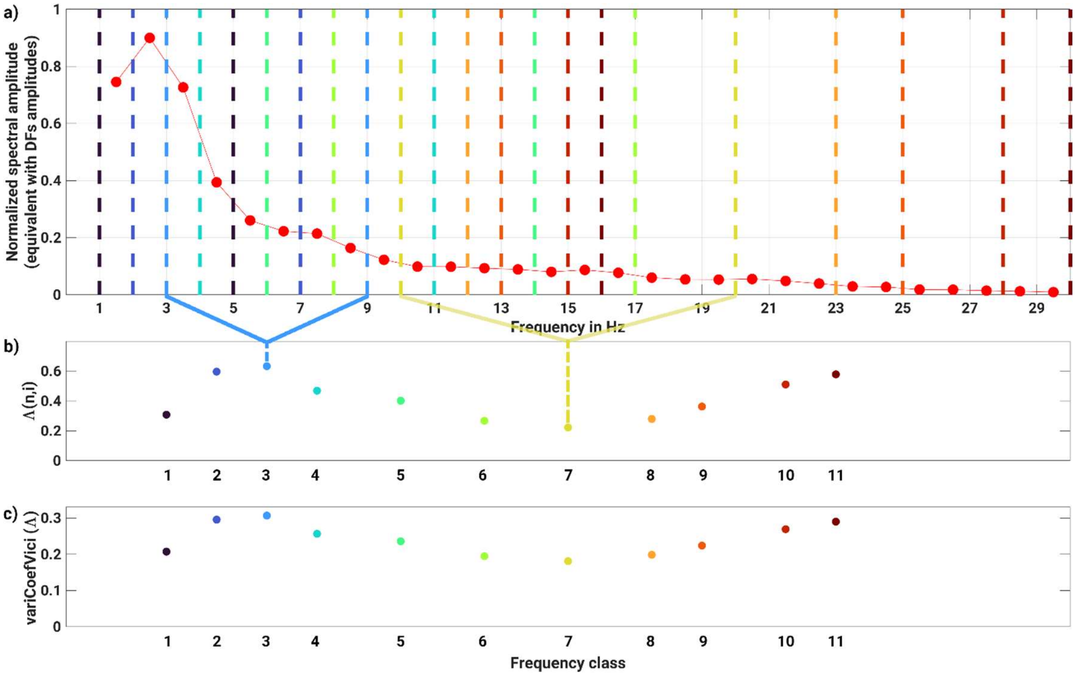

Fig. B6 Effect of equation (7) on determination of *variCoefVici*. a) normalized spectral amplitude of typical LF microearthquake in EEVF and borders of defined signal classes. Borders of signal classes are marked by colourful dash lines. Each colour represents one signal class. b) value of *Λ* obtained for each signal class is plotted. c) *variCoefVici* obtained for each signal class in connection with corresponding *Λ* is plotted. Signal classes having max. and min. values of *Λ* are selected and marked to demonstrate extreme effects of using equation 7

1.5.3 The second step of the Local Search (LS-2)

After LS-1, the program takes each line of the confident list as a reference line and search in the SSD-files of the secondSts for any coherent signal anomaly. It uses the same conditions through a local search on the SSD-files like the ones which were used in the LS-1, but this time it involves both categories of stations including mastSt and secondSt (not only the mastSt) and it declares a detected event, if the counter variable exceeds a value of 2.

This selection process can be regulated by the parameters: ”minLocSearCohStNum” and “maxLocSearStNum“ in the control-file. By this means, all the secondary stations, which have recorded signals of events (e.g., not disturbed due to high noise), get a chance to be involved in the detection. At the end of this step, the local-search-detection-list (LSD-list) is prepared. There, for each detected event, station codes of all the involved stations in event declaration, either mastSt or secondSt, are written next to the event date and time point, and event signal class.

1.5.4 Global (net-wide) Search (GS)

Each line of the LSD-list includes date, time, signal class, and the station codes of the stations that have contributed to the detection of the event. The task of this part of the program is time clustering of the events from the LSD-list to build up a global detection list. To describe how the program works, we explain this by an example: consider the first two lines of a LSD-list. We need to know, whether the event at the second line is connected to the first line or not. If the sources of the events given in both lines are the same and located in the seismic target zone, the time difference between the declared events would never exceed a certain limit of time. This time limit can be estimated by referring to the netDelay elements which have already been provided in section 1.2.5. If, for example, stations A, B, and C are the stations in the second line of the LSD-list, we correspondingly find the elements in netDelay which are pointed by the stations A, B, and C. Regarding the seismic target zone, the maximum value of those elements is estimated to be the maximum acceptable time difference between the second and the first line of the LSD-list. If the time difference between the first and the second line is less than the estimated value, the program accepts both lines as one event and writes the following information into a line in a new list called ”GD-list” (Global Detection list): the date and the time of the first line in the LSD-list, concatenated station list resulting from the first and the second line, the time difference between the first and the second line as the network-wide signal duration, and the signal class of the event (if the event is the result of merging several lines, the signal class, which is written in the GD-list, is the value of the signal class that is most often found as signal class within the collected lines).

1.6 Output files:

Detected events for each day of data is listed in a set of txt files. Each txt file contains a certain part of the detected events. For example, the detection results in connection with the target zone-1 are found in a txt file which its file name contains the word “Zone-1”. Also, the events which were detected by a minimum number of X stations (X is a number) are found in a txt file which its file name contain the word “StX”. In this way, for example, if one wants to see the events detected by minimum number of 5 stations in the data of the date February 1, 2023 and in connection with the target zone-1, must see the txt file name “date20230201St5Zon-1.txt” in the set of the outputs.

2 CONTROL-FILE ADAPTATION IN ASSOCIATION WITH THE TEST EXAMPLE

We adapted the control-file of the program (Table B2) to search a wide range of signals. This is due to the previous studies, concerning the variety of the observed signals in the East Eifel Volcanic Field (Hensch et al., Geophys. J. Int., 216, pp 2025–2036, 2019). The search covers the frequency ranges belonging to the observed LF events and tectonic events by considering 11 band width search limits (11 signal classes). We set the seismic target zone to have a center between the epicenter of the reported deep LF events and the center of the Laacher See crater, with the radius of 25 km. The control-file parameters are adjusted to search events possibly occurring in two different depth zones limited between: 3 km and 30 km, and 30 km and 50 km. The used velocity model is KIT5 by Ritter et al., J. Seism. (in revision).

Table B1. Control file parameters

Short Description	**Parameter Name**
Station codes and coordinates in decimal degree	stInfo
P-wave velocity in km/s per depth	velP
S-wave velocity in km/s per depth	velS
Minimum source distance between synthetic source positions	minSor2SorDis
Location of the target seismic zone center in decimal degree	targCen
Target seismic zone radius in km	targRadi
Target seismic zone upper depth in km	targDep1
Target seismic zone lower depth in km	targDep2
Signal to noise window length ratio (integer value)	sig2NoisWinLenRatio
Narrow-bands signal to noise power threshold	monoBanSig2NoisTher
Band width search limits (signal classes)	sigClas
Decomposing narrow-band list	monoBanList
Max acceptable number of events per day	maxEvPerDay
Min. threshold for searching coherencies in sigClasPower	sigClas2NoisTher
Variation coefficient search vicinities (in eq. 6) are controlled by:	variCoefViciEffectFactor
Local search and event declaration condition:	
minimum number of stations with coherent signal anomaly	minLocSearCohStNum
maximum number of stations involved in local event search	maxLocSearStNum
Regarding the noise level or station position relative to the target:	
More important stations (optional)	morImpoSt
Less important stations (optional)	lesImpoSt

Table B2. Control file (Parameters) used in this study

Parameter Name	**Parameter Value**
stInfo	[DP02 50.418 7.318],
	[DP04 50.150 7.055],
	[DP07 50.155 7.531],
	[DP10 50.420 7.586],
	[DP12 50.544 7.433],
	[ABH 49.882 7.548],
	[FACH 50.355 7.993],
	[OCHT 50.339 7.357],
	[LAGB 50.360 7.102],
	[FSH 50.076 7.109],
	[AHRW 50.541 7.076],
	[BHE 50.353 7.180],
	[TDN 50.575 6.945],
	[BIW 50.731 7.837]
velP velS Depth	[5.53 3.24 -0.9],
	[5.53 3.25 1],
	[5.65 3.32 2],

	[5.75 3.38 3],
	[5.75 3.55 5],
	[6.09 3.73 8],
	[6.10 3.77 10],
	[6.20 3.77 12],
	[6.32 3.80 15],
	[6.43 3.83 19],
	[8.00 4.76 70]
minSor2SorDis	3
targCen	[50.38 7.31]
targRadi	25
targDep1 (zone1, zone2, zone3)	3, 30, 45
targDep2 (zone1, zone2, zone3)	30, 50, 70
sig2NoisWinLenRatio	3
monoBanSig2NoisTher	0.7
sigClas	[1 5], [2 7], [3 9], [4 11], [6 14], [8 17], [10 20], [12 23], [13 25], [15 28], [16 30]
monoBanList	[1 2 3 4 5 6 7 8 9 10 11 12 13 14 15 16 17 18 19 20 21 22 23 24 25 26 27 28 29 30]
maxEvPerDay	600
sigClas2NoisTher (zone1, zone2, zone3)	2.5, 2, 2
variCoefViciEffectFactor (zone1, zone2, zone3)	2.7, 2.9, 3.1
minLocSearCohStNum	3
maxLocSearStNum	5
morImpoSt	DP12, AHRW, OCHT, BHE, LAGB
lesImpoSt	DP04, FSH

Appendix C: for chapter six (moved magma volume estimation)

C.1 - Location of the Low Frequency (LF) events

Dataset

The DEEP-TEE dataset includes nearly ten years of continuous seismological records from a continuously upgraded seismic network (Ritter et al., 2024). Our study is limited to the time period between July 2014 (start of recording) and December 2022, in 2023 and 2024 hardly any magmatic low-frequency (LF) events occurred. In addition, we skip eight hours of recordings during daytime (7:15 UTC to 15:15 UTC), because the increased level of man-made noise is too high in most records and there are too many quarry blasts with similar waveforms as LF events what hides the latter (Koushesh and Ritter, 2024).

We apply the A6-DFMSD detector (Koushesh and Ritter, 2024) for finding LF events with dominant frequencies between 1 Hz and 11 Hz. Between July 2014 and December 2022, the detection procedure finds overall 462 LF events of which 332 events can be located with VELEST (Kissling et al., 1994).

Quality classes for arrival time picks

First arrival onsets of P- and S-phases are picked manually and the events are classified into the qualities A, B and C according to the precision of the pick times, from the best to the lowest pick uncertainty respectively. In Figure 1 the quality classes A, B and C are marked with black, blue and green colored dots, respectively.

The classification of the events was done manually and according to the readability of the P- and S-phases which is mostly affected by the level of the signal-to-noise ratio (SNR) rather than the type of the arrival phases like an emergent or impulsive waveform. In general, it is a qualitative decision (background noise, coherence with neighboring station recordings etc.) rather than a pure quantitative one, but it includes a quantitative component:

- class A: the SNR of the onsets is low enough that we could pick the phases within an uncertainty range of 0.01 s to 0.05 s,
- class B: the uncertainty for the best observed pick is in the range of 0.01 s to 0.1 s,
- class C: the uncertainty for the best observed pick is in the range of 0.01 s to 0.15 s,
- we refrain picking phases which have an uncertainty of more than 0.4 s uncertainty.

This classification means that not all picks of an event need to be as precise as given above, so there may be outliers with an uncertainty less than 0.4 s. This flexibility is necessary because the seismic phases are very weak and sometimes the SNR is very low. P-waves onsets are picked on the vertical component, final S-wave onsets on transverse or radial components; rotation is done after an initial location of the events.

Event location procedure

The initial absolute locations of the events were obtained using VELEST (Kissling et al., 1994), where the 1-D P- and S-wave seismic velocity models KIT6 and the corresponding station correction values are taken from Ritter et al. (2024). To better image the structure where the LF events occur, we use HypoDD (Waldhauser and Ellsworth 2000 and Waldhauser 2001) to determine relative locations and correspondingly location uncertainties for each event. To avoid unrealistic solutions, we remove some events with relatively a large location uncertainties (outliers).

We define a large location uncertainty, if it exceeds the mean error plus one standard deviation of the location error of all events. This selection threshold is marked by a red line in Fig. 1a and it is about 2 km. Since the results of the relocation using HypoDD are affected by the number of possible linked events for clustering, the relative relocations are highly influenced by the participating events into the location process. Hence, to find a stable location result, we apply HypoDD in the SVD solution mode (Waldhauser and Ellsworth 2000 and Waldhauser 2001) and randomly resample the input data with a jackknife method to generate 100 different input datasets. For this we randomly select 80% of the events in class A, 60% of the events in class B and 40% of the events in class C to generate the 100 test input datasets. Figure 1b shows how many times each event is involved into this random selection.

For some of the events, HypoDD cannot find links to any neighboring event and for some events there are only a few links depending on the randomly selected events in a input dataset. Therefore, these events are missing in the related relocation step and Fig. 1c shows the subsequent relocation occurrence for each event. To extract the most stable results out of the relocated events, we only focus on those events which have enough linked events as found by the jackknifing routine. Therefore, we consider events as outliers if they have a relatively small number of relocation results. For this selection we consider three thresholds corresponding to each quality class: each threshold is defined as the mean minus one standard deviation determined from the number of relocations with all events of the same class. In Fig. 1c these thresholds are plotted as red lines.

To find the most stable values for the latitude (lat.), longitude (lon.) and depth for each event, we define a bin with a length of 200 m and discretize the relocation parameters of the events accordingly. The final relocation parameters for each event are the values which are repeated most often though the jackknifing. Fig. C.1.2 presents the distribution of the relocation parameters around the most repeating values. There, the red dots mark the borders around the most repeating values for which the solutions are within the borders which contain 68% of all solutions for each relocation parameter for each event.

Results

Following the jackknife selection process, the best determined 289 LF events out of the locatable 332 LF events can be relocated for a final stable and reliable solution. The difference of 43 events can be explained by not finding enough links to neighboring events for a stable HypoDD solution. The 289 locations are analyzed and discussed in the following. In Table C.3.1 absolute hypocentral parameters of the LF events calculated by VELEST (Kissling, Kradolfer, & Maurer, 1995) and the final relocated hypocentral parameters determined by HypoDD (Waldhauser F. , 2001) and passed through the jackknife validity test are summarized. In Fig. C.1.3a the top view of the relative locations is shown (the same figure as Fig. 6.3 in the main text). The SW-NE and

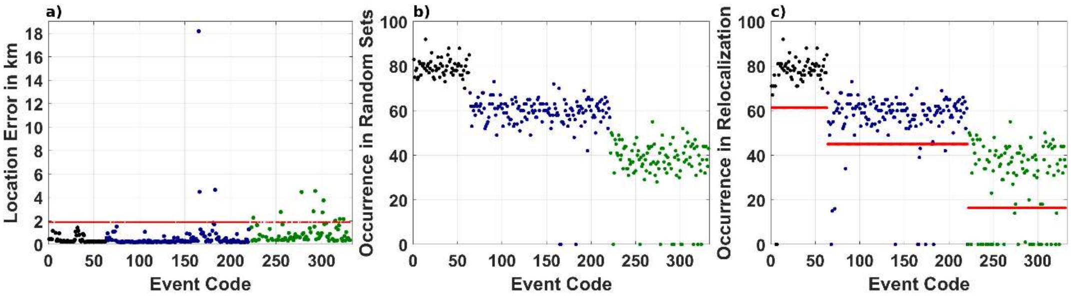

Fig. C.1.1: a) the total relocation errors for each event after applying HypoDD using the SVD solution; the events are ordered according to the quality classes of the picks, A-C (marked with black, blue and green) from left to right. The red line is the threshold which is determined from the mean plus the standard deviation of all the location errors for finding outliers. b) participation or reoccurrence of each event for all 100 randomly selected input datasets before applying HypoDD and searching for links to neighbors. c) participation or reoccurrence status of each event after applying HpoDD to the randomly selected input dataset. The red lines indicate the outlier thresholds for the three quality classes A-C.

the NW-SE cross-sections of the locations are plotted in Figs. C.1.3b and C.1.3c, respectively. The NW-SE direction corresponds to the widest lateral distribution (ca. 8 km) of the LF events whereas the SW-NE direction is the shortest (ca.5 km).

To crosscheck the correct functionality of the HypoDD relocations with respect to the LF events, we applied HypoDD in the SVD solution mode also to the 203 known strongest tectonic events ($0.8 < ML < 2.8$) in the region during the same time period and hence recorded with the same seismic station configuration. The strongest events are used to well determine the onset times of the P- and S-phases. These tectonic events occurred at the most active fault in the region called Ochtendung Fault whose strike direction of ca. 145° from north is well known (Ahorner, 1983; Weber, 2012; Ritter et al., 2024). In Figure C.1.3a, the tectonic events (green dots) are mostly well aligned along the trend of the Ochtendung Fault, what indicates the reliability of the HypoDD relocation results. Tectonic events north of the LSV are not related with the Ochtendung Fault which terminates at about 50°24', and have a wider lateral scatter. Since we focus on LF events in this study, we do not include the tectonic events in the vertical cross sections for clarity.

Fig. C.1.4 shows the relocation results of those 68% hypocenter solutions from the 100 jackknife runs for which the hypocenter parameter values are closest to the most repeated values. As in Figure C.1.3, the same SW-NE and NW-SE cross-sections also are plotted. These hypocenter solutions are the most stable solutions of the relocation testing for each event (the final solution is indicated as star plotted at the same location as in Fig. C.1.3). The 68% closest solutions indicate the uncertainty range for the relative relocations and outline a very similar structure as in Fig. C.1.3.

In Fig. C.1.5 the time history of the LF events versus depth is plotted. The two boxes highlight the events which occurred inside the east cluster in the Neuwied Basin NW of Koblenz). Although these shallow events (<10 km depth) are ~10 km away from the main cluster (the translithospheric channel close to LSV), we argue that they are also related to magmatic fluids, possibly

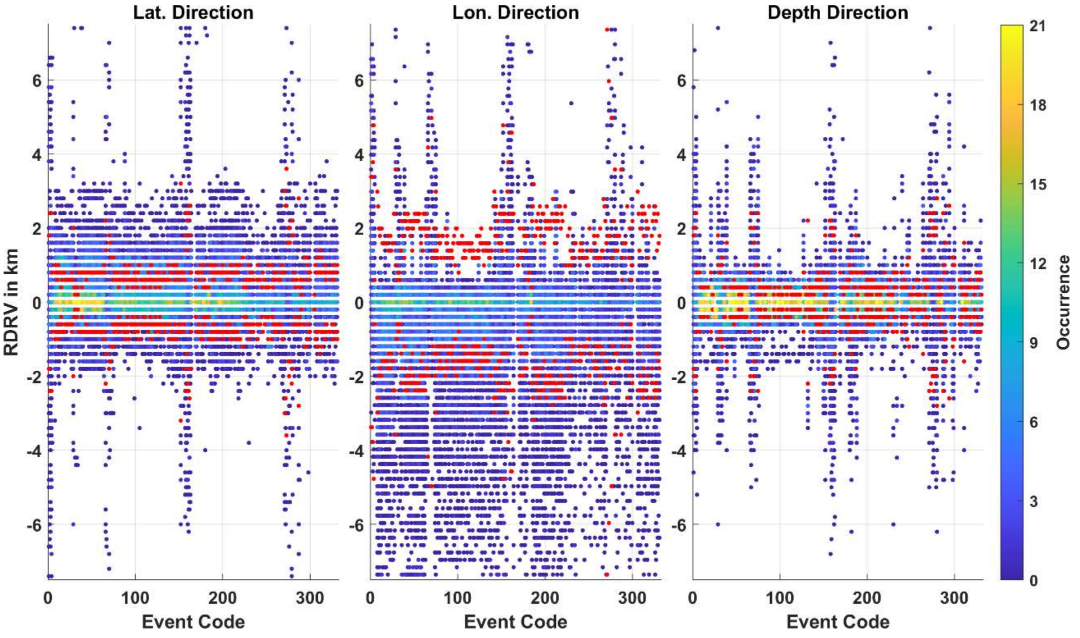

Fig. C.1.2: Occurrence (in color) and spatial distribution of hypocenter solutions for 200 m wide bins and 100 relocations. The RDRV values represents the relative distance to the most repeating value which is set to 0 km distance. Red dots outline the 1-σ distance. The location parameters are event latitude (lat.), event longitude (lon.) and event depth.

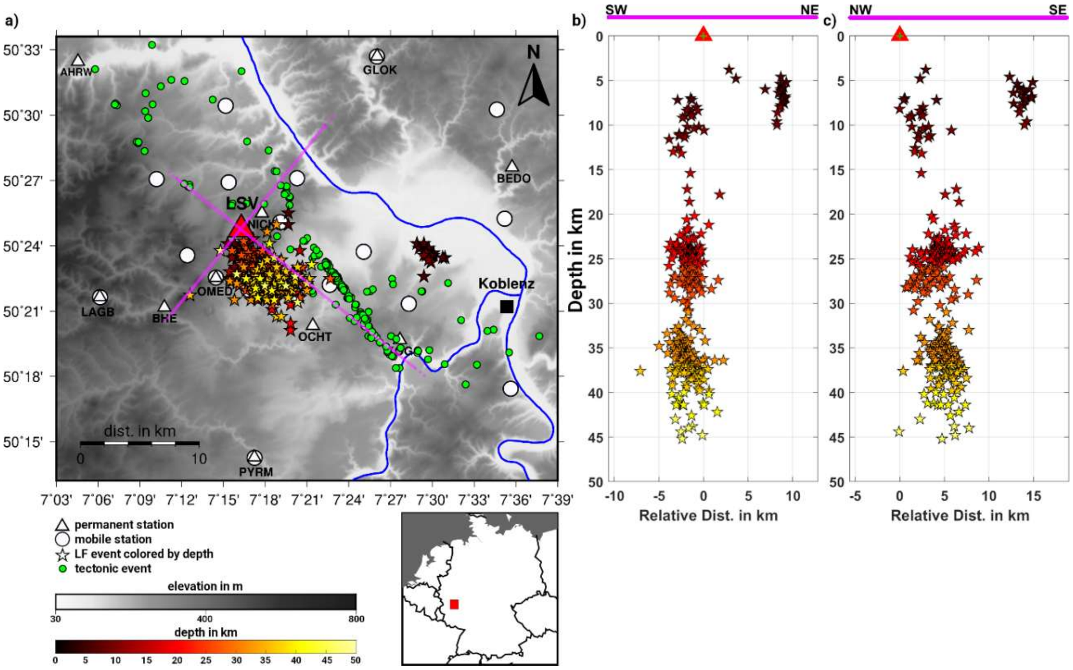

Fig. C.1.3: a) map view of the low-frequency and tectonic event locations using HypoDD. b) SW-NE cross-section along the short lateral extension of the seismically active structure with LF events beneath the LSV. c) NW-SE cross-section along the widest lateral extension of the seismically active structure with LF events beneath the LSV.

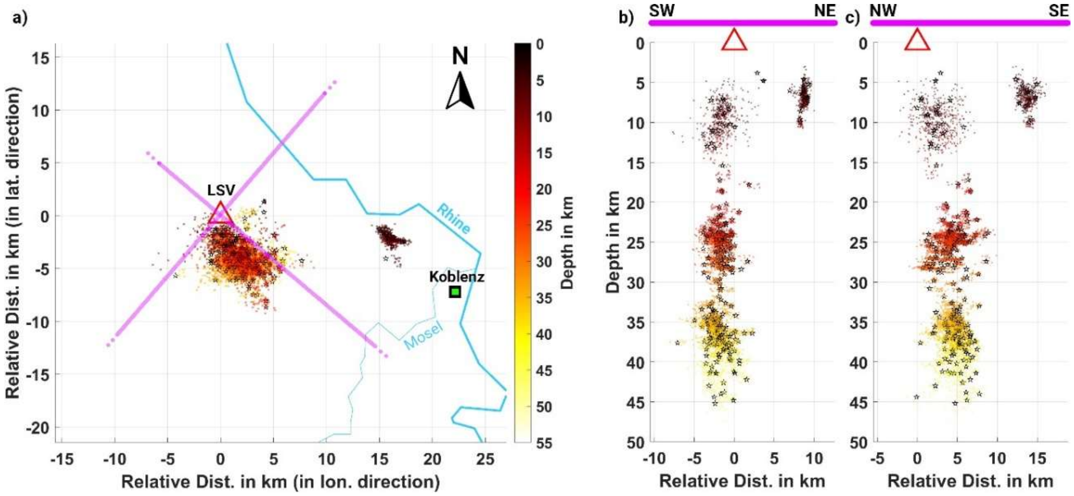

Fig. C.1.4: Spatial 1-σ uncertainty range of the relative HypoDD solutions (68% range). Stars indicate the final preferred hypocenter location (Fig. C.1.3) and the dots are the closest solutions for the 100 input datasets of the jackknife testing. The red triangle is at the position of the Laacher See Volcano.

supercritical gases such as CO_2: a) their frequency content is low with a dominant frequency peak at ~4 Hz; this is well below the frequency range of the local tectonic earthquakes (Fig. 6.2 in the main text), b) their spatial distribution Figs. C.1.3 and C.1.4 is more like a channel than a rupture plane of an earthquake zone, c) there are magmatic CO_2 emissions in the Neuwied Basin (Bräuer et al., 2013; Berberich et al., 2019). The east cluster was briefly active in autumn 2016 and then again in 2019 and 2020. This episodic activity may be related with a low flux of gas which needs to accumulate for some time to build enough pressure for open pathways.

In the main cluster beneath LSV the LF event activity is also episodic. There are time intervals of several months without measurable seismic signals, e.g.,:

- from 2015 to summer 2016 when only one event series occurred,
- in the first half of 2020,
- since summer 2022.

In June 2017 and in the second half of 2021 there is a relative strong activity. During these swarm-like event occurrences, ~240 LF events were detected. Up to now, no clear spatial relation between the events with an episodic swarm was discovered. However, similar to the mechanism of the shallow events in the Neuwied Basin, an accumulation of buoyant material can be envisaged which is needed to built up enough pressure for the jerky opening process inside cracks as described in Supplementary Information C.2.

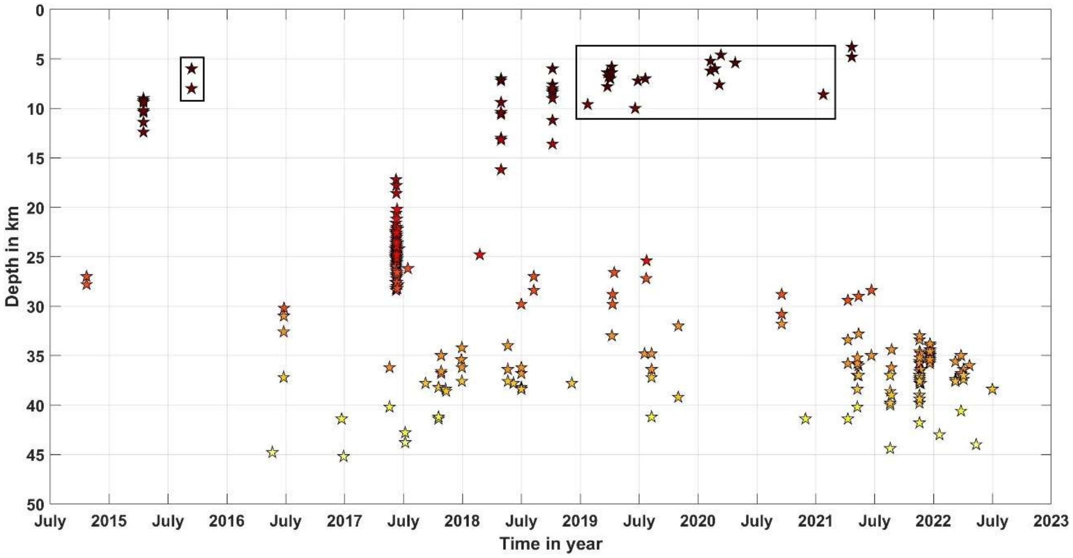

Fig. C.1.5: Time history and depth distribution of the LF events. The two boxes indicate the events which occurred NW of Koblenz in the Neuwied Basin. Color for depth as in Fig. C.1.4.

C.2 Melt volume estimation

Background

We use a mechanical model based on a ‘chain of cracks connected by narrow channels’ (Fig. C.2.1) as originally suggested and formulated by Aki et al. (1977) and Aki and Koyanagi (1981), to estimate the fluid or melt volume transported through the lithosphere. This transportation mechanism establishes a relationship between the observed peak-to-peak amplitude of the seismic wave pulses and the fluid or melt flow volume. The assumption is that a fluid with overpressure inside a crack causes a stress concentration at the tip of the crack what results in a tensile failure (Griffith’s criterion). As the crack expands in a jerky motion, the melt is injected into the host rock and afterwards the crack is closed again. During this rock failure, tremor-like seismic waves are excited. The formalism by Aki et al. (1977) and Aki and Koyanagi (1981) was developed to estimate the magma flow rate for Hawaiian magmatism in the crust and upper mantle but has no regional limitation.

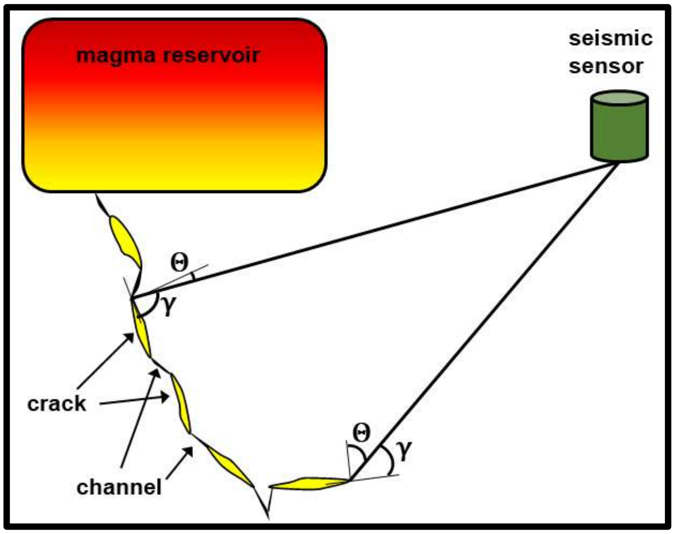

Fig. C.2.1: Conceptual model with a ‘chain of cracks connected by narrow channels’ for melt transport, after Aki et al. (1977).

Method

Following Aki et al. (1977) and Aki and Koyanagi (1981) the root mean square (RMS) P- or S-wave amplitude of tremor or LF events, excited by crack opening due to an over-pressured fluid, can be expressed as

$$RMS(U^p) = \frac{\lambda + 2\,\mu\, cos^2(\theta)}{4\,\pi\,\rho\,\alpha^3\, r}\, W\Delta u\, \frac{2\cos(\gamma)}{\alpha}\,\frac{L}{T}\left(\frac{1}{v^2} - \frac{\cos^2(\gamma)}{\alpha^2}\right)^{-\frac{1}{2}} \qquad (1),$$

$$RMS(U^s) = \frac{sin(2\theta)}{4\,\pi\,\beta\, r}\,\frac{WL\,\Delta u}{T}\left(\frac{2\,\mathrm{T}\cos(\gamma)}{\alpha\, L}\right)^{\frac{1}{2}}\left(\frac{1}{v^2} - \frac{\cos^2(\gamma)}{\alpha^2}\right)^{-\frac{1}{2}} \qquad (2).$$

Equation (1) is from Aki and Koyanagi (1981, eq. 5) and equation (2) is from Aki et al. (1977, eq. 31) but corrected to match with the assumptions given in Fig. 8 of Aki and Koyanagi (1981). The RMS of the function *f(t)* in this Fig. 8 should be equal to:

$$RMS(f(t)) = W\Delta u \left(\frac{2\ \mathrm{L}\cos(\gamma)}{\alpha\, T}\right)^{\frac{1}{2}} \left(\frac{1}{v^2} - \frac{\cos^2(\gamma)}{\alpha^2}\right)^{-\frac{1}{2}} \qquad (3),$$

instead of:

$$RMS(f(t)) = W\Delta u\ \frac{2\cos(\gamma)}{\alpha}\ \frac{L}{T} \left(\frac{1}{v^2} - \frac{\cos^2(\gamma)}{\alpha^2}\right)^{-\frac{1}{2}} \qquad (4)$$

with a difference in the central term of:

$$\left(\frac{T\,\alpha}{2\ L\ cos(\gamma)}\right)^{\frac{1}{2}} \qquad (5).$$

The RMS of the function $f(t)$ is given in Aki and Koyanagi (1981) as a part of equation (5). The theoretical parameters U^p and U^s are replaced with the measured seismic P- and S-wave amplitudes A^p and A^s. W, L and Δu are the crack dimensions which describe the involved fluid volume and the time duration T is the time duration of an acoustic wave for traveling a distance of 2 L in the melt (eq. 8). In Table C.2.1 the parameters are listed which are used in the previous and the following equations.

Table C.2.1: Parameters for estimating the involved fluid or melt volume.

W : width of the crack,

L : length of the crack,

Δu : displacement at the crack,

q : flow rate of the fluid / melt,

q_{tv} : total volume estimated from q across the lithosphere,

a : side length of a cube with an equivalent volume to q_{tV},

T : the time duration for an acoustic wave for traveling a distance of 2 L in the melt,

t : duration of the fluid / melt injection during a LF event,

A^p, A^s : measured peak-to-peak displace-ment amplitude of P- and S-waves,

U^p, U^s : theoretical P- and S-wave amplitudes due to a jerky crack opening,

ρ : density of medium,

α , β : P-, S-wave velocity,

λ, μ : Lame's constants of the host rock,

v : acoustic wave velocity of the fluid / melt,

r : distance between source (crack) and recording station,

θ : angle between the normal to the crack and the direction to the recording station (as shown in Figs. A1 and A2),

γ : angle between the direction of melt movement and the recording station (as shown in Figs. A1 and A2

Rearranging equations (1) and (2) and inserting the following relations (6 - 10)

$$RMS(U^p) = \frac{A^p}{2\sqrt{2}} \;, \qquad RMS(U^s) = \frac{A^s}{2\sqrt{2}} \tag{6,}$$

$$q = \frac{W\,L\,\Delta u}{T} \tag{7,}$$

$$T \sim \frac{2L}{v} \tag{8,}$$

$$\alpha = \sqrt{\frac{\lambda + 2\mu}{\rho}} \tag{9,}$$

$$\beta = \sqrt{\frac{\mu}{\rho}} \tag{10}$$

gives the estimates for flow rates based on measured P- and S-wave amplitudes:

$$q^p = \frac{4\,\pi\,\alpha^3}{\alpha^2 - 2\beta^2(1 - cos^2(\theta))} \frac{r\,A^p}{2\,\sqrt{2}} \left(\frac{\alpha\,v}{4\cos(\gamma)} \left(\frac{1}{v^2} - \frac{\cos^2(\gamma)}{\alpha^2} \right) \right)^{1/2} \tag{11,}$$

$$q^s = \frac{4\,\pi\,\beta}{\sin(2\theta)} \frac{r\,A^s}{2\,\sqrt{2}} \left(\frac{\alpha\,v}{4\cos(\gamma)} \left(\frac{1}{v^2} - \frac{\cos^2(\gamma)}{\alpha^2} \right) \right)^{1/2} \tag{12}$$

as derived after Aki et al. (1977) and Aki and Koyangi (1981).

With *n* as the number of LF events per depth interval and the time duration *t* of the injection process, the total volume q_{tv} involved in the fluid flow through the lithosphere of the EEVF is obtained by the following summation:

$$q_{tV} = \sum_{depth \sim 6\,km}^{45} q_{depth}\, n_{depth}\, t \tag{13.}$$

<u>Parameter selection</u>

It is not known what kind of magmatic fluid is transported: magmatic melt, superfluid magmatic gases or a mixture of both. For the volume estimation in equations (11) and (12) this affects the parameter acoustic velocity *v* in the medium, but small differences in *v* do not cause a significant difference in the result (see below). Because we observe very deep processes, even below the Moho, we prefer to interpret the fluid as melt, which contains solved gases due to the high ambient pressure. Xenolith data from the West Eifel Volcanic Field support the occurrence of melt injections, which are found as veins in the rock samples (Shaw et al., 2005 & 2018; Witt-Eickschen et al., 2003).

Concerning the estimated total volume q_{tV} we note that the result of such a calculation provides an upper limit for the volume of melt transported in the lithosphere, because during the melt migration process the same melt volume may be involved several times. This means that a batch of melt can be reactivated for another upward or sideward movement along a crack with overpressure. Local stress changes during the pressurization of a crack can be also responsible for the opening of neighbouring cracks. In this way an episodic time with increased activity can occur; such episodic activities are actually observed in the East Eifel Volcanic Field (Fig. C.1.5). Aseismic melt transportation is neglected in our model and may increase the volume of migrated fluid. Our seismic observations are limited from 3:15 pm to 07:15 am (UTC) during night time (see main text), hence we simply apply a coefficient of 1.5 to the number of events in each depth interval to compensate the observationally missed part of the seismic event detection during day time. The total number of actually observed LF events (located events and the ones that occurred during swarms without good location due to overlapping waveforms, see Fig. C.1.5 in Supplementary Information A) is 400. With a correction for missing events during day time (see below) we finally add up 600 events in eq. (13). This might not be fully realistic and in future studies this assumption might be replaced with the exactly detected magmatic activity during day time. To average over local amplitude anomalies and cover a reasonable range of r, θ and γ, we studied the amplitudes at six seismic stations (DEP01, DEP08, DEP10, DEP12, OCHT and AHRW) which are spread across the DEEP-TEE network. Their individual geometrical parameters are given in Table C.2.2. As most of our 400 LF events have a very low signal-to-noise ratio and are not always observed at all stations, we measure the amplitudes for a relatively strong event with magnitude *ML* 1.6. In Fig. C.2.3 the waveforms and their amplitude ranges are displayed. For the summation in eq. (13) we assume an average *ML* of ca. 0.6 (LGB, 2024) and correct the measured ground motion amplitudes from Fig. C.2.3 with a factor of 0.1.

The input parameters seismic velocity (α, β), which depend on rock physics and ambient pressure and temperature, are relatively well constrained (Ritter et al., 2024) and large variations are not expected. The observational parameters (t, A^p, A^s) and the hypocentral distance r are also well constrained. However, we tested a reasonable parameter range (Table C.2.2, column 2) to determine the sensitivity of these different parameters.

The largest uncertainty in estimating q_{tv} is related with the direction of the fluid movement (yellow arrow in Fig. C.2.2) and the geometry of the aligned cracks. These parameters determine the angles θ and γ and hence the sine and cosine terms in equations (11) and (12) which can have a significant influence on the volume estimations. To explore these variations, we assume three possible extreme scenarios regarding the geometry and spatial orientation of the chain of cracks connected by narrow channels in respect with the observational point (seismic station position). These three scenarios are schematically depicted in Fig. C.2.2 and they are used to test the influence of θ and γ. In scenarios A and B melt rises in a vertical dike-like intrusion and in scenario C there is a horizontal sill-like intrusion. We expect that not only one of these scenarios happens in the EEVF, but actually a mixture of melt intrusion types in different directions is going on inside the translithospheric channel (Fig. 6.1b in the main text). Thus, the different events are recorded with a large variation of θ and γ.

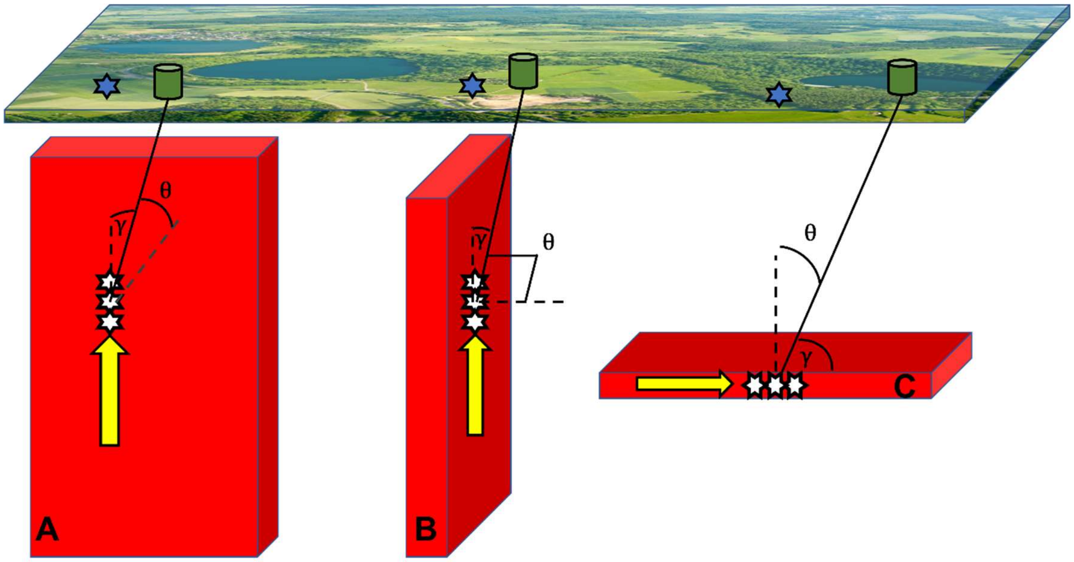

Fig. C.2.2: Three scenarios for dike (A, B) and sill (C) intrusion structures in which fluids or melt move with overpressure along cracks (Fig. C.2.1). Different relative positions and orientations of the plane with the chain of the cracks for the melt flow control the angles γ and θ in respect to the seismic station positions.

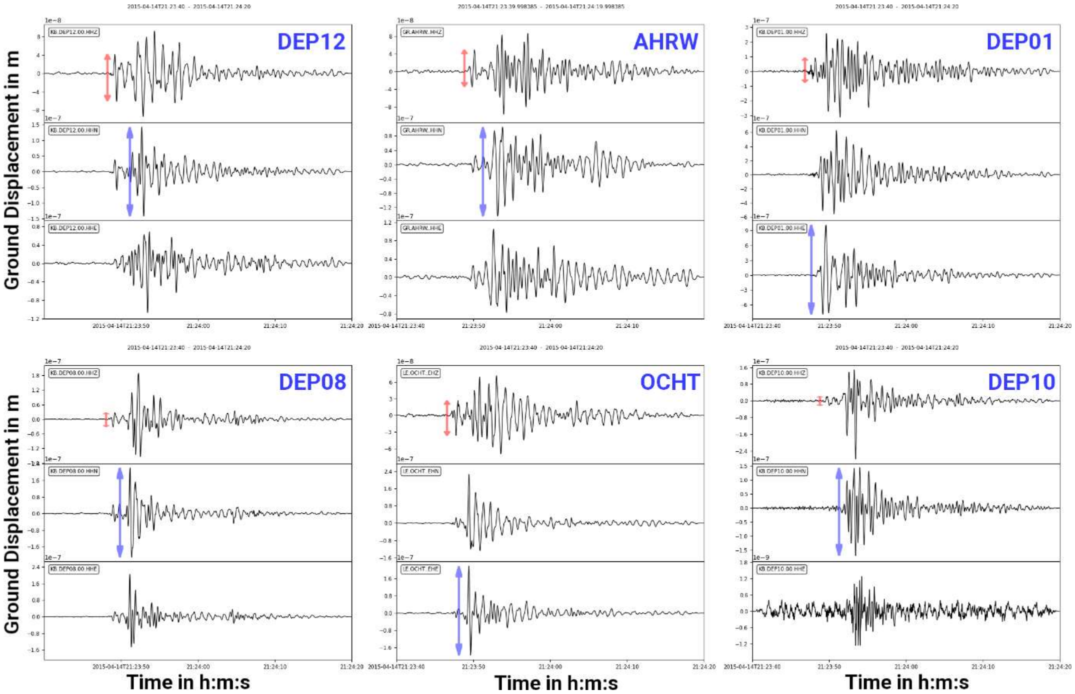

Fig. C.2.3: Waveforms (vertical, north-south and east-west) of the low frequency event on 14. April 2015 (*ML* 1.6) with peak-to-peak amplitude readings for P- and S-waves (A^p, A^s) at six stations of the DEEP-TEE network (DEP12, AHRW, DEP01, DEP08, OCHT, and DEP10). Red and blues arrows indicate A^p and A^s amplitudes, respectively. For numerical values see column 3 in Table C.2.2.

Results and uncertainties

At first, we test the sensitivity of the input parameters using two observations, A^p and A^s, measured at station DEP12. For our observational period of July 2014 – December 2022 and under consideration of the three different melt intrusion scenarios A, B and C together with the chosen uncertainties of the input parameters listed in Table C.2.2 (column 2), the moved fluid or melt volume q_{tv} through the lithosphere is estimated to be in the range of (1.5 – 3,699) 10^3 m^3. To better illustrate this quantity, we convert it to an equivalent cube which accordingly has side lengths a of 12 – 155 m. Dike A and sill C scenarios result in similar q_{tv} values, whereas dike B scenario has a higher flow volume (Table C.2.3).

The variation of q_{tv} differs for variations of the input parameters in eq. (11) and (12) in different ways. Tested variations of α, β, v and r affect q_{tv} by ca. 30% to 35% (Table C.2.2, column 2). Changes in t, A^p and A^s influence linearly the volume q_{tv}. The above highest value of q_{tv} is e.g. due to the tested long duration of 20 s for t (duration of melt injection) which is not observed in the seismic waveforms. Hence such an extreme value seems to be unlikely. A^p and A^s vary well in the observations and are an obvious source for uncertainties in the estimation of q_{tv}. Variations due to scenarios A, B and C and their influence on θ and γ cause uncertainties of 20-850%. However, these fluctuations in q_{tv} are presumably averaged out for our 600 events, if different mechanisms of diking and sill intrusions appear collocated in the translithospheric channel.

Excluding unlikely extreme parameter values in column 2 of Table C.2.2 and choosing the average/preferred and measured values in column 3 of Table C.2.2 together with the amplitude values from station DEP12 limits q_{tv} in the range of (15.5 – 370) 10^3 m^3 equivalent to cube side lengths a of 25 – 72 m.

Similarly, using the measurements of A^p and A^s from the six seismic stations DEP01, DEP08, DEP12, DEP10, AHRW, and OCHT together with the scenarios A, B and C, we calculate melt volumes of (8 -1,100) 10^3 m^3 or cubes with 20 – 103 m side length (Fig. 6.4 in the main text and Table C.2.4). The related mean values are $q_{tv} = 137\ 10^3\ m^3$ ($a = 51.6$ m) and the medians are $q_{tv} = 29.4\ 10^3\ m^3$ ($a = 30.9$ m) between 2014 and 2022. The scatter in Fig. 6.4 indicates a range between 3 10^5 m^3 and 10^4 m^3 which is reasonable taking into account the uncertainty of the input parameters.

Our mean and median values can be converted into an average flow rate of about 16.3 10^3 m^3/yr and 3.5 10^3 m^3/yr, respectively. These are low rates compared to estimations of Tomlinson et al. (2020) who calculated 20-100 10^3 m^3/yr for the 20,000 years of time before the massive eruption 13,000 yrs ago. However, despite the large uncertainties of the input parameters and limitations in seismological observation, we think that our calculations of flow rates provide a reasonable estimation of the order of melt involved and is a useful model for future research of magmatic processes in the Eifel.

Table C.2.2: Parameter ranges for calculating and testing the sensitivity of q_{tv}. Column two: range for testing; column three: values taken for estimation of q_{tv} with amplitude measurements at seismic stations DEP01, DEP08, DEP10, DEP12, OCHT and AHRW. The seismic velocities α and β are varied by ±10% relative to the depth-dependent values of model KIT6 in Ritter et al. (2024). Parameters r, θ and γ vary depending on the hypocentral depths and station positions.

parameter	**range for sensitivity tests**	**selected value for the final q_{tv} calculation**
v in km s^{-1}	1 - 4	2
α in km s^{-1}	$0.9\ v_p – 1.1\ v_p$	KIT6 model
β in km s^{-1}	$0.9\ v_s – 1.1\ v_s$	KIT6 model
r in km	$0.7\ r – 1.3\ r$ (r rel. to DEP12)	for DEP01: 7.51 - 51.46 for DEP08: 15.65 - 53.26 for DEP10: 21.15 - 55.13 for DEP12: 21.33 - 55.20 for OCHT: 6.43 - 51.32 for AHRW: 24.52 - 56.51
t in s	0.2 - 20	2
A^s in m	$0.05\ A^s – 0.5\ A^s$ A^s (at DEP12)	0.1 A^s (at DEP01) = $17.99\ 10^{-8}$ 0.1 A^s (at DEP08) = $4.29\ 10^{-8}$ 0.1 A^s (at DEP10) = $3.15\ 10^{-8}$ 0.1 A^s (at DEP12) = $2.84\ 10^{-8}$ 0.1 A^s (at OCHT) = $4.11\ 10^{-8}$ 0.1 A^s (at AHRW) = $2.48\ 10^{-8}$
A^p in m	$0.05\ A^p – 0.5\ A^p$ A^p (at DEP12)	0.1 A^p (at DEP01) = $16.40\ 10^{-9}$ 0.1 A^p (at DEP08) = $5.72\ 10^{-9}$ 0.1 A^p (at DEP10) = $4.28\ 10^{-9}$ 0.1 A^p (at DEP12) = $10.17\ 10^{-9}$ 0.1 A^p (at OCHT) = $6.22\ 10^{-9}$ 0.1 A^p (at AHRW) = $8.30\ 10^{-9}$
θ in degree	Dike A 8.09 - 67.51 (DEP12)	DEP01: 23.53 - 82.31 DEP08: 11.05 - 73.24 DEP10: 8.15 - 67.68 DEP12: 8.09 - 67.51 OCHT: 27.80 - 83.63 AHRW: 7.03 - 64.49
	Dike B 89 (DEP12)	89
	Sill C 22.49 – 81.91 (DEP12)	DEP01: 7.69 - 66.47 DEP08: 16.76 - 78.95 DEP10: 22.32 - 81.85 DEP12: 22.49 - 81.91 OCHT: 6.37 - 62.20 AHRW: 25.51 - 82.97

γ in degree	Dike A	22.49 – 89 (DEP12)	DEP01: 7.69 - 66.47 DEP08: 16.76 - 78.95 DEP10: 22.32 - 81.85 DEP12: 22.49 - 81.91 OCHT: 6.37 - 62.20 AHRW: 25.51 - 82.97
	Dike B	1 – 89 (DEP12)	DEP01: 7.69 - 66.47 DEP08: 16.76 - 78.95 DEP10: 22.32 - 81.85 DEP12: 22.49 - 81.91 OCHT: 6.37 - 62.20 AHRW: 25.51 - 82.97
	Sill C	8.09 – 89 (DEP12)	DEP01: 56.77 - 86.15 DEP08: 50.52 - 81.62 DEP10: 49.08 - 78.84 DEP12: 49.04 - 78.76 OCHT: 58.90 - 86.82 AHRW: 48.51 - 77.25

Table C.2.3: Cumulative volume q_{tV} during 2014 - 2022 as equivalent cube side length a based on amplitude measurements at station DEP12 and testing the ranges of the input parameters listed in column 2 of Table C.2.2 for the scenarios A, B and C.

Wave type	**Dike A** ***a* in m**	**Dike B** ***a* in m**	**Sill C** ***a* in m**	**Total range** ***a* in m**
P-wave	12 – 57	29 – 135	12 – 56	12 – 155
S-wave	12 - 54	33 – 155	14 – 50	

Table C.2.4: Cumulative volume of q_{tV} during 2014 – 2022 as equivalent cube side length a based on amplitude measurements at six stations. The values in column 3 of Table C.2.2 are used as the input parameters for this calculation considering scenarios A, B and C.

Wave type	**Dike A** ***a* in m**	**Dike B** ***a* in m**	**Sill C** ***a* in m**	**Total range** ***a* in m**	**Total mean** ***a* in m**	**Total median** ***a* in m**
P-wave	20 – 38	43 – 63	20 – 26	20 – 103	51.6	30.9
S-wave	25 – 46	65 – 103	29 – 68			

C.3 List of the localizable LF events plus the waveform and spectrum example for a sequence of low frequency events at ca. 33 - 36 km depth below the East Eifel Volcanic Field.

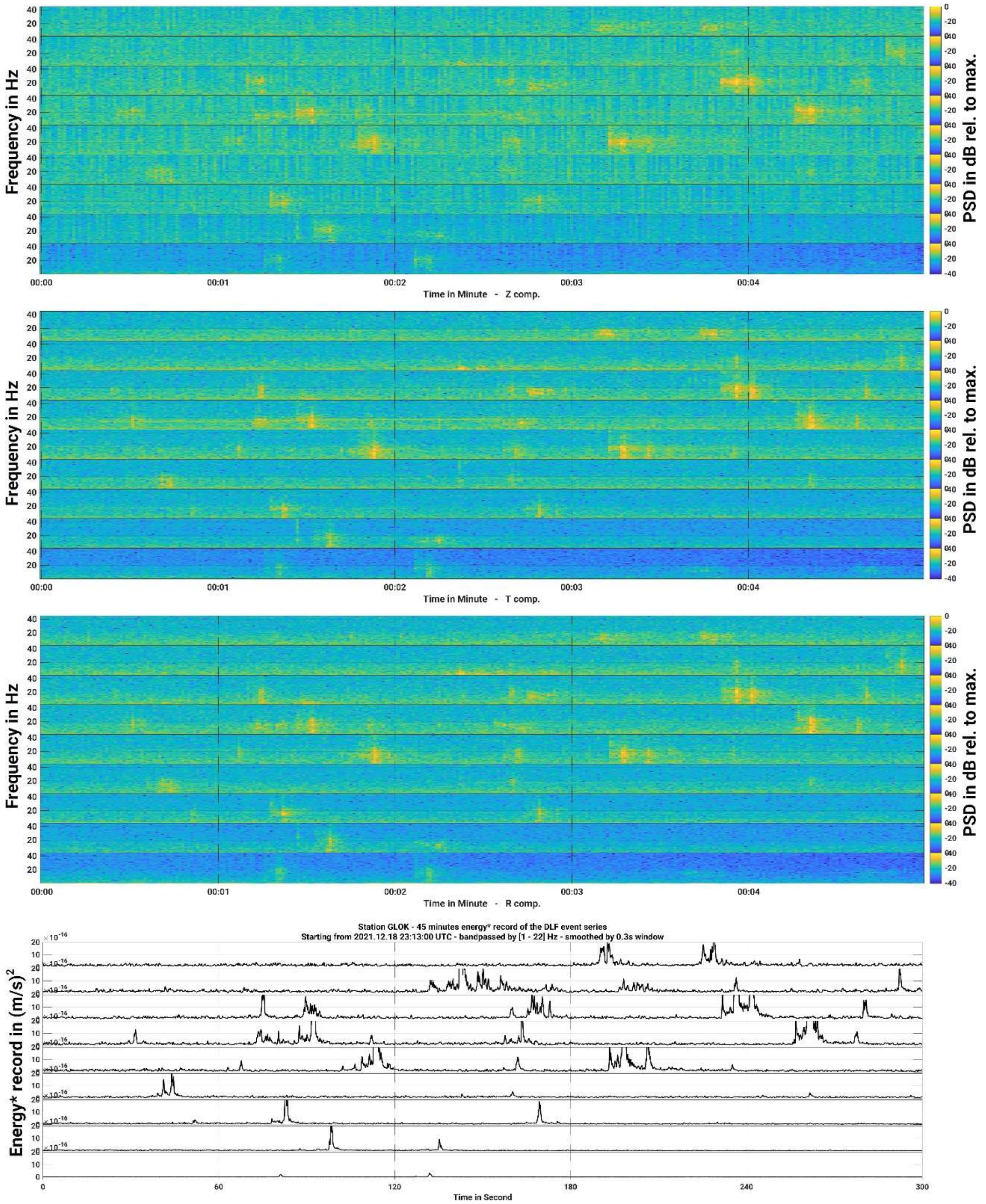

Fig. C.3.1: A sequence of DLF events, recorded during the night of 18./19. December 2021 between 23:13:00 and 23:58:00 (UTC) at station GLOK. The three spectrograms for the vertical (Z), transverse (T) and radial (R) components contain clear low-frequency events. The lower diagram shows the energy of the recordings as squared and summed amplitudes $(A_Z^2 + A_T^2 + A_R^2)^{1/2}$ see Kouchesh and Ritter (2024) for processing. In this representation, low-amplitude signals are enhanced.

Table C.3.1 the absolute hypocentral parameters of the LF events calculated by VELEST (Kissling, Kradolfer, & Maurer, 1995) and the final locations determined by the relative relocation algorithm HypoDD (Waldhauser F. , 2001)

		Absolut location solution using VELEST									Relative location solution using HypoDD (after jackknife test)		
Class	Ev. code	Origin date & time	Lat. in dec. degree	Lon. in dec. degree	Depth in km	ERX in km	ERY in km	ERZ in km	Gap in degree	RMS in s	Lat. in dec. degree	Lon. in dec. degree	Depth in km
A	001	20150414 21:23:45.055	50.3962N	7.2858E	11.010	2.3	1.6	2.6	75	0.36	50.3910	7.2884	10.40
A	002	20150414 21:25:53.705	50.3948N	7.2703E	11.830	2.4	1.9	3.7	76	0.19	50.3820	7.2688	11.00
A	003	20150414 21:26:53.384	50.4003N	7.2546E	9.136	2.3	1.6	3.6	85	0.21	50.3910	7.2604	9.20
A	004	20150414 21:28:33.247	50.4003N	7.2735E	8.912	2.1	1.4	3.4	68	0.32	50.3892	7.2856	9.00
A	005	20150912 1:31: 3.126	50.4047N	7.4673E	3.790	2.6	2.0	5.0	92	0.11	50.3982	7.4844	6.40
A	006	20160426 20:25:49.514	50.3872N	7.5223E	6.230	3.0	2.5	4.6	83	0.18	-- -- --	-- -- --	-- -
A	007	20160428 19: 9:58.505	50.3913N	7.4954E	5.843	3.7	2.3	4.8	177	0.14	-- -- --	-- -- --	-- -
A	008	20160518 21:16:46.799	50.3541N	7.3311E	42.820	3.9	3.9	4.1	86	0.16	50.3766	7.3360	44.80
A	009	20160623 15:14:34.200	50.3714N	7.3314E	35.711	2.4	1.8	3.8	48	0.18	50.3766	7.3416	37.20
A	010	20160623 17:58:59.173	50.3709N	7.2882E	33.948	4.0	2.6	4.5	64	0.19	50.3694	7.2912	32.60
A	011	20160624 17:55:25.513	50.3792N	7.2946E	30.691	2.3	2.0	2.7	50	0.12	50.3748	7.3024	30.20
A	012	20161220 18:28:11.719	50.3534N	7.3002E	40.090	3.7	3.3	4.3	87	0.21	50.3676	7.2884	41.40
A	013	20170517 3:48:51.043	50.3669N	7.3455E	37.750	3.9	2.3	4.3	133	0.14	50.3766	7.3416	36.20
A	014	20170604 20:36:32.951	50.3751N	7.2996E	23.728	2.0	2.6	3.7	92	0.07	50.3748	7.2996	24.80
A	015	20170606 19:22: 2.357	50.3710N	7.3160E	23.401	3.1	1.7	3.4	95	0.16	50.3694	7.3024	24.60

A 016	20170606	19:23: 3.145	50.3713N	7.3053E	24.472	2.9	2.3	3.8	103	0.14	50.3712	7.2996	25.00
A 017	20170606	20:54: 6.609	50.3685N	7.2784E	24.255	3.1	2.5	4.3	87	0.16	50.3694	7.2800	24.40
A 018	20170607	10:55:49.214	50.3842N	7.3031E	26.086	2.0	2.1	2.2	54	0.29	50.3910	7.2856	26.20
A 019	20170607	11: 2:29.275	50.3810N	7.2977E	26.046	2.8	1.9	2.9	56	0.16	50.3928	7.3052	27.20
A 020	20170607	11: 7:35.929	50.3757N	7.3257E	27.400	3.5	2.3	2.3	107	0.16	50.3748	7.3080	27.20
A 021	20170607	11: 8:33.781	50.3788N	7.2844E	23.437	2.0	1.6	4.2	51	0.36	50.3766	7.2772	24.20
A 022	20170607	11:35:24.297	50.3746N	7.3057E	24.560	1.8	1.8	3.7	52	0.19	50.3766	7.3024	25.60
A 023	20170607	20:59:17.039	50.3749N	7.3089E	23.571	2.1	1.5	3.1	52	0.16	50.3712	7.2968	24.60
A 024	20170607	21:18:29.779	50.3820N	7.3191E	24.511	2.3	1.7	3.3	51	0.29	50.3748	7.3136	24.40
A 025	20170609	0:43: 2.879	50.3762N	7.2959E	23.624	2.7	2.1	3.8	66	0.17	50.3748	7.3080	24.20
A 026	20170609	2: 7:50.383	50.3735N	7.3066E	23.332	2.7	1.9	3.4	57	0.09	50.3748	7.3024	24.40
A 027	20180605	22:34:41.988	50.3729N	7.3123E	37.478	2.5	1.8	3.6	65	0.20	50.3712	7.3108	37.80
A 028	20180630	3:29:12.984	50.3731N	7.3126E	36.595	2.6	1.8	4.6	58	0.09	50.3712	7.3164	36.80
A 029	20181005	1:27:56.479	50.3996N	7.2716E	9.030	1.9	2.6	3.7	54	0.10	50.3946	7.2912	8.40
A 030	20190322	21:35: 9.702	50.3892N	7.5171E	6.065	3.2	1.9	4.8	170	0.21	50.3928	7.4928	6.40
A 031	20190323	3: 9:37.144	50.3934N	7.4871E	6.996	2.3	1.5	4.3	107	0.53	50.3928	7.4984	7.80
A 032	20190617	22: 2:52.389	50.3840N	7.5295E	4.318	3.8	1.9	4.1	183	0.18	50.3892	7.4956	10.00
A 033	20190625	21:18: 3.029	50.3908N	7.5240E	6.376	3.2	1.7	3.9	82	0.25	50.3928	7.5012	7.20
A 034	20190719	0:56: 3.274	50.3965N	7.5109E	7.986	4.3	2.0	2.7	113	0.13	50.3910	7.5124	7.00
A 035	20190721	16:43:51.113	50.3754N	7.2965E	27.214	2.2	1.7	3.3	54	0.24	50.3712	7.2968	27.20
A 036	20190807	21:13:39.219	50.3837N	7.2954E	38.050	2.7	3.6	3.0	59	0.17	50.3712	7.3024	36.40
A 037	20191029	17:43:52.984	50.3755N	7.3117E	39.450	3.1	3.0	4.6	49	0.22	50.3640	7.2856	39.20
A 038	20200221	18:27: 4.950	50.3976N	7.4763E	5.555	2.3	1.5	4.6	81	0.20	50.3928	7.4984	6.00
A 039	20200309	21: 8:13.319	50.3938N	7.4844E	9.681	2.3	2.4	4.6	152	0.33	50.4018	7.4816	4.60

A 040	20210407	22:28:43.340	50.3707N	7.3167E	35.681	1.8	1.8	2.7	41	0.12	50.3712	7.3024	35.80
A 041	20210506	21:59:47.373	50.3737N	7.3088E	37.250	2.1	2.2	2.6	39	0.19	50.3694	7.3108	37.00
A 042	20210510	18:39: 0.484	50.3664N	7.3117E	35.192	2.2	1.8	3.3	43	0.16	50.3694	7.3052	36.00
A 043	20210619	19: 9:10.298	50.3667N	7.3197E	36.191	3.0	2.1	4.0	44	0.17	50.3658	7.3108	35.00
A 044	20210822	1:18:35.463	50.3619N	7.3184E	34.417	2.7	2.8	4.3	51	0.15	50.3712	7.3024	34.40
A 045	20211117	2:16:54.154	50.3655N	7.3178E	36.084	2.9	2.5	4.0	73	0.09	50.3658	7.3136	35.60
A 046	20211117	2:17:25.057	50.3623N	7.2940E	36.329	3.5	2.6	4.2	81	0.15	50.3604	7.2968	35.20
A 047	20211117	2:42: 4.710	50.3658N	7.2839E	36.183	3.0	2.4	4.4	81	0.26	50.3730	7.3052	36.80
A 048	20211117	2:52: 7.584	50.3687N	7.3117E	37.017	3.2	2.6	3.5	73	0.18	50.3658	7.3024	37.80
A 049	20211117	2:53:16.302	50.3692N	7.3100E	35.257	3.0	2.8	4.3	72	0.14	50.3658	7.3080	34.60
A 050	20211120	2:57:39.857	50.3675N	7.3146E	35.772	3.4	2.8	4.3	73	0.14	50.3622	7.2912	34.80
A 051	20211218	23:26:44.161	50.3737N	7.2809E	35.761	3.3	2.8	4.7	75	0.17	50.3730	7.3080	35.20
A 052	20211218	23:29:19.880	50.3705N	7.3016E	35.391	3.7	2.8	4.4	74	0.11	50.3712	7.2912	34.60
A 053	20211218	23:34:41.155	50.3637N	7.3077E	34.682	3.1	2.7	4.5	77	0.12	50.3658	7.2856	34.40
A 054	20211218	23:36: 5.512	50.3679N	7.3047E	36.986	3.9	2.6	4.3	75	0.08	50.3694	7.2940	34.80
A 055	20211218	23:36:13.977	50.3610N	7.2949E	35.037	3.1	2.6	4.6	81	0.11	50.3676	7.2940	34.00
A 056	20211218	23:44:10.497	50.3683N	7.2958E	35.735	3.5	2.8	4.4	76	0.14	50.3694	7.2940	35.20
A 057	20211218	23:45:37.231	50.3654N	7.3074E	34.091	3.2	2.6	4.5	76	0.20	50.3730	7.3052	34.40
A 058	20211218	23:49:26.017	50.3681N	7.2875E	35.015	2.8	2.5	4.3	77	0.12	50.3712	7.2660	34.40
A 059	20211218	23:54: 8.506	50.3781N	7.2892E	36.976	2.8	2.8	4.6	70	0.09	50.3766	7.2884	35.60
A 060	20211218	23:54:59.734	50.3706N	7.2942E	34.864	3.4	3.0	4.3	75	0.10	50.3748	7.2828	35.20
A 061	20220306	16: 3: 4.567	50.3661N	7.3090E	36.250	3.2	2.4	4.1	65	0.19	50.3658	7.3192	35.60
A 062	20220419	19:44:23.171	50.3632N	7.3115E	34.638	2.4	1.9	3.7	46	0.21	50.3694	7.3080	36.00
A 063	20220629	20:25:49.682	50.3710N	7.3376E	37.731	3.6	2.6	3.8	57	0.24	50.3694	7.3220	38.40

B 064	20141021	0:54:45.631	50.3566N	7.3054E	24.451	2.9	2.8	4.0	128	0.21	50.3658	7.2772	27.80
B 065	20141021	0:55: 3.476	50.3673N	7.2848E	25.960	3.9	3.3	4.6	93	0.06	50.3766	7.2660	27.00
B 066	20150414	21:24:44.990	50.3955N	7.2703E	11.948	3.7	2.3	4.2	129	0.18	50.3820	7.2884	10.20
B 067	20150414	21:29: 9.332	50.3834N	7.2651E	8.020	3.5	2.7	4.4	111	0.36	50.3802	7.2856	11.40
B 068	20150414	21:29:12.261	50.3974N	7.2680E	14.383	4.9	3.6	4.7	153	0.03	-- -- --	-- -- --	-- -
B 069	20150414	21:29:28.080	50.3375N	7.2187E	15.482	4.6	3.3	4.8	182	0.06	50.3226	7.2772	12.20
B 070	20150414	21:31:45.978	50.4025N	7.2822E	10.880	2.2	1.6	3.5	67	0.42	50.3874	7.2744	11.00
B 071	20150911	19:15: 4.043	50.3969N	7.4675E	5.850	2.1	2.2	4.5	80	0.18	50.3946	7.4928	8.00
B 072	20150911	21:50: 7.311	50.3883N	7.5218E	1.017	3.1	2.5	0.0	197	0.14	50.3928	7.5096	5.20
B 073	20150911	23: 8:42.171	50.3963N	7.4673E	5.600	2.7	3.0	4.9	144	0.12	50.3766	7.4900	6.00
B 074	20160624	1: 6:34.106	50.3780N	7.3095E	33.722	2.3	2.5	4.2	50	0.17	50.3712	7.3108	31.00
B 075	20161226	19:29:58.210	50.3479N	7.3372E	45.223	3.9	2.8	4.2	60	0.41	50.3694	7.2996	45.20
B 076	20170604	20:37:59.688	50.3649N	7.3177E	21.588	2.6	2.1	3.4	101	0.19	50.3586	7.3136	22.40
B 077	20170604	20:38:18.261	50.3955N	7.2937E	24.382	3.1	2.8	4.4	95	0.16	50.3802	7.2940	24.20
B 078	20170606	0:21:46.255	50.3670N	7.3231E	25.934	2.7	3.5	4.0	89	0.19	50.3748	7.3052	25.20
B 079	20170606	0:22:19.094	50.3805N	7.3012E	26.978	2.8	2.0	2.4	89	0.30	50.3838	7.2856	27.60
B 080	20170606	0:27: 0.648	50.3711N	7.3108E	24.348	3.1	2.0	3.4	54	0.13	50.3694	7.3164	25.00
B 081	20170606	0:27:15.189	50.3917N	7.2932E	23.013	2.3	2.8	4.6	134	0.11	50.3838	7.3024	22.80
B 082	20170606	0:27:22.850	50.3815N	7.2968E	25.740	2.6	2.1	4.5	88	0.08	50.3802	7.2856	26.00
B 083	20170606	3: 4:24.126	50.3706N	7.3141E	23.933	2.4	2.0	3.9	68	0.11	50.3712	7.3192	24.60
B 084	20170606	3:44:17.255	50.3887N	7.2708E	11.317	3.8	2.5	4.0	137	0.57	50.3982	7.2072	10.80
B 085	20170606	3:44:27.430	50.3719N	7.3100E	21.311	2.7	2.3	3.7	104	0.19	50.3658	7.3220	21.60
B 086	20170606	19:21:51.063	50.3808N	7.3200E	23.960	3.5	3.8	4.5	97	0.17	50.3640	7.3360	24.40
B 087	20170606	20:55:50.314	50.3663N	7.3060E	24.460	3.8	3.0	4.4	106	0.09	50.3748	7.3220	24.20

B 088	20170606	20:59:49.282	50.3787N	7.2960E	21.320	2.9	3.2	4.3	117	0.24	50.3586	7.2912	23.20
B 089	20170606	22:46:14.154	50.3673N	7.3031E	24.586	4.3	2.1	4.3	106	0.09	50.3640	7.3024	24.00
B 090	20170607	10:49: 9.888	50.3657N	7.3177E	26.488	2.8	2.2	3.3	70	0.33	50.3838	7.3136	25.80
B 091	20170607	11:15: 7.940	50.3677N	7.3248E	23.712	2.5	1.5	4.5	70	0.33	50.3676	7.3192	25.20
B 092	20170607	11:35:47.652	50.3675N	7.3189E	24.963	2.8	1.9	4.6	70	0.31	50.3694	7.3080	27.60
B 093	20170607	11:41: 4.408	50.3767N	7.3045E	24.760	2.6	1.8	3.8	75	0.14	50.3784	7.2912	26.00
B 094	20170607	11:41: 4.367	50.3764N	7.3041E	24.920	2.4	1.7	3.8	75	0.16	50.3802	7.2940	26.40
B 095	20170607	17:12:43.385	50.3731N	7.3242E	23.895	4.2	1.9	4.2	106	0.02	50.3748	7.3164	24.80
B 096	20170607	18:36:29.177	50.3705N	7.3040E	24.838	3.6	2.8	3.8	96	0.12	50.3676	7.3192	25.00
B 097	20170607	18:50:53.537	50.3820N	7.3126E	24.393	3.5	2.0	3.9	69	0.16	50.3838	7.3052	25.20
B 098	20170607	19: 4:40.838	50.3697N	7.3160E	23.390	4.9	2.6	4.1	97	0.09	50.3748	7.2912	24.20
B 099	20170607	19:37: 7.333	50.3750N	7.3430E	24.069	3.1	2.2	4.1	124	0.21	50.3766	7.3304	24.00
B 100	20170607	20:23:44.933	50.3746N	7.3511E	23.050	4.9	2.6	4.7	93	0.07	50.3694	7.3472	24.00
B 101	20170607	20:59:43.501	50.3616N	7.2955E	23.538	3.5	2.5	4.1	104	0.18	50.3640	7.2996	23.40
B 102	20170607	20:59:56.435	50.3798N	7.3032E	23.787	3.7	1.7	4.6	62	0.07	50.3802	7.3052	24.20
B 103	20170607	21:16:52.799	50.3793N	7.3168E	24.738	3.6	2.3	4.0	54	0.15	50.3712	7.3360	24.80
B 104	20170607	21:17:44.485	50.3737N	7.3163E	24.279	2.9	3.1	4.0	118	0.16	50.3730	7.3276	24.20
B 105	20170608	0:36:16.869	50.3805N	7.2701E	28.000	4.0	3.2	1.7	132	0.26	50.3964	7.2604	28.20
B 106	20170608	1:58:18.214	50.3682N	7.3291E	21.280	2.9	2.1	4.8	84	0.13	50.3640	7.3276	18.60
B 107	20170608	2:16:41.380	50.3743N	7.3155E	25.578	2.7	2.3	4.6	97	0.19	50.3766	7.3304	24.20
B 108	20170608	3: 0:11.859	50.3713N	7.3041E	24.010	4.0	2.1	4.4	104	0.07	50.3676	7.3136	24.20
B 109	20170608	16:23:29.601	50.3751N	7.3137E	21.651	2.9	1.6	4.5	83	0.14	50.3748	7.2968	22.80
B 110	20170608	18:36:17.571	50.3663N	7.3216E	21.124	3.0	3.1	4.7	90	0.09	50.3550	7.3304	22.20
B 111	20170608	20: 5:28.645	50.3770N	7.2973E	25.803	2.8	2.3	4.3	114	0.20	50.3766	7.3052	24.00

B 112	20170608	20:12:15.932	50.3935N	7.2899E	26.261	2.6	2.5	4.2	136	0.25	50.4054	7.2856	25.40
B 113	20170608	20:26:59.758	50.3775N	7.3029E	23.990	2.3	3.5	4.1	62	0.09	50.3802	7.3024	24.40
B 114	20170608	20:27:46.336	50.3821N	7.3001E	23.020	2.7	2.4	3.8	66	0.11	50.3784	7.3052	24.00
B 115	20170608	20:28: 2.343	50.3736N	7.3093E	22.625	2.5	1.8	3.9	56	0.11	50.3784	7.3024	23.80
B 116	20170608	20:30:30.966	50.3819N	7.3139E	24.603	3.4	2.3	3.8	54	0.13	50.3838	7.3164	25.40
B 117	20170608	21:29:53.179	50.3947N	7.2750E	28.505	2.6	2.3	1.2	100	0.21	50.3982	7.2772	28.00
B 118	20170608	21:40:55.720	50.3882N	7.2951E	25.710	3.3	2.5	4.8	76	0.11	50.3964	7.2856	25.60
B 119	20170608	22:53: 9.082	50.3706N	7.3148E	22.187	2.4	1.7	4.5	54	0.10	50.3712	7.3052	25.00
B 120	20170609	0:34:40.113	50.3875N	7.2972E	21.220	2.3	2.3	4.7	51	0.16	50.3766	7.2996	23.00
B 121	20170609	0:34:52.590	50.3806N	7.3004E	21.337	2.6	1.9	4.4	88	0.20	50.3712	7.3080	21.80
B 122	20170609	0:43:47.927	50.3730N	7.3044E	23.840	3.9	3.7	3.9	105	0.05	50.3784	7.2968	24.00
B 123	20170609	0:44:49.393	50.3820N	7.3081E	25.552	3.1	2.6	4.0	89	0.17	50.3856	7.3052	25.60
B 124	20170609	3:11:39.305	50.3748N	7.2991E	25.847	3.2	3.2	4.3	111	0.06	50.3694	7.2828	27.00
B 125	20170609	3:12:12.573	50.3876N	7.2655E	27.948	3.9	2.9	1.4	81	0.20	50.3910	7.2772	27.60
B 126	20170609	3:13:55.747	50.3936N	7.2767E	28.480	3.5	3.4	1.9	82	0.09	50.3946	7.2800	28.00
B 127	20170609	4:34: 4.070	50.3516N	7.3187E	25.669	2.5	3.3	4.7	69	0.17	50.3406	7.3304	24.20
B 128	20170609	4:34:12.479	50.3730N	7.3281E	25.354	2.6	2.8	4.7	115	0.22	50.3730	7.3164	22.80
B 129	20170609	16:47:47.394	50.3954N	7.2688E	28.160	3.6	3.9	4.1	142	0.12	50.3892	7.2772	27.00
B 130	20170609	16:47:59.669	50.3895N	7.2815E	23.937	2.6	2.7	4.3	96	0.07	50.3838	7.2828	25.00
B 131	20170609	16:51:56.409	50.3774N	7.2988E	22.474	2.7	2.3	3.9	87	0.11	50.3766	7.2940	23.80
B 132	20170610	17:54:51.571	50.3640N	7.3215E	27.148	2.8	2.9	4.8	101	0.15	50.3766	7.3052	28.20
B 133	20170610	19:53:41.023	50.3791N	7.2969E	22.811	2.4	2.4	3.4	50	0.13	50.3766	7.2968	23.60
B 134	20170610	20: 1:42.081	50.3787N	7.3122E	22.068	3.0	3.2	3.9	85	0.13	50.3928	7.3024	22.20
B 135	20170610	20: 7:50.292	50.3812N	7.2881E	24.416	2.2	2.1	4.6	87	0.22	50.3820	7.2940	25.20

B 136	20170613	21:54:28.743	50.3716N	7.2965E	27.952	3.0	3.1	2.0	110	0.18	50.3676	7.2968	27.80
B 137	20170615	18:58:43.300	50.3910N	7.2812E	23.270	4.7	2.7	4.3	95	0.12	50.3874	7.2800	24.40
B 138	20170704	19: 4:50.366	50.3660N	7.3304E	41.252	3.3	2.3	4.1	71	0.18	50.3712	7.3192	42.60
B 139	20170713	0:47:21.078	50.3726N	7.2919E	26.162	2.3	2.2	4.4	67	0.17	50.3730	7.2940	26.20
B 140	20170816	20:35: 2.551	50.3927N	7.4709E	9.050	3.8	3.2	4.2	165	0.08	-- -- --	-- -- --	-- -
B 141	20170907	0: 7:56.783	50.3702N	7.3260E	38.790	4.1	2.3	4.8	126	0.17	50.3802	7.3248	37.80
B 142	20171016	22: 1:31.891	50.3583N	7.3283E	41.387	3.5	2.2	4.4	59	0.10	50.3712	7.3500	41.40
B 143	20171016	22: 2:35.315	50.3652N	7.3193E	36.241	2.3	2.4	4.3	59	0.26	50.3748	7.3220	38.20
B 144	20171025	0: 1:49.150	50.3691N	7.3457E	37.150	3.7	2.3	3.9	133	0.30	50.3712	7.3360	36.80
B 145	20171025	0: 2: 4.800	50.3674N	7.3293E	35.996	2.7	2.0	4.5	56	0.27	50.3640	7.3220	35.40
B 146	20171025	0: 2:13.679	50.3673N	7.3294E	34.861	1.7	2.2	4.3	50	0.36	50.3640	7.3276	36.60
B 147	20171108	1:48:34.381	50.3698N	7.3297E	37.931	4.2	4.0	4.4	128	0.07	50.3856	7.2968	38.40
B 148	20171110	2:50: 8.761	50.3724N	7.3262E	37.846	3.0	2.2	3.9	106	0.18	50.3784	7.3360	38.60
B 149	20171226	14:11:28.096	50.3721N	7.3198E	35.129	2.5	2.0	4.3	70	0.15	50.3712	7.2828	35.40
B 150	20171228	7:52:57.952	50.3640N	7.3043E	36.929	3.2	2.3	4.8	58	0.21	50.3694	7.2828	36.20
B 151	20180223	0:37:46.044	50.3767N	7.2971E	24.706	3.0	2.9	4.4	81	0.15	50.3820	7.2968	25.00
B 152	20180428	2:43:50.212	50.3985N	7.2529E	11.760	2.7	2.7	4.1	76	0.20	50.3802	7.2576	13.00
B 153	20180518	18: 2:17.030	50.3685N	7.3197E	34.514	2.4	1.7	4.3	49	0.12	50.3730	7.2912	36.40
B 154	20180630	3:30:58.669	50.3733N	7.3354E	37.772	2.3	1.6	3.7	49	0.18	50.3766	7.3164	38.20
B 155	20180630	3:31: 0.567	50.3895N	7.3025E	37.020	4.6	4.5	4.1	117	0.05	50.3838	7.3136	38.40
B 156	20180807	22:32:17.609	50.3843N	7.3180E	27.930	3.7	3.8	2.4	69	0.12	50.3766	7.3248	27.00
B 157	20181005	1:26:45.798	50.4121N	7.2385E	7.528	2.1	2.1	2.1	72	0.30	50.4018	7.2548	8.20
B 158	20181005	1:27: 4.778	50.4070N	7.2703E	7.622	1.6	1.8	2.0	58	0.19	50.3874	7.2772	8.40
B 159	20181005	1:28: 9.475	50.3688N	7.2866E	6.040	2.5	2.0	4.4	59	0.35	50.3694	7.2884	7.20

B 160	20181005	1:29:13.475	50.3873N	7.2699E	7.387	1.9	2.4	3.3	85	0.18	50.3910	7.2856	8.80
B 161	20181005	1:29:43.452	50.3931N	7.2622E	7.890	1.6	2.1	2.1	87	0.15	50.3910	7.2660	9.00
B 162	20181005	1:29:55.392	50.3952N	7.2724E	11.209	2.3	2.4	3.3	54	0.21	50.3748	7.2828	11.20
B 163	20181005	1:31:21.199	50.4158N	7.2749E	9.198	1.9	2.7	3.5	97	0.22	50.3928	7.2912	8.00
B 164	20181204	1:28:19.749	50.3692N	7.3297E	37.352	4.1	3.1	3.8	70	0.20	50.3676	7.3080	37.80
B 165	20190205	16:49:51.809	50.3897N	7.4751E	1.090	4.7	4.1	0.2	183	0.06	-- -- --	-- -- --	-- -
B 166	20190222	3:18:49.582	50.3726N	7.5617E	4.016	4.2	3.0	1.6	258	0.22	-- -- --	-- -- --	-- -
B 167	20190322	21:52:24.091	50.4095N	7.4378E	5.390	3.8	2.0	4.6	167	0.17	50.4036	7.4564	7.40
B 168	20190325	19:33:51.215	50.3866N	7.5268E	7.654	3.0	2.4	3.3	178	0.42	50.3946	7.5096	0.00
B 169	20190401	22:16:21.926	50.3947N	7.4998E	7.377	3.4	1.8	4.8	112	0.31	50.3946	7.5012	7.00
B 170	20190406	0:15:40.425	50.3946N	7.4893E	6.198	3.1	2.3	4.7	108	0.21	50.3982	7.4956	5.80
B 171	20190406	15:51: 4.217	50.3682N	7.3646E	36.221	3.3	2.1	4.7	114	0.16	50.3658	7.3500	33.00
B 172	20190408	20: 8:31.806	50.3817N	7.2973E	31.626	4.8	2.6	4.8	119	0.16	50.3856	7.2716	29.80
B 173	20190413	22:15:12.283	50.3745N	7.2954E	28.296	2.6	2.1	1.4	39	0.22	50.3748	7.2968	26.60
B 174	20190708	23: 2:36.459	50.3796N	7.4855E	12.771	4.5	3.4	3.9	187	0.19	-- -- --	-- -- --	-- -
B 175	20190716	15:34:10.140	50.3756N	7.2992E	36.683	4.2	3.2	4.7	101	0.19	50.3586	7.2632	34.80
B 176	20190722	21:12:32.238	50.3668N	7.3111E	24.555	2.8	2.1	3.8	68	0.22	50.3712	7.2996	25.40
B 177	20190807	21: 8: 8.903	50.3782N	7.3225E	40.467	4.2	3.3	4.5	79	0.31	50.3748	7.2772	41.20
B 178	20190807	21:13:48.311	50.3803N	7.3188E	36.730	2.3	2.4	3.8	33	0.20	50.3766	7.3052	37.20
B 179	20190807	21:14: 2.735	50.3735N	7.3124E	35.194	2.9	2.6	4.7	61	0.05	50.3712	7.3108	34.60
B 180	20200207	23:30:25.984	50.3846N	7.4959E	11.992	2.9	2.1	4.5	88	0.32	50.3928	7.4984	6.20
B 181	20200208	4:53:40.502	50.3933N	7.5106E	3.478	2.8	1.7	4.6	154	0.21	50.3910	7.5152	5.20
B 182	20200305	1:15:13.200	50.3961N	7.5387E	6.296	3.5	2.1	4.6	250	0.15	50.4018	7.4900	7.60
B 183	20200408	3:41: 4.379	50.3928N	7.5569E	6.500	3.6	2.2	3.2	255	0.30	-- -- --	-- -- --	-- -

B 184	20200423	21:29:41.843	50.3915N	7.4954E	8.559	3.1	2.2	4.9	158	0.25	50.3964	7.4900	5.40
B 185	20200915	17: 4:25.762	50.3896N	7.3200E	31.049	3.5	2.4	3.9	124	0.20	50.3928	7.2716	30.80
B 186	20201128	15:23: 8.610	50.3601N	7.3259E	41.411	2.8	2.8	4.7	65	0.20	50.3658	7.3080	41.40
B 187	20210407	22:28: 5.653	50.3562N	7.3043E	40.819	3.1	3.1	2.9	50	0.23	50.3712	7.2996	41.40
B 188	20210506	22:42:50.459	50.3676N	7.3310E	35.380	3.0	2.1	4.5	54	0.20	50.3694	7.3080	35.80
B 189	20210510	18:38:21.500	50.3840N	7.3100E	39.424	4.0	2.9	3.4	87	0.19	50.3838	7.2968	37.00
B 190	20210510	18:38:32.330	50.3703N	7.3022E	35.100	2.5	2.1	4.2	42	0.25	50.3802	7.3080	32.60
B 191	20210620	6:30:56.331	50.3848N	7.2907E	28.630	3.2	3.0	1.2	74	0.24	50.3946	7.2940	28.40
B 192	20210817	11:28:34.662	50.3662N	7.3210E	38.010	3.8	3.1	4.9	78	0.22	50.3784	7.3052	38.60
B 193	20210817	11:28:42.825	50.3724N	7.3327E	38.922	4.1	2.4	4.6	102	0.17	50.3748	7.2940	40.00
B 194	20210817	11:29: 9.450	50.3681N	7.3259E	39.670	3.2	2.8	4.8	49	0.26	50.3730	7.3360	39.80
B 195	20210821	5:51: 9.921	50.3748N	7.3362E	39.785	3.1	2.9	4.3	46	0.14	50.3730	7.3332	39.00
B 196	20211117	2:16:29.406	50.3673N	7.3126E	38.307	3.4	2.3	3.4	73	0.19	50.3694	7.2996	37.40
B 197	20211117	2:41:44.773	50.3722N	7.3062E	39.533	4.3	2.7	4.6	71	0.11	50.3730	7.3024	39.00
B 198	20211117	2:42:16.074	50.3714N	7.2966E	37.960	3.2	2.7	4.8	74	0.15	50.3748	7.3108	35.80
B 199	20211117	2:53: 6.855	50.3869N	7.3309E	39.875	3.2	2.6	4.4	60	0.13	50.3766	7.2884	37.20
B 200	20211117	2:55:23.755	50.3644N	7.3030E	35.833	3.7	2.8	4.7	102	0.22	50.3586	7.2828	33.40
B 201	20211117	3:19:23.194	50.3613N	7.2929E	36.818	3.9	2.7	4.2	82	0.16	50.3622	7.2940	35.20
B 202	20211117	3:33:17.257	50.3639N	7.3005E	36.340	3.4	2.5	4.2	78	0.12	50.3604	7.2996	33.00
B 203	20211117	3:33:22.349	50.3814N	7.3177E	38.197	3.7	2.8	4.9	67	0.15	50.3892	7.3024	39.60
B 204	20211117	3:33:52.580	50.3659N	7.3177E	37.768	4.0	2.6	4.4	73	0.22	50.3694	7.3304	37.80
B 205	20211117	3:35:52.267	50.3491N	7.3071E	39.269	4.0	2.9	4.4	86	0.18	50.3460	7.3136	37.40
B 206	20211120	23:56:56.013	50.3624N	7.3181E	37.761	3.6	2.5	3.0	75	0.18	50.3586	7.3024	37.80
B 207	20211120	23:57:15.759	50.3954N	7.3178E	38.134	2.9	2.8	3.9	59	0.28	50.4162	7.3136	36.40

B 208	20211218	23:20: 9.886	50.3635N	7.3253E	36.610	3.9	2.5	4.7	73	0.16	50.3658	7.3136	35.60
B 209	20211218	23:26:49.515	50.3639N	7.2890E	34.456	2.9	4.5	4.8	81	0.12	50.3694	7.2828	35.60
B 210	20211218	23:27:28.141	50.3719N	7.3040E	35.197	3.8	2.6	4.6	88	0.12	50.3676	7.2996	33.60
B 211	20211218	23:32: 9.021	50.3658N	7.3017E	33.872	2.8	2.5	4.5	76	0.18	50.3676	7.2940	34.60
B 212	20211218	23:32: 9.235	50.3778N	7.3088E	36.477	4.4	3.3	4.9	68	0.09	50.3730	7.2576	35.60
B 213	20211218	23:35:29.798	50.3752N	7.3171E	34.153	3.7	3.1	4.7	94	0.13	50.3838	7.2744	33.80
B 214	20211218	23:38:28.565	50.3723N	7.3163E	38.293	3.4	2.4	4.0	70	0.13	50.3712	7.2968	35.40
B 215	20211218	23:38:31.546	50.3772N	7.2827E	36.680	3.1	3.7	4.7	72	0.12	50.3730	7.2800	35.40
B 216	20220324	2: 8: 0.849	50.3683N	7.3010E	39.459	3.1	2.4	3.5	43	0.14	50.3658	7.2912	37.00
B 217	20220324	2: 8: 3.781	50.3604N	7.3147E	40.017	4.1	2.9	4.1	77	0.11	50.3586	7.3108	40.60
B 218	20220401	7: 2:34.641	50.4032N	7.3282E	37.718	3.4	3.0	4.5	98	0.15	50.4108	7.3024	36.40
B 219	20220401	7: 3:27.766	50.3888N	7.3081E	39.781	2.9	2.3	3.0	50	0.21	50.3820	7.2912	37.40
B 220	20220510	0:23:32.360	50.3574N	7.3678E	45.448	3.3	2.7	4.8	61	0.26	50.3568	7.3388	44.00
B 221	20221018	1:49:28.794	50.3920N	7.5042E	13.539	3.2	3.2	4.7	164	0.22	-- -- --	-- -- --	-- -
C 222	20150927	3: 9:39.051	50.3915N	7.2766E	0.011	2.5	1.6	4.2	121	0.67	-- -- --	-- -- --	-- -
C 223	20170517	3:48:32.808	50.3935N	7.3190E	39.260	3.9	3.1	3.0	125	0.14	50.4018	7.3052	40.20
C 224	20170604	20:37: 5.211	50.3636N	7.3058E	23.754	3.7	2.9	3.9	101	0.10	50.3694	7.3136	25.00
C 225	20170604	20:38:57.766	50.3586N	7.3487E	23.658	4.1	3.9	4.0	148	0.19	-- -- --	-- -- --	-- -
C 226	20170606	0:21:54.901	50.3746N	7.2797E	25.505	4.1	2.2	4.0	92	0.17	50.3730	7.2604	25.80
C 227	20170606	0:22:36.969	50.3711N	7.3125E	23.861	4.0	2.3	3.9	96	0.12	50.3694	7.3052	25.00
C 228	20170606	3:44:45.338	50.3716N	7.3067E	25.620	2.9	3.1	3.8	102	0.13	50.3730	7.3080	26.00
C 229	20170606	19:21:10.869	50.3839N	7.3278E	24.910	3.9	2.2	3.7	89	0.17	50.3928	7.3024	28.20
C 230	20170606	19:21:30.181	50.3579N	7.3123E	16.771	2.2	2.7	4.5	98	0.08	50.3640	7.3220	17.20
C 231	20170606	19:23:16.575	50.3909N	7.3007E	24.341	2.7	3.7	4.1	125	0.20	50.3838	7.3164	23.60

C 232	20170606	19:23:44.418	50.3307N	7.3500E	26.289	3.0	3.0	3.2	78	0.38	50.3514	7.3080	25.00
C 233	20170606	20:54:16.846	50.3980N	7.3020E	20.030	2.4	2.9	2.1	133	0.31	-- -- -- -- -- -- -- -		
C 234	20170606	20:54:29.975	50.3929N	7.2155E	18.000	4.9	3.0	4.7	155	0.88	50.3748	7.3780	27.40
C 235	20170606	20:58:44.007	50.3828N	7.3176E	29.680	4.9	3.9	4.3	86	0.10	50.3838	7.3444	28.40
C 236	20170606	21: 0:56.298	50.3908N	7.3016E	24.220	3.9	4.4	4.6	124	0.23	-- -- -- -- -- -- -- -		
C 237	20170606	23:24:23.403	50.3819N	7.4110E	22.960	4.6	3.2	4.2	88	0.15	-- -- -- -- -- -- -- -		
C 238	20170607	11:40:34.669	50.3458N	7.3310E	2.710	3.7	1.8	4.9	117	0.26	-- -- -- -- -- -- -- -		
C 239	20170607	17:20:29.773	50.3847N	7.2945E	17.832	3.6	2.9	4.8	124	0.09	50.3784	7.2940	20.60
C 240	20170607	17:51:39.302	50.3990N	7.3254E	18.970	4.4	3.6	4.2	136	0.22	50.3964	7.3416	17.80
C 241	20170607	18:16: 0.801	50.3757N	7.2914E	25.170	4.0	1.9	4.0	51	0.10	50.3838	7.2968	26.00
C 242	20170607	18:16:44.675	50.3687N	7.2881E	20.520	2.9	2.6	2.8	120	0.10	-- -- -- -- -- -- -- -		
C 243	20170607	19:34:40.372	50.3597N	7.3345E	24.110	3.2	3.6	4.9	104	0.23	50.3352	7.3304	23.80
C 244	20170607	19:37:23.203	50.3819N	7.2833E	26.074	3.8	2.7	4.6	130	0.10	-- -- -- -- -- -- -- -		
C 245	20170607	19:41:54.904	50.3919N	7.3131E	24.626	4.2	2.3	4.5	121	0.12	50.3874	7.2800	24.20
C 246	20170607	21: 1:50.406	50.3615N	7.3122E	23.747	2.5	1.8	4.2	93	0.13	50.3604	7.3024	23.40
C 247	20170607	21:19:10.274	50.3735N	7.2897E	21.984	3.1	3.1	4.3	118	0.17	-- -- -- -- -- -- -- -		
C 248	20170607	21:39:53.918	50.3806N	7.3246E	24.944	4.2	3.0	3.6	120	0.03	50.3802	7.3080	22.60
C 249	20170608	0:59:14.306	50.3470N	7.2791E	19.300	3.3	3.0	4.4	109	0.14	-- -- -- -- -- -- -- -		
C 250	20170608	15:54: 8.609	50.3744N	7.2998E	23.984	3.4	2.1	4.7	111	0.07	50.3766	7.2996	24.80
C 251	20170608	16:22:52.306	50.3774N	7.3088E	24.585	4.7	3.6	4.3	116	0.03	50.3802	7.3052	24.80
C 252	20170608	19:48:10.132	50.3742N	7.3054E	25.132	3.5	3.1	4.6	111	0.05	50.3802	7.2996	24.60
C 253	20170608	19:49:38.470	50.3814N	7.3317E	22.933	3.3	2.8	4.3	137	0.15	50.3820	7.3416	21.20
C 254	20170608	20:55:49.943	50.4160N	7.3054E	29.196	4.8	3.7	4.8	144	0.13	-- -- -- -- -- -- -- -		
C 255	20170608	20:59: 5.421	50.3574N	7.2606E	22.980	4.6	4.0	3.8	118	0.14	-- -- -- -- -- -- -- -		

C 256	20170608	22:53:25.215	50.3836N	7.2856E	22.807	2.1	2.9	4.2	93	0.20	50.3964	7.2744	24.00
C 257	20170608	23:49:25.225	50.3971N	7.2725E	22.350	2.7	2.7	4.6	83	0.10	50.3892	7.2716	25.20
C 258	20170609	0:36:15.640	50.3772N	7.2986E	23.030	4.0	3.2	4.4	124	0.07	50.3748	7.2912	23.60
C 259	20170609	0:36:17.909	50.3864N	7.2900E	24.578	3.1	2.7	4.7	130	0.15	50.3982	7.2716	24.80
C 260	20170609	0:44:20.408	50.3958N	7.2713E	26.763	2.2	3.4	2.4	141	0.14	50.3964	7.2772	27.00
C 261	20170609	3:15:43.621	50.3939N	7.2973E	28.390	4.4	3.9	4.0	132	0.07	50.4000	7.2744	27.60
C 262	20170609	4:34:20.639	50.3848N	7.3029E	22.710	3.6	3.9	3.6	127	0.04	-- -- -- -- -- -- -- -		
C 263	20170610	1: 6:44.192	50.3925N	7.2796E	27.605	3.1	3.1	1.6	98	0.04	50.3910	7.2828	26.80
C 264	20170610	1: 6:55.071	50.3903N	7.2912E	26.000	3.4	4.0	2.8	94	0.06	50.3856	7.2996	20.20
C 265	20170610	1:29:48.238	50.3827N	7.3193E	24.390	3.0	2.3	4.8	69	0.27	50.3910	7.2996	26.40
C 266	20170610	17:40:25.081	50.4151N	7.2804E	28.658	4.5	4.9	3.4	152	0.08	50.4036	7.2744	28.20
C 267	20170704	19: 4:28.069	50.3616N	7.3461E	44.950	4.2	3.5	4.8	106	0.06	50.3694	7.3248	43.80
C 268	20171016	21:59:20.881	50.3826N	7.3492E	37.188	3.4	3.2	4.7	147	0.05	50.3910	7.3108	41.20
C 269	20171228	7:38:48.657	50.3700N	7.2909E	37.822	2.8	2.8	3.7	96	0.19	50.3730	7.3136	37.60
C 270	20171228	7:41:17.977	50.3867N	7.3217E	35.534	3.5	3.6	4.9	125	0.20	50.3892	7.3192	34.20
C 271	20180428	2:39:24.608	50.4100N	7.2570E	7.235	2.1	2.5	3.1	80	0.22	50.4000	7.2632	7.00
C 272	20180428	2:39:40.310	50.4021N	7.2575E	9.887	2.4	2.6	4.1	82	0.21	50.3964	7.2716	9.00
C 273	20180428	2:40:37.396	50.4049N	7.2466E	11.991	3.1	3.1	4.7	87	0.08	50.3838	7.2632	12.60
C 274	20180428	2:41:14.054	50.4652N	7.2367E	8.650	2.5	2.6	4.9	110	0.27	50.4342	7.2856	7.80
C 275	20180428	2:41:53.119	50.3992N	7.3329E	11.192	4.8	3.1	4.3	142	0.06	50.3802	7.3332	10.60
C 276	20180428	2:42:14.963	50.3896N	7.2701E	9.880	2.1	2.5	4.1	85	0.14	50.3748	7.2576	11.60
C 277	20180428	2:42:40.887	50.4140N	7.2644E	16.355	3.1	3.3	4.9	82	0.07	50.3892	7.2828	15.40
C 278	20180428	2:44:10.424	50.3834N	7.2594E	4.476	1.7	2.3	4.8	73	0.28	-- -- -- -- -- -- -- -		
C 279	20180428	2:44:23.840	50.3917N	7.2675E	13.100	3.3	3.3	4.3	82	0.05	50.3820	7.2744	13.20

C 280	20180428	2:44:57.560	50.4144N	7.2524E	5.660	2.1	2.5	4.0	82	0.15	50.4018	7.2632	7.20
C 281	20180518	18: 2:37.229	50.3694N	7.3366E	35.134	3.0	2.2	4.3	58	0.21	50.3730	7.3136	34.00
C 282	20180518	18: 3: 6.198	50.3700N	7.3462E	40.112	2.7	2.1	4.5	111	0.21	50.3712	7.3332	37.60
C 283	20180630	3:29:22.331	50.3670N	7.3122E	31.630	2.8	2.9	4.0	68	0.17	50.3676	7.3164	29.60
C 284	20180630	3:30: 6.835	50.3776N	7.3277E	37.597	3.1	2.4	4.2	107	0.07	50.3784	7.3332	36.40
C 285	20180807	22:42: 5.706	50.3933N	7.2866E	29.241	4.1	2.3	4.4	63	0.08	50.3928	7.2744	28.40
C 286	20180925	19:14:33.420	50.3082N	7.4103E	31.315	3.7	3.1	4.5	71	0.18	50.3370	7.3304	37.60
C 287	20181005	1:29:24.670	50.4022N	7.2606E	8.250	2.3	3.1	4.6	102	0.07	50.4018	7.2800	10.20
C 288	20190122	21:23:18.743	50.3879N	7.4848E	8.170	3.2	2.5	4.8	157	0.26	50.3874	7.4984	9.60
C 289	20190326	19:36:49.450	50.3939N	7.4982E	7.716	4.5	2.4	3.5	157	0.19	50.3910	7.5124	6.80
C 290	20190405	21: 7:24.269	50.3966N	7.5257E	15.349	4.3	3.2	4.8	166	0.12	50.3928	7.4928	6.40
C 291	20190406	15:50:27.334	50.3568N	7.3529E	34.551	3.3	2.2	4.7	101	0.36	-- -- --	-- -- --	-- -
C 292	20190408	20: 8:18.223	50.3774N	7.2859E	32.042	3.8	2.5	4.1	175	0.32	50.3694	7.2688	28.80
C 293	20190408	21:54:48.196	50.3968N	7.4995E	12.565	4.1	2.7	4.9	155	0.14	-- -- --	-- -- --	-- -
C 294	20191030	0: 2:16.395	50.3695N	7.3203E	36.729	3.4	2.7	4.6	100	0.23	50.3676	7.3192	32.20
C 295	20200208	6:14:39.461	50.3878N	7.5184E	1.840	4.5	2.5	0.5	244	0.14	-- -- --	-- -- --	-- -
C 296	20200915	17: 4: 9.336	50.3903N	7.3066E	27.682	3.8	2.4	4.1	119	0.29	50.3964	7.2968	28.80
C 297	20200915	17: 4:14.925	50.3773N	7.2964E	34.176	4.2	2.7	4.8	94	0.19	50.3802	7.2884	31.80
C 298	20210123	2:14:21.766	50.3917N	7.4741E	8.980	2.7	2.7	4.8	116	0.24	50.3928	7.4900	8.60
C 299	20210407	22:28:24.821	50.3510N	7.3106E	33.490	4.0	3.4	4.8	84	0.27	50.3550	7.3080	29.40
C 300	20210407	22:46:39.016	50.3684N	7.3442E	36.146	4.0	3.6	4.5	152	0.22	50.3640	7.3024	33.40
C 301	20210419	5:19:46.745	50.4193N	7.3177E	2.980	4.2	2.4	4.0	132	0.37	-- -- --	-- -- --	-- -
C 302	20210420	4: 5:37.236	50.4206N	7.3378E	0.010	2.8	2.0	4.6	171	0.37	-- -- --	-- -- --	-- -
C 303	20210420	4:12:42.904	50.4168N	7.3380E	3.900	3.1	2.5	3.9	87	0.31	50.4162	7.3276	3.80

C 304	20210420	4:26:59.929	50.4315N	7.3689E	3.597	4.5	3.8	4.7	291	0.18	-- -- -- -- -- -- -- -		
C 305	20210420	5:29:20.267	50.4237N	7.3178E	5.070	4.3	1.8	3.3	132	0.31	50.4252	7.3276	4.80
C 306	20210506	22: 0:15.218	50.3633N	7.2975E	39.901	3.4	2.9	4.2	80	0.12	50.3604	7.2912	40.20
C 307	20210506	22: 6: 5.066	50.3680N	7.3071E	40.430	4.1	3.9	4.5	121	0.22	50.3460	7.3192	38.40
C 308	20210506	22:30:36.747	50.3812N	7.3234E	37.075	3.2	2.7	4.5	98	0.22	50.3694	7.3080	35.00
C 309	20210510	18:40:29.701	50.3581N	7.3325E	31.295	4.2	3.8	4.3	91	0.12	50.3604	7.3416	29.00
C 310	20210521	23:49:30.092	50.4158N	7.2730E	6.524	3.3	4.0	4.1	199	0.10	-- -- -- -- -- -- -- -		
C 311	20210817	11:30:36.607	50.3886N	7.3205E	45.460	4.7	3.0	3.8	87	0.12	50.3964	7.2464	44.40
C 312	20210817	11:37: 2.161	50.3855N	7.2871E	41.279	4.0	2.9	4.7	80	0.27	50.3730	7.2856	37.00
C 313	20210821	5:51:12.327	50.3687N	7.3030E	38.163	3.9	3.2	4.5	130	0.24	50.3748	7.3164	36.20
C 314	20211117	2:16:31.640	50.3650N	7.3021E	37.464	3.0	2.8	3.8	77	0.19	50.3676	7.2912	37.00
C 315	20211117	2:27:35.828	50.3505N	7.2808E	30.741	4.0	3.5	4.7	133	0.12	-- -- -- -- -- -- -- -		
C 316	20211117	2:42:19.954	50.3823N	7.3034E	45.420	4.7	3.5	3.9	124	0.24	50.3838	7.3388	39.80
C 317	20211117	2:51:47.652	50.3732N	7.3183E	37.460	4.0	2.8	4.7	69	0.21	50.3694	7.3080	37.20
C 318	20211117	2:55:39.587	50.3661N	7.2595E	39.920	4.2	2.9	4.7	84	0.31	50.3622	7.2100	37.60
C 319	20211117	2:56:42.090	50.3862N	7.3456E	45.338	4.8	3.5	4.5	67	0.08	50.3856	7.3556	42.20
C 320	20211117	3: 9:18.578	50.3762N	7.2955E	40.160	4.1	3.9	4.2	70	0.18	-- -- -- -- -- -- -- -		
C 321	20211117	3:11: 7.316	50.3363N	7.2693E	48.659	4.3	3.9	4.0	114	0.44	50.3658	7.2156	48.20
C 322	20211117	3:19:33.196	50.3591N	7.3140E	42.009	4.8	3.2	4.9	102	0.14	50.3604	7.3276	39.40
C 323	20211117	3:36:14.765	50.3657N	7.3193E	39.142	3.5	2.6	4.5	72	0.17	50.3658	7.3332	37.60
C 324	20220117	23:56: 5.887	50.3815N	7.3090E	30.455	3.2	2.5	4.7	65	0.48	-- -- -- -- -- -- -- -		
C 325	20220117	23:56:10.482	50.3713N	7.3068E	43.008	3.3	3.0	4.3	49	0.18	50.3784	7.2660	43.00
C 326	20220306	16: 3:20.889	50.3714N	7.3252E	37.109	3.4	3.0	4.2	84	0.22	50.3748	7.3192	35.60
C 327	20220306	16: 3:23.750	50.3764N	7.3880E	38.175	4.3	2.8	4.4	102	0.40	50.3748	7.3528	37.40

C 328	20220306	16: 3:32.820	50.3673N	7.3153E	38.324	4.5	4.1	4.0	151	0.11	50.3622	7.2996	37.60
C 329	20220324	2: 7:53.019	50.3670N	7.2994E	40.845	4.6	3.9	3.5	88	0.09	50.3802	7.3136	36.80
C 330	20220324	2: 8: 6.470	50.3667N	7.3297E	36.924	4.3	3.0	4.6	70	0.21	50.3640	7.3080	35.00
C 331	20220401	7: 3: 8.723	50.3765N	7.3282E	41.632	2.9	3.1	4.6	66	0.22	50.3694	7.3192	37.00
C 332	20221017	21:55:36.832	50.3927N	7.5234E	6.939	3.4	3.2	4.6	178	0.04	-- -- -- -- -- -- -- -		

a) The events that they did not participate in the jackknifing due to their large absolute location errors are:
165, 166, 183, 225, 255, 278, 291, 293, 301, 302, 315, 320 and 324.

b) The events that for them HypoDD could not find any relocalization solution are:
6, 7, 68, 140, 174, 221, 222, 233, 236, 237, 238, 242, 244, 247, 249, 254, 262, 295, 304 and 310.

Both sets of the above events in (a) and (b) are marked by -- -- -- in the table where their relocation parameters using HypoDD are supposed to be written.

c) The event 69, 72, 84, 167, 168, 196, 274, 286 and 321 are considered as the outliers after applying the acceptance thresholds depicted in Fig. c.1.1a
All the above sets of events (in a, b and c) are ignored while plotting the results.